

Active Stall Control of Horizontal Axis Wind Turbines
A dedicated study with emphasis on DBD plasma actuators

Balbino Dos Santos Pereira, Ricardo

DOI

[10.4233/uuid:e1462fab-b35c-4506-aa93-45d37eaf7872](https://doi.org/10.4233/uuid:e1462fab-b35c-4506-aa93-45d37eaf7872)

Publication date

2016

Document Version

Final published version

Citation (APA)

Balbino Dos Santos Pereira, R. (2016). *Active Stall Control of Horizontal Axis Wind Turbines: A dedicated study with emphasis on DBD plasma actuators*. [Dissertation (TU Delft), Delft University of Technology]. <https://doi.org/10.4233/uuid:e1462fab-b35c-4506-aa93-45d37eaf7872>

Important note

To cite this publication, please use the final published version (if applicable).
Please check the document version above.

Copyright

Other than for strictly personal use, it is not permitted to download, forward or distribute the text or part of it, without the consent of the author(s) and/or copyright holder(s), unless the work is under an open content license such as Creative Commons.

Takedown policy

Please contact us and provide details if you believe this document breaches copyrights.
We will remove access to the work immediately and investigate your claim.

ACTIVE STALL CONTROL FOR HORIZONTAL AXIS WIND TURBINES

A DEDICATED STUDY WITH EMPHASIS ON
DBD PLASMA ACTUATORS

ACTIVE STALL CONTROL FOR HORIZONTAL AXIS WIND TURBINES

A DEDICATED STUDY WITH EMPHASIS ON
DBD PLASMA ACTUATORS

Proefschrift

ter verkrijging van de graad van doctor
aan de Technische Universiteit Delft,
op gezag van de Rector Magnificus prof. ir. K. C. A. M. Luyben,
voorzitter van het College voor Promoties,
in het openbaar te verdedigen

op maandag 3 oktober 2016 om 10:00 uur door

Ricardo Balbino DOS SANTOS PEREIRA

Mestre em Engenharia Aeroespacial
Instituto Superior Técnico, Lisboa, Portugal
geboren te Almada, Portugal.

This dissertation has been approved by:

promotor: Prof. dr. G. J. W. van Bussel
copromotor: Dr. M. Kotsonis

Composition of the doctoral committee:

Rector Magnificus	voorzitter
Prof. dr. G. J. W. van Bussel	Technische Universiteit Delft
Dr. M. Kotsonis	Technische Universiteit Delft

Independent members:

Prof. dr. G. A. M. van Kuik	Technische Universiteit Delft
Prof. dr. K. Fujii	Tokyo University of Science, Japan
Prof. dr. J. A. C. Falcão de Campos	Instituto Superior Técnico, Portugal
ir. P. Fuglsang	Siemens Wind Power A/S, Denmark
Prof. dr. ir. L. L. M. Veldhuis	Technische Universiteit Delft, reserve member

Other members:

Ir. W. A. Timmer	Technische Universiteit Delft
------------------	-------------------------------



Keywords: Horizontal Axis Wind Turbines, Active Stall Control, Flow Control, DBD Plasma Actuation

Printed by: Ridderprint

Front & Back: Ricardo Pereira

ISBN 978-94-6299-417-1

Copyright © 2016 by R. Pereira

An electronic version of this dissertation is available at
<http://repository.tudelft.nl/>.

PREFACE

This book is the culmination of 5 very intense years of my life. An unforgettable experience, often stressful and exhausting, but most definitely rewarding, and much more enjoyable than I had thought. Looking back on this period, there are a number of people to whom I am deeply thankful.

First, I thank my promoter Gerard van Bussel, for believing in me, and giving me the opportunity to take on the task of doing a PhD. And for helping and supporting me whenever I needed. Also, I am very grateful to Nando Timmer, my non-official-but-de-facto cool co-supervisor. For his priceless advice. Royal class aerodynamic insight, but also pieces of wisdom about the little of things that make life so grand. Thank you for all the hour-long chats I will never forget.

I would also like to thank my co-promoter, Marios Kotsonis. Just to think that plasma actuators were not originally in my job description, and I ended up doing most of my research on the topic. Of course, plasma actuators are sexy, but it really was your passion about plasmas and experimental aerodynamics that was absolutely contagious. You are truly an enormous source of inspiration to me, with a most exemplar attitude. I seek to treat others in the same way you treated me.

My fourth paragraph goes to Daniele Ragni. Dani, I just love your no-bullshit attitude. I am deeply thankful for all your help, practical, technical, and on every other field. Your love for science is inspiring, and even more admirable is how you do not compromise your principles on the road to become a "famous" scientist. Godspeed my friend, may you live long and prosper!

Also, I am deeply thankful to Sylvia Willems. Behind a sometimes not-so-friendly face, hides a personality that is most kind, absolutely sweet. Thank for all your help with bureaucratic, logistic and official issues, and for your ever-lasting patience towards my chronic messiness. And for always lending me your ear. Also, I would take the opportunity to thank Ruud van Rooij. Being Nando's lifelong buddy and office-mate, you often joined in our most pleasant chit-chats. Throughout the years I admit I often dreaded to receive yet another FLOW email from you, but I deeply appreciate the technical-and-to-the-point advice you provided on a myriad of topics, and the way you handled all the project management/financial issues, and allowed me to concentrate on my research.

A good working atmosphere makes a productive environment, and for that I have to thank all my Wind Energy colleagues. In particular, Linda, for your smile, Wim and Michiel, for your advice, and Gijs, for the delightful discussions on sculpting and on rock'n'roll. And of course, many thanks to all my PhD colleagues with whom I shared the struggle and frustration in "killing the PhD beast". Claudia, Busra, Ben and Giuseppe, from the beginning you made me feel I was in the right place. Lorenzo, Maarten, Wei, Ashim, Sachin, Ye, Zhi, Uwe, Sebastien, thank you for all the good times, and your help whenever I needed. Special big-up to Rene, for translating the summary to dutch. And deep appreciation for my su-

per office mate Etana, from monday to saturday, 11 to 22. Thank you for all the nice (often heated) discussions, delicious lunches and genuine friendship. Obrigado !

I also would like to thank my friends from across the street, Aerodynamics PhD students, in particular to my hilarious mediterranean friends, Theo and Giuseppe. And a deep word of gratitude also to the Aerodynamics' laboratory technicians, Stefan Bernardy and Leo Molenwijk. You made my life so much easier, and I have learned a great deal from you.

Also, I would like to thank the thesis committee members, for their availability and interest in my research, and also for their comments and suggestions to the text which helped to make my message more clear.

Because there is life beyond science, I now show my gratitude to all the people who somehow kept me relatively sane during the crazy PhD years, outside the university. Starting with my good friends Will and Steve, thank for your company, high discussions and awesome times. Always a smile on my face when I think of you.

Music is a big part of my life, one that brings me so much joy, and that I know I can never get away from. My 'brothers' João and Jack, from the bottom of my heart, thank you so much. I cant quite put into words how I feel about the music we do together. I do know the best way to express it is to continue playing :)

Also, I want to thank my trusty side-kicks, paranimfen Vera and Gaël. My dear sister Vera, you are my oldest accomplice, lifelong friend and companion, and I know I can always count on you. Thank you for all the support, in every step of the way. And you are not so stupid : P

And Gaël, old friend. You are the kindest, sweetest, most well-intentioned person I know. And you are the brightest too. Thank you for letting some of your inner light reflect onto me. Thank you for all the amazing scientific contributions (to almost every chapter of this thesis). And above all thank for your friendship, it has been an absolute pleasure. And quoting Incubus "Don't let the world bring you down, not everybody here is that fucked up and cold".

Mom and Dad, words cant express how much you mean to me. Thank you, thank you for everything. Dad, you were the first person to make me question the universe around me, and unveiled the tip of iceberg that is the world of Science. Mom, you show me everyday what it means to be kind and strong. I am still trying to keep up with your lesson.

Finally, a word for my loving partner through almost all of the PhD adventure. Joana, you taught me about love, for bitter and better. May the Cosmos be kind to you in your journey.

*Ricardo Balbino dos Santos Pereira
Vale de Milhaços, September 2016*

SUMMARY

The contribution of sustainable Wind Energy (WE) to the global energy scenario has been steadily increasing over the past decades. In the process, Horizontal Axis Wind Turbines (HAWT) became the most widespread and largest WE harvesting machines. Nevertheless, significant challenges still lie ahead of further expansion of HAWT, namely concerning system robustness and cost-of-energy(COE) competitiveness. This dissertation studies a HAWT design concept termed modern Active Stall Control (ASC). With this concept HAWT power regulation is achieved using flow control actuators to trim the aerodynamic loads across the operational envelope. The underpinning idea is that as the aerodynamic loads are trimmed by flow control actuators without pitching the blades, the pitch system may be mitigated. In turn, this might lead to decreased failure-rates and down-time, and thus eventually present a more cost-effective solution than state-of-the art HAWTs. Going specifically into ASC, if aerodynamic load trimming is performed it is necessary to employ a flow control actuator. From different flow control actuator types, since the aim is to reduce the maintenance and operational costs of ASC machines, actuators with few mechanical parts become more interesting. As such the present research also focuses on the Alternating Current Dielectric Barrier Discharge (AC-DBD) plasma actuator, owing among other things to its absence of moving parts, negligible mass and virtually unlimited bandwidth of actuation.

A preliminary study on the feasibility of active stall control to regulate HAWT power production in replacement of the pitch system is conducted. By taking the National Renewable Energy Laboratory 5 MW turbine as reference, a simple blade element momentum code is used to assess the required actuation authority. Considering half of the blade span is equipped with actuators, the required change in the lift coefficient to regulate power is estimated in $\Delta C_l = 0.7$. Concerning actuation technologies, three flow control devices are investigated, namely Boundary Layer Transpiration, Trailing Edge Jets and Dielectric Barrier Discharge plasma actuators. Results indicate the authority of the actuators considered is not sufficient to regulate power, since the change in the lift coefficient is not large enough. Especially if a pitch-controlled machine is used as baseline case. Active stall control of Horizontal Axis Wind Turbines appears feasible only if the rotor is re-designed from the start to incorporate active-stall devices.

Regarding AC-DBD plasma actuators, three specific topics are investigated. The different studies aim at DBD performance characterization, namely at the influence of external flow on DBD plasma momentum transfer and on the frequency response of actuator flow region characteristic of DBD pulse operation. Both these topics are important to bridge the gap between academic-laboratory employment of DBD and large-size industrial applications. Finally regarding DBD plasma actuator modeling, a method is developed to describe plasma actuation effects in integral boundary layer formulation, and coupled to a viscous-

inviscid panel code (similar to XFOIL), while an experimental campaign is carried to validate the predictions. The three DBD plasma studies are further described below.

Addressing cross-talk effects between DBD plasma actuators and external flow, a study is carried out in which an actuator is positioned in a boundary layer operated in a range of free stream velocities from 0 to 60 m/s , and tested both in counter-flow and co-flow forcing configurations. Electrical measurements and a CCD camera are used to characterize the DBD performance at different external flow speeds, while the actuator thrust is measured using a sensitive load cell. Results show the power consumption is constant for different flow velocities and actuator configurations, while the plasma light emission is constant for co-flow forcing but increases with counter-flow forcing for increasing free stream velocities. The measured force is constant for free stream velocities larger than 20 m/s , with same magnitude and opposite direction for the counter-flow and co-flow configurations. In quiescent conditions the measured force is smaller due to the change in wall shear force by the induced wall-jet. In addition to the experimental study, an analytical model is presented to estimate the influence of external flow on the actuator force. It is based on conservation of momentum through the ion-neutral collisional process while including the contribution of the wall shear force. Model results compare well with experimental data at different external flow velocities, while extrapolation to larger velocities shows variation in actuator thrust of at least 10% for external speed $U = 200 m/s$.

Concerning the response of DBD actuator region flow to pulsed operation, a methodology is provided to derive the local frequency response of flow under actuation, in terms of the magnitude of actuator induced velocity perturbations. The method is applied to an AC-DBD plasma actuator but can be extended to other kinds of pulsed actuation. For the derivation, the actuator body force term is introduced in the Navier-Stokes equations, from which the flow is locally approximated with a linear-time-invariant (LTI) system. The proposed semi-phenomenological model includes the effect of both viscosity and external flow velocity, while providing a system response in the frequency domain. Experimental data is compared with analytical results for a typical DBD plasma actuator operating in quiescent flow and in a laminar boundary layer. Good agreement is obtained between analytical and experimental results for cases below the model validity threshold frequency. These results demonstrate an efficient yet simple approach towards prediction of the response of a convective flow to pulsed actuation. Future application of the methodology might include actuation scheduling design and optimization for different flow control scenarios.

The third study specifically addressing DBD plasma actuators presents a methodology to model the effect of DBD plasma actuators on airfoil performance within the framework of a viscous-inviscid airfoil analysis code. The approach is valid for incompressible, turbulent flow applications. The effect of (plasma) body forces in the boundary layer is analyzed with a generalized form of the von Kármán integral boundary layer equations. The additional terms appearing in the von Kármán equations give rise to a new closure relation. The model is implemented in a viscous-inviscid airfoil analysis code and validated by carrying out an experimental study. PIV measurements are performed on an airfoil equipped with DBD plasma actuators over a range of Reynolds number and angle of attack combinations. Balance measurements are also collected to evaluate the lift and drag coefficients. Results show the proposed model captures the magnitude of the variation in IBL parameters from DBD actuation. Additionally the magnitude of the lift coefficient variations (ΔC_l) induced

by plasma actuation is reasonably estimated. As such, this approach enables the design of airfoils specifically tailored for DBD plasma flow control.

Transitioning into ASC rotor design, and building on the previously presented, a methodology is introduced for designing airfoils suitable to employ actuation in a wind energy environment. The novel airfoil sections are baptized WAP (Wind Energy Actuated Profiles). A genetic algorithm based multiobjective airfoil optimizer is formulated by setting two cost functions, one for wind energy performance and the other representing actuation suitability. The wind energy cost function considers 'reference' wind energy airfoils while using a probabilistic approach to include the effects of turbulence and wind shear. The actuation suitability cost function is developed for HAWT active stall control, including two different control strategies designated by 'enhanced' and 'decreased' performance. Two different actuation types are considered, namely boundary layer transpiration and DBD plasma. Results show that using WAP airfoils provides much higher control efficiency than adding actuation on reference wind energy airfoils, without detrimental effects in non-actuated operation. The WAP sections yield an actuator employment efficiency that is 2 to 4 times larger than obtained with reference wind energy airfoils. Regarding geometry, WAP sections for decreased performance display an upper surface concave aft-region compared to typical wind energy 'reference' airfoils, while retaining common sharp nose and S-tail (characteristic aft-loading) features. Results show there is much to gain in designing airfoils from the beginning to include actuation effects, especially compared to employing actuation on already existing airfoils, which ultimately might pave the way for novel HAWT control strategies.

Finally addressing the complete rotor planform design, an optimization study tailors a HAWT rotor to ASC operation, in a aero-structural-servo formulation. The study considers the aerodynamic and structural loads are in static equilibrium, and as such no unsteady effects are taken into account. The optimization includes planform geometry design but also actuation scheduling, rated rotational speed and spanwise laminate skin thickness. Results show that, compared to variable-pitch turbines, ASC planform displays increased chord at inboard stations with decreased twist angle towards the tip, resulting in increased AOA. Actuation is employed to trim the (static) loads across the operational wind speed envelope and hence reduce load overshoots and associated costs. Comparing with state-of-the-art pitch machines, the expected COE of the ASC rotor does not indicate a significant decrease, but appears to be at least competitive with pitch-controlled HAWTs if the pitch system is effectively mitigated. Additionally, and though not explicitly considered in the present work, it is foreseen ASC might become interesting if the actuation system allows for further OM cost reduction via fatigue load-alleviation, since the actuation trimming load system is anyhow included in an ASC machine.

SAMENVATTING

De bijdrage van duurzame windenergie in de wereldwijde energievoorziening is stabiel toegenomen in de laatste decennia. Gedurende dit proces werden Horizontale-As Windturbines (HAWT) de wijdst verspreidde en grootste machines om windenergie te produceren. Toch liggen er nog belangrijke uitdagingen in het verschiep van de verdere uitbreiding van HAWTs, namelijk betreffende de robuustheid van het systeem en de concurrentiepositie van de energieprijis. Dit proefschrift bestudeert een HAWT ontwerpconcept genaamd moderne Active Stall Control (ASC). Met dit concept wordt het reguleren van het HAWT vermogen gedaan door actuatoren die de stroming regelen, om zo de aerodynamische belastingen te trimmen gedurende het bedrijf. Het onderliggende idee is dat, wanneer de belastingen kunnen worden beperkt door deze actuatoren en zonder te pitchen, het pitchsysteem daarmee onnodig wordt. Dit kan leiden tot lagere storingsfrequenties en kortere uitvaltijd, dus een kosteneffectieve oplossing vergeleken met de modernste HAWTs. Betreffende ASC, voor het trimmen van aerodynamische belastingen is een actuator nodig om de stroming te regelen. Tussen verschillende actuatortypes, omdat het doel is om de kosten van onderhoud en bedrijf van ASC machines te verlagen, worden actuators met weinig mechanische onderdelen interessanter. Daarom focust het huidige onderzoek zich ook op de Alternating Current Dielectric Barrier Discharge (AC-DBD) plasma-actuator, gekenmerkt door het hebben van geen bewegende onderdelen, een lage massa en een nagenoeg oneindige bandbreedte van actuatie.

Allereerst is er een voorstudie gedaan naar de haalbaarheid van actieve stallregeling om de energieproductie te beheersen in plaats van het pitchsysteem. Met de National Renewable Energy Laboratory 5 MW turbine als referentie werd een simpele blade element momentum code gebruikt om de vereiste mate van actuatie in te schatten. Er vanuit gegaan dat de helft van het blad is uitgerust met actuators, moet de liftcoefficient veranderd kunnen worden met $\Delta C_l = 0.7$. Betreffende actuator technieken zijn drie verschillende apparaten getest om de stroming te regelen, namelijk Boundary Layer Transpiration, Trailing Edge Jets en Dielectric Barrier Discharge actuators. De resultaten geven aan dat deze niet voldoende verandering in liftcoefficient teweeg kunnen brengen, zeker niet als een pitchgeregelde machine wordt gebruikt als voetlijn. Actieve stallregeling van horizontale-as windturbines lijkt alleen haalbaar te zijn als de rotor vanaf het begin wordt herontworpen met actuators.

Met betrekking tot AC-DBD plasma-actuators werden drie specifieke onderwerpen onderzocht. De verschillende studies richtten zich tot het karakteriseren van de DBD prestaties, namelijk de invloed van de externe stroming op de impuls overbrenging van DBD plasma en de frequentierespons van de stromingsveld in betrekking tot de gebruikte DBD puls. Beide onderwerpen zijn belangrijk om de kloof te overbruggen tussen DBD apparatuur gebruikt in academische laboratoria en die in grootschalige industriële toepassingen.

Tot slot, betreffende het modeleren van DBD plasma-actuators, is er een methode ontwikkeld om de effecten van plasma-actuatie te beschrijven in een integrale grenslaagformulering, gekoppeld aan een viscous-inviscid panel code (soortgelijk als XFOIL), terwijl een experiment was uitgevoerd om te voorspellingen te valideren. De drie studies naar DBD plasma-actuators worden beneden verder beschreven.

Allereerst, betreffende de overspraakeffecten tussen DBD plasma-actuators en de externe stroming, is er een studie uitgevoerd waarin een actuator is gepositioneerd in een grenslaag onder instroomsnelheden variërend van 0 tot 60 m/s en getest in configuraties van co- en contrastroming. Elektrische metingen en een CCD camera zijn gebruikt om de DBD prestaties te karakteriseren in verschillende snelheden van de externe stroming, terwijl de stuwkracht van de actuator is gemeten door een gevoelige druksensor. De resultaten laten zien dat de vermogensconsumptie constant blijft voor verschillende stroomsnelheden en actuatorconfiguraties, terwijl de plasma-lichtemissie alleen constant blijft onder costroming, maar verhoogt onder contrastroming met toenemende stroomsnelheden. De gemeten kracht blijft constant voor instroomsnelheden hoger dan 20 m/s, met dezelfde grootte en omgekeerde richting in situaties met contrastroming en costroming. In rustige omstandigheden is de gemeten kracht kleiner door de verandering in schuifkracht langs de muur door de geïnduceerde muurstroom. Naast de experimentele studie is er ook een analytisch model gepresenteerd om de invloed van de externe stroming op de actuatorkracht in te schatten. Dit is gebaseerd op het behoud van impuls door het ion-neutrale collisionproces inclusief de bijdrage van de schuifkracht langs de muur. Modelresultaten stemmen goed overeen met de experimentele data in verschillende externe stroomsnelheden, maar een extrapolatie naar hogere snelheden laat zien dat er tenminste 10% variatie is in de stuwkracht van de actuator bij een externe stroomsnelheid van $U = 200$ m/s.

Voor de respons van de stroming over de DBD actuator op het pulseren is er een methodologie gegeven om de locatie frequentierespons af te leiden van de geactueerde stroming, wat betreft de grootte van de door de actuator geïnduceerde snelheidsveranderingen. De methode is toegepast op een AC-DBD plasma-actuator, maar kan worden uitgebreid naar andere soorten gepulseerde activering. Voor de afleiding is de term voor de actuatorkracht geïntroduceerd in de Navier-Stokes-vergelijkingen, waarmee de stroming lokaal wordt benaderd met een linear-time-invariant (LTI) systeem. Het voorgestelde semi-fenomenologische model omvat de effecten van beide de viscositeit en de externe stroomsnelheid, terwijl de respons van het systeem in het frequentiedomein wordt voorgesteld. Experimentele data is vergeleken met analytische resultaten voor een typische DBD plasma-actuator in een rustige stroming en in een laminaire grenslaag. Er is een goede overeenstemming behaald tussen de analytische en experimentele resultaten voor gevallen onder de frequentie waarvoor het model gevalideerd is. De resultaten demonstreren een efficiënte doch simpele aanpak voor het voorspellen van de respons van een convectieve stroming op een gepulseerde actuatie. Een toekomstige toepassing van de methodologie zou zich kunnen richten op het plannen van actuatie en het optimaliseren voor verschillende scenario's voor stromingsregeling.

De derde studie die zich specifiek richt op DBD plasma-actuators presenteert een methodologie om het effect van DBD plasma-actuators op vleugelprofielen te modeleren in het raamwerk van een viscous-inviscid code voor de analyse van vleugelprofielen. De aanpak geldt voor onsamendrukbare, turbulente stromingen. Het effect van (plasma-)lichaamskrachten

in de grenslaag is geanalyseerd met een gegeneraliseerde vorm van de von Karman integrale grenslaagvergelijkingen. De aanvullende termen die voorkomen in de von Karman vergelijkingen leiden tot een nieuwe sluitingsformulering. Het model is geïmplementeerd in een viscous-inviscid code voor de analyse van vleugelprofielen en gevalideerd in een experimentele studie. PIV metingen zijn uitgevoerd over een vleugelprofiel uitgerust met DBD plasma-actuators over een serie aan combinaties van Reynoldsgetallen en invalshoeken. Balansmetingen zijn ook verzameld om de lift- en weerstandscoefficienten te bepalen. Resultaten laten zien dat het voorgestelde model de grootte van de variatie van IBL parameters van de DBD actuatie vastlegt. Daarnaast wordt de grootte van de liftcoefficientvariaties (ΔC_l) geïnduceerd door plasma-actuatie redelijk goed geschat. Zodoende biedt deze aanpak de mogelijkheid tot het ontwerp van vleugelprofielen toegepast op het regelen van de stroming met DBD plasma-actuators.

Voor de transitie naar ASC rotorontwerp, en voortbordurend op wat voorafgaand is gepresenteerd, is een methodologie geïntroduceerd om vleugelprofielen te ontwerpen geschikt voor actuatie in een windenergieomgeving. Deze nieuwe profielen zijn gedoopt tot WAP (Wind Energy Actuated Profiles). Een meerdoelig optimalisatieprogramma voor vleugelprofielen op basis van een genetisch algoritme is geformuleerd door twee kostfuncties te formuleren: de één voor windenergieprestaties en de ander voor de geschiktheid voor actuatie. De kostfunctie voor windenergie gebruikt de 'referentie' vleugelprofielen met een probabilistische aanpak om de effecten van turbulentie en windschering mee te nemen. De kostfunctie die de geschiktheid voor actuatie representeert is ontwikkeld voor HAWT actieve stallregeling, inclusief twee verschillende regelingsstrategieën aangeduid met 'verhoogde' of 'verlaagde' prestaties. Twee verschillende types actuering zijn bekeken, namelijk grenslaagtranspiratie en dielectric barrier discharge plasma. Resultaten laten zien dat het gebruik van WAP vleugelprofielen leidt tot een veel efficiëntere regeling dan referentieprofielen waar actuators naderhand op worden geplaatst, zonder nadelige effecten tijdens bedrijf zonder actuering. De WAP secties geven een actueringsrendement van een factor 2 tot 4 hoger dan wat gehaald is met de referentieprofielen. Wat betreft de geometrie hebben WAP secties met verlaagde prestaties een bovenzijde met achter een ietwat ingevallen vorm, vergeleken met typische 'referentie'-windenergieprofielen, terwijl ze de beschikken over de gebruikelijke scherpe neus en S-staart (karakteristiek achter-geladen). Resultaten laten zien dat er veel te winnen valt wanneer vleugelprofielen vanaf het begin worden ontworpen voor actueringseffecten, vooral vergeleken met wanneer actuering wordt toegepast op bestaande profielen, wat daarmee de weg vrijmaakt voor nieuwe HAWT regelstrategieën.

Tot slot betreft het ontwerp van de complete rotorvorm heeft een optimalisatiestudie een HAWT rotor op maat gemaakt voor ASC operatie in een aero-structureel-servo formulering. Het effect omvatte een ontwerp van de geometrie, maar ook de planning van de regeling, nominale rotatiesnelheid en de huiddikte van het laminaat in de spanwijdterichting. Resultaten laten zien dat, vergeleken met variabele-pitchturbines, de ASC vorm een bredere koordlengte heeft bij de binnenboordse secties met een verkleinde bladhoek richting de tip, wat leidt tot een hogere invalshoek. Actuatie wordt toegepast om de belastingen over de operationele windsnelheden te trimmen en daarmee de doorschot en bijbehorende kosten te verminderen. Vergeleken met de modernste pitchmachines geeft de verwachte COE van

de ASC rotor geen significantie verlaging aan, maar lijkt het tenminste concurrerend te zijn met pitchgeregelde HAWTs zo lang het pitchsysteem ontweken wordt. Daarnaast, alhoewel het in dit onderzoek niet expliciet naar voren komt, is het voorzien dat ASC interessant kan worden als het actueringsysteem kan zorgen voor nog verdere kostenreductie van OM via de vermindering van vermoeiingsbelastingen, omdat het actueringsysteem hoe dan ook aanwezig is in een ASC machine.

CONTENTS

Summary	vii
Samenvatting	xi
1 Introduction	1
1.1 The Need for Power Regulation	2
1.2 Active Stall Control of Horizontal Axis Wind Turbines	2
1.3 Dielectric Barrier Discharge Plasma Actuators	4
1.4 Research Goals	5
1.5 Thesis Outline	6
I Feasibility Study of Active Stall Control for Horizontal Axis Wind Turbines	9
2 conceptual study of Active Stall Control for HAWT	13
2.1 Introduction	14
2.2 Blade Element Momentum Method	15
2.3 Required Authority	17
2.4 Actuator Simulation.	19
2.4.1 Boundary Layer Transpiration	20
2.4.2 Trailing Edge Jets	22
2.4.3 Dielectric Barrier Discharge Actuators	23
2.5 Discussion	31
2.6 Conclusion	33
II DBD Plasma actuator characterization and modeling	35
3 Effect of External Flow Velocity on momentum transfer of DBD actuators	39
3.1 Introduction	40
3.2 Experimental set-up	41
3.2.1 Wind tunnel and load cell	41
3.2.2 Plasma actuator	41
3.2.3 Baseline boundary layer	43
3.3 Experimental results	44
3.3.1 Power consumption and plasma light emission	44
3.3.2 Force measurements.	46
3.4 Momentum transfer Model	50
3.4.1 Ionized fraction and ion drift velocity	54
3.4.2 Model Predictions	55
3.5 Conclusion	56

4	Frequency Response of Flow under AC-DBD pulse actuation	59
4.1	Introduction	60
4.2	Actuator Region Flow as a Linear-Time-Invariant System	61
4.2.1	Linear-Time-Invariant System	62
4.3	The DBD Plasma Actuator Case	63
4.3.1	DBD Plasma Actuator LTI System	64
4.3.2	Linearization Validity	65
4.4	Influence of Viscosity	66
4.5	Experimental Validation	69
4.5.1	Experimental Data Processing	69
4.5.2	Comparison with Measurements	71
4.5.3	Applications and Outlook	74
4.6	Conclusion	74
5	Modeling DBD Plasma Actuators in Integral Boundary Layer Formulation	77
5.1	Introduction	78
5.2	IBL Equations with Force Terms.	78
5.2.1	The Boundary Layer Approximation	79
5.2.2	Integral Boundary Layer Momentum Equation with Force Terms	81
5.2.3	IBL Energy Equation with Force Terms.	81
5.2.4	Non-dimensional IBL Equations with Force Terms.	82
5.2.5	Compact Form of the Body Force Terms	83
5.3	Plasma Specific Treatment of the Force Terms	84
5.3.1	The Plasma Force Field	84
5.3.2	Compact Integral Plasma Terms Estimation	85
5.3.3	The Energy Interaction Coefficient.	86
5.4	Experimental Campaign	88
5.4.1	Flow Facility	88
5.4.2	Airfoil Section	88
5.4.3	Airfoil Model	90
5.4.4	Plasma actuator	91
5.4.5	Particle Image Velocimetry Set-up	91
5.4.6	Experimental Results.	91
5.5	Comparison with Experimental Results.	93
5.6	Conclusions.	94
III	Active Stall Control Rotor Design	97
6	Design of Actuated Airfoils for Wind Energy	101
6.1	Introduction	102
6.2	Optimization Set-Up	102
6.3	Cost Function Definition	103
6.3.1	CF1 - Wind Energy Suitability	103
6.3.2	CF2 - Actuation Suitability.	107

6.4	Actuation Modelling	109
6.4.1	Boundary Layer Transpiration	109
6.4.2	Dielectric Barrier Discharge Plasma Actuator	110
6.5	Results	111
6.5.1	Post-Processing	111
6.5.2	BLT Airfoil Section Geometries and Trends.	112
6.5.3	Plasma Actuation Airfoil Section Geometries and Trends	115
6.5.4	WAP Aerodynamic Performance	116
6.5.5	Considerations on the Effect of the Reynolds Nr and Roughness.	118
6.6	Conclusions.	118
7	Planform Optimisation ASC rotor	121
7.1	Introduction	122
7.2	Aero-Structural Framework.	122
7.3	Actuation System Modelling	123
7.3.1	Control Strategy	123
7.3.2	Actuated Airfoil Section	125
7.3.3	Actuation Power Consumption	127
7.4	Optimization Set-Up	129
7.4.1	Optimization Constraints	130
7.5	Cost Function Definition	131
7.5.1	HAWT Operational Envelope.	131
7.5.2	HAWT Cost Model	131
7.6	Results	133
7.7	Discussion and COE	135
7.8	Conclusion	137
8	Conclusion	139
8.1	Conclusions.	140
8.1.1	ASC feasibility study	141
8.1.2	DBD actuator characterization and modeling	141
8.1.3	ASC design and optimization	143
8.2	Recommendations	144
	Bibliography	147
	Appendixes	157
	List of Publications	163

1

INTRODUCTION

Imagine the world is an infinite, horizontal, omni-gravitic-iso-potential field. As babies we crawl, we reach everything, but at the same time our world is intrinsically 2 dimensional, and we lack perspective. As we grow up and learn to walk, the world is ours to explore, possibilities are endless. But as we trod the world we inevitably take steps. With every step comes a footprint, and as such the often tredded paths dig valleys. Finally, as we grow old we have become so accostummed with the safety of the familiar valley that it is very hard to step outside, nearly impossible to climb out of the valley and explore what was once our whole world of possibilities and perspectives.

Steve van Bennekom

The world growing energy need requires our attention. Sustainable energy technologies emerge as a reality, and a foreseeable future solution to deliver the amount of energy globally consumed. Among different renewable sources, the contribution of Wind Energy (WE) to the global energy scenario [53] has been steadily increasing over the last decades. Nevertheless, future challenges lie ahead of the expansion of WE harvesting installations.

Horizontal Axis Wind Turbines (HAWT) are by far the most common and largest WE harvesting machines. This dissertation studies a HAWT design concept termed Active Stall Control (ASC), in which power regulation is achieved using flow control actuators to trim the aerodynamic loads across the operational envelope. Regarding flow control actuation devices, the present research focuses on the Dielectric Barrier Discharge Plasma actuator, though other active flow control (AFC) technologies are considered.

1.1. THE NEED FOR POWER REGULATION

HAWTs are the most widespread configuration for WE harvesting machines, though other topologies exist. In the early days of HAWT dissemination, from the 1980's, WE harvesting machines were relatively small [111] [90]. Most HAWT were stall-controlled machines, with fixed-speed and fixed-pitch rotors, and thus power regulation across different wind speeds was achieved by aerodynamic stalling of the rotor blades [142]. As such, early HAWT achieved maximum power capture near rated wind speeds, and typically produced less power at higher wind speeds.

In the following decades HAWT became more widespread [53], and also considerably larger. Broadly speaking, by 2000s the HAWT power regulation strategy paradigm had shifted to variable-speed, variable pitch machines [60]. By pitching the blades and controlling the rotational speed across the wind speed envelope, this strategy allows for increased power production compared to early stall-controlled machines. In addition, pitch regulated machines experience decreased aerodynamic load fluctuation [23], and overall load envelope magnitude when compared to early stall-controlled machines, which allows for larger, more slender rotor blades.

Figure 1.1 shows both an early stall-controlled HAWT and a state-of-the-art pitch controlled machine. An illustration of the power production versus wind speed for different HAWT power regulation strategies is shown in figure 1.2.



Figure 1.1: Different HAWT machines - (*left*) Stall-controlled Vestas V17 - (*right*) Pitch-controlled Enercon E126

1.2. ACTIVE STALL CONTROL OF HORIZONTAL AXIS WIND TURBINES

In the last few years the trend towards larger machines and further offshore installation demands for robust design solutions. In remote offshore installations reliability and avail-

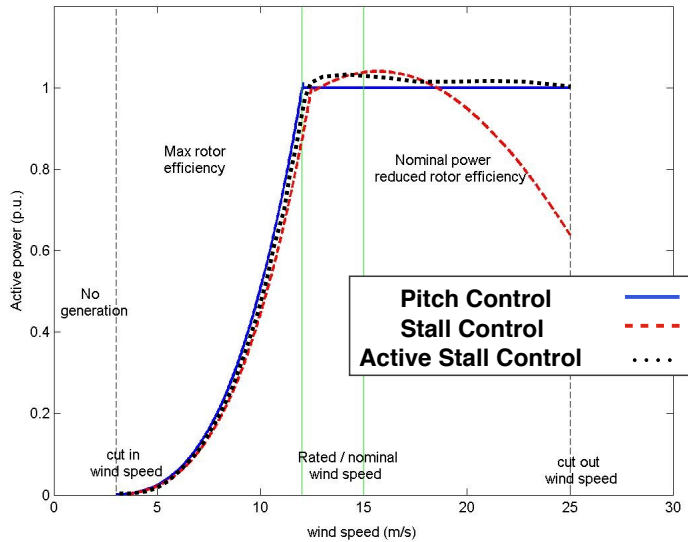


Figure 1.2: An example of different HAWT control strategies (adapted from [95])

ability [41] may become cost-drivers, and as such any improvement in component life time and overall decreased maintenance and repair time is valuable. To meet the new challenge, different concepts for rotors of the future have been proposed, in a wide range of complexity and controllability. Some recently considered concepts include bend-twist passive stall controlled machines [24], yaw-controlled HAWT [33] and the more mature 'Smart Rotor' concept [11] [5] [12].

This dissertation investigates the concept of modern Active Stall Control (ASC) for HAWT power regulation. The idea behind the ASC concept is that the HAWT pitch system could be mitigated (*i.e.* less used) by employing flow control actuators to trim the aerodynamic loads. The flow control actuators actively promote aerodynamic stalling of the blades, thus named Active Stall Control. This added control capability would allow for regulating the HAWT power production across the operational envelope, without using the pitch system. In the modern ASC concept the HAWT is equipped with a pitch system, but it is used in emergency situations only [1]. As such, it would be possible to mitigate the pitch system which may result in decreased failure rates and replacement and overhaul costs, ultimately aiming at a more cost effective WE machine than current pitch controlled technology [60]. The envisioned ASC power curve for different wind speeds is also shown in figure 1.2.

This dissertation studies different aspects of ASC HAWT, attempting at an holistic design approach. The ASC rotor planform and power regulation strategy are designed simultaneously and in integrated fashion. Additionally, this dissertation addresses the design of airfoils specifically tailored for actuation [99] in a WE environment. Such custom airfoil sec-

tions allow for efficient [72] ASC employment, thus ultimately enabling a fair comparison between ASC and other HAWT concepts.

1.3. DIELECTRIC BARRIER DISCHARGE PLASMA ACTUATORS

The concept of ASC for HAWT relies on employing flow control actuators to limit the aerodynamic loads on the turbine rotor and regulate the power production at different wind speeds. In the past, distinct AFC technologies were proposed for application in HAWTs, with excellent reviews given in [6] and [59]. Keeping in mind this research work investigates ASC for remote offshore HAWT, it is desirable that the active flow control system is robust and reliable. As such, this dissertation considers AFC technologies with no moving parts, which should in principle decrease the required maintenance and hence contribute to increased actuation system robustness. Throughout this research work special attention is dedicated to Alternating Current Dielectric Barrier Discharge (AC-DBD) plasma actuators.

Over the last 15 years DBD plasma actuators became very popular among the flow control community. Owing to their negligible mass, large operational bandwidth, absence of moving parts and simple construction, DBD plasma actuators have been considered for a myriad of flow control scenarios. Successful flow control applications include turbulent drag reduction [63], transition delay [48] and streamwise vortex generation [62], and a thorough review on plasma actuators for aerodynamic flow control is given in [96].

Regarding topology, DBD plasma actuators consist of 2 electrodes separated by a dielectric (barrier) layer [113]. The operating principle consists in applying large voltages ($O(kV)$) at high frequencies ($O(kHz)$) to the electrodes, such that the surrounding air is ionized. As the ions collide with neutral air species [86], momentum is effectively transferred to the air, without employing any moving parts. Figure 1.3 illustrates the DBD plasma actuator configuration. It is noted that this dissertation addresses only the alternating current (AC) variation of DBD plasma actuator. As such, throughout this thesis the terminology *DBD* refers specifically to alternating current DBD plasma actuators (and not to *e.g.* the NS-DBD variant).

In recent years several studies proposed AC-DBD plasma actuators as flow control devices for WE machines. In an academic context, applications for performance improvement of both vertical axis [47] and horizontal axis turbines [99] [34] have been studied. More interestingly, the continued research work undertaken at *TOSHIBA* on DBD employment for HAWT enhancement is of paramount importance towards future industrial application. Tanaka *et al.* have carried out the first field test of HAWT equipped with DBD actuators [129] and later managed to scale up the DBD enhanced HAWT application to *MegaWatt* class machines [130].

This dissertation addresses somewhat fundamental aspects of AC-DBD characterization and modeling. Though numerous studies have experimentally characterized DBD performance [67] [132] [8] and modeled DBD behaviour with different levels of fidelity [86] [101] [76], this dissertation addresses topics of specific relevance to DBD actuation employment in HAWT. The present research work aims at characterizing and modeling DBD actuation in a HAWT environment, but it is noted that the developed methodologies may be extrapolated to different actuation technologies and flow control scenarios. All in all, the underlying philosophy is that with increased insight into DBD performance and more ac-

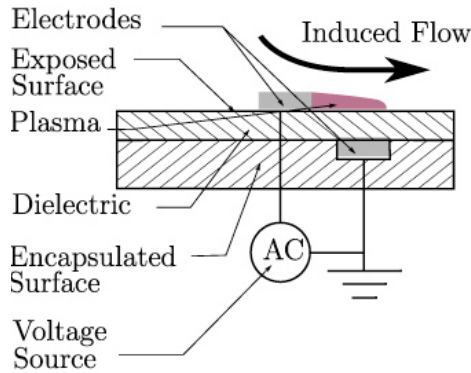


Figure 1.3: Schematic Representation of a DBD Plasma actuator (adapted from [46])

curate DBD modeling, more efficient [72] DBD actuation employment on HAWT machines might be achieved than previous efforts showed [130].

1.4. RESEARCH GOALS

As mentioned before, this dissertation investigates the concept of ASC for HAWT, with emphasis on the AC-DBD plasma actuator as flow control technology. The research goals specifically concerning ASC for HAWT may be stated as:

- Assess the feasibility of the ASC concept and identify main trends and bottlenecks
- Design airfoil sections specifically tailored to ASC operation
- Investigate the optimal rotor design to perform ASC of HAWT
- Compare the ASC performance with state-of-the-art HAWT machines, particularly in terms of the cost of energy

This dissertation contemplates different flow control devices, as to realize ASC. Special attention is dedicated to the DBD plasma actuator, even though the developed tools may have a general application. The main research goals specifically addressing DBD characterization and modeling can be written as:

- Determine the influence of the operating environment on the performance of DBD actuators, focusing on the effect of external flow
- Analyze the local frequency response of the flow in the vicinity of DBD plasma actuators

- Model the effect of DBD plasma actuators in integral boundary layer formulation (IBL)
- Implement the DBD plasma IBL formulation in a viscous/inviscid calculation code, to enable airfoil design including DBD plasma effects

1.5. THESIS OUTLINE

The structure of this dissertation reflects the research goals as formulated in the previous section. It consists of 3 parts:

Part I describes a preliminary study carried out to investigate the feasibility of the ASC concept. It corresponds to chapter 2.

Part II is focused on DBD plasma actuators characterization and modeling in the context of ASC. In chapter 3 a study is performed to assess the effect of external flow on DBD performance. Both experimental characterization and analytical modeling are carried out. Chapter 4 provides a methodology to analyze the local frequency response of flow under DBD actuation. The proposed phenomenological approach may be used for design and optimization of DBD plasma actuation for flow control applications. Chapter 5 presents a model of DBD plasma actuators in integral boundary layer (IBL) formulation. The approach is validated with an experimental campaign, showing the potential the presented formulation may have by enabling airfoil design including the effect of DBD actuation.

Part III describes the design of the Active Stall Controlled Rotor. Chapter 6 explains a methodology developed to design airfoils suited to employ actuation in a wind energy environment. Both DBD plasma and Boundary Layer Transpiration (BLT) are considered as actuation technologies and results indicate (2 to 4 times) more efficient airfoil sections may be obtained. Finally, chapter 7 describes the planform design of the ASC rotor, in a servo-structural-aerodynamic optimization framework. The potential reduction in cost of energy is investigated by comparing the ASC rotor with state-of-the-art pitch controlled machines

At last, the main conclusions of this dissertation and recommendations for future research are given in chapter 8. A flowchart describing the dissertation outline is shown below in figure 1.4

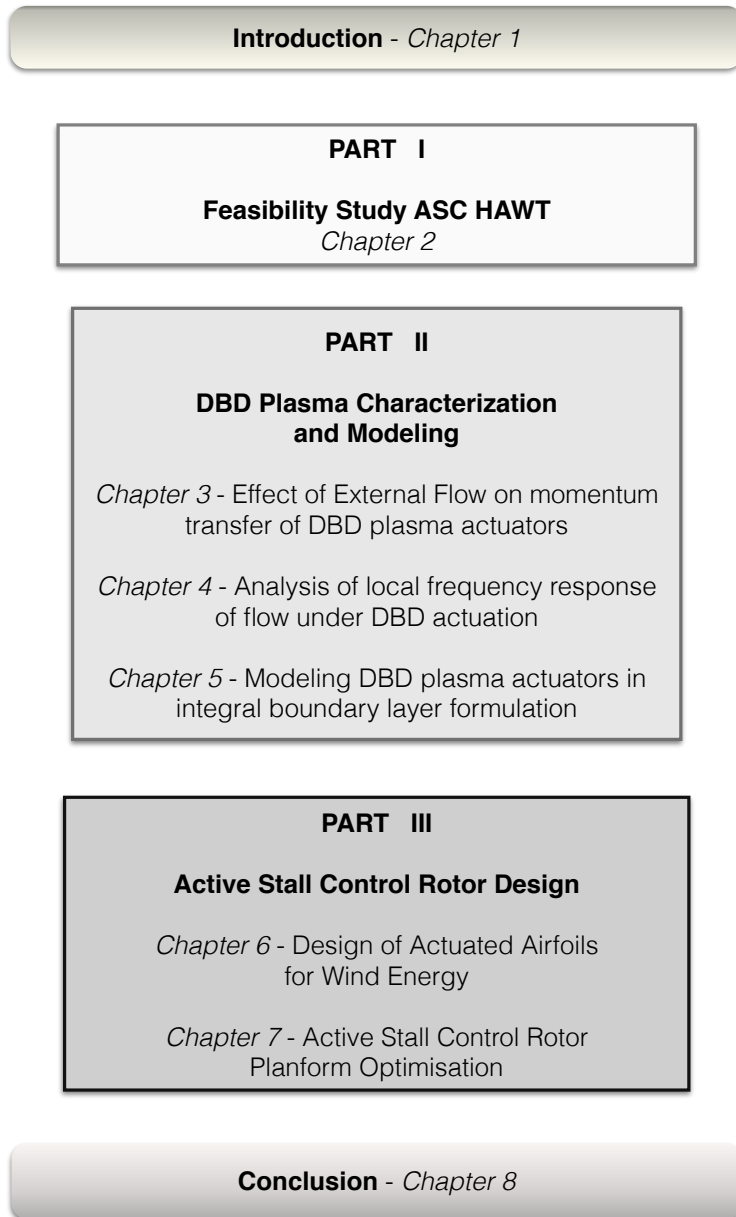


Figure 1.4: Dissertation Layout



**FEASIBILITY STUDY OF ACTIVE
STALL CONTROL FOR HORIZONTAL
AXIS WIND TURBINES**

This part of the dissertation presents an initial feasibility study of the active stall control concept, consisting of chapter 2. The reference turbine *NREL - 5MW* machine is used as a starting point for the investigation, considering different actuation scenarios.

2

CONCEPTUAL STUDY OF ACTIVE STALL CONTROL FOR HAWT

*Sugarman, wont you hurry, I am tired of these scenes,
for a blue coin, wont you bring back, all those colors to my dreams*

Sixto Rodriguez

The increasing size of Horizontal Axis Wind Turbines and the trend to install wind farms further offshore demand more robust design options. If the pitch system could be eliminated, the availability of Horizontal Axis Wind Turbines should increase. This chapter investigates the use of active stall control to regulate power production in replacement of the pitch system. A feasibility study is conducted using a blade element momentum code and taking the National Renewable Energy Laboratory 5 MW turbine as baseline case. Considering half of the blade span is equipped with actuators, the required change in the lift coefficient to regulate power was estimated in $\Delta C_l = 0.7$. Three actuation technologies are investigated, namely Boundary Layer Transpiration, Trailing Edge Jets and Dielectric Barrier Discharge actuators. Results indicate the authority of the actuators considered is not sufficient to regulate power, since the change in the lift coefficient is not large enough. Active stall control of Horizontal Axis Wind Turbines appears feasible only if the rotor is re-designed from the start to incorporate active-stall devices.

2.1. INTRODUCTION

The tendency to increase the size of offshore Horizontal Axis Wind Turbines (HAWT), together with the trend of installing wind farms further offshore, drives the search for more robust designs. Modern HAWTs deployed offshore are variable speed and pitch-controlled. However if the pitch system can be eliminated the maintenance costs are expected to decrease and the availability will increase, which might end up in a lower cost of energy. The power harvested by a wind turbine rotor is given by:

$$P = \Omega Q \quad (2.1)$$

where Ω is the rotational speed and Q represents the aerodynamic torque. Usually wind turbines are designed to produce electrical power at different wind speeds, U , and power control strategies are required to regulate power production. In this respect, modern HAWTs can be divided in two main types, fixed-pitch and variable-pitch machines. For wind speeds below rated, both control solutions impose a constant tip-speed-ratio, $\lambda = \Omega R/U$, by increasing the rotational speed as the wind speed increases. Such a control strategy keeps the HAWT at the optimum operational point, maximizing aerodynamic efficiency. This maximizes the power coefficient, C_P , defined as:

$$C_P = \frac{P}{0.5\rho\pi R^2 U^3} \quad (2.2)$$

where ρ is the air density and R represents the turbine's radius. In other words, for low wind speeds HAWTs harvest as much power as they are capable of. Near and above rated wind speeds the control strategy differs. The rotational speed is usually limited above rated wind speed since the aerodynamic forces are proportional to Ω^2 . Designing HAWTs for larger rated power means designing the blades to withstand higher loads, which is more expensive, and it is not profitable since very large wind speeds do not occur often. This means that at wind speeds above rated it becomes necessary to "waste" some aerodynamic power. In variable-pitch machines the blades are pitched for wind speeds above rated [60], usually decreasing the angle of attack (AOA). This is done in such a way that the rotor aerodynamic torque is kept constant, and equal to the rated generator torque. The rotational speed is also kept constant and thus the power output is constant above rated wind speed. For fixed-pitch machines, the most efficient way of regulating power at wind speeds above rated is to decrease the rotational speed [23], increasing the AOA beyond the stall angle. However, keeping the power constant above rated wind speeds means that the generator must handle larger torque magnitudes than at rated wind speed. Comparing both solutions, pitch-controlled HAWTs are expected to require more maintenance, because of the pitch mechanism. According to [23] the pitch mechanism and bearings have a failure rate which amounts to 14.3% of the total components failure. Fixed-pitch machines however require a larger, more expensive generator, to cope with the large torques experienced above rated wind speeds. For the same rated power, the generator in a fixed-pitch HAWT must be 40% larger, and more expensive [23], than for a variable-pitch machine.

The challenge is thus to come to a solution that combines the advantages of both designs, i.e. eliminating the pitch system while keeping the torque bounded below the value occurring at rated wind speed. This means that circulation at the blade section, and hence

the loading, must be controlled without pitching the blade, i.e. without changing the angle of attack. The present chapter investigates the feasibility of using active stall control rotors as an alternative for pitch controlled rotor blades. Active stall control in the context of the present research means the application of add-ons that actively provoke stall. The National Renewable Energy Laboratory (NREL) 5MW machine [60] is used as a benchmark. A Blade Element Momentum (BEM) code is used to evaluate three different actuation technologies for active stall control: Boundary Layer Transpiration (BLT), Trailing Edge Jets (TEJ), and Dielectric Barrier Discharges (DBD).

2.2. BLADE ELEMENT MOMENTUM METHOD

The BEM method is used to simulate the HAWT aerodynamics. For each radial section, the local forces acting on the blade are decomposed considering figure 2.1.

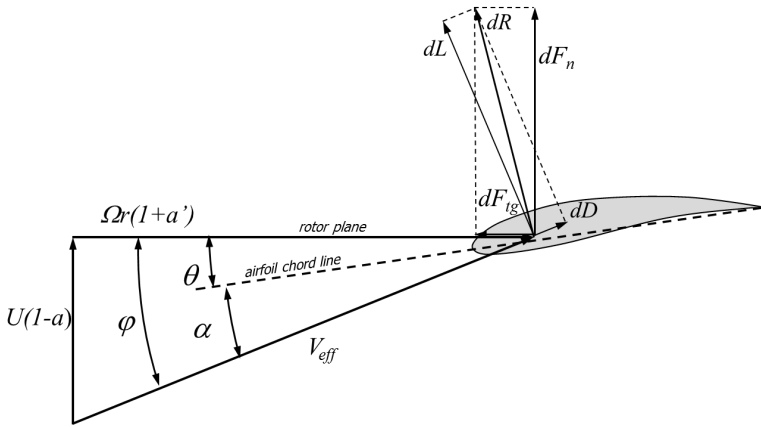


Figure 2.1: Blade Element Decomposition (courtesy of Nando Timmer)

where V_{eff} is the effective speed at the blade section at radius r , and a and a' are the axial and tangential induction factors, respectively. The inflow angle is expressed by ϕ , and the local twist and AOA are represented by θ and α respectively. The aerodynamic forces acting on the blade section can be decomposed into components parallel and normal to the rotor plane, according to

$$\begin{cases} dF_{n_b} = dL \cos \phi + dD \sin \phi \\ dF_{t_b} = dL \sin \phi - dD \cos \phi \end{cases} \quad (2.3)$$

where dL and dD represent the section's lift and drag, dF_n is the force component normal to the rotor plane and dF_t is the force component tangential to the rotor plane. The subscript 'b' denotes the force decomposition refers to a single blade. Integrating the axial force over the entire blade and summing for the 'B' blades, the thrust force is obtained, T . Integrating the tangential force multiplied by the local radius over the whole blade and

summing for the ' B ' blades, the aerodynamic torque is obtained, represented by Q . BEM models divide the streamtube of the HAWT rotor in concentric annuli, assuming each ring at a given radial position is not influenced by the others. For each radial position, BEM models assume values of the axial and tangential induction factor, and based on the geometry of the blade, they compute the local angle of attack. Lift and drag of each blade section are then calculated using look-up tables for the lift and drag coefficient as a function of AOA. These look-up tables take into account rotational augmentation affecting the inboard blade sections. By considering all blades the axial force at each annulus is obtained. Assuming axisymmetric operation, this axial force corresponds to the thrust at each radial section:

$$dT = B(dL \cos\phi + dD \sin\phi) \quad (2.4)$$

Finally the axial force is inserted in the momentum equation and the axial induction factor of each radial station is iterated until convergence is reached, using:

$$C_t(r) \equiv \frac{dT}{0.5\rho U^2 2\pi r dr} = 4a(r)(1 - a(r)) \quad (2.5)$$

where C_t is the thrust coefficient. The present study does not consider heavily loaded rotors since the focus is on wind speeds above rated. Accordingly expression 2.5 is not corrected for the turbulent wake state [91]. The tangential induction factor is derived from the axial induction factor at each radial section by matching the power production from the actuator disk and from the blade element decomposition, according to [91]. The present BEM model includes the so called "tip-correction", from Shen et al [117], which accounts for the fact there is a finite number of blades using a factor F :

$$F = \frac{2}{\pi} \arccos \left[\exp \left(-g \frac{B(R-r)}{2R \sin\phi} \right) \right] \quad (2.6)$$

where g is an empirical coefficient dependent on the number of blades and tip-speed-ratio, expressed by:

$$g = \exp[-0.125(B\lambda - 21)] + 0.1 \quad (2.7)$$

The empirical coefficients of Shen's model were derived using experimental data from two distinct rotors at different tip-speed ratios [117]. Finally the sectional blade aerodynamic coefficients are calculated using:

$$\begin{cases} C_l^{corr} = FC_l \\ C_d^{corr} = FC_d \end{cases} \quad (2.8)$$

where C_l and C_d are the lift and drag coefficients respectively, without the tip-correction, and the ' $corr$ ' superscript denotes the coefficient with the tip-correction. The lift and drag coefficients are defined with:

$$\begin{cases} C_l = \frac{dL}{0.5\rho c V_{eff}^2} \\ C_d = \frac{dD}{0.5\rho c V_{eff}^2} \end{cases} \quad (2.9)$$

where c represents the airfoil section's chord. The implemented BEM code has been validated against the commercial wind turbine design tool *GH Bladed*.

2.3. REQUIRED AUTHORITY

Regardless of the actuation type employed, one must assess how much actuator authority is necessary to keep the power output constant at wind speeds above rated. The larger the actuated area the larger the authority of the whole control system will be, for a given authority of the individual actuators. The actuated section of the HAWT blades is considered to start from the tip of the blades because outboard sections provide greater control over the blade loads, since they contribute more to T and Q due to the larger dynamic pressure and larger radius. This choice is also made because near the root stall delay is expected [123], since the local magnitude of the Coriolis force hampers flow separation. In other words, any actuator with the purpose of promoting flow separation, and thus decrease circulation, is less effective in the root region, and it is thus justified to consider actuation in the outboard region of the blade. At this point it is noted that in this chapter only steady simulations of HAWT aerodynamics are carried out. Though unsteady phenomena have a significant impact on the instantaneous power production [81], in the present ASC feasibility study only steady HAWT aerodynamics is considered to assess the required actuation authority.

The NREL 5 MW machine [60] was used as a baseline turbine, and three different actuated lengths of the blade were considered, namely $L = \{21; 29; 37\} m$, measured from the tip of the blade. These lengths match the transition of the airfoil sections in the NREL 5 MW blade, as shown in figure 2.2.

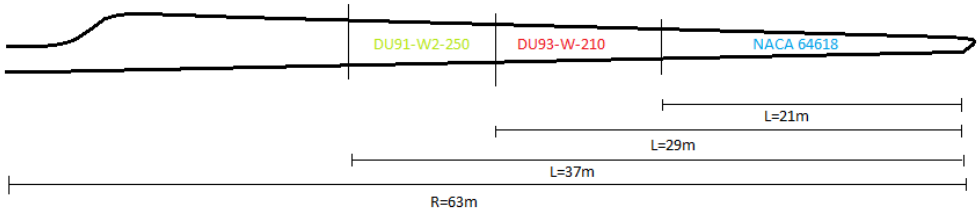


Figure 2.2: Considered Actuated Regions

It is assumed that actuators change the sectional lift, and associated circulation, but not drag, i.e. it is assumed the drag is the same as obtained with an airfoil without actuation. In a fixed-pitch machine, increasing the wind speed beyond rated increases the AOA and consequentially drag; however, larger wind speeds also mean a larger inflow angle and thus a decreased contribution of the drag to the rotor torque. The sensitivity of the local power coefficient, dC_P , to changes in the lift and drag coefficient is expressed by:

$$\Delta(dC_P) = \frac{\partial(dC_P)}{\partial C_l} \Delta C_l + \frac{\partial(dC_P)}{\partial C_d} \Delta C_d \quad (2.10)$$

Assuming the rotational speed and wind speed at the rotor plane remain constant, regardless of the actuation employed, the partial derivatives are estimated:

$$\left\{ \begin{array}{l} \frac{\partial(dC_p)}{\partial C_l} = \frac{\Omega^3 Bc(r)r^2}{2\pi U^3} \sin\phi \\ \frac{\partial(dC_p)}{\partial C_d} = \frac{\Omega^3 Bc(r)r^2}{2\pi U^3} \cos\phi \end{array} \right. \quad (2.11)$$

Clearly C_p is more sensitive to changes in the drag coefficient since it is expected that $\phi < 45 \text{ deg}$ at the outboard sections, even at above-rated wind speeds. The absolute change in the drag coefficient should however be smaller than the absolute change in the lift coefficient. The magnitude of these changes is estimated by looking at the lift and drag polar of the outboard sections subjected to largest AOA, *i.e.* at cut-out wind speed, and comparing it with the optimum AOA. This is illustrated in table 2.1, where $\Delta C_{l_{max}}$ and $\Delta C_{d_{max}}$ are the maximum values of the aerodynamic coefficients occurring within the wind speed envelope considered:

Table 2.1: Aerodynamic Coefficient Envelope

	$C_{l_{opt}}$	$C_{d_{opt}}$	$C_{l_{max}}$	$C_{d_{max}}$	ΔC_l	ΔC_d
NACA64618	0.898	0.005	1.453	0.118	0.555	0.113
DU93-W-210	0.888	0.007	1.402	0.108	0.514	0.101

Table 2.1 shows ΔC_l is much larger than ΔC_d . Still, the effect of changes in C_d in the local power coefficient may be comparable to the effect of the variation in C_l , depending on the actuator and airfoil employed. Nevertheless, because ΔC_d is small and since no concrete information is available for the actuator-induced drag, it is assumed only the sectional lift changes. An actuator which decreases circulation also increases drag, since flow separation is provoked; this means assuming the drag remains the same with/without actuation overestimates the required ΔC_l to be imposed by the actuator.

Different values of C_l are imposed over the actuated portion of the blades and the total aerodynamic power is computed for each combination of sectional C_l and actuated length of the blade. This is done for different wind speeds above rated, $U = \{13; 17; 21; 25\} \text{ m/s}$, covering the above rated envelope of operation. For each of the wind speeds considered, results in figure 2.3 show the aerodynamic power obtained is varying linearly with imposed C_l . This is expected since the torque produced by a blade section is proportional to the local C_l , and also because the contribution of the unactuated inboard sections to the total aerodynamic torque is very small, compared to the actuated outboard region of the blade. The required C_l to reduce the power produced to the rated value, for a given wind speed and actuated blade portion, is found at the intersection with the 'Rated' power line. It is clear that a substantial part of the blade needs to be actuated if the power is to be kept at the rated value, which is understandable since in a pitching HAWT circulation changes over the entire blade as it is pitched. The C_l required to keep the aerodynamic torque at the rated value does not change significantly as different wind speeds are imposed, *e.g.* for $L = 29 \text{ m}$ we have $C_l \in [0.58; 0.7]$. It is also interesting to investigate what is the required ΔC_l , with respect to the blade without actuation, and what AOA occur. Figure 2.4 illustrates this for an actuated length $L = 29 \text{ m}$, for the considered wind speeds. The actuator must be able to decrease the lift coefficient considerably if power regulation is to be achieved. For

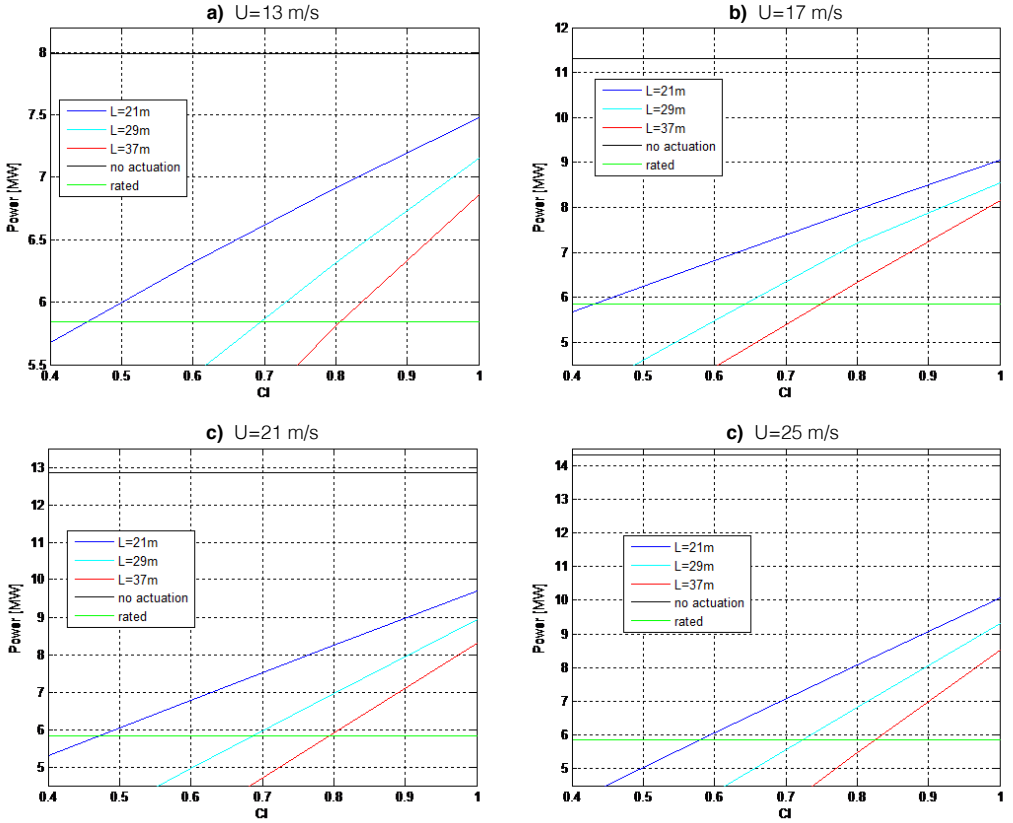


Figure 2.3: Power vs C_l for different actuated lengths, at different wind speeds, $U = 13\text{m/s}$ (a), $U = 17\text{m/s}$ (b), $U = 21\text{m/s}$ (c), $U = 25\text{m/s}$ (d)

the considered baseline turbine at the mid-span airfoil $\Delta C_l = 0.65$ with $\alpha \in [7.5; 22] \text{ deg}$, and at the tip region $\Delta C_l \in [0.52; 0.8]$ with $\alpha \in [7.5; 19] \text{ deg}$. One should keep in mind that these values are obtained for the baseline turbine, which was designed to be a variable pitch machine; nevertheless, the required change in the lift coefficient is quite large and is to be obtained at very large α . Additionally, one should also recall the ΔC_l values estimated for HAWT power regulation were obtained in steady simulations. In reality, due to *e.g.* atmospheric turbulence, blade vibrations, wind shear, etc., the power production is not constant in time, which may indicate that a larger ΔC_l actuator requirement is needed to keep power constant.

2.4. ACTUATOR SIMULATION

In the past, several actuator types were contemplated for application in HAWTs. Distinct actuation objectives have been considered, such as emergency braking [56] or fatigue mitigation [6]. A good review of available actuation technologies is given in [59] and [6]. The

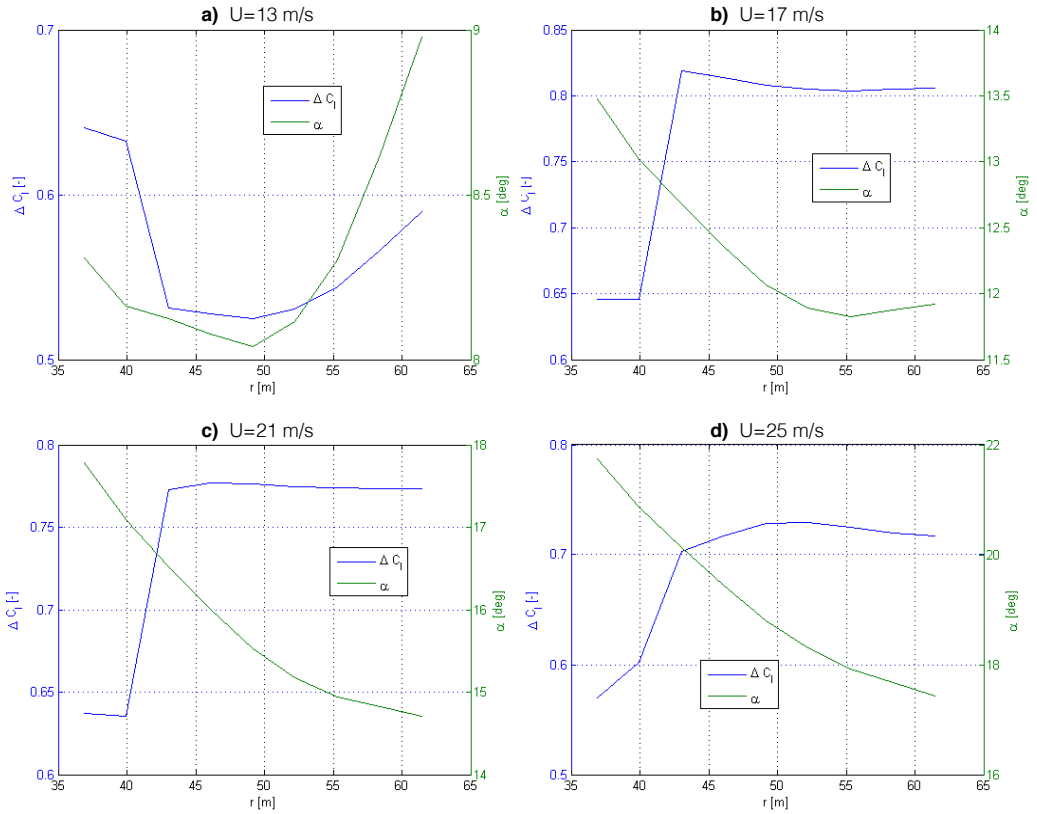


Figure 2.4: Required ΔC_l and α for different wind speeds, $U = 13$ m/s (a), $U = 17$ m/s (b), $U = 21$ m/s (c), $U = 25$ m/s (d)

present study focuses on 3 types of actuators, namely BLT, TEJ and DBD plasma actuators. These technologies were selected because they include no moving parts, which should reduce the maintenance required and hence contribute to increased actuation system robustness.

2.4.1. BOUNDARY LAYER TRANSPIRATION

The first actuation type considered for the modern ASC concept is boundary layer with transpiration, *i.e.* with air being blown/sucked, perpendicularly to the airfoil surface. Since the goal is to decrease the circulation, in the present study only blowing is considered. The aerodynamic code *RFOIL_suc_V2* is used to simulate BLT; this program is an adaptation of Drela's XFOIL [35], using a viscous-inviscid algorithm in which the Euler equations are coupled to an integral boundary layer (BL) formulation. *RFOIL_suc_V2* accounts for the stall delay caused by the HAWT blade's rotation, based on user-provided radial pressure gradient and local solidity. In the present case however rotational effects are neglected since only outboard blade sections are considered. The code also allows for different porous

chordwise regions and transpiration velocities to be imposed. RFOIL_suc_V2 is described and experimentally validated in [31], for different suction velocities and aft porous lengths. The transpiration velocities are modelled as perturbations, while the BL hypothesis is still assumed. More specifically, the closure relationship used for the skin friction coefficient to solve von Kármán's integral BL equation assumes that the turbulent structures are unchanged by the imposed transpiration [31]. In two dimensional incompressible flows, introducing the BL approximation in the continuity equation yields:

$$\frac{\partial u}{\partial x} + \frac{\partial v}{\partial y} = 0 \implies O[v] = \frac{V_{eff}}{\sqrt{Re}} \quad (2.12)$$

where u and v are the velocities in x and y direction, respectively, and Re represents the Reynolds number of operation. Considering BLT, at each chordwise station the transpiration velocity coincides with v . In the present case $Re \approx 10 \times 10^6 \implies O[v] \approx V_{Eff} \times 10^{-3}$, meaning the code from [31] should not be used while imposing large transpiration speeds since its validity becomes questionable. Also, the ability of this tool to predict airfoil flows with large separated regions is limited. This is because the effect of the BL on the potential flow is modelled only to first order effects, meaning that only small equivalent airfoil shape changes may be captured. Moreover the shape of the wake is calculated based on the inviscid solution, which again is only valid when the flow is separated over a small portion of the airfoil. Despite these limitations, this tool was considered adequate to estimate the potential for sectional lift coefficient manipulation through BLT. Employing more accurate methods such as direct numerical simulation implied a very large computational effort, and was not suitable for a preliminary study on active stall control of HAWTs.

Simulations are performed at $Re = 10 \times 10^6$, which matches the conditions found at a 5MW machine at rated wind speeds and above. Different airfoils, different porous regions and various transpiration velocities are considered. Results show that when BL blowing is applied near the trailing edge (TE) the reduction in C_l is small, when compared to the clean configuration. As the AOA increases, TE blowing has practically no-effect since the flow in the TE region is anyhow separated. When blowing is applied in the leading edge (LE) area considerable changes in the aerodynamic loading are obtained, and the C_l remains practically constant for high angles of attack. Figure 2.5 shows the results obtained for the DU93-W210 and NACA 64618 profiles, which are used in the baseline turbine. The lift curves are obtained imposing a porous region located on the airfoil suction side, ranging from $x/c_{por} \in [0.05; 0.2]$. As the blowing speed increases the lift decreases, which is expected since separation takes place further upstream. The blowing velocities indicated, V_b , are relative to the free stream velocity; The relation of the lift decrease with the blowing speed is identical for both airfoils, *e.g.* $V_b = 0.006 \implies \Delta C_l \approx 0.2$. Also, the lift decrease compared to the unactuated case is much smaller before stall occurs naturally, *i.e.* for small AOA. The effect of the porous region location and length was tested. Prolonging the porous region further downstream did not decrease the lift coefficient, possibly because flow separation is anyhow taking place at chordwise positions more upstream than $x/c = 0.2$. When the porous region started before $x/c = 0.05$ convergence was only obtained for small angles of attack, meaning that the decrease in the lift coefficient provoked by the transpiration could not be quantified.

It appears that, for large angles of attack, the decrease in lift coefficient varies linearly

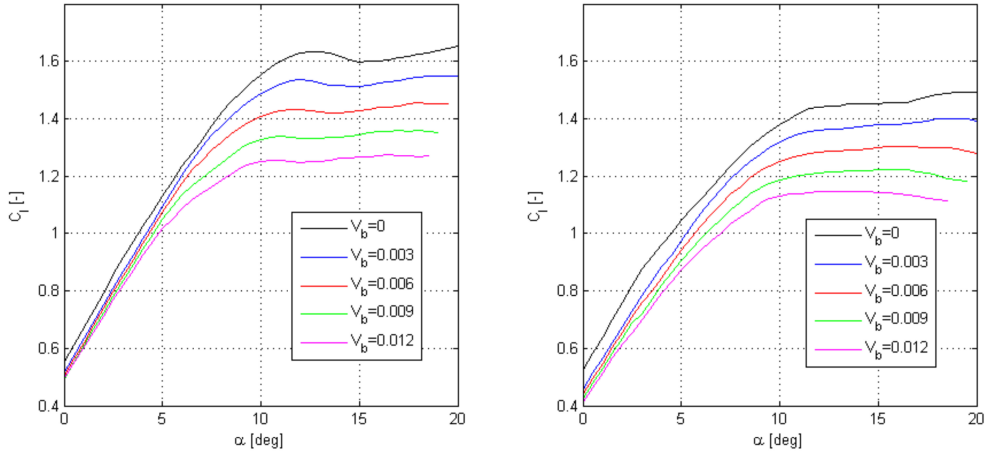


Figure 2.5: C_l vs α for different blowing speeds V_b applied at $x/c \in [0.05; 0.2]$. *Left*- DU93 - W - 210 and *Right* - NACA64618

with imposed blowing speed. Extrapolating this trend, if one assumes half the blade is actuated and the porous region ranges from $x/c_{por} \in [0.05; 0.2]$, power regulation should be achieved imposing $V_b = 0.021$. Earlier separation could perhaps be obtained at a more upstream location, with a smaller mass flow, but this cannot be predicted with the aerodynamic tool used.

At this point it should be mentioned that on most HAWT blades there is a spar around the region of maximum thickness. It is foreseen that it may become complicated to employ a porous surface at the spar region, and as such this factor must be taken into when considering real implementation of BLT on HAWT blades. This issue is further addressed in chapter 6 of this dissertation.

2.4.2. TRAILING EDGE JETS

There is interest in TE devices since they are capable of producing a significant change in lift [6]. As hinted by its designation, trailing edge jets (TEJ) are jets of air which exit the airfoil contour located at the TE region. TEJs are usually placed at a chordwise position around $x/c \in [0.9 - 0.95]$, and the blown air jet creates a stagnation streamline exiting the airfoil, different than the one obtained without actuation; this changes the Kutta condition and thus the circulation and aerodynamic loading of the airfoil section. If the TEJ is placed on the suction surface it will act to decrease the circulation, and vice-versa. When compared to other TE devices such as flaps, TEJ have fewer moving parts and should thus be more robust [17]. It is usual to characterize TEJs using the jet momentum coefficient, defined as:

$$C_\mu = \frac{\dot{m}_{jet} \cdot U_{jet}}{0.5 \rho U_\infty^2 A} \quad (2.13)$$

where m_{jet} is the jet mass flow rate, U_{jet} is the jet velocity, ρ is the air density and A is the blade section area; this quantity expresses the ratio of the net momentum of the jet to the dynamic pressure of the free stream flow. For an incompressible fluid $\rho_{jet}=\rho$, and in two dimensions expression 2.13 reduces to:

$$C_\mu = \frac{U_{jet}^2 h_{jet}}{0.5U_\infty^2 c} \quad (2.14)$$

in which h_{jet} is the chordwise width of the jet exit. Results from [15] show Re has negligible influence on the ΔC_l obtained with a given TEJ configuration. Figure 2.6 shows the effect of TEJ on the sectional lift of the *NACA0018* airfoil. The change in lift is not symmetric for the lower and upper surface jets. According to [15], this is because the BL development is different at the two sides. For large angles of attack, the BL is thicker at the suction surface, which means TEJ will have a larger effect on pressure surface (which decreases C_l). It is clear that ΔC_l is proportional to $\sqrt{C_\mu}$, which is also reported in [106]. Even though

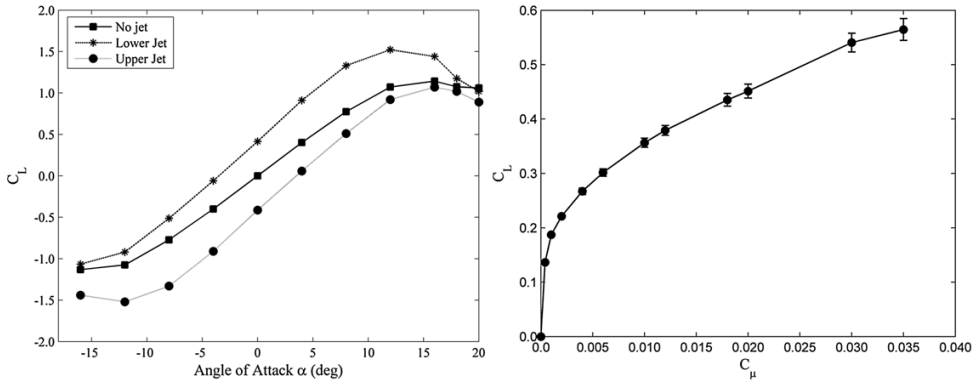


Figure 2.6: C_l of a *NACA 0018* airfoil at $Re = 6.6 \times 10^5$ and $Ma = 0.176$ with TEJ located at $x/c = 0.9$ and $h_{jet} = 0.006c$ from [15]. *Left* - C_l vs α for $C_\mu = 0.012$ and *Right* - C_l vs C_μ for $\alpha = 0^\circ$

figure 2.6 illustrates the influence of TEJ for a specific airfoil, comparable results are found for different airfoils [15],[22]. Accordingly the present study assumes the same $C_l = f(C_\mu)$ dependence applies. It is also verified that the authority of TEJ is reduced for large AOA since flow separation naturally occurs in the TE area. At AOA beyond stall the TEJ has no practically effect.

2.4.3. DIELECTRIC BARRIER DISCHARGE ACTUATORS

DBD actuators consist of two electrodes with a thickness in the order of $10^{-5}m$, separated by a dielectric with a thickness of up to a few *mm*. The air is ionized by applying a large cyclic electric potential difference at the electrodes, and the local electric field transfers momentum to the air. The actuator is represented in figure 2.7 and the interested reader is referred to [132], [96] for a more detailed description. These devices have no moving parts or pneumatic systems, which makes them attractive in applications where robustness is important,

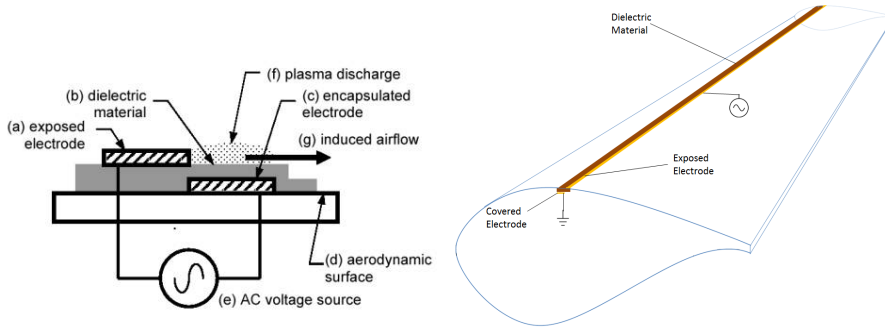


Figure 2.7: Plasma Actuator Diagram - *Left* DBD Representation - *Right* Working Schematic of DBD Actuator on HAWT Blade

such as offshore wind turbines. Another important characteristic of DBD plasma actuators is the virtually unlimited bandwidth of operation [9]. As further discussed in chapters 3 and 4 of this dissertation, because of the operating principle and (electric) force generation mechanism, DBD plasma actuators act almost instantaneously [38], with a response time $O(10^{-7})$ s. The main issue associated with using the present DBD state of the art is that at large Re there is not sufficient authority. However, by optimizing the electric signal and geometry of the actuator it is possible to produce a body force that is one order of magnitude larger [132] than previous studies indicate. A scheme of the working configuration of the DBD actuator on the HAWT blade is also indicated in figure 2.7.

In the present study the authority of the DBD actuator is analyzed by investigating whether the device is able to provoke separation under the flow conditions of the baseline turbine. In aerodynamics, separation is considered to take place when there is flow reversal, which implies there is a streamline exiting the airfoil surface. At this chordwise point the flow detaches from airfoil surface, *i.e.* it separates. If an airfoil operates at large α , the flow on the suction-side naturally separates, leading to a decreased suction length and consequentially lift reduction. Accordingly, determining whether or not an actuator induces or delays separation enables the estimation of how much authority, in terms of ΔC_l , is achieved. Over the years several criteria have been put forward to determine if separation occurs, different for laminar and turbulent flow. A good review is given in [122]. For simplicity in the current study it is initially assumed that the DBD acts as a point force by considering the total force transferred to the air. It is assumed that the actuator force $F_{act} = 0.2 N/m$, since this is the maximum value obtained in experimental studies dedicated to maximizing the actuator body force [132]. The actuator is assumed to operate at $V_{eff} = 60 m/s$, corresponding to the effective velocity at rated rotational speed with $r/R = 0.75$.

LAMINAR FLOW

There is no consensus among the wind energy community on how much of the flow experienced by HAWT blades is laminar. While rotational effects tend to delay transition [52], blade contamination cannot be avoided [139] and leads to early transition. Moreover,

wind turbulence intensity also influences the transition process [94]. Consequentially, in HAWT environment laminar flow should also be considered. In the current study Thwaites' method [21] is used to predict separation in the laminar regime, according to which there is separation if

$$\beta = -0.09 = \frac{\theta^2}{\nu} \frac{dU_e}{dx} \quad (2.15)$$

where β is a pressure gradient parameter, θ is the BL momentum thickness, ν is the kinematic viscosity and U_e is the local velocity external to the BL, obtained in inviscid flow. More complex methods of predicting laminar separation exist, but Thwaites' approach is used in a straight-forward fashion since the momentum produced by the actuator can be supposed to modify the momentum thickness directly. The BL momentum thickness at each chordwise position translates the decrease in momentum the BL flow has sustained; this thickness is the distance perpendicular to the wall that, in inviscid flow, yields the momentum flux that matches the momentum deficit. By multiplying this distance with the density and local external velocity, the total force exerted on the air by the wall up to the considered chordwise position is determined [21]. This is expressed by:

$$F_{wall} = \rho \theta U_e^2 \quad (2.16)$$

Assuming the density and external velocity do not change as actuation is employed, the new local momentum thickness is obtained from equation 2.16 by adding the actuator force to the wall force. Thwaites' criterion is then employed to see whether separation is provoked.

Simulations were performed for the laminar regime, for $\alpha = \{8; 11; 14; 17\}$ deg. Figure 2.8 shows the value of the pressure gradient parameter β obtained by applying the actuator at each chordwise position, and also the separation threshold. The actuator will increase the momentum thickness locally and not over the whole laminar BL. However, figure 2.8 provides insight on where it is more advantageous to place the actuator since it shows, for each chordwise station, what is the maximum increase (in absolute value) in β obtained by employing a DBD actuator. Results are shown only for the laminar regime, i.e. upstream of the transition point since the criterion is only valid for laminar flow. Thwaites' criterion was derived for a flat plate, but in the present case $\frac{\partial U_e}{\partial x}$ was replaced with $\frac{\partial U_e}{\partial s}$, where ds represents the elemental contour of the airfoil in the LE area. Using more than one actuator yields a larger force of actuation, but it does not add linearly [132]. Different actuator forces were considered, ranging from 0.2 to 0.8 N/m. The aerodynamic code RFOIL was used to estimate the evolution of the BL variables along the contour of the *NACA64618* airfoil $Re = 10 \times 10^6$. Minding figure 2.8 it is clear that the angle of attack of operation has a small influence on the location of the suction peak, indicated in the figures above by a zero value of β . The suction peak is moving upstream with increasing angles of attack. More importantly, the figures indicate it is not possible to provoke LE separation with DBD actuators operating in laminar flow since $\beta > -0.09$. This is the case for all the simulated α , even considering rather optimistically an actuator force of 0.8 N/m.

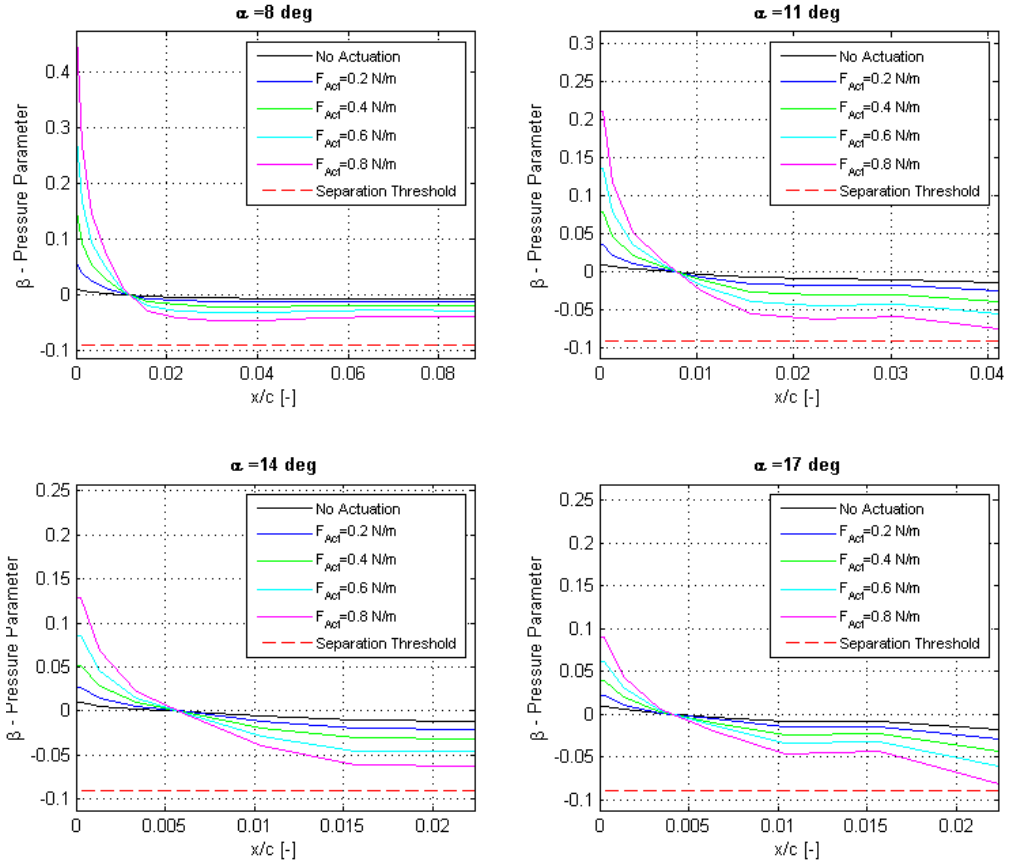


Figure 2.8: Laminar Separation Criteria as DBD actuation is applied for $\alpha = [8; 11; 14; 17]$ at $V_{eff} = 60$ m/s

TURBULENT FLOW

For turbulent flow, separation is predicted with the Stratford criterion[127]. Other turbulent separation criteria exist, mostly based on the local shape BL factor H . Such methods however cannot be used straightforwardly because only the total thrust of the actuator is known from experiments, which translates into a change in θ ; the change in BL displacement thickness δ^* is not known, and thus the change in H cannot be directly estimated. According to Stratford separation takes place when:

$$C'_p \sqrt{x' \frac{dC'_p}{dx}} = K \left(\frac{Re}{10^6} \right)^{0.1} \quad (2.17)$$

where C'_p is the canonical pressure coefficient and x' is the effective BL length and K is

an empirical constant. The canonical pressure coefficient is defined based the maximum speed over the airfoil, U_{max} , occurring at the suction peak. This is expressed by:

$$C'_p = \frac{p - p_{min}}{0.5\rho U_{max}^2} \quad (2.18)$$

where p_{min} is the minimum pressure, occurring at the suction peak. The effective BL length is introduced to account for the development of the BL prior to the suction peak. 'Effective length' is the length the BL would need to develop in a zero-pressure-gradient such that approximately the same values of the integral BL quantities are obtained. In the present case, the effective length is smaller than the actual length, since up to the suction peak the pressure gradient is favourable, and thus the boundary rate of growth is smaller than in a flat-plate configuration. For the cases under consideration the suction peak is located upstream of the transition point, as seen in figure 2.8. According to [21], the effective laminar length at the suction peak is given by:

$$x'_{lam_{suc}} = \int_0^{x_{suc}} \left(\frac{U_e(x)}{U_{max}} \right)^5 dx \quad (2.19)$$

where x_{suc} denotes the chordwise position where the suction peak is located. From that point up to the transition location, the effective BL length is calculated with:

$$x'_{tr} = x'_{lam_{suc}} + (x_{tr} - x_{suc}) \quad (2.20)$$

Assuming that during transition the momentum thickness θ remains constant[21], the effective turbulent BL length is computed by equating it with the laminar momentum thickness and reversing the expression for the flat plate solution:

$$\theta_{tr_{lam}} = \theta_{tr_{turb}} = x'_{turb_{tr}} 0.036 (Re_x)^{-\frac{1}{5}} \quad (2.21)$$

where Re is calculated using the free-stream velocity. Downstream of the transition point, the effective turbulent BL length is calculated using

$$x'_{turb} = x'_{turb_{tr}} + (x - x_{tr}) \quad (2.22)$$

One should note the position of the stagnation point changes as different α are imposed. This is taken into account by changing the lower limit of the integral in expression 2.19.

For the turbulent case it is necessary to assume more of the actuator's characteristics than in the laminar regime. The geometric parameters of the DBD actuator are chosen to match the configuration yielding the largest thrust [132]. The dielectric material is Teflon with a thickness of 6.3 mm, the exposed electrode length is 12.7 mm and covered electrode length is 25 mm. By applying 25 kV_{rms} at 2.2 kHz in a positive sawtooth waveform this actuator should yield $F_{act} = 0.2 N/m$. The body force volume is characterized by a height $h = 2 mm$, measured perpendicular to wall, and a length $l = 25 mm$, which is the same as the covered electrode. Regarding the spatial distribution of the force field, the body force density in the streamwise direction, with units N/m^3 , is estimated with:

$$F_x = A \sin\left(\frac{\pi x}{l}\right) \sin\left(\frac{\pi y}{h}\right) \quad (2.23)$$

where the origin of the coordinate system is situated at the upstream side of the exposed electrode, and $x \in [0; l]$ and $y \in [0; h]$. An illustration of the implemented body force spatial distribution is shown in figure 2.9. This body force distribution yields ellipse-like

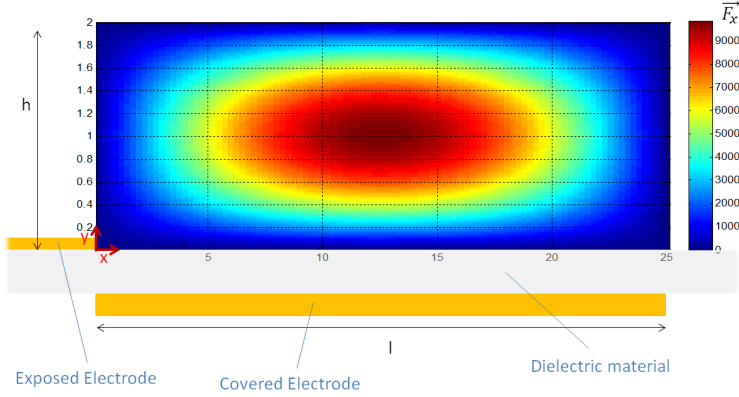


Figure 2.9: Assumed DBD Body Force Spatial Distribution for Turbulent Separation Assessment

lines of iso-magnitude, and it is assumed based on the experimental results of [69]. The largest magnitude of the body force is obtained at $(x, y) = (l/2, h/2)$ and it takes the value A , which can be calculated by integrating in x and y and substituting the values of the specific actuator under consideration:

$$F_{xTotal} = 0.2 = A \int_0^h \int_0^l \sin\left(\frac{\pi x}{l}\right) \sin\left(\frac{\pi y}{h}\right) dx dy = \frac{4Alh}{\pi^2} \Rightarrow A = 9870 N/m^3 \quad (2.24)$$

The turbulent separation criterion does not depend explicitly of the local velocity profile, and accordingly the BL is characterized by integral parameters. The actuator's force distribution in the y direction is thus collapsed into a single point, and the body force varies only in the x direction according to:

$$F_x(x) = \frac{2A}{\pi} \sin(\pi x/l) \quad (2.25)$$

The influence of the actuator on the flow is thus introduced in the separation criterion by noticing that the body force density, in N/m^3 , is equivalent to a pressure gradient, dp/dx , in Pa/m . The effect of the DBD actuator is introduced in the LHS of equation 2.17. Different actuator chordwise positions and α are considered. The RHS of equation 2.17 is the threshold for separation to occur. Figure 2.10 shows that without actuation, the separation point moves upstream as α increases. This is indicated by the intersection of the case '*No Actuation*' with '*Separation Threshold*'. The influence of the actuator on the flow is signalled by the bulges at the different chordwise positions. The maximum value of each bulge is obtained at the centre of the encapsulated electrode, since at this point the body force and thus pressure gradient are largest, leading to a local maximum in the

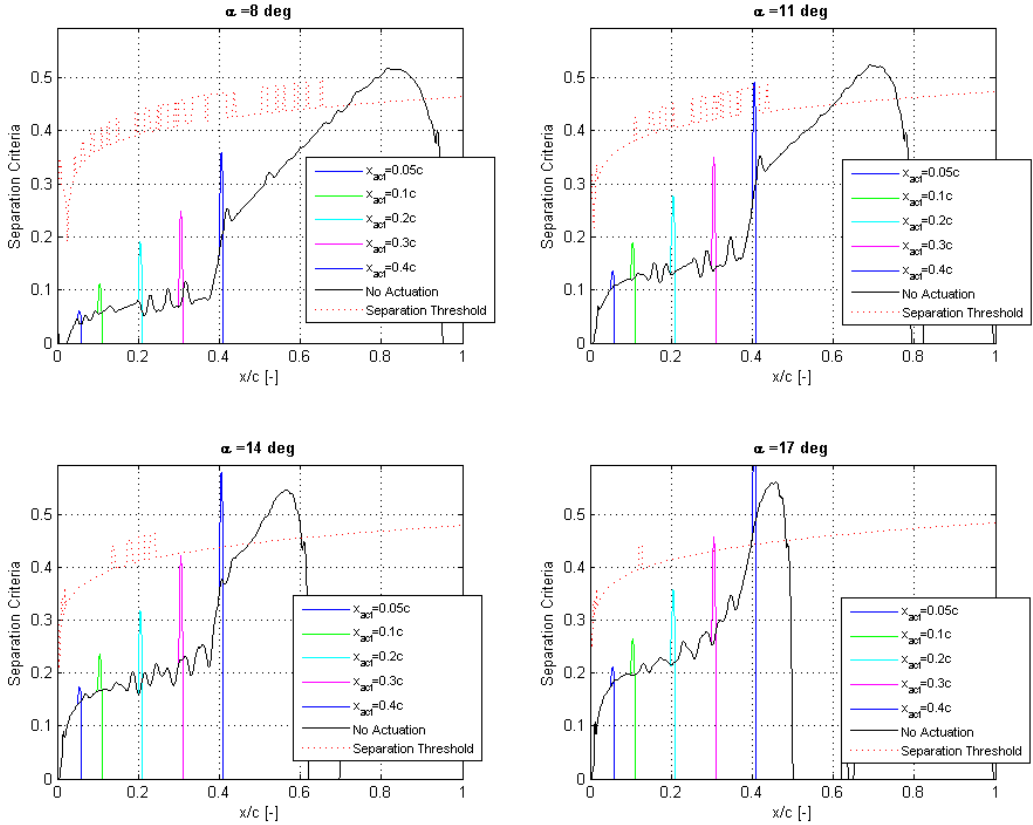


Figure 2.10: Turbulent Separation Criteria as DBD actuation is applied for $\alpha = [8; 11; 14; 17]$ at $V_{eff} = 60 \text{ m/s}$

LHS of the separation criterion. The large drop immediately downstream of the actuator is explained because the pressure rise provoked by the DBD is spatially confined. Accordingly, the model assumes a localized pressure decrease just after the actuator, leading to a decrease in the separation criterion. It is clear that the actuator brings the flow closer to separation, i.e. closer to the dashed line. Results indicate the DBD is capable of provoking separation as α increases; for $\alpha = 11 \text{ deg}$ and $\alpha = 17 \text{ deg}$ separation is predicted at $x/c = 0.4$ and $x/c = 0.3$ respectively. As smaller α and more upstream positions are considered it appears the actuator does not separate the flow.

FROM SEPARATION TO ACTUATOR AUTHORITY

Even though results indicate separation could not always be provoked by DBD actuators, it is important to estimate the ΔC_l obtained in case separation is provoked. This is done by introducing the Kirchhoff-Helmholtz trailing edge separation law, reviewed in [133]. According to this expression the suction side separation point, f , is related to the airfoil nor-

mal force coefficient, C_n :

$$C_n = C_{n0} + \frac{dC_n}{d\alpha} \left(\frac{1 + \sqrt{f}}{2} \right)^2 \alpha \quad (2.26)$$

where C_n is the sectional force in the direction perpendicular to the airfoil chord, defined as $C_n = C_l \cos \alpha + C_d \sin \alpha$. The slope of $C_n(\alpha)$ at small α is represented by $dC_n/d\alpha$, and C_{n0} is value the normal coefficient takes when $\alpha = 0$. These constants are adjusted for the airfoil under consideration. The separation point is measured from the LE, meaning that when the suction side flow is completely attached $f = 1$, and when the flow is separated from the LE we have $f = 0$.

In the past DBD actuators were used successfully to control separation, namely reattaching the flow in the LE region [108]. However, the momentum transferred by DBD actuators appears to be too small to consider circulation control through Kutta condition manipulation, even as suitable TE geometries are employed [68]. Accordingly, the expected changes in the lift curves when imposing DBD actuators should resemble what is obtained with BLT, rather than what is obtained with TEJ. In other words, one expects that DBD are capable of altering the C_l curve at large AOA, while not affecting the sectional lift for small AOA. Figure 2.11 illustrates the ΔC_l obtained for different separation positions and considering different AOA, for the *NACA64618* airfoil. The change in the sectional lift is obtained

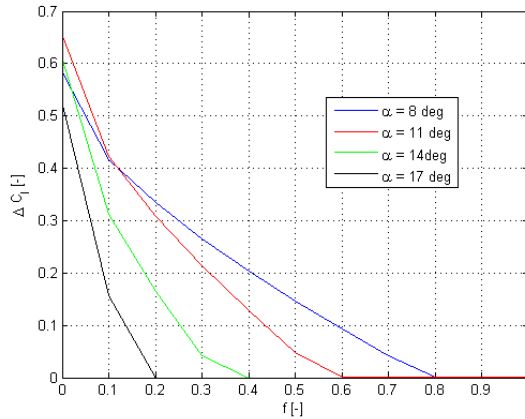


Figure 2.11: ΔC_l vs f for different AOA - *NACA64618* at $Re = 10 \times 10^6$

from the change in C_n resulting from the Kirchoff law, by considering that the drag is not altered by the actuator. If separation occurs near the LE considerable decrease in the sectional lift coefficient should be possible, e.g. $\Delta C_l = 0.4$ for $f = 0.1$ at $\alpha = 11$ deg. Moreover, the larger α is, the smaller f should be to produce given change in the lift coefficient. This is expected since the separation point moves upstream with increasing α when no actuation is applied. Combining figures 2.10 and 2.11 the authority of DBD actuators is estimated

in $\Delta C_l \approx 0.13$ for $\alpha = 11 \text{ deg}$. One should note V_{eff} has a large influence on the achieved ΔC_l since the absolute pressure gradient depends on the square of the effective velocity. This implies larger ΔC_l should be obtained at the mid-span area. Figure 2.11 also shows that $\Delta C_l < 0.7$ for the considered range of α . This result is obtained for a particular airfoil, but nevertheless it indicates the required decrease in sectional lift is not achieved even if separation is provoked at the LE. Recalling figure 2.4, to regulate power through active stall above rated speeds it is necessary to have $\Delta C_l \approx 0.7$, considering half the span is actuated. Separation would have to be provoked before the LE to obtain such a change in sectional lift, but this situation cannot be modelled with Kirchhoff's law.

2.5. DISCUSSION

The different actuation types are now compared. The power consumption of each actuator is analysed considering $\Delta C_l = \{0.2; 0.4\}$ is imposed over half the blade $L = 30 \text{ m}$. This is not sufficient to regulate the aerodynamic power captured by the HAWT, but may be used to compare the energy consumption of the different actuation types.

Considering BLT, the pressure difference between the flow in the suction peak region and the air inside the blade should be sufficient to drive BLT. This is assumed because at the outer half of the HAWT blade the dynamic pressure is large, since V_{eff} is large, and consequently the absolute pressure difference is also large. Moreover, the desired transpiration velocity can be obtained by tailoring the porous material characteristics [89]. Accordingly, the power required to employ BLT is estimated by looking at the turbine as a centrifugal pump. The required air mass rate per unit span is estimated with:

$$\dot{m}_{BLT} = V_b V_{Eff} \frac{x}{c_{por}} c \rho \quad (2.27)$$

The power consumed per unit span is then

$$dP_{BLT} = \frac{1}{2} \dot{m}_{BLT} (\Omega r)^2 dr \quad (2.28)$$

which under the assumption $V_{eff} \approx \Omega r$ is integrated over the considered blade span yielding:

$$P_{BLT} = 0.5 V_b \frac{x}{c_{por}} \rho \Omega^3 \int_{r=30}^{r=60} r^3 c(r) dr \quad (2.29)$$

For the TEJ case, expression 2.14 is inverted to obtain the required air mass per unit span:

$$U_{jet} = U_\infty \sqrt{\frac{0.5cC_\mu}{h_{jet}}} \implies \dot{m}_{TEJ} = U_{jet} h_{jet} \rho \quad (2.30)$$

The power consumption of the pneumatic system involved in providing the jet is computed by calculating the amount of energy required to accelerate the air flow from still-stand to

the speed at which it is ejected in the jet. The expression for the power per unit span is written as:

$$dP_{TEJ} = \frac{1}{2} \frac{\dot{m}_{TEJ} U_{jet}^2}{\eta_{Pump}} dr \quad (2.31)$$

where $\eta_{Pump} \approx 0.95$ represents the efficiency of the pump used to drive the pneumatic system. Integrating over the span and assuming $h_{jet} = 0.006c$ [15] we come to:

$$P_{TEJ} = 0.5 \times \frac{0.006\rho\Omega^3}{\eta_{Pump}} \left(\frac{0.5C_\mu}{0.006} \right)^{3/2} \int_{r=30}^{r=60} r^3 c(r) dr \quad (2.32)$$

Regarding DBD actuators, power consumption is estimated based on the actuator thrust, according to the empirical relationship from [132]:

$$dP_{DBD} = \frac{F_{act}}{0.2} 700 dr \quad (2.33)$$

with the actuator force in N/m and power consumption in W/m . Given a ΔC_l and AOA of operation, the required separation location f is determined according to figure 2.11. The actuator is placed at this chordwise position and F_{act} is increased until separation is provoked (following Stratford's criterion). The required DBD power depends on several parameters, namely V_{eff} , α , ΔC_l and airfoil employed. In the present study we consider the *NACA64618* with $\alpha = [11; 14]^\circ$ and with $V_{eff} \approx \Omega r$.

Results obtained for the different actuators are presented in table 2.2. The actuation parameters used in each case are also shown. For $\Delta C_l = 0.2$ TEJ require the least power

Table 2.2: Actuator Power Comparison for $L = 30 m$

		BLT	TEJ	DBD $_{\alpha=11 deg}$	DBD $_{\alpha=14 deg}$
$\Delta C_l = 0.2$	Actuator Parameter	$V_b = 0.006$	$C_\mu = 0.0013$	$f = 0.3$	$f = 0.17$
	Power (kW/Blade)	19.9	4.9	32.6	94.7
	Air Flux (kg/s/Blade)	5.4	11.8	-	-
$\Delta C_l = 0.4$	Actuator Parameter	$V_b = 0.012$	$C_\mu = 0.015$	$f=0.12$	$f=0.07$
	Power (kW/Blade)	39.8	194.9	60.9	144.4
	Air Flux (kg/s/Blade)	10.8	40.0	-	-

of all actuators. On the other hand BLT appear to consume the least power for $\Delta C_l = 0.4$. This is explained because for TEJ ΔC_l is proportional to $\sqrt{C_\mu}$, while for BLT figure 2.5 shows $\Delta C_l \propto V_b$. The estimated power for the DBD actuators is dependent on the AOA. For $\alpha = 11 deg$ it is comparable to BLT, while for $\alpha = 14 deg$ it is considerably larger. For all actuation technologies, power consumption is significant compared with the total turbine power production; considering a 3 bladed HAWT employing BLT such that $\Delta C_l = 0.4$, actuation would consume approximately 2.4% of the turbine's power. Regarding DBD actuators, results indicate separation can not always be provoked. The actuator was modelled in a simple way and the criteria used were not developed to incorporate localized flow perturbations such as DBD actuators; nevertheless it appears the momentum transferred by

the actuator is not enough to provoke separation in all considered cases. CFD simulations could provide more insight on the actual effect of DBD actuators at large Reynolds numbers, since the present modelling used integral BL parameters, while the force field generated by DBD actuators varies both in space and time. The DBD actuator considered was optimized to yield the largest thrust force, since usually these actuators are used to delay separation and thus energize the BL. However the key parameter in provoking separation is not the total thrust force, in this case opposite to the flow direction, but rather the maximum body force obtained, which translates into a localized adverse pressure gradient. Experiments show [132] that by decreasing the exposed electrode length, while keeping all other parameters constant, the total thrust decreases but the thrust per meter increases. The maximum pressure gradient is thus increased, indicating this option should be explored in the future to design DBD actuators to provoke separation.

The present study indicates the required ΔC_l to regulate power is not attained with any of the actuators considered. The authority of each actuation type was assessed using uncomplicated models, but nonetheless the required change in circulation associated with the airfoil section is extremely large, and it seems none of the actuation mechanisms considered is suitable. This indicates airfoil redesign is necessary if power regulation through active stall control is to be accomplished. Airfoils designed to be sensitive to actuation could achieve the required ΔC_l . This however needs to be done prudently to avoid a point-design type of airfoil, since it is not suitable for HAWT applications given the wind stochastic nature and spatial gradients. Ultimately, airfoil design should be coupled to blade planform design while curtailing actuator power consumption such that a cost-effective solution is found.

2.6. CONCLUSION

A preliminary study on the feasibility of active stall control for HAWT was performed based on the NREL 5 MW baseline turbine. Results show a large portion of the blades must be actuated, and the actuators must be effective especially at large AOA. Different actuation technologies have advantages and drawbacks. LE blowing is able to produce LE stall, and thus has a large authority. TEJs can yield significant changes in the lift coefficient, but only in the linear region of the lift curve. DBD have no moving parts but transfer a limited amount of momentum to the air and it is thus not clear whether they provoke separation at the Reynolds numbers being considered. All in all, active stall control of HAWT could be feasible only if the blade and the airfoils were designed from the beginning to be active stall controlled.

II

DBD PLASMA ACTUATOR CHARACTERIZATION AND MODELING

The previous section showed it is necessary to further investigate the actuation system for ASC machines.

This Part of the dissertation is dedicated to diagnostics and modelling of DBD plasma actuators. In chapter 3 a study is performed to assess the effect of external flow on DBD performance. Both experimental characterization and analytical modeling are carried out. Chapter 4 provides a methodology to analyze the local frequency response of flow under DBD actuation. The proposed phenomenological approach may be used for design and optimization of DBD plasma actuation for flow control applications. Afterwards, chapter 5 presents a model of DBD plasma actuators in integral boundary layer (IBL) formulation. The approach is validated with an experimental campaign, showing the potential the presented formulation may have by enabling airfoil design including the effect of DBD actuation.

It is noted that chapter 5 corresponds to an AIAA article, whose first author is Gaël de Oliveira. Nevertheless the author of this dissertation had a significant contribution in the aforementioned article. Additionally, since modeling DBD actuation in integral boundary layer (IBL) formulation falls within the scope of the present research work, this chapter is included in the body of the dissertation

3

EFFECT OF EXTERNAL FLOW VELOCITY ON MOMENTUM TRANSFER OF DBD ACTUATORS

Happiness is a warm gun

John Lennon

This chapter investigates the effect of external flow velocity on AC-DBD performance. An experimental study is performed towards identifying cross-talk effects between DBD plasma actuators and external flow. An actuator is positioned in a boundary layer operated in a range of free stream velocities from 0 to 60 m/s, and tested both in counter-flow and co-flow forcing configurations. Electrical measurements are used for estimating the power consumption and the discharge formation is visualized using a CCD camera. The actuator's force is measured using a sensitive load cell. Results show the power consumption is constant for different flow velocities and actuator configurations. The plasma light emission is constant for co-flow forcing but shows a trend of increasing intensity with counter-flow forcing for increasing free stream velocities. The measured force is constant for free stream velocities larger than 20 m/s, with same magnitude and opposite direction for the counter-flow and co-flow configurations. In quiescent conditions the measured force is smaller due to the change in wall shear force by the induced wall-jet. An analytical model is presented to estimate the influence of external flow on the actuator force. It is based on conservation of momentum through the ion-neutral collisional process while including the contribution of the wall shear force. Satisfactory agreement is found between the prediction of the model and experimental data at different external flow velocities.

This chapter has been published in the Journal of Applied Physics Vol 116, 103301 (2014); doi: 10.1063/1.4894518AP

3.1. INTRODUCTION

Dielectric Barrier Discharge (DBD) plasma actuators have been gaining increased attention due to their attractive flow control abilities such as low weight, simple construction, high dynamic range of forcing and robustness. Excellent reviews on plasma actuators for aerodynamic flow control have been published recently [96, 28, 16, 25, 83]. Due to the large degree of freedom in actuation configuration, geometric and electrical properties and flow control scenarios, an efficient and robust model of the actuator is highly desirable. Such a model can be used in CFD solvers and optimization algorithms in order to maximize the performance of the plasma actuator system. Such a model has been extensively used in the form of a volume distributed body force roughly corresponding to the plasma cloud region [119][68]. Several levels of fidelity exist for plasma body force models ranging from simple phenomenological models [57] to highly detailed first principles models [85] as well as experimentally derived force distributions [69]. Nevertheless, one major assumption made during derivation and application of these body force models is their total independence from the external flow. This leads to an uncoupled functional relation in which the body force affects the flow field but the flow field does not affect the force. The rationale behind this approach is based on the collisional model of momentum transfer. This specifies that the Coulombian force exerted on the charged species in the plasma region is transferred without loss to the surrounding neutral air. This assumption is intuitively valid for very low external flow conditions or plasma actuators operating in quiescent flow. On the other hand, in the case where the actuator is operating in a high velocity flow ($\mathcal{O}(100 \text{ m/s})$) then the drift velocity of the heavy charged species (positive and negative ions) starts becoming comparable with the convective velocity of the neutral air. In such case the momentum transfer is expected to be a function of the relative average velocity between ions and neutrals and as such dependent on the external flow.

Based on these hypotheses it is commonly argued that, for incompressible fluid flow applications, the fluid characteristic time scales are much larger than those of the plasma dynamics, hence enabling the decoupling between the fluid and plasma physics [58] when employing body force modeling. However, the effect of the external flow velocity on the DBD operation has been reported [103] to affect the breakdown voltage, discharge type and plasma light emission. In fact, the light pulse duration of the microdischarges has been recorded to decrease by one order of magnitude [103, 74] already at $M=0.2$, unequivocally demonstrating that the external flow has an influence on the operation of DBD, even for incompressible regimes.

Even though the DBD force is a crucial parameter when considering actuator design and applications, it remains unclear what is the effect of the external flow on the momentum transferred to the air. To this date only the pioneering work of Roth et al. [113] has attempted measuring the plasma induced force under external velocity conditions, albeit with different objectives. Additionally, the effect of orientation of the plasma actuator in co-flow or counter-flow forcing has also received little attention [112]. The present study addresses these issues. The momentum transferred by the DBD actuator is quantified by employing a load-cell to measure the plasma force under conditions of external flow. Power consumption and light emission are also registered. Finally a simple theoretical model is presented to assess the influence of the external flow on the momentum transferred by the DBD plasma actuator.

3.2. EXPERIMENTAL SET-UP

3.2.1. WIND TUNNEL AND LOAD CELL

Measurements were conducted in an open-circuit low speed windtunnel, employing a rectangular section of 40×15 cm. The length of the test section was approximately 1 m from the end of the diffuser to the outlet of the wind tunnel. The diffuser was specifically modified in order to increase the maximum achievable free stream velocity of the wind tunnel from 40 m/s to 60 m/s. The free stream velocity varied from 0 to 60 m/s, with 10 m/s steps for the present study. The bottom wall of the tunnel test section was fitted with an access port in which a zero-friction floating flat plate was placed with a surrounding gap of less than 1 mm. A sketch of the experimental setup is given in figure 3.1. The floating flat plate measured 187×110 mm and was used as a base on which the plasma actuator was secured. The floating part (including the actuator) was attached to an electronic ME-Meßsysteme KD-40S strain-gage load cell, with nominal force range of ± 2 N sensitivity of 2 mV/V and linearity of 0.1% of the nominal range. As the load cell is an analog device the accuracy of measurement is defined by the signal to noise ratio which is well below the expected force production of the tested actuator. The load cell was conditioned and sampled at 100 Hz using a 16 bit strain gage conditioner from National Instruments.

3.2.2. PLASMA ACTUATOR

A DBD plasma actuator was tested in co-flow and counter-flow forcing. In the co-flow configuration the actuator forcing is in the direction of the flow, while in counter-flow the actuator forcing is opposite to the flow direction (Figure 3.2). The actuator was constructed and positioned on the floating plate using thin rectangular copper electrodes made of self-adhesive copper tape separated by a dielectric layer. The dielectric material was PMMA (Plexiglas), with a thickness of 3 mm. The thickness of both electrodes was 60 μ m including the adhesive layer. The width of the exposed electrode was 10 mm and the width of the encapsulated electrode was 20 mm, as to not constrain plasma formation in the streamwise direction. The encapsulated electrode was covered with Kapton tape in order to prevent formation of plasma on the lower side of the plate. No horizontal gap was formed between the two electrodes. The effective spanwise length of the metallic electrodes (along which plasma is generated) was $w = 125$ mm. The actuator was powered by a TREK 20/20C HV amplifier (± 20 kV, ± 20 mA), imposing a sinusoidal signal of 40 kV_{pp} applied voltage and 2 kHz carrier frequency on the exposed electrode while keeping the covered electrode at ground potential. The power and ground connections to the actuator were established using low friction linear slip ring connectors in order to minimize mechanical reaction forces, which could contaminate the sensitive load cell measurements.

Additionally to the force measurements, the behavior of the actuator was further characterized by electrical power measurements and light emission intensity measurements. The power consumption was derived using the monitor capacitor technique [3]. The procedure involved a capacitor connected in series with the circuit, inserted between the DBD encapsulated electrode and the ground. An electrolytic capacitor was employed for the present study with capacitance of $C = 2.7$ μ F. The voltage across the capacitor terminals was sampled using a 16-bit National Instruments Analog Input module at 100 kHz, resulting in 50 points per excitation cycle. Previous studies [61] employed a larger number of points per

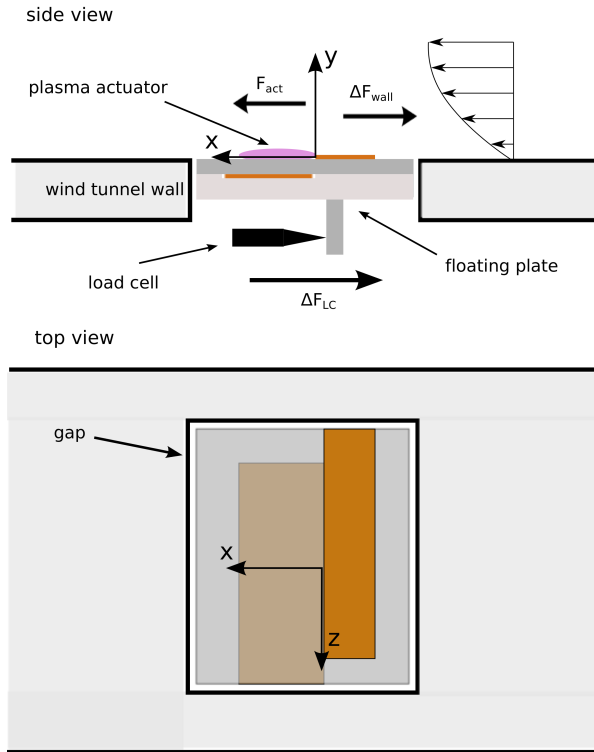


Figure 3.1: Arrangement of the experimental setup (not to scale). Direction of forces corresponds to co-flow forcing configuration.

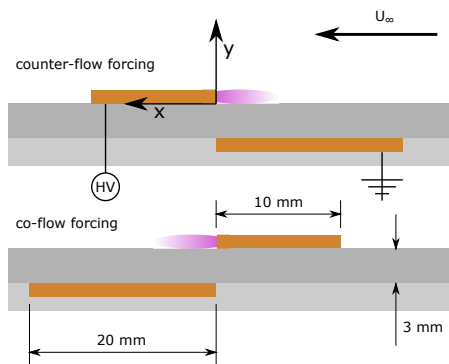


Figure 3.2: Geometrical configuration of the actuator in counter-flow and co-flow forcing configurations (not to scale).

excitation cycle, but in the present work 50 points were found sufficient to estimate the power consumption since the results demonstrated small standard deviation. Instantaneous power was estimated using the time-derivative of the capacitor's voltage multiplied by the capacitance and the applied voltage. Integrating over an excitation period the power consumption was derived, according to:

$$P(t) = V_{amp}(t) \cdot i_{cap}(t) = V_{amp}(t) \cdot C \frac{\partial V_{cap}(t)}{\partial t}$$

$$\Rightarrow P_{avg} = \frac{1}{T} \int_0^T P(t) dt \quad (3.1)$$

An alternative to the described technique would be the Lissajous method, estimating the DBD power consumption by calculating the area of the Lissajous curve (Figure 3.4). The influence of the external flow on the DBD plasma light emission was also investigated by using a CCD digital camera (LaVision Imager Pro LX, 4870 x 3246 pixels, 12 bit) to capture the discharge area light intensity while the actuator was operating at the different flow conditions. A reference picture, with the actuator switched off, was taken and subtracted from the images obtained with actuation. The imaged field of view was 25×40 mm and acquisition was performed for a total integration time of 1 s per case.

3.2.3. BASELINE BOUNDARY LAYER

The wind tunnel wall boundary layer is characterized to establish the state and scale of the flow in which the actuator is operating. Considering Figure 3.1, velocities are measured along the y direction, at the inner edge of the exposed electrode (x=0), by using a traversing system equipped with a metallic Pitot tube of inner diameter 0.2 mm measuring total pressure. The total pressure in the boundary layer and the reference static pressure in the wind tunnel were sampled at 1 Hz for 30 sec. using a Mensor DPG 2400 digital manometer. The velocity profile $U(y)$ of the boundary layer was characterized through the shape factor H_{12} , defined in incompressible fluid as:

$$H_{12} = \frac{\delta_1}{\delta_2} = \frac{\int_0^\infty \left(1 - \frac{U(y)}{U_\infty}\right) dy}{\int_0^\infty \frac{U(y)}{U_\infty} \left(1 - \frac{U(y)}{U_\infty}\right) dy} \quad (3.2)$$

where δ_1 and δ_2 are integral boundary layer parameters defining the displacement thickness and momentum thickness respectively [114]. The upper limit of the integrals in equation 3.2 was set at δ_{99} , corresponding to the wall distance at which $U(\delta_{99}) = 0.99U_\infty$ [114]. The wall shear stress of the non-forced boundary layer was determined from the measured velocity profile according to:

$$\tau_{wall} = \mu \frac{\partial U}{\partial y} \Big|_{y=0} \quad (3.3)$$

where $\mu = 1.85 \times 10^{-5} \text{ kg/ms}$ is the air dynamic viscosity. Table 3.1 shows the wind tunnel wall boundary layer is turbulent ($H_{12} \leq 1.5$) for the considered velocities, except for

$U_\infty = 10 \text{ m/s}$ which can be considered laminar-transitional [114]. For all free stream velocities, the exposed electrode's thickness is smaller than the viscous sublayer thickness [21] ($y_{elec}^+ < 10$), indicating the flow is hydrodynamically smooth. Table 3.1 also shows the representative air speed occurring in the plasma body force region. The plasma body force region is the volume in which the actuator transfers momentum to the air, roughly corresponding to region above the covered electrode, up to a height of a few mm [69]. The representative air speed U_0 is the velocity 'felt' by the plasma due to the wind tunnel wall boundary layer, computed as the average velocity in the BL up to the height of the body force region:

$$U_0(U_\infty) = \frac{1}{h} \int_{y=0}^h U(y) dy \quad (3.4)$$

where h is the height of the body force region. For this study the value of h was taken equal to 1 mm based on previous measurements [69].

U_∞ (m/s)	δ_{99} (mm)	H_{12}	τ_{wall} (Pa)	U_0 (m/s)
10	10.1	2.02	0.058	1.4
20	9.5	1.28	1.04	10.3
30	10.4	1.32	1.38	13.9
40	9.6	1.29	2.03	20.2
50	9.2	1.31	2.62	24.5
60	8.9	1.27	3.18	30.7

Table 3.1: Non-actuated boundary layer characteristics.

3.3. EXPERIMENTAL RESULTS

3.3.1. POWER CONSUMPTION AND PLASMA LIGHT EMISSION

The DBD actuator power consumption's dependency on the external flow speed has been determined via the monitor capacitor measurements. Figure 3.3 illustrates the power obtained for both the co-flow and counter-flow configuration, and figure 3.4 shows the Lissajous curve obtained by plotting the capacitor charge versus the amplifier voltage, for the counter-flow case.

It is apparent that DBD power consumption does not change with varying external flow speed for the specific testing conditions (actuator setting, flow regime etc.). The small difference in the magnitude of the power consumption between both configurations is attributed to small discrepancies in the construction and assembly of the actuators rather than an influence of the external flow speed direction. The Lissajous curve obtained shows virtually no variation with external flow speed, also for the co-flow configuration (not shown). It is clear that, the integrated value of the DBD power consumption is not affected by the external flow. However, using time resolved techniques such as a shunt resistor in combination with a high sampling rate acquisition ($O(GHz)$) the impact of the external flow was demonstrated on the topology of the individual microdischarges [103].

The imaged discharge is shown in Figure 3.5 for the counter-flow configuration at the two extreme freestream velocities. Figure 3.6 illustrates the variation of light intensity in the

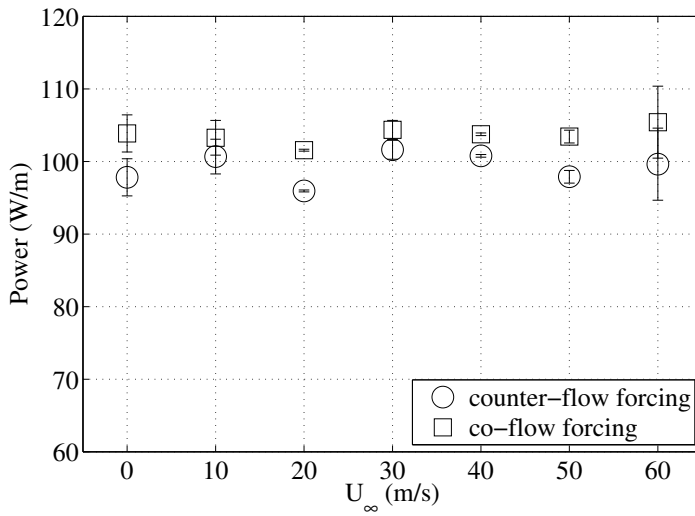


Figure 3.3: Power consumption

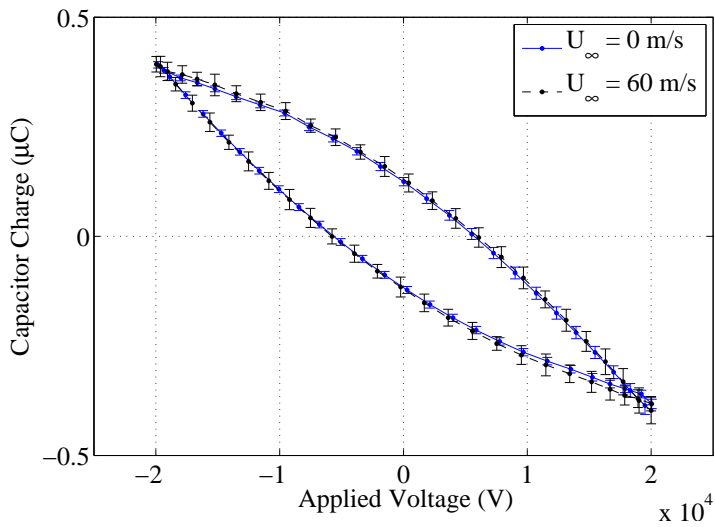


Figure 3.4: Lissajous curve for counter-flow forcing

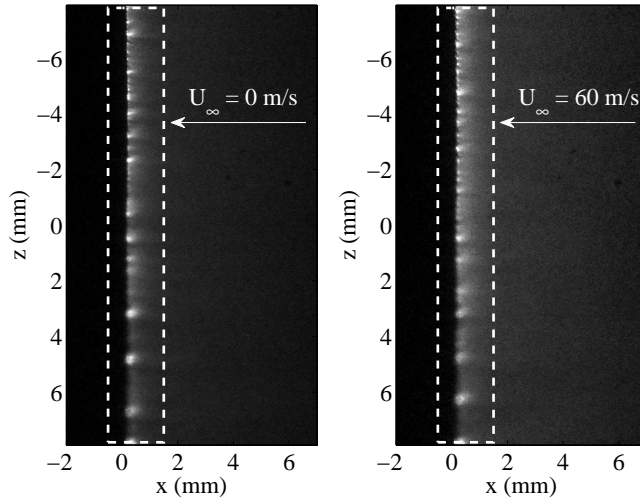


Figure 3.5: Light intensity of the discharge in counter-flow forcing configuration. White rectangle indicates the integration length for estimation of intensity (Fig.3.6).

actuator region for both counter-flow and co-flow forcing configurations including detail of the vicinity of the covered electrode's inner edge. The light intensity has been averaged over a spanwise length of 16 mm and normalized with the maximum for each case. It is apparent that in the co-flow forcing configuration, the plasma light emission is weakly dependent of the external flow velocity until the maximum tested velocity (60 m/s). Kriegseis et al. [74] observed similar weak dependence for low velocities but a clear trend of decreasing intensity for higher velocities.

In contrast, for counter-flow forcing the present measurements show a clear trend towards increasing light emission length with increasing free stream velocity. These observations indicate a dependence on actuator orientation regarding the light intensity of the discharge, which can suggest a species-specific collisional behavior with neutral air molecules.

3.3.2. FORCE MEASUREMENTS

Prior to any analysis it is useful to define some referencing terms regarding the measured quantities. The plasma discharge is exerting a volume distributed body force on the surrounding neutral air. This shall be defined as the *body force*. The integrated in space value of the *body force* is the total force the actuator is exerting on the flow and shall be named *force*. For this entire study, all definitions correspond to sufficiently long observation times, and as such time averaged values.

The force produced by the actuator is determined by the difference of the load cell force reading obtained with and without actuation. This difference however includes also the change in the skin friction developed at the wall due to actuation. This is naturally expected

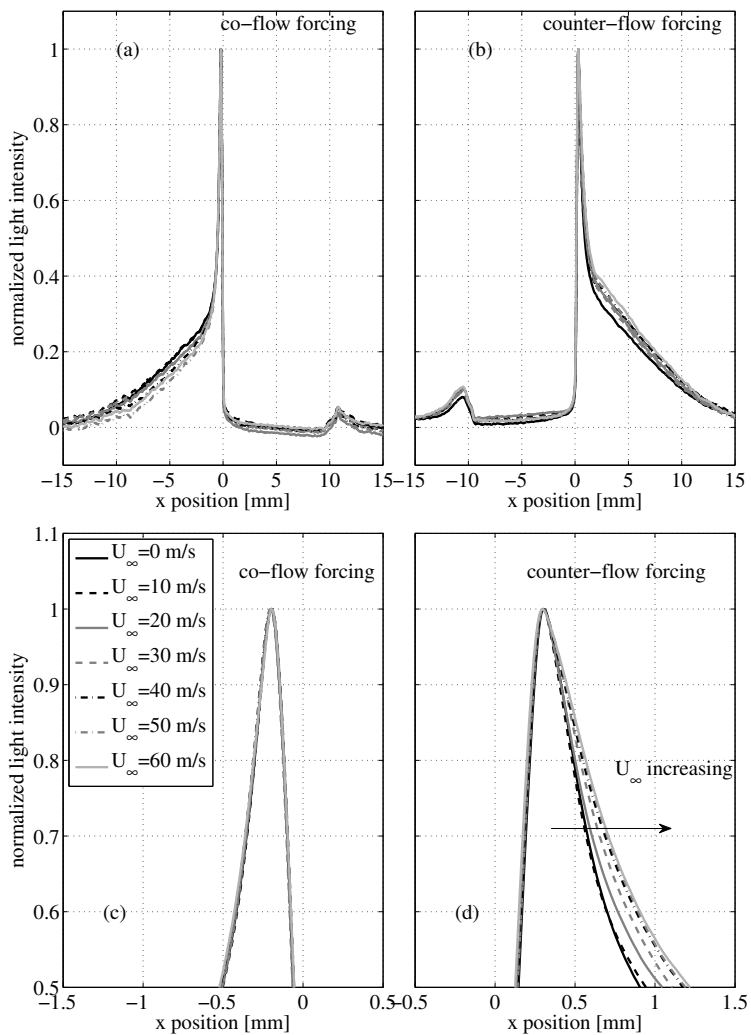


Figure 3.6: Integrated and normalized light intensity of the discharge for (a) co-flow and (b) counter-flow forcing. Detail near the electrode edge for (c) co-flow and (d) counter-flow forcing.

since the actuator is able to change the boundary layer profile at low velocities[113]. In the case of co-flow forcing, actuation would result in a "fuller" velocity profile with larger gradient at the wall. As such, co-flow forcing results into increase of skin friction. Similarly, counter-flow forcing results in reduction in skin friction. Equation 3.5 expresses this relationship, where the subscripts *LC*, *act* and *wall* represent the load cell, actuator and wall respectively, and the double subscripts *on* and *off* represent the DBD actuator being switched on or off. The direction of these forces is indicated in Figure 3.1 for the co-flow forcing configuration while for the counter-flow forcing case the direction is reversed.

$$\begin{cases} \Delta \vec{F}_{LC} = \vec{F}_{LC_{on}} - \vec{F}_{LC_{off}} = \vec{F}_{act} + \Delta \vec{F}_{wall} \\ \Delta \vec{F}_{wall} = \vec{F}_{wall_{on}} - \vec{F}_{wall_{off}} \end{cases} \quad (3.5)$$

In order to minimize measurement uncertainty the reaction force registered by the load cell is measured for 30 actuation cycles. In each cycle the actuator remains off for 0.5 s and operates for the next 0.5 s. The average force over the 30 cycles is averaged to produce the final value. This is done for all considered wind tunnel speeds, both in the counter-flow and co-flow DBD configurations. Results obtained are shown in Figure 3.7, where the absolute values of the forces are displayed. The error bars in Figure 3.7 show the standard deviation of the measurements. However the bias error due to the load cell (0.1 % of the full range) is not included.

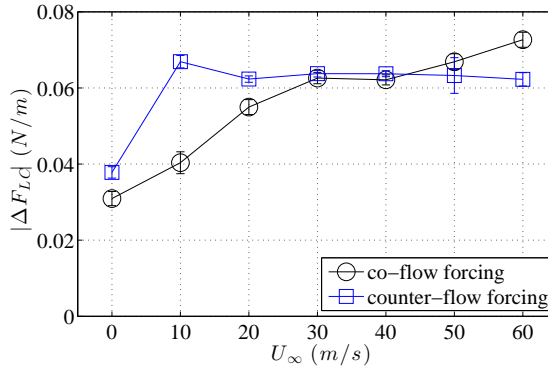


Figure 3.7: Measured force difference between actuator *on* and *off*.

Figure 3.7 shows the measured difference ($|\Delta \vec{F}_{LC}|$) in force between actuator *on* and *off* for all tested velocities. It should be noted here that the reaction force on the load cell is presented here in absolute value. The direction of the force exerted on the flow from the operation of the actuator is downstream for co-flow forcing configuration and upstream for counter-flow forcing configuration.

The behaviour of the measured force is analysed first for the co-flow configuration. It is apparent that for quiescent flow ($U_\infty = 0$ m/s) the measured force is significantly smaller than that corresponding to higher free stream velocities. This can be explained keeping in

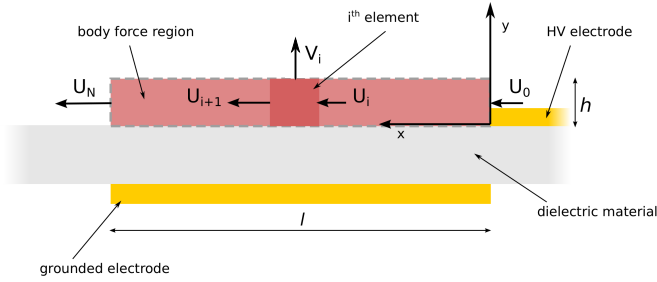


Figure 3.8: Computational model schematic for the co-flow forcing configuration.

mind the developed flow field due to plasma actuation in quiescent conditions. Several studies [96, 28] have demonstrated a wall parallel jet directed in the direction of forcing. The jet develops a shear stress at the wall which is always opposing the actuator force. Thus the load cell will register the difference of the two forces. In the case of higher free stream velocities ($> 20 \text{ m/s}$) the force at the wall is due to boundary layer skin friction. Nevertheless, the difference in skin friction between the *on* and *off* case is much lower since the boundary layer is already turbulent (Table 3.1). Essentially this indicates that for high free stream velocities the actuator is no longer able to change the flow skin friction and most probably the flow itself. As such the load cell is registering only the integrated body force due to plasma and hence a larger force. The load cell force value for $U_\infty = 10 \text{ m/s}$ indicates that the actuator is still able to change the skin friction at this velocity, albeit less than in quiescent flow. The general behaviour of the registered values stresses the importance of scrutinising integral force measurements as they will most likely underestimate the forcing strength of the actuator if performed in quiescent conditions.

An additional observation concerns the values at free stream velocities of 50 m/s and 60 m/s . At these velocities the trend of the measured load cell force shows an increase. This cannot be readily explained at this point. The measurements at these conditions have been repeated in order to exclude any measurement or repeatability error.

The forcing behaviour corresponding to counter-flow forcing configuration shows small variations compared to co-flow forcing. In quiescent flow the value of measured force is in the same order as the co-flow forcing case as would be expected. Small differences can be attributed to manufacturing inconsistencies between the two actuators as was already suggested from the power measurements (Figure 3.3). In contrast, the value of F_{LC} is notably higher at $U_\infty = 10 \text{ m/s}$ for counter-flow forcing. This indicates the important role of the wall skin friction in these measurements. As indicated in Table 3.1 the shape factor of the non-actuated boundary layer at $U_\infty = 10 \text{ m/s}$ indicates laminar flow. On the other hand, when the actuator is forcing the BL upstream it is likely to induce transition. As such the skin friction force is expected to considerably increase with counter-flow actuation at this specific velocity. In this case the direction of the actuator force (\vec{F}_{act}) is the same as the direction of the wall skin friction increase ($\Delta\vec{F}_{wall}$), their sum results into the increased measured force at $U_\infty = 10 \text{ m/s}$. For higher velocities, the boundary layer is fully turbulent and the actuator does not appear to affect the wall friction force.

In general the load cell measurements indicate that, apart from wall skin friction effects occurring at low velocities, the external flow does not considerably affect the plasma actuator force (\vec{F}_{Act}) for the considered free stream velocities, boundary layer characteristics and actuator settings. The two points at velocities $U_\infty = 50$ and 60 m/s in co-flow forcing configuration cannot be currently explained. Nevertheless, these trends cannot be safely extrapolated to higher velocities without further testing. Especially when the convective velocity of the external flow starts approaching the drift velocities of the heavy charged species in the plasma region (ions), the total momentum transfer model can no longer be used.

3.4. MOMENTUM TRANSFER MODEL

The experimental measurements indicate a small influence of the external flow on the force of the plasma actuator up to free stream velocities of 60 m/s . Nevertheless, plasma actuators have been suggested for applications such as laminar flow control or separation control in conditions where free stream velocities of up to 300 m/s can be encountered (such as subsonic airliners). Applications to supersonic [78] and even hypersonic [4] velocities have also been suggested. A simple analytical model is now presented to estimate the impact of the external flow velocity on the momentum transferred by the DBD actuator for a large range of free stream velocities.

The region in which the plasma body force is significant is divided in N elements along the streamwise direction. Impermeability of the wall and fluid incompressibility are assumed. As such free stream velocities above 250 m/s (100 m/s in the plasma region) will not be considered. Considering Figure 3.8, mass conservation in the i -th element is expressed as:

$$\nabla \cdot \vec{U} = 0 \rightarrow \frac{U_{i+1} - U_i}{dl} + \frac{V_i}{h} = 0 \quad (3.6)$$

where \vec{U} represents the fluid velocity vector with components U and V in the x and y direction respectively. The plasma region height is denoted by h and the length of each element by dl . The total length of the body force region is given by the covered electrode's width, $l = 0.02 \text{ m}$, which is the maximum possible extent of the plasma formation.

Momentum conservation in the x direction may be expressed by:

$$\begin{aligned} dF_x &= \int \int \vec{U}(\rho \vec{U} \cdot \vec{n}) dA = \\ &= \rho(U_{i+1}^2 - U_i^2) \cdot h + \frac{U_{i+1} + U_i}{2} \rho \cdot V_i \cdot dl \end{aligned} \quad (3.7)$$

where dF_x represents the force in the x direction acting on the fluid element, ρ is the air density, dA is the elemental area and \vec{n} is the vector normal to element surface pointing outwards. Rearranging equation 3.6 and introducing it in equation 3.7 we obtain:

$$dF_x = \frac{1}{2} \rho \cdot h (U_{i+1}^2 - U_i^2) \quad (3.8)$$

Furthermore, the left-hand-side of equation 3.8 is decomposed according to:

$$dF_x = dF_{act} + dF_{shear} \quad (3.9)$$

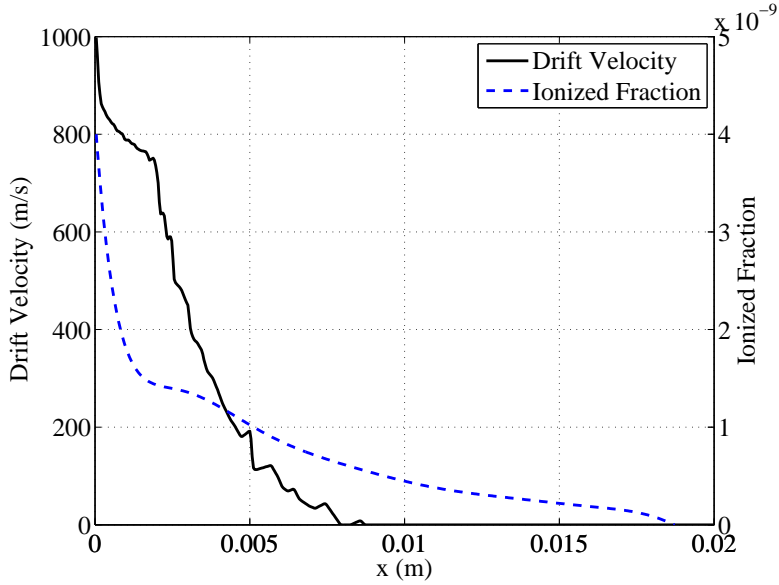


Figure 3.9: Imposed ion drift velocity and ionization fraction spatial distribution

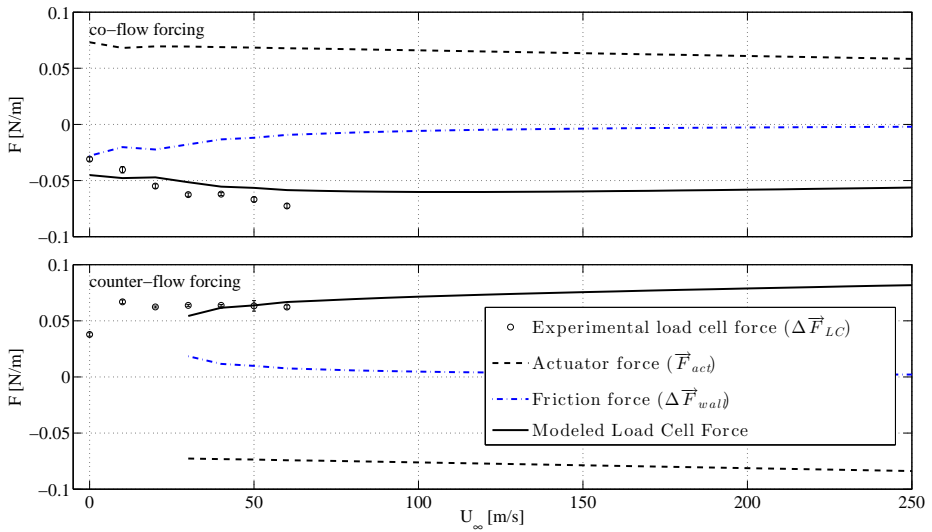


Figure 3.10: Model vs load cell results.

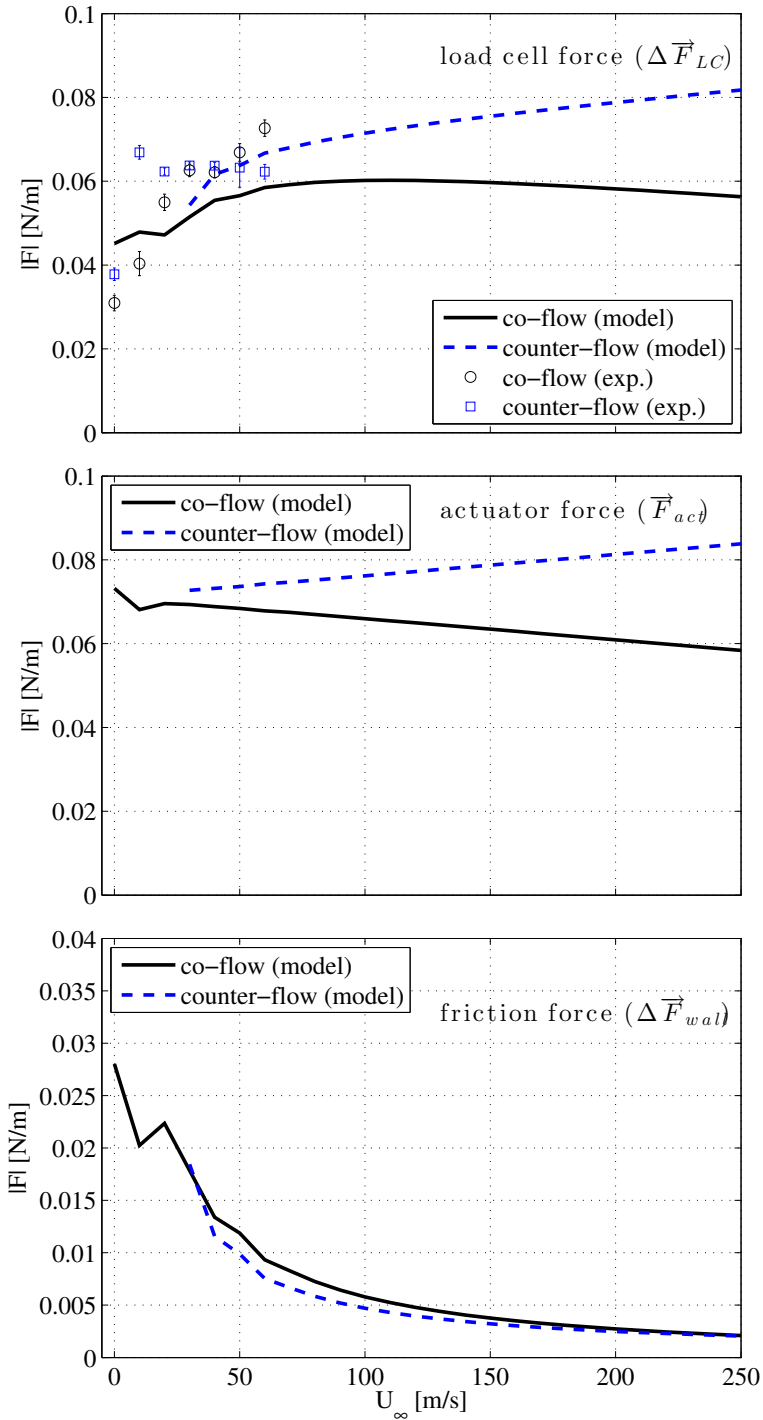


Figure 3.11: Individual absolute force terms for co-flow and counter-flow as predicted by the analytical model.

where dF_{act} denotes the x component of the force produced by the DBD actuator and dF_{shear} represents the shear force arising from viscosity of the fluid at each element. At this point no assumption is made regarding the direction of forces.

The momentum of the charged species is assumed to be transferred through collisions to neutral molecules (N_2 and O_2) such that, across each fluid element, the velocity after the collisional process is the same for all particles. This is not necessarily true for a collision between two particles, but it is assumed enough collisions occur such that the ion momentum is evenly distributed to the flow across each element considered (statistical equilibrium). For simplicity, no distinction is made between positive ions, negative ions and free radicals. The momentum added to the flow at each element is estimated with:

$$dp_i = \rho h i_D (V_D - U_i) dl \quad (3.10)$$

in which dp_i is the change in momentum, i_D represents the fraction of ionised species in the plasma compared to neutral air molecules and V_D is the drift velocity of the ions. From Newton's second law, the body force at each element is given by:

$$dF_{act} = \frac{dp_i}{dt} \quad (3.11)$$

The characteristic time during which momentum transfer across each element is performed is estimated using the mean free path λ , according to:

$$dt = \frac{\lambda}{V_D} \quad (3.12)$$

Following [8], the value $\lambda = 60 \text{ nm}$ is imposed in the present model. As mentioned earlier, the resultant force which the finite element of fluid is experiencing is partly due to developed shear forces due to viscosity. Shear forces are present both at the wall ($y = 0$) and at the upper edge ($y = h$) of the fluid element. Maintaining simplicity for the present model, a first order approximation is taken for the estimation of the wall shear stress. As such, the gradient of velocity normal to the wall is estimated using the average velocity in the element (U_i) at the representative height ($y = kh$). The representative height is defined assuming a linear velocity profile, where kh is the distance from the wall at which U_0 yields the same wall shear stress as determined experimentally:

$$\frac{\mu U_0}{kh} = \tau_{wall} \implies k = \frac{\mu U_0}{h \tau_{wall}} \quad (3.13)$$

Different values for the representative height are used for different external flow speeds, and in quiescent conditions it is assumed $k = 0.5$, corresponding to a wall jet with the same height of the considered control volume. The shear force at the upper edge of the fluid element is kept constant throughout the considered control volume. Its value is set such that the boundary layer is in force equilibrium when no plasma is employed. The shear force at each fluid element is then computed with:

$$dF_{shear} = dF_{edge} + dF_{wall} \approx \frac{\mu}{kh} (U_0 - U_i) dl \quad (3.14)$$

Rearranging equation 3.8 and inserting the actuator and shear forces, the streamwise velocity at the following fluid element ($i + 1$) is obtained using a marching scheme, as a function of the velocity at i :

$$U_{i+1}^2 = U_i^2 + 2 \frac{V_D}{\lambda} i_D (V_D - U_i) dl + 2 \frac{\mu}{\rho k h^2} (U_0 - U_i) dl \quad (3.15)$$

Equation 3.15 is used in order to obtain the streamwise velocity distribution over the whole body force region. From mass conservation (equation 3.6) the respective wall normal velocity distribution (V_i) can be calculated. In order to initiate the marching procedure the velocity at the first element is necessary (U_0). This can be taken from the experimental baseline boundary layer measurements (Table 3.1).

Substituting into equation 3.7, the total force exerted on the fluid over the plasma region, which includes both plasma body force and viscous shear force, is estimated with:

$$F_x = \rho h (U_N^2 - U_0^2) + \sum_{i=0}^N \frac{U_i + U_{i+1}}{2} \rho V_i dl \quad (3.16)$$

The wall shear force over the plasma body force region is computed with:

$$F_{wall} = - \sum_{i=0}^N \mu \frac{U_i}{kh} dl \quad (3.17)$$

The shear force at the upper edge of the control volume is calculated with:

$$F_{edge} = \frac{\mu U_0}{kh} l \quad (3.18)$$

And the isolated plasma body force (F_{act}) is given by:

$$F_{act} = F_x - (F_{edge} + F_{wall}) \quad (3.19)$$

3.4.1. IONIZED FRACTION AND ION DRIFT VELOCITY

The analytical model requires the spatial distribution of the ionized fraction $i_D(x)$. This can be computed using first principles numerical models [85] or directly measured [30, 92]. A lower complexity solution is to estimate the charge density based on the light intensity of the plasma region as was measured in section 3.3.1. It can be assumed that the intensity of light emitted by the discharge is proportional to the ionized fraction [103]. Accordingly, the ionized fraction spatial distribution is obtained from the experimental results illustrated in Figure 3.6. The maximum value, occurring at the exposed electrode's edge, is scaled to match the value reported by [92]. The imposed ionized fraction distribution is shown in Figure 3.9.

The spatial distribution of the average ion drift velocity $V_D(x)$ is obtained from the electrostatic field. The Poisson equation is solved considering the geometry of the electrodes and dielectric arrangement displayed in Figure 3.2. The relative permittivity of Plexiglas is taken as $\epsilon_r = 3$ and the potential of the exposed electrode is set to the maximum amplitude of the electric signal imposed, $V = 20kV$. The spatial distribution of the horizontal component of the electric field at the body force region, $E_x(x)$, is determined using:

$$E_x(x) = \frac{1}{h} \int_{y=0}^h E_x dy(x) \quad (3.20)$$

where h represents the body force height.

The ion drift velocity is derived from experimental data [140] using

$$V_D = 0.8V_{DN_2^+} + 0.2V_{DO_2^+} \quad (3.21)$$

where the values 0.8 and 0.2 account for the molar fraction of Nitrogen and Oxygen ions in atmospheric air. The spatial distribution of the ion drift velocity is computed assuming the electric field from equation 3.20, and illustrated in Figure 3.9. It must be noted here that for the drift velocity calculation only positive ions are considered. The drift velocity of negative ions (O^- , O_2^-) is of the same order of magnitude [93] and as such does not effect the model predictions considerably.

3.4.2. MODEL PREDICTIONS

The results obtained with the analytical model are now compared with the experimental force measurements for different external flow speeds. Calculations are performed imposing $N = 1000$ elements. Figure 3.10 shows force values for the co-flow and counter-flow DBD configuration respectively. Additionally, Figure 3.11 shows the individual terms of related forces. The velocity U_0 imposed in the computational model corresponding to each external flow velocity is given in table 3.1. An important note to be made concerns the direction of these forces. Both plasma actuator (\vec{F}_{act}) and wall friction force ($\Delta\vec{F}_{wall}$) are imposed on the flow. As such a positive sign indicates downstream direction and vice versa. The load cell force ($\Delta\vec{F}_{LC}$) is the reaction force imposed on the load cell. As such its direction is always opposite of the sum of $\vec{F}_{act} + \Delta\vec{F}_{wall}$.

For the co-flow DBD configuration, the modeled actuator force, \vec{F}_{act} , weakly decreases with increasing external flow velocity for $U_\infty \geq 20 m/s$. This is due to the difference between the velocity of the air molecules and the drift velocity of the charged species, which is decreased, and thus the momentum transferred to the air is lower, according to equation 3.10. Additionally, the change in wall shear force, $\Delta\vec{F}_{wall}$, decreases with increasing external flow velocity. The wall shear force is calculated from the streamwise velocity, U_i , with equation 3.14. As the external flow velocity increases, the momentum added by the plasma is decreased, from equation 3.10. Additionally, equation 3.15 shows that if U_i is increased, the variation in streamwise velocity provoked by the DBD actuator is decreased, even if the momentum added to the flow by the plasma is kept constant. This leads to smaller changes in the velocity profile and hence decreases the variation of the wall shear force between the cases with and without actuation. In contrast, for low velocities and quiescent conditions, the effect of wall friction force is considerable. Care should thus be taken in interpreting force measurements done in quiescent conditions as the inclusion of wall friction forces can lead to underestimation of the plasma force.

Regarding the counter-flow DBD configuration, the model has been applied for velocities higher than $20 m/s$. The rationale behind this choice lies on the ability of the actuator to induce flow separation when acting against the flow as predicted by the present model. Nevertheless, due to the complexity of phenomena following separation (laminar-turbulent

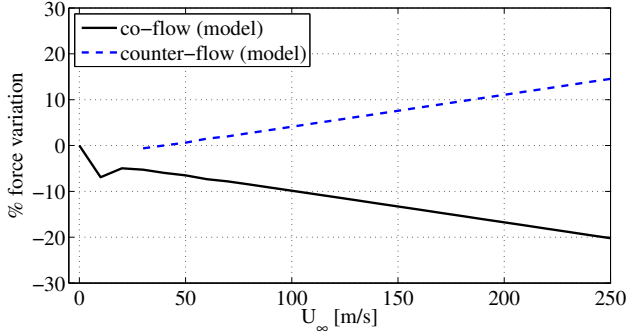


Figure 3.12: Modeled actuator force variation for different external flow speeds

transition, coherent structures shedding etc.), the model is deemed not accurate enough to treat such case. The absolute plasma force ($F_{act}^{\vec{}}$) value increases weakly with increasing free stream velocity, as the difference between convective air velocity and charged species drift velocity becomes more pronounced.

In general, the predictions of the presented analytical model correspond sufficiently well with the experimental results for both counter-flow and co-flow forcing configurations. Additionally, the model predicts a variation of the isolated plasma force for velocities which approach the order of magnitude of the charged species drift velocity. Figure 3.12 shows the modeled actuator force variation as different external flow speeds are imposed.

3.5. CONCLUSION

An experimental study was undertaken to assess the influence of the external flow velocity on the momentum transfer capability of DBD plasma actuators. Both counter-flow and co-flow configurations were tested. The actuator power consumption did not change significantly as different external flow speeds were applied, both in the counter-flow and co-flow DBD configurations. The plasma light emission did not change for co-flow forcing. In contrast, a clear trend of increasing intensity for increasing free stream velocity was observed in the case of counter-flow forcing.

The DBD plasma actuator force was measured with a load cell experimental set-up. For $20 \text{ m/s} \leq U_\infty \leq 60 \text{ m/s}$ the measured force is increasing in the case of co-flow forcing. The underlying cause of the behavior in the range above 50 m/s is unclear and further investigation is needed. In counter-flow forcing the measured force is nearly constant. The measured force captures the actuator body force together with the change in wall shear force. Results indicate significant changes are obtained in the wall shear force for low free stream velocities or quiescent conditions. Such an effect is of course dependent of the actuator's strength and on the external flow speed. Previous DBD optimization studies aiming at force maximization were mostly conducted in quiescent conditions, meaning the actuator's force was likely underestimated since the change in wall shear was neglected. Consequentially, the present study stresses that DBD plasma actuators may already be stronger than is claimed,

which is very encouraging for future research since the reduced momentum transfer capability is often their greatest drawback.

The challenge of determining the force produced by DBD actuators in the presence of external flow is considerable. On one hand, as large external flow speeds are imposed the actuator induced velocity changes are small and cannot be accurately measured to perform a momentum balance, which would yield the DBD force. On the other hand, a load cell set-up captures the actuator body force together with wall shear force changes. A simple analytical model is proposed to estimate the influence of the external flow velocity on the momentum transfer of DBD actuators. The model is based on momentum conservation during ion-neutral collisional processes and utilizes experimentally observed ion spatial distribution and drift velocity. The contribution of the wall shear force arising from the fluid viscosity is also included. Satisfactory agreement between modeled results and experimental data was obtained for the co-flow DBD configuration at different external flow speeds. For the counter-flow DBD configuration good agreement was also found, except for the cases in which flow reversal was predicted.

4

FREQUENCY RESPONSE OF FLOW UNDER AC-DBD PULSE ACTUATION

If minerals are to plants as plants are to animals, there must exist other levels of consciousness, to which we are, by definition, unaware of

Professor Antena (Mário de Sá-Carneiro)

This chapter provides a methodology to derive the local frequency response of flow under actuation, in terms of the magnitude of actuator induced perturbations. The method is applied to a DBD plasma actuator but can be extended to other kinds of pulsed actuation. The actuator body force term is introduced in the Navier-Stokes equations, from which the flow is locally approximated with a linear-time-invariant system. The proposed semi-phenomenological model includes the effect of both viscosity and external flow velocity, providing a system response in the frequency domain. A validity criterium is additionally devised for the estimation of the threshold frequency below which the developed approach can be applied. Analytical results are compared with experimental data for a typical DBD plasma actuator operating in quiescent flow and in a laminar boundary layer. Good agreement is obtained between analytical and experimental results for cases below the model validity threshold frequency. Results demonstrate an efficient and simple approach towards prediction of the response of a convective flow to pulsed actuation.

4.1. INTRODUCTION

Flow control devices are employed in a variety of scenarios with multiple control objectives. Actuators with different working principles including pneumatic, shape-morphing and plasma actuators have been considered for flow control applications, with comprehensive reviews given in [116, 6, 59]. Regardless of the specific control objective, knowledge of the base flow characteristics is necessary for efficient actuation employment [72]. Accordingly most flow control applications rely on length and velocity scales representative of the flow domain and geometry to prescribe actuator operation. A typical scenario is airfoil separation control [108, 115] in which the optimal actuation frequency is determined based on the free stream velocity and airfoil chord. On the other hand, laminar-turbulent transition control [48, 67] is governed by smaller actuation scales. For such applications the actuation frequency is often adjusted to control Tollmien-Schlichting waves [20], and tailored to the specific boundary layer receptivity [66]. In general, and for any flow control application including transition and airfoil separation control, the flow response to actuator perturbations depends on specific base flow characteristics, hydrodynamic instabilities, non-linearity, etc [44]. The present study considers the flow response to actuator induced perturbations is represented by subsystem H_2 , as illustrated in figure 4.1. However, to capture the physical behavior of flow control systems it is also necessary to consider the dynamic response of the perturbation generation system itself, *i.e.* the dependence of the actuator induced perturbations on the base flow characteristics [71]. The subsystem describing the actuator and the generation of perturbations is illustrated by system H_1 in figure 4.1.

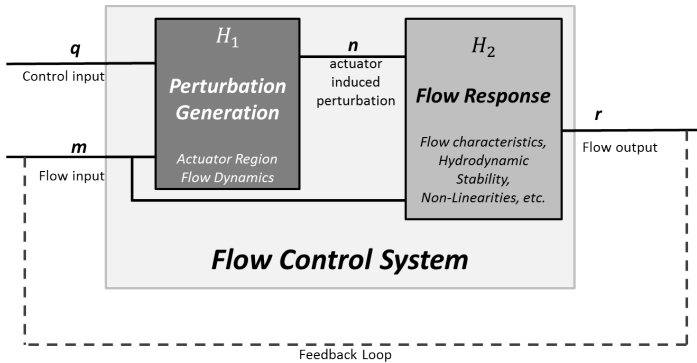


Figure 4.1: Illustration of subsystems in a flow control application

The current effort focuses on the actuator region flow dynamics, represented by system H_1 in figure 4.1. Many flow control devices operate only at relatively low frequencies ($O(10^1) Hz$); particularly pneumatic actuators [115, 37] may have mechanical constraints which impede operation at high actuation frequencies. However, flow control devices with large dynamic range such as DBD actuators [96] will operate both at low and high frequencies (up to 400 Hz). Accordingly, such broadband flow control devices may induce different flow perturbations at different actuation frequencies [9]. This chapter thus provides a

methodology to estimate the local frequency response of flow under actuation, in terms of the magnitude of actuator induced perturbations. The method is applied to a typical DBD plasma actuator. The actuator region flow is approximated with a linear-time-invariant system, including the influence of externally imposed flow and viscosity. Finally, analytical results are compared with experimental data.

4.2. ACTUATOR REGION FLOW AS A LINEAR-TIME-INVARIANT SYSTEM

The perturbation induced by the flow control device depends on the type of actuation employed. The present study focuses on non-thermal DBD plasma actuators [2, 115], meaning the flow control device does not induce significant temperature gradients [136] and consequently air density and viscosity are unaffected by actuation. Additionally, the actuator operates at relatively low external flow velocities, and as such compressibility effects are neglected. The analysis of flow under actuation is restricted to convectively unstable flows [55], such as laminar boundary layers. Accordingly, flows governed by global and/or absolute instability are not accounted for [55]. Finally, the large spanwise extent typically employed by plasma actuators ensures minimal edge effects and near two-dimensional flow when considering the mid-span location [71].

Under these assumptions, the 2D incompressible Navier-Stokes equations in the presence of actuator body forces [70] are expressed as:

$$\frac{\partial \vec{U}}{\partial t} + \vec{U} \cdot \nabla \vec{U} = +\nu \nabla^2 \vec{U} - \frac{\nabla P}{\rho} + \frac{\vec{f}_{ACT}}{\rho} \quad (4.1)$$

In order to explicitly introduce the effect of actuator induced perturbations, the flow is decomposed in the sum of a steady base flow (\vec{U}_0 , P_0) and a fluctuation or perturbation component (\vec{u} , p). The velocity, pressure and force fields are decomposed with

$$\vec{U}(X, Y, t) = \vec{U}_0(X, Y) + \vec{u}(X, Y, t) \quad (4.2)$$

$$P(X, Y, t) = P_0(X, Y) + p(X, Y, t) \quad (4.3)$$

$$\vec{f}_{ACT} = \vec{f}_{ACT}(X, Y, t) \quad (4.4)$$

Inserting expressions (4.2-4.4) in equation 4.1 and subtracting the mean values yields the expression for the disturbances:

$$\frac{\partial \vec{u}}{\partial t} + (\vec{u} \cdot \nabla) \vec{u} + (\vec{U}_0 \cdot \nabla) \vec{u} + (\vec{u} \cdot \nabla) \vec{U}_0 = +\nu \nabla^2 \vec{u} - \frac{\nabla p}{\rho} + \frac{\vec{f}_{ACT}}{\rho} \quad (4.5)$$

The current approach considers flow control devices acting parallel to the streamwise direction [2, 115], coincident with the X component. Conservation of momentum in the principal actuator body force direction is regarded as representative of the actuator region flow dynamics. By following boundary layer hypothesis [114], and recalling that equation 4.5 describes the perturbed flow field, the following approximations are made:

$$\begin{cases} U_{0y} \ll U_{0x} \\ \frac{\partial U_{0x}}{\partial X} \ll \frac{\partial u_x}{\partial X} \end{cases} \quad (4.6)$$

where subscripts x and y indicate velocity component in the X and Y direction respectively. Introducing the approximations from 4.6 in equation 4.5 it is possible to express conservation of momentum in the X direction of the actuator perturbed flow:

$$\frac{\partial u_x}{\partial t} + \frac{\partial u_x}{\partial X} (U_{0x} + u_x) + u_y \left(\frac{\partial U_{0x}}{\partial Y} + \frac{\partial u_x}{\partial Y} \right) = \underbrace{\nu \left(\frac{\partial^2 u_x}{\partial X^2} + \frac{\partial^2 u_x}{\partial Y^2} \right) - \frac{1}{\rho} \frac{\partial p}{\partial X} + \frac{f_{ACTx}}{\rho}}_{f_x / \rho} \quad (4.7)$$

The RHS of equation 4.7 translates f_x / ρ , that is the force per unit mass acting in the X direction, with three terms representing viscosity, pressure and actuator contributions.

4.2.1. LINEAR-TIME-INVARIANT SYSTEM

The present work employs linear-time-invariant(LTI) theory [125] to study the dynamic system defined in equation 4.7. A LTI system was chosen to approximate the actuator region flow for two reasons. First, LTI theory is well understood and established, and provides simple analytical solutions [135], while higher order systems often cannot be solved analytically. Second, in eq 4.7 the time derivative is only first order, and as such no second order time derivative (non-linear in time) terms are explicitly present.

In general a LTI system is written in state-space representation as:

$$\begin{cases} \dot{m} = Am + Bq \\ n = Cm + Dq \end{cases} \quad (4.8)$$

where m is the state and \dot{m} is the time derivative of the state, q represents the control input and n is the output, as also shown in figure 4.1. Matrices A, B, C and D describe the linear relationships between the variables. The present study regards momentum conservation in the X direction as representative of the actuator region flow dynamics. As such the LTI system is defined as:

$$\begin{cases} m \equiv u_x \\ q \equiv f_x \\ n = m \equiv u_x \end{cases} \quad (4.9)$$

Applying the Laplace transform [143] to the set of equations in 4.8, it is possible to arrive at the transfer function $G(s)$ of the LTI system. The ratio between perturbation velocity and input force is expressed with:

$$\frac{u_x(s)}{f_x(s)} = G(s) = C(sI - A)^{-1}B + D \quad (4.10)$$

where $s = j\omega$ represents the forcing frequency imposed by the actuator and I is the identity matrix. It is evident however, that the dynamic system defined by eq 4.7 cannot be readily evaluated as a LTI system because of the velocity spatial derivatives. Accordingly, further actuator related topology information is necessary to obtain the frequency response of the actuator region flow.

4.3. THE DBD PLASMA ACTUATOR CASE

The flow under DBD plasma actuation is analyzed using a single element control volume encompassing the plasma body force region. This is represented in figure 4.2, where the plasma region height and length are denoted by h and l respectively. For simplicity it is assumed the velocities normal to the control volume surface are constant over each edge. Referring to figure 4.2, the velocities in the control volume are approximated with:

$$\left\{ \begin{array}{l} u_x \equiv u \\ u_y \equiv -v \\ U_{0x} \equiv U_0 \\ U_x(0) = U_0 \\ U_x(l) = U_0 + u \end{array} \right. \quad (4.11)$$

Using these approximations and recalling the incompressibility assumption, it is possible to write mass conservation in the control volume with:

$$\nabla \cdot \vec{u} = 0 \rightarrow \frac{u}{l} - \frac{v}{h} = 0 \quad (4.12)$$

It is assumed the DBD actuator is operating in a (locally) flat plate configuration. Additionally it is noted that pressure fluctuations arising from actuation employment are negligible [67] compared to the plasma body force, meaning the streamwise pressure gradient may be neglected:

$$\frac{\partial p}{\partial X} \approx 0 \implies p(0) = p(l) \quad (4.13)$$

In order to approximate the actuator region flow with a LTI system, the present study considers steady [42, 132] DBD actuation employment. Under steady or constant actuation the velocity perturbation induced by the DBD actuator corresponds to the non-transient or equilibrium velocity perturbation. Under these assumptions momentum conservation in the X direction is written as:

$$\begin{aligned} F_X &= \int \int \rho U_x (\vec{U} \cdot \vec{n}) dA = \\ &= \rho((U_0 + u)^2 - U_0^2) \cdot h - \frac{U_0 + U_0 + u}{2} \rho \cdot v \cdot l \end{aligned} \quad (4.14)$$

where F_X represents the total force in the X direction acting over the whole control volume, dA is the element area and \vec{n} is the vector normal to the control volume surface pointing outwards. Reworking equation 4.12 and introducing it in expression 4.14 yields:

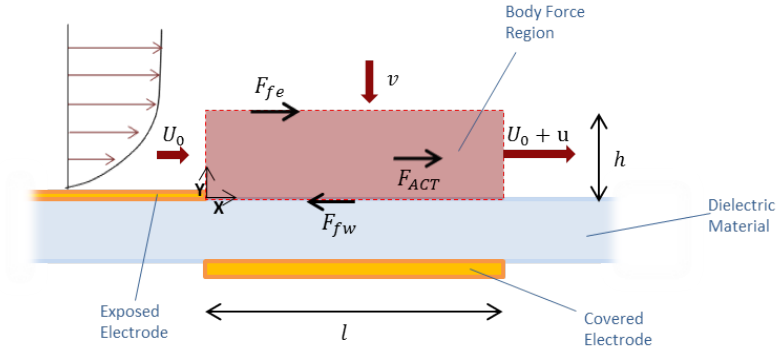


Figure 4.2: DBD Actuator Control Volume (Not to scale)

$$F_X = \frac{\rho \cdot h \cdot u}{2} (2U_0 + u) \quad (4.15)$$

which can be rearranged to explicitly yield the streamwise velocity perturbations in the control volume:

$$u = -U_0 + \sqrt{U_0^2 + \frac{2F_X}{\rho h}} \quad (4.16)$$

4.3.1. DBD PLASMA ACTUATOR LTI SYSTEM

At this point it is noted that expression 4.16 translates the velocity perturbations obtained with constant actuation employment, corresponding to the non-transient or equilibrium actuator induced velocity perturbation. In order to capture the non-equilibrium response typical for pulsed actuation expression 4.16 is used to linearize the dynamic system representing the actuator region flow.

Equation 4.7 from section 4.2 is now revisited such that the frequency response of the actuator region flow can be derived with LTI theory (equation 4.10). To this end, and consistently with equations 4.12 and 4.14, the variation of streamwise velocity perturbation ∂u_x can be approximated by the plasma region control volume perturbation velocity u , illustrated in figure 4.2. Additionally, an order of magnitude analysis is used to relate streamwise and wall normal characteristic length with the geometry of the body force region of DBD actuators. These approximations are expressed by:

$$\begin{cases} \partial u_x \approx u \\ \partial X \approx l \\ \partial Y \approx h \end{cases} \quad (4.17)$$

Introducing mass conservation (equation 4.12) and the approximations from equations 4.11 and 4.17 in expression 4.7 produces:

$$\begin{aligned} \frac{\partial u}{\partial t} + \frac{u}{l}(U_0 + u) + \frac{hu}{l}\left(\frac{U_0}{h} + \frac{u}{h}\right) &= \frac{f_x}{\rho} \\ \Rightarrow \underbrace{\frac{\partial u}{\partial t}}_{\text{unsteady}} + \underbrace{\frac{2}{l}(U_0 + u)}_{\mathbf{A \ matrix}} u &= \underbrace{\frac{1}{\rho}}_{\mathbf{B \ matrix}} f_x \end{aligned} \quad (4.18)$$

where the terms corresponding to the LTI space-state representation matrices (eqs 4.8) are highlighted. The steady actuation induced velocity perturbation from equation 4.16 is inserted in the A matrix, in order to linearize the dynamic system. The actuator region flow transfer function is finally written as:

$$\begin{aligned} \frac{u(s)}{f_x(s)} = G(s) &= C(sI - A)^{-1}B + D = \\ &= \frac{1}{\rho} \frac{1}{s + \frac{2\sqrt{U_0^2 + \frac{2F_X}{\rho h}}}{l}} \end{aligned} \quad (4.19)$$

Expression 4.19 shows the LTI system is a low-pass filter. Accordingly the magnitude of the actuator induced perturbations (u) decreases as higher forcing frequencies are imposed. The cut-off frequency f_{CO} of the low-pass filter is given by the absolute value of the pole p :

$$f_{CO} = -p_{G(s)} = \frac{2\sqrt{U_0^2 + \frac{2F_X}{\rho h}}}{l} \quad (4.20)$$

These characteristic attributes of the LTI system indicate that as larger base velocities (U_0) are considered the cut-off frequency increases. Ultimately this leads to an increase of the range of possible actuation frequencies at larger external flow velocities, which matches experimental evidence [71]. It should be kept in mind however the current analysis of flows under actuation is restricted to convectively unstable flows [55], such as laminar boundary layers.

4.3.2. LINEARIZATION VALIDITY

The actuator region flow transfer function (equation 4.19) is obtained by linearizing the dynamic system in equation 4.7. The actuator induced velocity perturbation from equation 4.16, which is used for the linearization, was obtained considering steady [42],[132] actuation. The present work, however, aims at determining the frequency response of the actuator region flow and thus focuses on unsteady forcing, which for the DBD plasma actuator in practice often corresponds to pulsed actuation [71, 9].

In the context of DBD plasma pulsed operation [71, 9], the actuation period may be separated into the *on* and *off* stage, designated respectively by t_{ON} and t_{OFF} . The pulse frequency f_p is defined as the frequency at which the actuator switches *on* and *off*. This is different from the frequency of the high voltage signal which creates and sustains the plasma via the DBD mechanism, usually termed carrier frequency f_{AC} . The duty cycle DC is the

percentage of the time period the actuator is *on* over one actuation period. A schematic of a typical actuation signal is shown in figure 4.3.

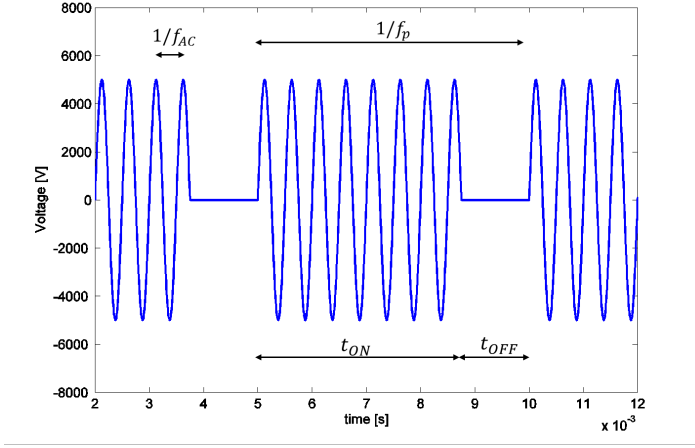


Figure 4.3: Sample of the voltage signal with characteristic actuation values $f_{AC} = 2kHz$, $f_p = 200Hz$ and $DC = 75\%$

The validity of the proposed linearization is analyzed by recalling expression 4.18. Since the A matrix is calculated using the steady velocity perturbation (expression 4.16), one expects the LTI system is a suitable approximation of the actuator region flow only if the A matrix term is larger than the unsteady term:

$$\frac{\partial u}{\partial t} < \frac{2}{l} (U_0 + u) u \quad (4.21)$$

The validity criterium 4.21 implicitly assumes the DBD plasma induced forces act instantaneously. In reality DBD plasma ion-neutral collisional processes and associated microdischarges have very small characteristic ($O(10^{-7})$ s) time scales [38], much smaller than typically found in DBD pulsed operation [9, 71]. Accordingly, for the purpose of modelling DBD actuator pulsed operation, the actuation pulse frequency f_p may be related with the representative time step with:

$$\frac{1}{\partial t} \approx f_p \quad (4.22)$$

Introducing the pulse frequency in expression 4.21 and recalling order of magnitude arguments from expression 4.17 it is possible to set the validity criterium for the proposed LTI approximation with:

$$f_p < f_{p_{MAX}} = \frac{2}{l} (U_0 + u) \quad (4.23)$$

4.4. INFLUENCE OF VISCOSITY

Up to this point the actuator region flow dynamics was expressed as a function of the force acting in the streamwise direction f_x . Even though the force experienced by the actuator

region flow is due to the actuator employment, the plasma body force is not the only force component; shear forces associated with fluid viscosity appear as a reaction force, opposing to the plasma thrust. Previous work [107, 104] has shown the actuation induced shear force and the plasma body force are of the same order of magnitude for low base flow velocities. Accordingly, shear forces arising from viscosity are explicitly considered in the current modelling effort.

By recalling that the contribution of the pressure gradient is negligible (eq 4.13), and referring to figure 4.2, the forces acting on the control volume are:

$$F_X = F_{ACT} + F_{SHEAR} \quad (4.24)$$

where F_{ACT} is the spatially integrated plasma body force over the control volume, often referred to as thrust [132]. F_{SHEAR} denotes the integral of viscous forces arising from actuator induced velocity perturbations, approximated with:

$$F_{SHEAR} \approx F_{fw} + F_{fe} = \int_0^l (\tau_w + \tau_h) dX \quad (4.25)$$

where F_{fw} and F_{fe} illustrated in figure 4.2 denote the wall friction force and control volume's upper edge friction force, respectively. In equation 4.25 symbols τ_w and τ_h correspond to shear stress at the wall ($Y = 0$) and at the control volume's upper edge ($Y = h$) respectively. As mentioned before, these shear forces are to be understood as arising from the actuator induced perturbations. Analogously to the actuator induced velocity perturbations, the present study assumes the actuator causes a perturbation to the shear forces.

If the actuator operates in quiescent conditions there is no externally imposed flow ($U_0 = 0$). In this case all flow velocities are induced by the actuation. As such, maximum actuator induced velocities (eq 4.16) occur at quiescent conditions. To obtain the velocity field \vec{u} the present study uses particle image velocimetry data from a previous experiment [71]. The quiescent shear forces are estimated (eq 4.25) for this particular DBD actuator configuration with:

$$\begin{aligned} F_{SHEAR}(U_0 = 0) &\approx \tau_0 l \\ &\approx \rho v \int_0^l \left(\frac{\partial u_x}{\partial Y}(X, 0) + \frac{\partial u_x}{\partial Y}(X, h) \right) dX \end{aligned} \quad (4.26)$$

in which τ_0 is the representative shear stress in quiescent flow and steady actuation. Table 4.1 shows the relevant experimental parameters for the particular DBD configuration. Figure 4.4 illustrates the experimental streamwise evolution of shear stresses over the actuator region in quiescent flow and steady actuation, obtained with eq 4.26.

In case the actuator operates in an externally imposed flow ($U_0 \neq 0$), the present study considers a first order approximation to estimate the actuator induced shear force:

$$F_{SHEAR}(U_0) \approx -\frac{u(U_0)}{u_0} \tau_0 l \quad (4.27)$$

where u_0 corresponds to quiescent operation. The induced velocity perturbation including shear forces is obtained by inserting expressions 4.24 and 4.27 in eq 4.15. Algebraic manipulation yields:

$$u = -\left(U_0 + \frac{\tau_0 l}{\rho h u_0}\right) + \frac{1}{\rho h} \sqrt{\left(\rho h U_0 + \frac{\tau_0 l}{u_0}\right)^2 + 2 \rho h F_{ACT}} \quad (4.28)$$

The obtained variation of viscous perturbation velocity (u) with base flow velocity (U_0) under steady actuation is shown in figure 4.4. The shear force calculated with eq 4.27 for different base flow speeds is also shown in figure 4.4. The actuator force is assumed constant for the range of considered base (and external) flow velocities [104].

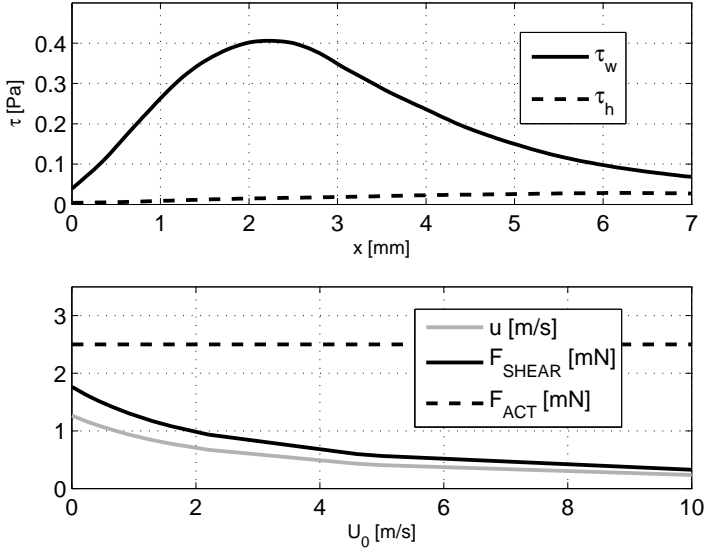


Figure 4.4: *top*-Experimental shear stress distribution [71] and *bottom*- modeled perturbation velocity and shear versus external velocity

At this point the contribution of shear forces is included in the LTI system. Inserting the viscous perturbation velocity (eq 4.28) in the A matrix term of expression 4.18 yields

$$\frac{\partial u}{\partial t} + \underbrace{\frac{2}{l} \left(\sqrt{\left(U_0 + \frac{\tau_0 l}{\rho h u_0} \right)^2 + \frac{2 F_{ACT}}{\rho h}} - \frac{\tau_0 l}{\rho h u_0} \right)}_{A \text{ matrix}} u = \frac{f_x}{\rho} \quad (4.29)$$

Recalling the streamwise pressure gradient can be neglected (eq 4.13), it is possible to use an order of magnitude analysis and express the RHS of expression 4.29 with:

$$f_x \approx \frac{F_X}{lh} \approx \frac{F_{ACT} + F_{SHEAR}}{lh} \approx f_{ACT} + f_{SHEAR} \quad (4.30)$$

Finally, the actuator region flow system from expression 4.7 is approximated with:

$$\frac{u(s)}{f_{ACT}(s)} = \frac{u(s)}{f_x(s)} \frac{F_X}{F_{ACT}} = \frac{F_X}{F_{ACT}} \frac{1}{\rho} \frac{1}{s + \frac{2}{l} \left(\sqrt{(U_0 + \frac{\tau_0 l}{\rho h u_0})^2 + 2 \frac{F_{ACT}}{\rho h} - \frac{\tau_0 l}{\rho u_0 h}} \right)} \quad (4.31)$$

Compared to expression 4.19 from section 4.3, eq 4.31 explicitly shows the contribution of viscous and actuator forces in the LTI system dynamics. The shear forces decrease the ratio between velocity perturbations and actuator force density (LHS of eq 4.31). In other words, and analogously to a mass-spring-damper system, viscous forces reduce the amplitude of (velocity) perturbations.

It is noted that expressions 4.29 to 4.31 implicitly assume the shear forces arise instantaneously from velocity perturbations. This hypothesis is consistent with the assumption of incompressible flow, on which the current modelling effort is based. Alternatively, the characteristic time for shear forces to adapt to (actuator induced) velocity perturbations over the entire control volume can be estimated using a representative length scale and the speed of sound [26]:

$$O(t_{SHEAR}) \approx \frac{l}{M} = 2 \times 10^{-5} s \quad (4.32)$$

in which M denotes the speed of sound in air at standard pressure and temperature. Expression 4.32 indeed confirms that, for modeling DBD pulsed actuation in moderate subsonic velocities, the shear forces may be considered to act instantaneously. Accordingly, the validity range of the LTI approximation is still determined by the criterium expressed in 4.23.

4.5. EXPERIMENTAL VALIDATION

The proposed approach is now tested against experimental results. The validation case [71] used a DBD plasma actuator constructed with copper electrodes and thin Kapton polyimide tape acting as dielectric barrier. The actuator was operated in pulse mode, and tested at different pulse frequencies (f_p), duty cycles (DC) and base flow velocities (U_0). The main characteristics of the actuator and data points are displayed in table 4.1.

4.5.1. EXPERIMENTAL DATA PROCESSING

The validation case [71] measured the velocity with a single hot-wire anemometer [64], effectively registering only the absolute velocity magnitude. The hot-wire probe was located at position $x = 7 \text{ mm}$ and $y = 0.75 \text{ mm}$, roughly corresponding to the location of maximum average induced velocity. Consistently with sections 4.2 and 4.3, the actuator induced velocity perturbations are assumed to be dominant in the streamwise direction X compared to wall normal Y velocity perturbations. This is expressed by the approximation:

$$|\vec{U}|_{EXP} = \bar{U} + u_{EXP} \approx U_x \approx U_{0,x} + u_x \quad (4.33)$$

where $|\vec{U}|_{EXP}$ denotes the experimental velocity (magnitude) registered. Symbol \bar{U} expresses the mean (time-averaged) velocity and u_{EXP} denotes experimental velocity perturbations. From the available measurements, the present study uses the velocity perturbations obtained with a pulse duty cycle $DC = 50\%$. This choice is motivated by two factors.

Parameter	Value
F_{ACT}	0.0025 N/m
τ_0	0.25 Pa
h	0.75 mm
l	7 mm
Voltage	10 kV _{pp}
f_{AC}	2 kHz
f_p	25; 50; 100; 200; 400 Hz
DC	{25; 50; 75; 100} %
ρ	1.2 kg/m ³
μ	1.8 × 10 ⁻⁵ N s/m ²
U_0	{0; 4.6} m/s

Table 4.1: Experimental parameters

First, the magnitude of the velocity fluctuations at $DC = 50\%$ is larger [71] than for any other duty cycle. Additionally, the signal waveform of a 50% duty cycle is closest to a single harmonic excitation, and as such better approximated by the LTI system defined in section 4.2.

For comparison between experimental and modelled results it is necessary to extract a representative velocity perturbation from the experimental velocity signal. This is achieved by approximating the measured velocity signal with a single harmonic signal, with frequency corresponding to the excitation pulse frequency f_p . The representative velocity perturbation u_{REP} is written with:

$$u_{REP}(t) = \beta \sin(2\pi f_p t + \phi) \quad (4.34)$$

where β is the amplitude and ϕ expresses the phase of the sinusoid. The representative velocity is obtained from input variables β and ϕ by formulating an optimization problem solved with the Nelder-Mead algorithm [77]. For each pulse frequency the difference between representative and experimental velocity is minimized:

$$\min \left(\int_{t_0}^{t_{END}} \int_{\tau_1}^{\tau_2} |u_{REP}(\tau) - u_{EXP}(\tau)| d\tau dt \right) \quad (4.35)$$

where τ_1 and τ_2 are chosen to capture 5 excitation cycles with:

$$\tau_2 - \tau_1 = \frac{5}{f_p} \quad (4.36)$$

and t_0 and t_{END} represent the convolution limits prescribing the time integration domain. An example of the single harmonic fit to the experimental velocity signal obtained with $f_p = 25$ and 100 Hz is illustrated in figure 4.5.

Even though higher harmonics are present in the experimental measurement [71], figure 4.5 indicates that the amplitude of the experimental velocity fluctuations is reasonably captured by employing a single harmonic. It is important to note that the above is a necessary compromise in the context of the LTI approximation. The proposed LTI methodology additionally considers the actuator forcing as a single harmonic. Despite this approximation the agreement of the single harmonic fit to the experimental measurement is capturing

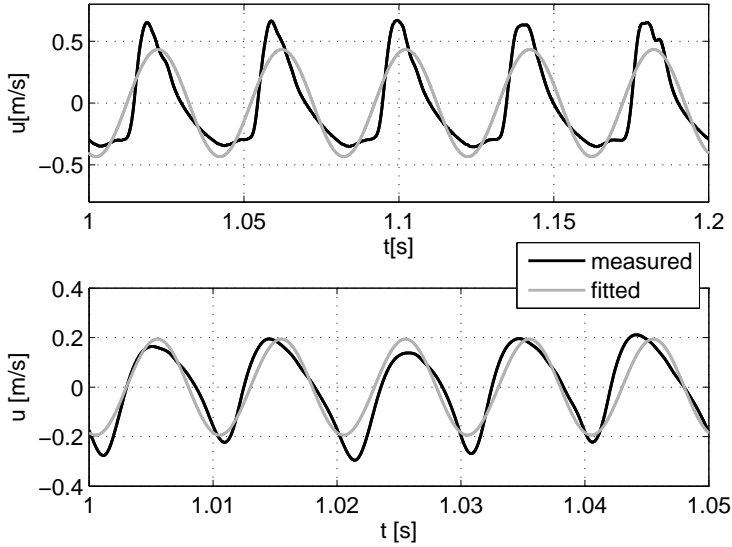


Figure 4.5: Experimental and fitted single harmonic perturbation velocity at quiescent conditions for $f_p = 25 \text{ Hz}$ (top) and $f_p = 100 \text{ Hz}$ (bottom)

the general dynamic response and as such the amplitude β of the fitted single harmonic is considered representative of the amplitude of experimental velocity fluctuations induced by the DBD actuator.

4.5.2. COMPARISON WITH MEASUREMENTS

Analytical and experimental results are compared using the magnitude L of the frequency domain transfer function $G(s)$. The magnitude of the analytical model is defined as:

$$L_{G(s)Mod} \approx 20 * \log\left(\frac{u(s)}{f_{ACT}(s)}\right) \quad (4.37)$$

Respectively, the experimental magnitude is expressed as:

$$L_{G(s)Exp} \approx 20 * \log\left(\frac{\beta(s)}{f_{ACT}(s)}\right) \quad (4.38)$$

The factor 20 used for magnitude definition is arbitrary and was chosen according to standard practice in LTI system analysis [125]. The model results are compared with experimental data in figures 4.6 and 4.7. The experimental error bars are calculated based on the uncertainty [67] in the actuator integrated force F_{ACT} . It is noted that figure 4.6 shows model results obtained at a pulse frequency $f_p = 0 \text{ Hz}$. Strictly speaking however, the proposed methodology assumes (expression 4.2) the velocity field to be unsteady ($f_p > 0 \text{ Hz}$), rendering the analysis not valid at $f_p = 0 \text{ Hz}$. Nevertheless, in practice DBD actuator pulse

operation is always used with $f_p > 0 \text{ Hz}$, and the value obtained at $f_p = 0 \text{ Hz}$ remains an indication of the system's static gain.

Figure 4.6 shows the results obtained in quiescent flow $U_0 = 0 \text{ m/s}$. For comparison, the model results obtained without viscosity ($f_X = f_{ACT}$) are also included. Results show the 'inviscid' system (eq 4.19) captures the low pass filter behaviour of the local flow observed in experimental data. As actuator pulse frequency increases the magnitude of induced velocity perturbations decreases. By introducing viscosity the analytical model predicts a weaker velocity perturbation compared to the 'inviscid' case, matching experimental results more closely. Figure 4.6 also highlights the behaviour of the LTI model as the validity criterium is approached (eq 4.23). The analytical model shows good agreement with experimental results for pulse frequencies below $f_p < 200 \text{ Hz}$, with model predictions mostly within measurement error. At higher excitation frequencies, the limit for the model validity is approached and analytical results deviate from experimental data points. The analytical model overestimates the magnitude of velocity perturbations since the unsteady contribution increases for increasing actuation pulse frequency (LHS of eq 4.18).

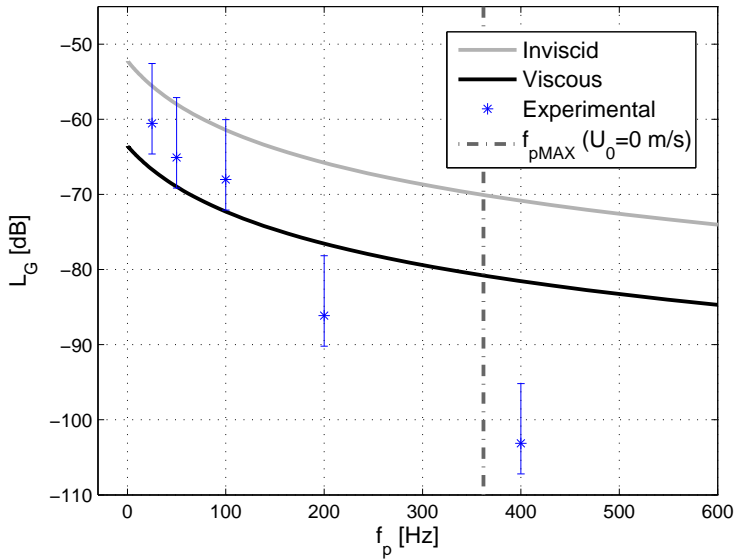


Figure 4.6: Modeled fluid system response, with experimental data from [71]- Influence of Viscosity in Quiescent case

Figure 4.7 shows the influence of velocity on the viscous actuator region flow. Experimental data for both quiescent and external flow with $U_0 = 4.6 \text{ m/s}$ are included. Analytical results show the static gain ($f_p = 0 \text{ Hz}$) of the LTI transfer function decreases with increasing external flow velocity, consistently with eq 4.16. Additionally it is evident that the presence of an external flow shifts the cut-off frequency, since the pole frequency increases with

increased external velocity (eq 4.20). This can be intuitively perceived as a "transition" of the flow from a more viscosity dominated regime to a more inertia dominated regime with the increase of the external velocity, effectively represented by an increasing local Reynolds number. At the higher velocities the viscous damping of any introduced perturbations is less than for the quiescent case.

Generally the agreement between experimental data and the analytical model is satisfactory for the external flow velocities considered. Particularly for f_p of 25 to 100 Hz results show a good match; the proposed model captures the steeper magnitude decrease for quiescent conditions, matching the experimentally measured larger magnitudes at higher frequencies obtained with external flow. It is also interesting to note that the analytical model is in good agreement with experimental data at $f_p = 200\text{Hz}$ under external flow, as opposed to the quiescent flow case. This result is consistent with the validity range of the LTI approximation, as expressed by eq 4.23.

Figures 4.6 and 4.7 compare 2D modelling results with experimental data taken at the plasma actuator mid-span location. Even though the large spanwise extent typically used in DBD applications ensures near 2D flow at the mid-span location, it can be expected that 3D phenomena will be present in the vicinity of the plasma actuator spanwise edge. Since the plasma force field component in the spanwise direction (not-shown) becomes non-negligible, induced spanwise flow velocity will also exist near the actuator's edge. Accordingly the results presented cannot be directly extrapolated for spanwise locations approaching the edge of the DBD plasma actuator.

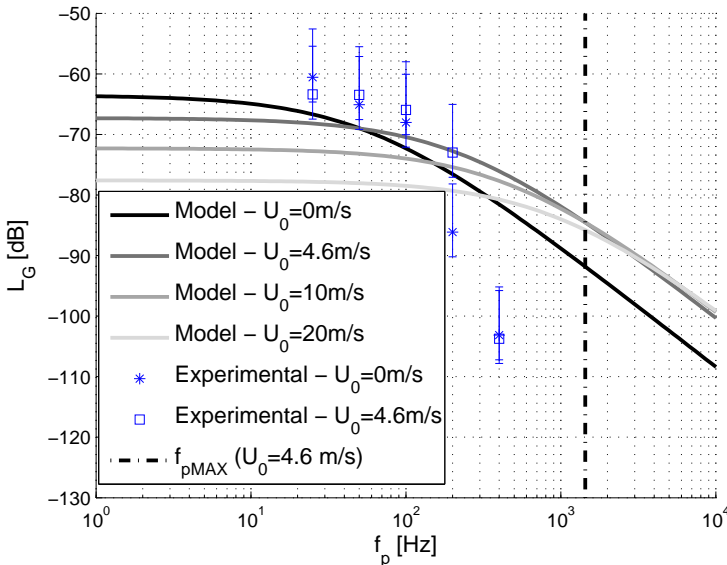


Figure 4.7: Modeled fluid system response, with experimental data from [71]- Influence of Velocity

4.5.3. APPLICATIONS AND OUTLOOK

Additionally to the experimentally available results, the prediction of the LTI model for higher external velocities $U_0 = 10$ and 20 m/s is shown in figure 4.7. The predictions illustrate the trend of actuator region flow frequency response at larger external velocities obtained with the proposed methodology. Such capability can enhance efforts of modelling and designing for control by providing an initial amplitude to Linear Stability Theory calculations for boundary layer flows [121]. Notably the e^N transition model [137] determines the occurrence of transition based on the amplification factor of (Tolmien-Schlichting waves) velocity perturbations by assuming an infinitesimal initial amplitude of the modelled perturbation. Improvements in prediction of transition location can be achieved by fixing the initial amplitude via a LTI approach.

Alternatively, the proposed model can be used to estimate and optimise the range of operation of a DBD actuator. For example, analytical results between $f_p = 1$ Hz and $f_p = 200$ Hz at quiescent flow show a velocity perturbation magnitude decrease $dL_G = 12.9$ dB, while for the same frequency range model results show that at $U_0 = 10$ m/s the velocity perturbation magnitude decreases by only $dL_G = 3.1$ dB. Consequently, in this specific case, actuator induced velocity perturbations could be considered damped at $f_p = 200$ Hz in quiescent flow, while with $U_0 = 10$ m/s the actuator would still generate significant velocity perturbations. Nevertheless care should always be taken that the LTI approximation is valid for the considered pulse frequency range (eq 4.23).

At this point a note needs to be made regarding the linearization procedure used in the proposed methodology. This is a necessary simplification in order to arrange the dynamical system in the LTI framework. The approach simplifies both the forcing input of the actuator as well as the output of the flow to single harmonic signals. Although the presented experimental results appear to be sufficiently approximated by the single harmonic fit, future efforts could include non-linear modeling of the actuator region flow. Explicitly incorporating the 2nd order terms from eq 4.7 would probably lead to increased fidelity; this is anticipated considering the experimental data points at higher frequencies in figure 4.7. The slope of the last two experimental points ($f_p = 200$ and $f_p = 400$ Hz) appears to be larger than predicted with the analytical model, approaching -60 dB/decade for quiescent operation, which is characteristic of higher order pole [125] behaviour. Nevertheless the present study indicates that the proposed method compares well with experimental data for the range of experimental pulse frequencies and external flow velocities. Results are encouraging given the model simplicity and accuracy obtained.

4.6. CONCLUSION

Actuators used in flow control applications are employed in different regimes, according to operational characteristics of the base flow. This chapter provides a methodology to estimate the local frequency response of flow under actuation. The method is applied to DBD plasma actuators operating in pulse mode. The analytical model includes the effect of external flow velocity and viscosity. Model results indicate increase of the operational frequency range of the actuator as the external flow velocity increases, while viscosity essentially decreases the magnitude of actuator induced perturbations. The model is compared with experimental data for a typical DBD plasma actuator operating in quiescent flow and in a laminar boundary layer. Reasonable agreement is obtained between analytical and experi-

mental results, with model predictions mostly within measurement error at pulse frequencies below the predicted validity criterium. Results demonstrate an efficient and simple approach towards prediction of the response of a convective flow to pulsed actuation, and may thus enhance future actuation scheduling design.

5

MODELING DBD PLASMA ACTUATORS IN INTEGRAL BOUNDARY LAYER FORMULATION

*Day destroys the night, night divides the day
tried to run, tried to hide
Break on through to the other side*

Jim Morrison

This chapter models the effect of DBD plasma actuators on airfoil performance within the framework of a viscous-inviscid airfoil analysis code. The approach is developed for incompressible, turbulent flow applications. Emphasis is placed on large Reynolds flow scenarios, while it is assumed the plasma body-force region is relatively small and acts inside the shear layer. The presence of body forces in the boundary layer is analyzed with a generalized form of the von Kármán integral boundary layer equations. The additional terms appearing in the von Kármán equations are treated for the particular case of plasma actuators, giving rise to a new closure relation. The model is implemented in a viscous-inviscid airfoil analysis code and validated by carrying out an experimental study. PIV measurements were performed on an airfoil equipped with DBD plasma actuators over a range of Reynolds number and AOA combinations. Balance measurements were also collected to evaluate the lift and drag coefficients. Results show the proposed model captures the magnitude of the variation in IBL parameters brought upon by the DBD actuator. Additionally the proposed methodology predicts the magnitude of the lift coefficient variations (ΔC_l) induced by plasma actuation. Ultimately the presented approach may enable the design of airfoils specifically tailored for DBD flow control, potentially decreasing the power required for successful active flow control applications.

This chapter has been presented at the 46th AIAA Plasmadynamics and Lasers Conference, AIAA Aviation, Dallas, Texas, Volume: AIAA 2015-3367 - DOI: 10.2514/6.2015-3367

5.1. INTRODUCTION

Within active flow control devices, plasma actuators have received particular attention over the last decade, owing to their large bandwidth, absence of moving parts and low power consumption. Several successful flow control applications have been reported, namely turbulent drag reduction [63], transition delay [48] and streamwise vortex generation [62]. Excellent reviews on plasma actuators for aerodynamic flow control have been published recently [96]. Among different applications, separation control remains very interesting especially because significant changes in sectional lift may be obtained. This could be used *e.g.* to trim a small aircraft by altering the elevator loading [40] or to increase the torque obtained with a horizontal axis wind turbine [129].

Due to the large degree of freedom in actuation configuration, geometric and electrical properties and flow control scenarios, an efficient and robust model of the actuator is highly desirable. Such a model can be used in CFD solvers and optimization algorithms in order to maximize the performance of the actuation system. Such a model has been extensively used in the form of a volume distributed body force roughly corresponding to the plasma cloud region [68] [119]. Several levels of fidelity exist for including the effect of DBD plasma actuators in flow control applications, ranging from simple phenomenological models [57] to highly detailed first principle models [85] as well as experimentally derived force distributions [69].

When considering airfoil design, the level of complexity of the computational methods used for aerodynamic calculation may be reduced, provided sufficient accuracy is preserved as to capture the relevant flow physics. A typical approach to evaluate the performance and subsequently design airfoils is through viscous-inviscid panel methods [35] [138], in which a potential flow problem is solved together with a viscous boundary layer (BL) computation. Previous efforts to include DBD actuators in a viscous-inviscid method [49] focused on the effect of the actuator on the external flow. However, the actuator body force region is typically only a few *mm* thick [69], meaning that DBD plasma actuators often operate in the shear layer. As such, the actuator influences the development of the boundary layer directly, but has only minimal direct influence on the external flow.

This chapter models the effect of DBD actuators in Integral Boundary Layer (IBL) formulation and compares model results with experimental data. Section 5.2 presents a generalized form of the *von Kármán Integral Boundary Layer Equations* to account for the presence of body forces. The body force terms of the generalized *von Kármán Integral Boundary Layer Equations* are treated for the specific case of DBD plasma actuators in section 5.3, in which a new closure relation is established to implement the model in inviscid/viscous airfoil calculation code RFOIL. Section 5.4 describes the experimental campaign in which an airfoil section equipped with two sets of DBD plasma actuators was tested at different operating conditions. Finally, section 5.5 compares modelled and experimental results, before conclusions are drawn in section 5.6.

5.2. IBL EQUATIONS WITH FORCE TERMS

In typical incompressible flow applications, the DBD actuator plasma behaves almost independently from the external flow field [8], [104]. Thanks to the weak coupling between phenomena, the plasma-kinetics challenge can be separated from the flow problem [76].

Accordingly, the aerodynamics of an airfoil with DBD actuation may be modeled by approximating solutions of the Navier-Stokes equations subject to prescribed external influences.

The plasma affects the flow by imposing body forces, thermal sources and fluid property changes. Even so, it is generally accepted that body forces dominate the actuation process, as typical temperature changes over cold plasmas rarely exceed a few degrees [Kotsonis2015]. Unsteadiness also arises due to the pulsating nature of the DBD plasma force field [101]. However, for constant actuation schedules the excitation takes place at the carrier frequency [9], [58], which is so high ($O(kHz)$) that it exceeds the flow's ability to respond¹.

For turbulent flows with constant actuation, the DBD plasma actuator essentially acts on the flow as a steady-state body force parallel to the airfoil surface. The body force magnitude varies in space, and experimental observations have shown that its spatial distribution exhibits nearly semi-elliptical iso-force lines [69]. These force patterns are approximately self-similar in the streamwise direction, and may thus be tackled with the kind of quasi-analytical treatments followed in mainstream boundary layer literature [114].

Considering the above, the effect of DBD plasma actuators on boundary layer development can be analysed with integral boundary layer methods, which are suitable for implementation in popular viscous-inviscid analysis codes such as RFOIL or XFOIL [35] [138]. To do so, a generalized form of the *Von Kármán Integral Boundary Layer Equations* must be found, considering the effect of body forces on the flow.

5.2.1. THE BOUNDARY LAYER APPROXIMATION

In order to derive a generalized form of the *Von Kármán Integral Boundary Layer Equations*, it is first necessary to find a generalized form of the *Boundary Layer Partial Differential Equations (PDE)*. Recalling that the large spanwise extent typically employed by plasma actuators ensures minimal edge effects and near two-dimensional flow at the mid-span location, the present study departs from the 2D incompressible Navier Stokes equations including actuator body forces [69]:

$$\begin{cases} \frac{\partial U}{\partial T} + U \frac{\partial U}{\partial X} + V \frac{\partial U}{\partial Y} = -\frac{1}{\rho} \frac{\partial P}{\partial X} + \nu \left(\frac{\partial^2 U}{\partial X^2} + \frac{\partial^2 U}{\partial Y^2} \right) + \frac{1}{\rho} F_x \\ \frac{\partial V}{\partial T} + U \frac{\partial V}{\partial X} + V \frac{\partial V}{\partial Y} = -\frac{1}{\rho} \frac{\partial P}{\partial Y} + \nu \left(\frac{\partial^2 V}{\partial X^2} + \frac{\partial^2 V}{\partial Y^2} \right) + \frac{1}{\rho} F_y \\ \frac{\partial U}{\partial X} + \frac{\partial V}{\partial Y} = 0 \end{cases} \quad (5.1)$$

Following an asymptotic analysis approach [144] [29], it is convenient to introduce a set of non-dimensional flow scales:

$$\begin{cases} x = \frac{X}{L} & y = \frac{Y}{\delta} \\ u = \frac{U}{U_e} & v = \frac{V}{U_e} \frac{L}{\delta} \\ p = \frac{P}{\rho U_e^2} & t = \frac{U_e}{L} T \end{cases} \quad (5.2)$$

The tangential flow scale L often corresponds to the airfoil chord while the normal length scale δ is usually associated with the boundary layer thickness. Introducing the *Reynolds*

¹This is not necessarily true for transition control or transient plasma excitation programs, as discussed for DBD pulse-mode actuation in chapter 4

number and noticing the above scale definition forms an homeomorphism, the Navier-Stokes equations can be rewritten exactly with the scaled variables:

$$\begin{cases} \frac{\partial u}{\partial t} + u \frac{\partial u}{\partial x} + v \frac{\partial u}{\partial y} = -\frac{\partial p}{\partial x} + \frac{1}{Re} \left(\frac{\partial^2 u}{\partial x^2} + \frac{L^2}{\delta^2} \frac{\partial^2 u}{\partial y^2} \right) + \frac{L}{\rho U_e^2} F_x \\ \frac{\partial v}{\partial t} + u \frac{\partial v}{\partial x} + v \frac{\partial v}{\partial y} = -\left(\frac{L}{\delta}\right)^2 \frac{\partial p}{\partial y} + \frac{1}{Re} \left(\frac{\partial^2 v}{\partial x^2} + \left(\frac{L}{\delta}\right)^2 \frac{\partial^2 v}{\partial y^2} \right) + \frac{L^2}{U_e^2 \delta} \frac{1}{\rho} F_y \\ \frac{\partial u}{\partial x} + \frac{\partial v}{\partial y} = 0 \end{cases} \quad (5.3)$$

By applying the order of magnitude operator to the x momentum conservation equation in system 5.3 and recalling the scaled variables (equation 5.2) have $O = 1$, an expression for the order of magnitude of the boundary layer thickness is obtained:

$$O\left(\frac{v}{U_e L} \left(\frac{L^2}{\delta^2}\right)\right) = O\left(1 - \frac{L F_x}{\rho U_e^2}\right) \quad (5.4)$$

When the plasma body force has smaller order of magnitude than the ratio between the local stagnation pressure and the longitudinal length scale, the traditional boundary layer scales remain appropriate:

$$O(F_x) \ll O\left(\frac{\rho U_e^2}{L}\right) \quad \Rightarrow \quad \frac{v}{U_e L} \left(\frac{L}{\delta}\right)^2 = O(1) \quad \Leftrightarrow \quad O(\delta) = O\left(\frac{L}{\sqrt{Re}}\right) \quad (5.5)$$

Feeding the approximate scale $\delta \simeq \frac{L}{\sqrt{Re}}$ into the momentum equations highlights the role of the Reynolds number :

$$\begin{cases} Re \left(\frac{\partial u}{\partial t} + u \frac{\partial u}{\partial x} + v \frac{\partial u}{\partial y} \right) = Re \left(-\frac{\partial p}{\partial x} + \frac{\partial^2 u}{\partial y^2} + \frac{L}{\rho U_e^2} F_x \right) + \frac{\partial^2 u}{\partial x^2} \\ \frac{\partial v}{\partial t} + u \frac{\partial v}{\partial x} + v \frac{\partial v}{\partial y} = Re \left(-\frac{\partial p}{\partial y} + \frac{1}{\sqrt{Re}} \frac{L}{\rho U_e^2} F_y \right) + \frac{1}{Re} \frac{\partial^2 v}{\partial x^2} + \frac{\partial^2 v}{\partial y^2} \\ \frac{\partial u}{\partial x} + \frac{\partial v}{\partial y} = 0 \end{cases} \quad (5.6)$$

It is now possible to perform the asymptotic approximation [144] [29] of the shear layer equations. Applying the Prandtl limit $Re \rightarrow \infty$ leads to the *Non-Dimensional Boundary Layer PDEs* with force terms:

$$\begin{cases} \frac{\partial u}{\partial t} + u \frac{\partial u}{\partial x} + v \frac{\partial u}{\partial y} = -\frac{\partial p}{\partial x} + \frac{\partial^2 u}{\partial y^2} + \frac{L}{\rho U_e^2} F_x \\ -\frac{\partial p}{\partial y} + \frac{1}{\sqrt{Re}} \frac{L}{\rho U_e^2} F_y = 0 \\ \frac{\partial u}{\partial x} + \frac{\partial v}{\partial y} = 0 \end{cases} \quad (5.7)$$

Inverting the scaling transformation with the approximation of equation 5.5 leads to the dimensional form of the *Boundary Layer PDEs*:

$$\begin{cases} \frac{\partial U}{\partial T} + U \frac{\partial U}{\partial X} + V \frac{\partial U}{\partial Y} = -\frac{1}{\rho} \frac{\partial P}{\partial X} + \nu \frac{\partial^2 U}{\partial Y^2} + \frac{1}{\rho} F_x \\ -\frac{\partial P}{\partial Y} + F_y = 0 \\ \frac{\partial U}{\partial X} + \frac{\partial V}{\partial Y} = 0 \end{cases} \quad (5.8)$$

5.2.2. INTEGRAL BOUNDARY LAYER MOMENTUM EQUATION WITH FORCE TERMS

At this point an exact integral ODE form of the *Boundary Layer PDEs* is sought. The first step consists in obtaining an integrable expression leading to the dimensional form of the *Integral Momentum Equation*. For this purpose, the edge velocity U_e is introduced and the continuity equation is rewritten as:

$$(U_e - U) \frac{\partial U}{\partial X} + (U_e - U) \frac{\partial V}{\partial Y} = 0 \quad (5.9)$$

Provided that the plasma body force is immersed in the shear layer, the Bernoulli equation is valid in all the outer flow, down to the edge of the boundary layer. Therefore, at the edge, the pressure gradient can be rewritten as a function of the velocity gradient² $\frac{\partial P}{\partial X} = -\rho U_e \frac{\partial U_e}{\partial X}$. With this in mind, adding equation 5.9 to momentum conservation in the x direction (equation 5.8) and neglecting the unsteady term yields:

$$-v \frac{\partial^2 U}{\partial Y^2} = U_e \frac{\partial U_e}{\partial X} - U \frac{\partial U}{\partial X} + (U_e - U) \frac{\partial U}{\partial X} - V \frac{\partial U}{\partial Y} + (U_e - U) \frac{\partial V}{\partial Y} + \frac{1}{\rho} F_x \quad (5.10)$$

In the present formulation the normal pressure gradient is neglected since the wall-normal plasma body force component is very small ($F_y \approx 0$) compared to the tangential component [69]. As such it is possible to write:

$$-v \frac{\partial^2 U}{\partial Y^2} = (U_e - U) \frac{\partial U_e}{\partial X} + \frac{\partial}{\partial X} (U_e U - U^2) + \frac{\partial}{\partial Y} (U_e V - UV) + \frac{1}{\rho} F_x \quad (5.11)$$

Finally, integrating in the Y -direction and reworking leads to the steady *Integral Boundary Layer Momentum Equation*, generalized with the additional (plasma) force terms:

$$\frac{\tau_w}{\rho} = \frac{\partial U_e}{\partial X} U_e \delta_1 + \frac{\partial}{\partial X} (U_e^2 \delta_2) - U_e V|_{Y=0} + \int_0^\infty \left(\frac{1}{\rho} F_x \right) dY \quad (5.12)$$

Which is written using the dimensional displacement thickness δ_1 , the dimensional momentum thickness δ_2 and the skin friction τ_w :

$$\delta_1 = \int_0^\infty \left(1 - \frac{U}{U_e} \right) dY \quad , \quad \delta_2 = \int_0^\infty \frac{U}{U_e} \left(1 - \frac{U}{U_e} \right) dY \quad (5.13)$$

$$\tau_w = \mu \left(\frac{\partial U}{\partial Y} \right)_{y=0} \quad (5.14)$$

5.2.3. IBL ENERGY EQUATION WITH FORCE TERMS

Obtaining the *Integral Energy Boundary Layer Equation* is more cumbersome, and as such only the most important steps of the derivation are shown here, also since most intermediate algebraic manipulation steps follow established literature [114]. Multiplying the steady

²From a first order asymptotic expansion point of view, prescription of outer flow pressure on the inner flow is the first component of the matching between the inner and the outer expansions. The feedback link is provided by the Lighthill interaction law. Both matching mechanisms keep their usual form as long as the plasma force cloud lies inside the boundary layer.

momentum equation by $2U$ and the continuity equation by $(U_e^2 - U^2)$ yields:

$$\begin{cases} -2\nu U \frac{\partial^2 U}{\partial Y^2} = 2UU_e \frac{\partial U_e}{\partial X} - 2U^2 \frac{\partial U}{\partial X} - 2UV \frac{\partial U}{\partial Y} + \frac{2U}{\rho} F_x \\ (U_e^2 - U^2) \frac{\partial U}{\partial X} + (U_e^2 - U^2) \frac{\partial V}{\partial Y} = 0 \end{cases} \quad (5.15)$$

Adding the two equations and reordering leads to:

$$-2\nu U \frac{\partial^2 U}{\partial Y^2} = 2UU_e \frac{\partial U_e}{\partial X} - 2U^2 \frac{\partial U}{\partial X} + (U_e^2 - U^2) \frac{\partial U}{\partial X} - 2UV \frac{\partial U}{\partial Y} + (U_e^2 - U^2) \frac{\partial V}{\partial Y} + \frac{2U}{\rho} F_x \quad (5.16)$$

Recalling the assumption of negligible wall-normal actuation body force, equation 5.16 can be reworked into an integrable form after extensive algebraic manipulations:

$$2\nu \left(\frac{\partial U}{\partial Y} \right)^2 - 2\nu \frac{\partial}{\partial Y} \left(U \frac{\partial U}{\partial Y} \right) = \quad (5.17)$$

$$= \frac{\partial}{\partial X} \left(U_e^3 \left(\frac{U}{U_e} \left(1 - \frac{U^2}{U_e^2} \right) \right) \right) + U_e^2 \frac{\partial}{\partial Y} \left(V \left(1 - \frac{U^2}{U_e^2} \right) \right) + \frac{2U}{\rho} F_x \quad (5.18)$$

Integrating in the Y -direction from the wall to the edge and reworking yields the *Integral Boundary Layer Energy Equation*, which is generalized since it includes the additional force terms:

$$\frac{2D}{\rho} = \frac{\partial}{\partial X} (U_e^3 \delta_3) - U_e^2 V|_{Y=0} + \int_0^\infty \left(\frac{2U}{\rho} F_x \right) dY \quad (5.19)$$

Equation 5.19 is formulated in terms of the dimensional energy thickness δ_3 and the energy dissipation D :

$$\delta_3 = \int_0^\infty \frac{U}{U_e} \left(1 - \frac{U^2}{U_e^2} \right) dY \quad , \quad D = \int_0^\infty \mu \left(\frac{\partial U}{\partial Y} \right)^2 dY \quad (5.20)$$

5.2.4. NON-DIMENSIONAL IBL EQUATIONS WITH FORCE TERMS

To obtain the non-dimensional integral momentum equation it is necessary to define some 'classic' non-dimensional groups. Starting with the skin friction coefficient C_f , shape factor $H = H_{12}$ and non-dimensional transpiration [31] velocity v_0 :

$$C_f = \frac{\tau_w}{\frac{1}{2}\rho U_e^2} \quad , \quad H_{12} = \frac{\delta_1}{\delta_2} \quad , \quad v_0 = \frac{V}{U_\infty} \Big|_{Y=0} \quad (5.21)$$

It is also convenient to define the non-dimensional displacement δ^* and momentum θ thicknesses:

$$\delta^* = \frac{\delta_1}{L} \quad , \quad \theta = \frac{\delta_2}{L} \quad (5.22)$$

Feeding these definitions into expression 5.12 leads to the non-dimensional *von Kármán Integral Momentum Equation*, generalized with an additional body force term:

$$\frac{C_f}{2} = (H_{12} + 2) \frac{\theta}{u_e} \frac{du_e}{dx} + \frac{d\theta}{dx} - \frac{v_0}{u_e} + \int_0^\infty \left(\frac{F_x}{\rho U_e^2} \right) dY \quad (5.23)$$

which employs the non dimensional edge velocity defined as:

$$u_e = \frac{U_e}{U_\infty} \quad (5.24)$$

The *Integral Energy Boundary Layer Equation* can also be made non-dimensional, but it is more convenient to utilize the *Integral Energy Shape Factor Boundary Layer Equation* for implementation in R/XFOIL. This equation is obtained by inserting the *Integral Momentum Equation* into the *Integral Energy Equation* . After long algebraic manipulations one obtains:

$$\begin{aligned} \frac{dH_{32}}{dx} = & \frac{2C_D}{\theta} - \frac{H_{32}}{\theta} \frac{C_f}{2} + \\ & + (H_{12} - 1) \frac{H_{32}}{u_e} \frac{du_e}{dx} - \frac{1}{\theta} (H_{32} - 1) \frac{v_o}{u_e} + \\ & + \frac{1}{\theta} \left(H_{32} \int_0^\infty \left(\frac{F_x}{\rho U_e^2} \right) dY - \int_0^\infty \left(\frac{2F_x}{\rho U_e^2} \frac{U}{U_e} \right) dY \right) \end{aligned} \quad (5.25)$$

Expression 5.25 is written in terms of two usual non-dimensional groups, the dissipation coefficient C_D and the energy shape factor $H_{32} = H^*$ defined as:

$$C_D = \frac{D}{\rho U_e^3} \quad , \quad H_{32} = \frac{\delta_3}{\delta_2} \quad (5.26)$$

5.2.5. COMPACT FORM OF THE BODY FORCE TERMS

The body force appears in the *Non-dimensional Integral Boundary Layer Equations* through two additional groups. In the presence of an actuator, the integral momentum equation has an additional term that depends only on the body force and the edge velocity U_e :

$$\int_0^\infty \left(\frac{F_x}{\rho U_e^2} \right) dY \quad (5.27)$$

For practical purposes, it is convenient to separate the plasma force contribution to momentum from the local flow characteristics:

$$\int_0^\infty \left(\frac{F_x}{\rho U_e^2} \right) dY = \frac{1}{2u_e^2} \int_0^\infty \left(\frac{F_x}{\frac{1}{2}\rho U_\infty^2} \right) dY \quad (5.28)$$

And define the Force Momentum Coefficient C_{FM} as a local property independent of the edge velocity:

$$C_{FM} = \int_0^\infty \left(\frac{F_x}{\frac{1}{2}\rho U_\infty^2} \right) dY \quad \Rightarrow \quad \int_0^\infty \left(\frac{F_x}{\rho U_e^2} \right) dY = \frac{C_{FM}}{2u_e^2} \quad (5.29)$$

The *Integral Energy Equation* exhibits a more complicated form in the presence of body forces, because the actuation effect depends on the velocity profile:

$$H_{32} \int_0^\infty \left(\frac{F_x}{\rho U_e^2} \right) dY - \int_0^\infty \left(\frac{2F_x}{\rho U_e^2} \frac{U}{U_e} \right) dY \quad (5.30)$$

The Force Momentum Coefficient, defined above, is identified to rewrite this statement in a more compact form:

$$H_{32} \frac{C_{FM}}{2u_e^2} - \int_0^\infty \left(\frac{2F_x}{\rho U_e^2} \frac{U}{U_e} \right) dY \quad (5.31)$$

The second parcel depends on the convolution of the boundary layer profile with the plasma force distribution. It is expressed in a shorter form by defining the force energy coefficient C_{FE} :

$$C_{FE} = \int_0^\infty \left(\frac{F_x}{\frac{1}{2}\rho U_\infty^2} u \right) dY \quad \Rightarrow \quad \int_0^\infty \left(\frac{2F_x}{\rho U_e^2} \frac{U}{U_e} \right) dY = \frac{C_{FE}}{u_e^3} \quad (5.32)$$

The force momentum coefficient C_{FM} and the force energy coefficient C_{FE} are used to rewrite the *Non-dimensional Integral Boundary Layer Equations* in a form appropriate for implementation in R/XFOIL.

$$\left\{ \begin{array}{l} \frac{\partial \theta}{\partial x} = \underbrace{\frac{C_f}{2}}_{\text{SkinFriction}} - \underbrace{(H_{12} + 2) \frac{\theta}{u_e} \frac{\partial u_e}{\partial x}}_{\text{PressureGradient}} + \underbrace{\frac{v_o}{u_e}}_{\text{Transpiration}} - \underbrace{\frac{C_{FM}}{2u_e^2}}_{\text{Plasma}} \\ \frac{\partial H_{32}}{\partial x} = \underbrace{\frac{2C_D}{\theta}}_{\text{Dissipation}} - \underbrace{\frac{H_{32}}{\theta} \frac{C_f}{2}}_{\text{PressureGradient}} + \underbrace{(H_{12} - 1) \frac{H_{32}}{u_e} \frac{\partial u_e}{\partial x}}_{\text{PressureGradient}} - \underbrace{\frac{1}{\theta} (H_{32} + 1) \frac{v_o}{u_e}}_{\text{Transpiration}} + \underbrace{\frac{1}{\theta} \left(H_{32} \frac{C_{FM}}{2u_e^2} - \frac{C_{FE}}{u_e^3} \right)}_{\text{Plasma}} \end{array} \right. \quad (5.33)$$

In equation 5.33 the contribution of each term is highlighted. The contribution of transpiration is also included for completeness and consistency with previous work [31], even if it is not employed in the present chapter.

5.3. PLASMA SPECIFIC TREATMENT OF THE FORCE TERMS

5.3.1. THE PLASMA FORCE FIELD

The plasma force field $F_x : \mathbb{R}^2 \rightarrow \mathbb{R}$ can be approximated with the product of two independent scalar weighting functions, $w^x, w^y : \mathbb{R} \rightarrow \mathbb{R}$ multiplied by a mean field density ϕ_x^p :

$$F_x = \phi_x^p w_{(Y, T_p)}^y w_{(X, X_0^p, L_p)}^x \quad (5.34)$$

For practical applications, the mean field density ϕ_x^p can be determined from experimental measurements by dividing the total force of the plasma actuator F_T^p with a representative field length L_p and thickness T_p :

$$\phi_x^p = \frac{F_T^p}{T_p L_p} \quad (5.35)$$

Since previous work [69] showed the plasma body force field isolines resemble semi-ellipses, the scalar weighting functions are selected to reproduce this spatial distribution. The stream-wise weighting function depends solely on the actuation start stance X_0^p and field length L_p :

$$w_{(x, X_0^p, L_p)}^x = \begin{cases} \frac{\pi}{2} \sin\left(\frac{\pi(x-x_0)}{L_p}\right) & , \quad \left(\frac{x-x_0}{L_p}\right) \in [0, 1] \\ 0 & , \quad \text{otherwise} \end{cases} \quad (5.36)$$

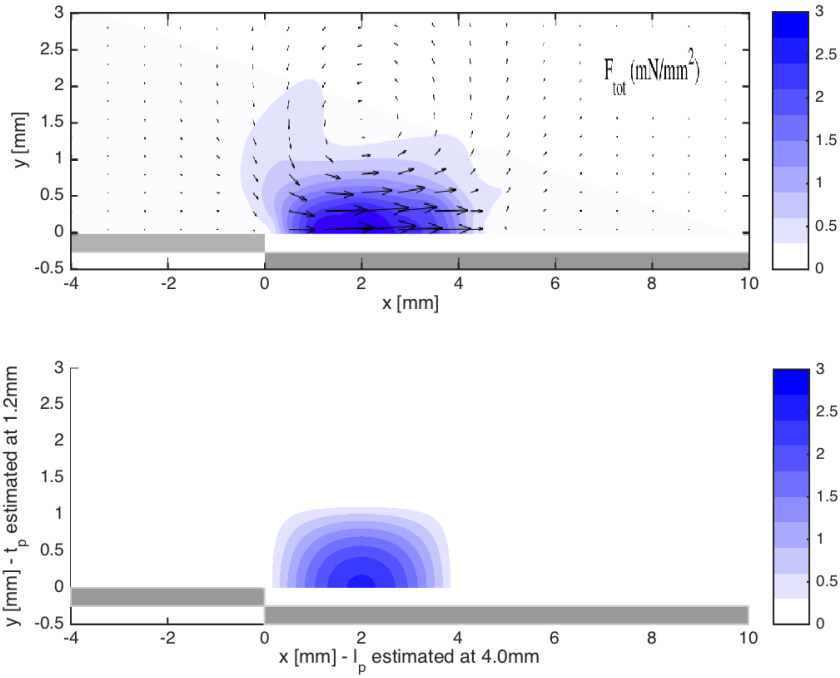


Figure 5.1: *top* - The force field distribution from reference [69] and *bottom* - its approximation

While the wall-normal weighting function is parametrized in terms of the representative field thickness T_p only:

$$w_{(y,T_p)}^y = \begin{cases} \frac{\pi}{2} \sin\left(\pi\left(\frac{y}{2T_p} + \frac{1}{2}\right)\right) & , \frac{y}{T_p} \in [0, 1] \\ 0 & , \text{otherwise} \end{cases} \quad (5.37)$$

Figure 5.1 illustrates the modelled and measured[69] plasma body force distribution, showing that the employed approximation captures the experimental force field topology. In this specific case the plasma body force region is parametrized with $T_p = 1.2 \text{ mm}$, $L_p = 4.0 \text{ mm}$ and $F_T^p = 0.03 \text{ N/m}$.

5.3.2. COMPACT INTEGRAL PLASMA TERMS ESTIMATION

Considering the plasma force field topology approximation from equations 5.36, 5.37 it is possible to further simplify the plasma force terms of the integral BL equations. The force momentum coefficient is independent of the boundary layer state, and hence fully defined

from the integral of the normal force distribution:

$$\begin{aligned}
 C_{FM} &= \int_0^\infty \left(\frac{F_x}{\frac{1}{2}\rho U_\infty^2} \right) dY = \int_0^\infty \left(\frac{\phi_x^p w_{(Y,T_p)}^y w_{(X,X_0^p,L^p)}^x}{\frac{1}{2}\rho U_\infty^2} \right) dY \\
 &= \frac{\phi_x^p w_{(X,X_0^p,L^p)}^x}{\frac{1}{2}\rho U_\infty^2} \int_0^\infty \left(w_{(Y,T_p)}^y \right) dY
 \end{aligned} \tag{5.38}$$

As such the force momentum coefficient C_{FM} admits a simple algebraic representation whenever the force distribution is self similar in the streamwise direction. The independence of the weighting functions is exploited to compute the integral analytically and write:

$$C_{FM(x)} = w_{(x,x_0^p,l^p)}^x C_{\phi_x^p}, \quad \text{with} \quad C_{\phi_x^p} = \frac{\phi_x^p T^p}{\frac{1}{2}\rho U_\infty^2} \tag{5.39}$$

The force energy coefficient C_{FE} depends on the combined effect of the force and the local flow field. It can be decomposed exactly into a product separating the contribution of the force magnitude from the role of the interaction between the force and velocity distributions:

$$\begin{aligned}
 C_{FE} &= \int_0^\infty \left(\frac{\phi_x^p w_{(Y,T_p)}^y w_{(X,X_0^p,a)}^x}{\frac{1}{2}\rho U_\infty^2} u_{(Y)} \right) dY \\
 &= \underbrace{w_{(x,x_0^p,l^p)}^x C_{\phi_x^p}}_{\text{Force Magnitude}} \underbrace{\int_0^\infty \left(\frac{w_{(y,T_p)}^y u_{(Y)}}{T^p} \right) dY}_{\text{Interaction}} \\
 &= C_{FM} C_{EI}
 \end{aligned} \tag{5.40}$$

5.3.3. THE ENERGY INTERACTION COEFFICIENT

The Energy Interaction coefficient C_{EI} introduced in equation 5.40 expresses the leverage of the plasma force on the energy of the boundary layer, and hence its capacity to affect the shape factors (H and H^*). It does not depend explicitly³ on x and can be rewritten easily across variable transformations:

$$C_{EI} = \int_0^\infty \left(\frac{w_{(y,T_p)}^y u_{(Y)}}{T^p} \right) dY = \int_0^{\tilde{t}^p} \left(\frac{w_{(y,\tilde{t}^p)}^y u_{(y)}}{\tilde{t}^p} \right) dy \tag{5.41}$$

Expression 5.41 only depends on one parameter and two functions:

- 1) A scaled plasma force field thickness, for example the ratio t_p between the plasma force field thickness T_p and the boundary layer thickness δ
- 2) The velocity profile function, which can be parametrized with two parameters, for example H and Re_θ when using Swafford's velocity profile model [128]

³But it depends implicitly on x . As shown later, it depends on H , Re_θ and \tilde{t}^p , where H and Re_θ depend on x .

- 3) The plasma force field wall-normal weighting function, whose definition was fixed in section 5.3.1

A three parameter closure relation for C_{EI} must therefore exist in the form:

$$C_{EI} = f(H, Re_\theta, \bar{t}^p) \quad , \quad with \quad \bar{t}^p = \frac{T^p}{\delta} \quad (5.42)$$

Due to the great sensitivity surrounding the boundary layer thickness definition [114], the \bar{t}^p scaled thickness parameter is not appropriate for the establishment of a robust closure relation. Fortunately, the boundary layer thickness can be recovered from any (H, Re_θ) tuple through Head's shape factor H_1 closure relation:

$$\begin{cases} H_1 = f(H, Re_\theta) \\ \delta = \delta_2(H_1 + H) \end{cases} \quad \Rightarrow \quad \exists (g: \mathbb{R}^2 \rightarrow \mathbb{R}) : \frac{\delta}{\delta_2} = g(H, Re_\theta) \quad (5.43)$$

The $\eta = \frac{y}{\delta_2}$ scaling and the t_θ^p ratio are now considered. The existence of g such that $\bar{t}^p = \frac{t_\theta^p}{g(H, Re_\theta)}$ implies that:

$$\exists (G: \mathbb{R}^3 \rightarrow \mathbb{R}^3) : (H, Re_\theta, \bar{t}^p) = G(H, Re_\theta, t_\theta^p) \quad (5.44)$$

So that it is equivalent to define the *Energy Interaction Coefficient Closure* in terms of the δ -scaled force thickness \bar{t}^p or the θ -scaled force field thickness t_θ^p :

$$C_{EI} = f(H, Re_\theta, t_\theta^p) \quad or \quad C_{EI} = \bar{f}(H, Re_\theta, \bar{t}^p) \quad (5.45)$$

Because the two closures can be written as compositions of closures of the remaining variables:

$$f = \bar{f} \circ G \quad (5.46)$$

As such, despite the loss of geometric similarity, the $\eta = \frac{y}{\delta_2}$ dimensionless scale does preserve information and form a valid basis to write a closure relation. From a practical standpoint, the fact that the momentum thickness admits a very robust definition outweighs the advantages derived from the instinctive nature of the geometric thickness as a scaling variable. Using t_θ^p , the Energy Interaction Coefficient is computed as:

$$C_{EI} = \int_0^{t_\theta^p} \left(\frac{w^y(\eta, t_\theta^p) u(\eta)}{t_\theta^p} \right) d\eta \quad , \quad with \quad \begin{cases} \eta = \frac{y}{\delta_2} \\ t_\theta^p = \frac{T^p}{\delta_2} \end{cases} \quad (5.47)$$

A numerical database for the *Energy Interaction Coefficient* C_{EI} is created by solving expression 5.47 for a range of velocity profiles (as a function of H and Re_θ) and scaled plasma body force thickness (t_θ^p). Figure 5.2 illustrates the influence of the velocity profile and scaled plasma thickness on the value of the Energy Interaction Coefficient.

For implementation into R/XFOIL, the C_{EI} numerical database plays the role of a closure relation. The code is linked to the numerical database so that C_{EI} values and their

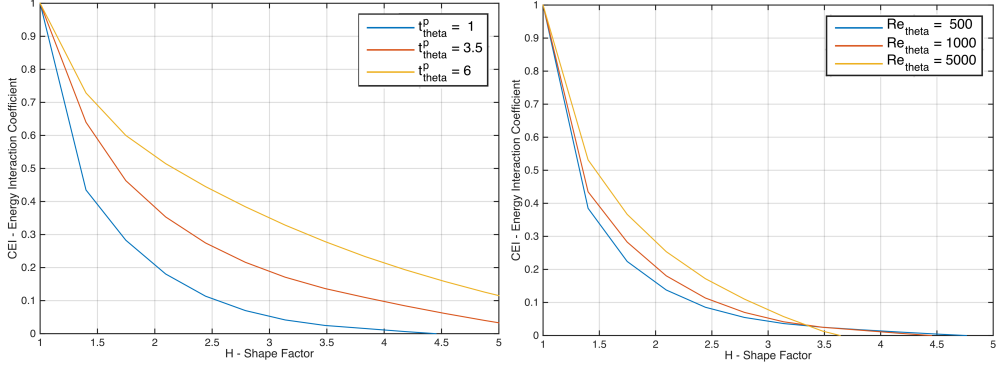


Figure 5.2: Small Perturbation Numerical Estimation of the Energy Interaction Coefficient - *left* - Influence of t_{θ}^p and *right* - Influence of Re_{θ}

derivatives are retrieved through tri-linear interpolation. As the code iterates through un-physical intermediate steps, it will request C_{EI} values over a wide range of $(H, Re_{\theta}, t_{\theta}^p)$ tuples. Data points are therefore distributed to optimize information density while providing appropriate asymptotic behavior. For low shape factors, use is made of the analytical limit:

$$\lim_{H \rightarrow 1} C_{EI} = 1 \quad , \quad \forall \quad Re_{\theta}, t_{\theta}^p \quad (5.48)$$

5.4. EXPERIMENTAL CAMPAIGN

For validation of the modelled DBD plasma actuator influence, an experimental campaign is carried out. An airfoil equipped with DBD plasma actuators is tested at different free stream velocities and incidences, as to obtain a suitable experimental database. The airfoil model included 2 sets of plasma actuators placed at different chordwise locations along the suction side. The experimental set-up and main results are now described.

5.4.1. FLOW FACILITY

The experimental investigation is carried out in a closed circuit low speed tunnel located at the TU Delft. The closed circuit configuration employs an octogonal test section of approximately $180 \times 125 \text{ cm}$. The contraction ratio is 17.6, resulting in a maximum test section velocity of 120 m/s and a low turbulence intensity of 0.07% at 75 m/s . In the current experimental study two free stream velocities were employed, $U_{\infty} = [20; 30] \text{ m/s}$.

5.4.2. AIRFOIL SECTION

The airfoil section was designed specifically for the experiment, by using a multi-objective airfoil optimizer [31]. The optimizer allows for transpiration (suction and blowing) to be included, and in the present case the effect of the plasma was considered by imposing an amount of uniformly distributed transpiration that yields an equivalent variation in BL momentum in streamwise direction, locally corresponding to x coordinate. Consistently with section 5.2, it is assumed the flow is incompressible and the plasma actuator does not af-

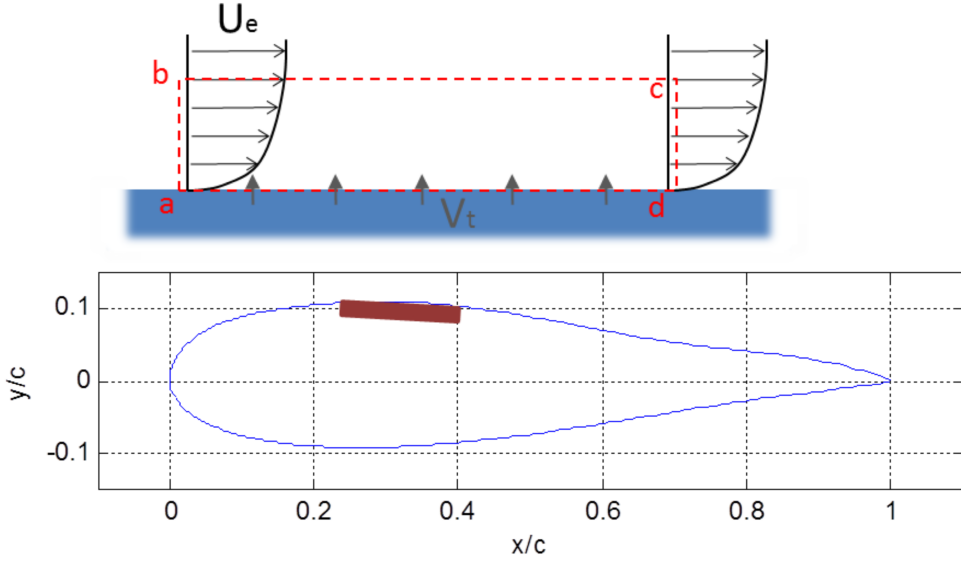


Figure 5.3: *top* - Equivalent Transpiration Control Volume - *bottom* - Airfoil Contour with indicated actuation

fect the edge velocity U_e . Referring to figure 5.3, the equivalent amount of transpiration is calculated by performing a momentum balance over the region of actuation:

$$F_T^p \approx F_X = \oint_{abcd} \rho \vec{U} \cdot (\vec{U} \cdot \vec{n}) ds \approx \int_b^c \rho V U_e dx \approx \rho V_t U_e L_p \quad (5.49)$$

where F_X corresponds to the force in the x direction integrated over the control volume and \vec{n} denotes the vector normal to the control volume surface pointing outwards. For the airfoil section design the plasma length was set at $L_p = 97.5 \text{ mm}$, as explained in section 5.4.4. Based on previous measurements [132], the actuator force was set at $F_{DBD} = 0.2 \text{ N/m}$, while $U_e = 30 \text{ m/s}$ is taken as representative velocity, yielding an equivalent transpiration speed $V \approx 0.06 \text{ m/s}$. This amount of transpiration was imposed in the airfoil optimizer for the case in which actuation is switched on. The airfoil section is designed for application in stall controlled horizontal axis wind turbines. The airfoil relative thickness is $\frac{t}{c} = 21\%$ and the optimization was set such that the aerodynamic performance was similar to wind energy airfoils with the same thickness, while for angles of attack beyond C_l/C_{dMAX} the optimizer aimed at:

$$C_Q = C_l \sin(\phi) - C_d \cos(\phi) = \text{constant} \quad (5.50)$$

where C_l and C_d represent the sectional lift and drag coefficients, respectively. The variable C_Q represents the non-dimensional blade section tangential force [91]. The inflow angle ϕ is defined [91] as:

$$\phi = \alpha + \theta \quad (5.51)$$

where α and θ denote the AOA and local twist respectively. In the present case $\theta = 3 \text{ deg}$, corresponding to the twist of the outer half of the NREL 5 MW machine blade [60]. Angles of

attack up to $\alpha \leq 20deg$ were considered. The resulting aerodynamic section is displayed in figure 5.3. It should be kept in mind that the approximation of using an equivalent amount of transpiration to simulate the effect of a DBD actuator is by no means accurate. Nevertheless this is not relevant since any airfoil shape will provide a range of BL development points that is suitable to capture the effect of DBD plasma under different operating conditions.

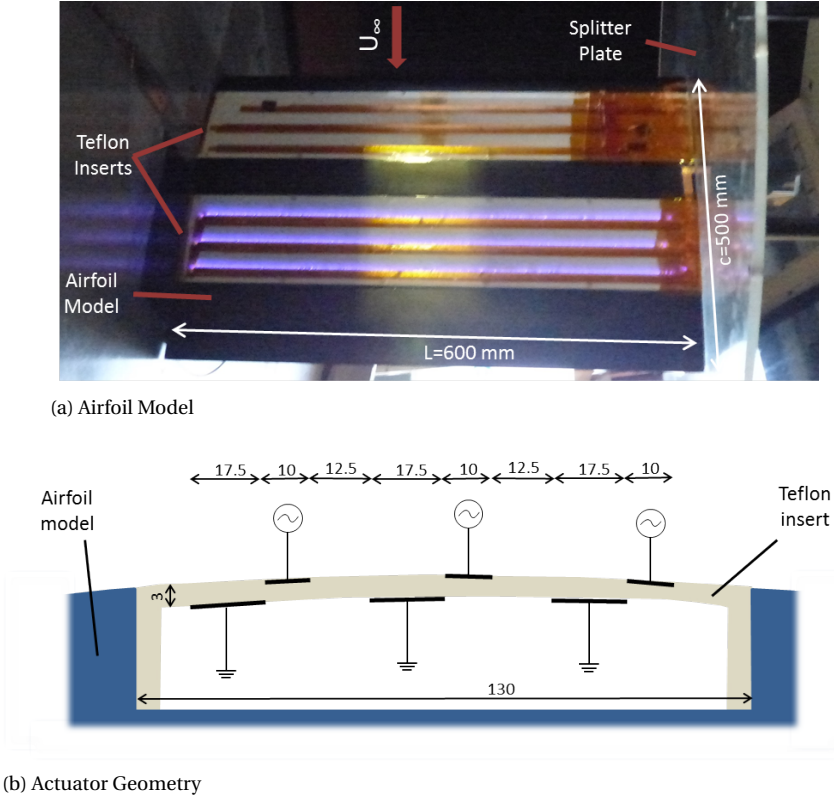


Figure 5.4: Experimental set-up

5.4.3. AIRFOIL MODEL

The airfoil model used in the experimental campaign has chord $c = 0.5m$ and span $L = 0.6m$, yielding an operational Reynolds number of $Re\{0.66; 1\} \times 10^6$. The model has two grooves measuring $130mm$ in the streamwise direction, and covering the whole span of the model. The grooves are centered at chordwise positions $\frac{x}{c} = \{0.25; 0.65\}$ on the suction side, corresponding to the fore or leading edge (LE) and aft or trailing edge (TE) actuation blocks respectively. Each groove has a corresponding insert which follows the airfoil surface. The inserts are made of Teflon, which acts as the insulator for the DBD actuator. A splitter plate is placed on the edge of the airfoil to minimize three dimensional effects. Figure 5.4a illustrates the experimental set-up.

5.4.4. PLASMA ACTUATOR

The present study considers an application to regulate the power production of HAWT, and hence the DBD actuator is mounted in the counter-flow configuration, meaning the plasma-induced force acts against the flow. For this study a triple DBD configuration is used. Each actuator consists of thin rectangular copper electrodes made out of self-adhesive copper tape separated by a dielectric layer. The dielectric material is Teflon, with a thickness of 3.0mm . The thickness of the electrodes is $60\mu\text{m}$. The width of the exposed electrode is 10mm and of the grounded electrode is 17.5mm . No horizontal gap exists between the two electrodes, and the distance between the edge of the grounded electrode and the edge of the exposed electrode of the following actuator is $w = 12.5\text{mm}$. To prevent unwanted plasma formation, kapton tape with thickness $50\mu\text{m}$ was applied on the edge of the exposed electrode farthest from the actuator's respective covered electrode. Figure 5.4b illustrates the actuator geometry, with dimensions in mm . The actuator is powered by a TREK 20/20C HV amplifier ($\pm 20\text{ kV}$, $\pm 20\text{ mA}$), imposing a square-wave signal with 40 kV_{pp} amplitude and 900 Hz frequency.

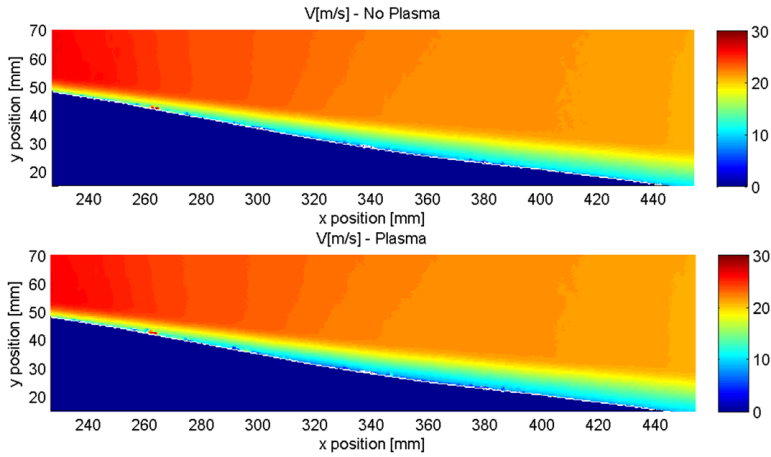
5.4.5. PARTICLE IMAGE VELOCIMETRY SET-UP

High speed PIV is applied to characterize the flow field in the vicinity of the actuator. A two component PIV configuration is chosen and the velocity field is sampled at the center of the airfoil model's span. The seeding particles at the mid-span of the actuator are illuminated by a light sheet of 2mm thickness generated by a Quantronix Darwin-Duo laser system with an average output of 80 W at 3 kHz . A Photron Fastcam SA1 high speed CCD camera of 1024×1024 pixels (full sensor size) is used to capture the field-of-view (FOV). The images are acquired in double-frame mode and are analyzed using Davis 7.4 (Labvision GmbH) with final integration window size of 12×12 pixels and overlap factor of 75% . The interrogation windows have been weighted using $4:1$ aspect ratio. For each of the configurations tested, 300 pairs of images were taken, yielding 300 instantaneous velocity vector fields. The large number of samples was taken to minimize the effect of instantaneous velocity oscillations, such as those caused by turbulence and separated flows. The representative velocity field for each configuration was obtained by averaging the instantaneous velocity vectors.

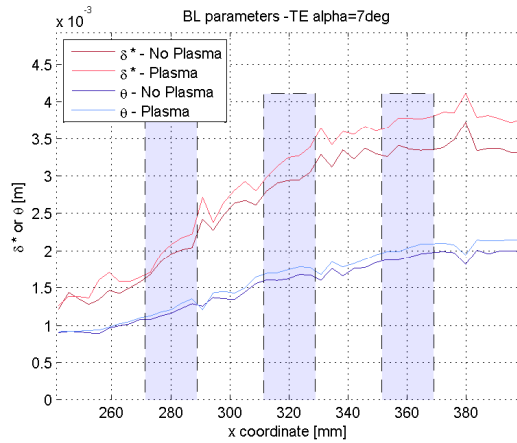
It is noted that even though the exact flow topology at large AOA is inherently 3D, and the formation and extent of stall cells is specifically related with the wind tunnel and airfoil model set-up, it is assumed the mid-span is the more representative region of a (theoretical) 2D flow. Or at least it is anticipated the best agreement between a 2D viscid-inviscid panel method and experimental data (figure 5.8) is obtained at the mid-span.

5.4.6. EXPERIMENTAL RESULTS

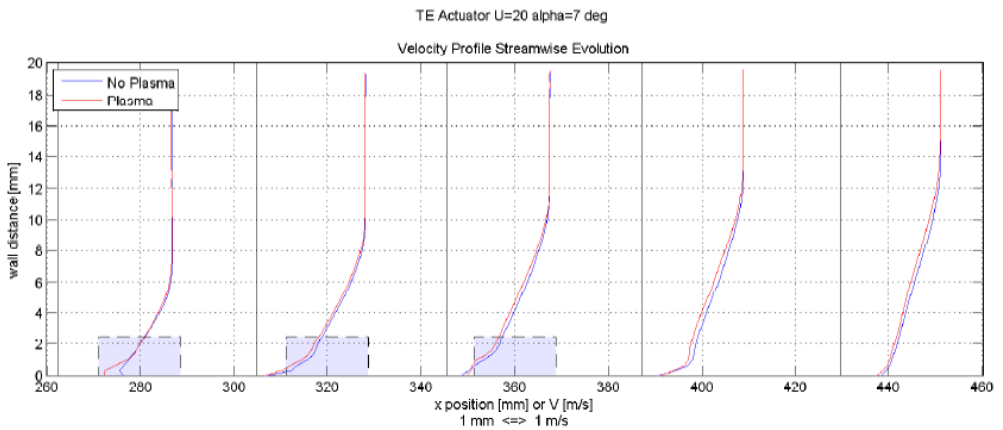
In the current study a different set of angles of attack was tested for each actuator. For the fore actuator, or LE actuator, the incidence was $\alpha = [10; 13; 16; 19; 22]\text{ deg}$ and for the aft actuator, or TE actuator, it was $\alpha = [4; 7; 10; 13; 16]\text{ deg}$. These sets of AOA were chosen such that both attached and separated flows were acquired. Figure 5.5a shows the obtained velocity field in the vicinity of the aft actuator block, for $\alpha = 7\text{ deg}$ and $U = 20\text{ m/s}$, both with and without employing the DBD actuator. Figures 5.5b and 5.5c show the development of the integral BL parameters and velocity profiles respectively. The dashed lines in figure 5.5c circumscribe the body force region of each individual plasma actuator.



(a) PIV results



(b) Integral BL parameters development



(c) velocity profiles

Figure 5.5: Experimental results for $\alpha = 7 \text{ deg}$ and $U = 20 \text{ m/s}$

In figure 5.5a one can see virtually no effect of the actuator, at least at the level of the flow topology. However, figure 5.5c clearly shows the effect of the DBD actuator since the BL velocity profile becomes less 'full', which is expected since the actuator is mounted in the counter-flow configuration. It should also be noted that the difference in the velocity profile obtained with and without actuation is initially restricted to a small distance from the wall ($h \approx 2\text{mm}$), roughly corresponding to the body force region [69], but increases for downstream stations. This is similar to what was previously observed in quiescent conditions [132]. The actuator-induced variation in the BL velocity profile is also noticeable in the evolution of the integral BL parameters, as illustrated in figure 5.5b. In general, similar trends were obtained for different angles of attack, actuator positions and free stream velocities.

Figure 5.5b also shows kinks on the IBL parameters' streamwise evolution. Similarly to chapter 3 of this dissertation, by computing [21] the wall coordinate y^+ using the electrode's thickness as length scale a value $y^+ \leq 10$ is obtained, which indicates the flow is hydrodynamically smooth. As such, the kinks 5.5b are believed to be caused by a combination of localized roughness introduced by the electrode's edge, extra insulating *kapton* tape used to prevent unwanted plasma formation (section 5.4.4) and the imperfect interface between the airfoil model grooves and the *Teflon* inserts (figure 5.4b).

5.5. COMPARISON WITH EXPERIMENTAL RESULTS

The outlined modelling approach is now compared with experimental results. Figure 5.6 shows the variation of the energy interaction coefficient C_{EI} with shape factor H . In general, the modelling approach yields reasonable agreement with experimental data. Figure 5.6 highlights the data-points obtained with the DBD actuator *ON* and *OFF*, showing no clear difference between both cases. Accordingly one may conclude modeling the actuator's influence with additional terms in von Kármán's integral equations but not explicitly altering the (Swafford) velocity profile is a suitable approximation. Figure 5.6 also shows the data-points obtained at different Re_θ values, showing that even at different Re_θ bins the modelling approach captures the experimental energy interaction coefficient behaviour.

Figure 5.7 illustrates the IBL parameters obtained for the plasma actuation at the LE block (figure 5.7a) and TE block (figure 5.7b). One should note the plasma actuator was modeled with one large force field with $L_p = 97.5\text{ mm}$, $t_p = 5\text{ mm}$ and $F_T^p = 0.2\text{ N/m}$. Essentially this corresponds to condensing the influence of the 3 individual DBD actuators in only one equivalent force field. Nevertheless, figure 5.7a shows the magnitude of the actuator-induced variation in IBL parameters is reasonably estimated, even though the proposed model does not match experimental results at all streamwise locations.

Figure 5.8 illustrates the lift and drag coefficient variation with AOA for $U = 20\text{ m/s}$, for both experimental and modeled cases. The viscous-inviscid code uses the e^N transition prediction method with $N = 14$, given that the wind tunnel is a low turbulence test facility. The experimental polars were obtained with a 6 component mechanical balance system. The experimental results in figure 5.8 have been corrected such that the slope in the linear region of the lift curve would match experimental results, by applying a simple scaling factor. This correction is applied because the experimental set-up presented significant 3D effects, both because of the finite span of the airfoil model (which led to flow leakage) and because of wind tunnel blockage at high angles of attack. As such, and since the experimen-

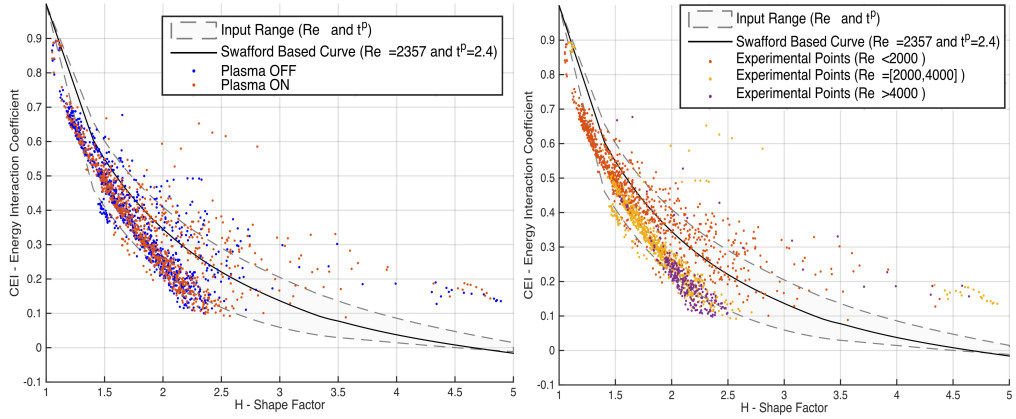


Figure 5.6: Energy Interaction Coefficient Comparison with Experimental Results - *left* - C_{EI} computation with and without plasma - *right* - C_{EI} computation over Re_θ bins

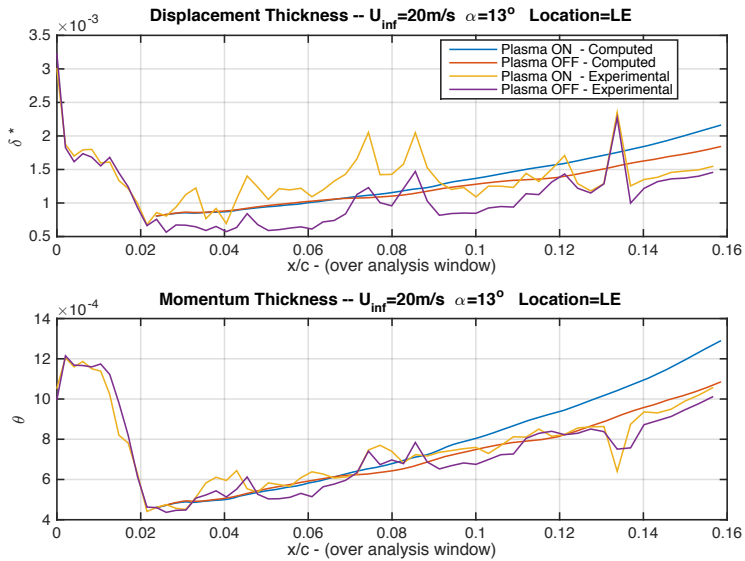
tal data is compared with a 2D numerical method, a simple scaling factor was applied such that the experimental lift slope at the linear region matches the computational results.

Figure 5.8 shows the agreement between the experimental data and computational results is always not good. Rather than the present DBD plasma IBL modeling approach, this is perhaps attributed to the viscid/inviscid panel code. The Reynolds number to which the used panel code [138] was tailored for is $Re = 3 \times 10^6$, meaning some deviations of C_l and C_d are expected at the experimental lower Reynolds number, especially for large angles of attack. Additionally, and as discussed in chapter 2 of this dissertation, viscous/inviscid panel codes are never accurate when predicting flow with large separated regions, such as for high AOA.

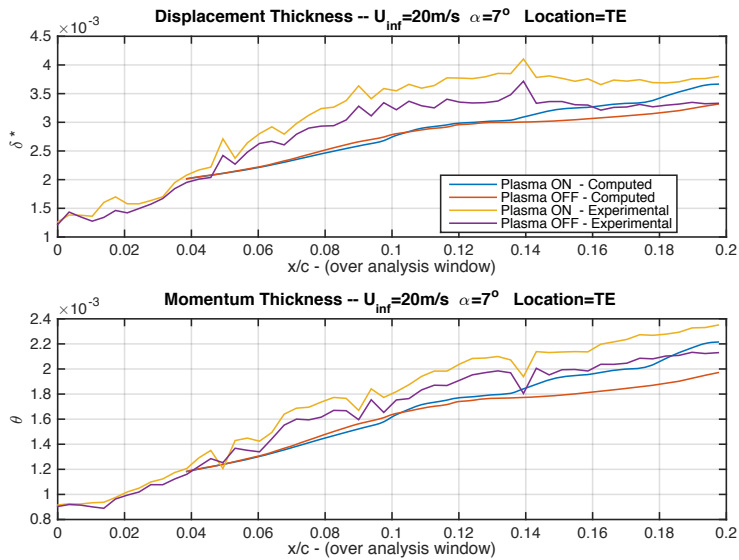
Nevertheless, figure 5.8 shows that modeled actuation-induced variation in lift coefficient ΔC_l is in the order of magnitude of experimental results, which is particularly encouraging. It is also clear the proposed approach captures the experimental trend of $\Delta C_{l_{TE}} > \Delta C_{l_{LE}}$ for $\alpha < 13 \text{ deg}$, and $\Delta C_{l_{LE}} > \Delta C_{l_{TE}}$ for $\alpha > 13 \text{ deg}$. This is explained because, from the airfoil section design, at small angles of attack the concavity at the TE actuator region makes the local pressure gradient more adverse. As such the flow is naturally brought close to separation, and when the TE actuator block is employed flow separation is achieved. For larger angles of attack the flow is naturally separated at the TE region, and as such the TE actuator block has a reduced impact. The LE actuator block however is able to promote earlier separation, and thus has a larger effect on the lift coefficient than TE actuation.

5.6. CONCLUSIONS

This chapter proposes a method to include the influence of DBD plasma actuators in viscous-inviscid codes used for airfoil design, suited to incompressible, turbulent flows. The influence of the plasma body-force is modelled by performing an asymptotic expansion to the Navier-Stokes equations, and introducing additional force terms in von Kármán integral



(a) LE actuation block at $U = 20\text{m/s}$ and $\alpha = 13\text{deg}$



(b) TE actuation block at $U = 20\text{m/s}$ and $\alpha = 7\text{deg}$

Figure 5.7: Modelled and Experimental Integral Boundary Layer Parameters Evolution

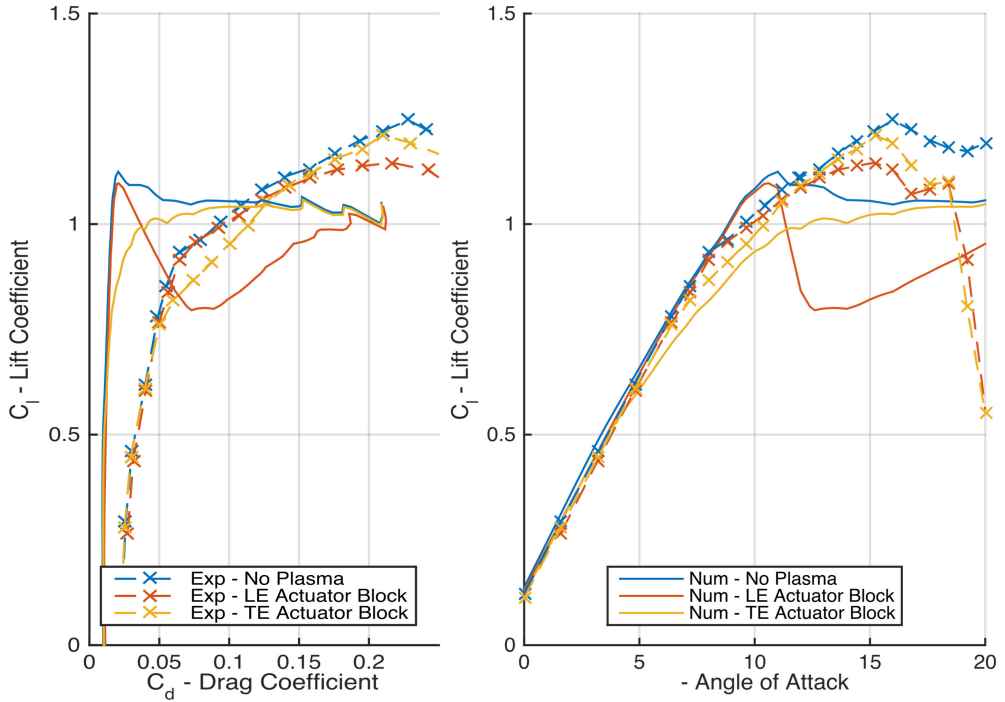


Figure 5.8: C_l and C_d Experimental and Computed Polars at $U_\infty = 20 \text{ m/s}$

equations. For validation, an experimental study was carried out in which PIV was performed on an airfoil equipped with DBD plasma actuators, and tested at different operational Reynolds number and angles of attack. Results show the proposed model captures the magnitude of the variation in IBL parameters brought upon by the plasma actuators. This is verified for different operating conditions. The proposed model also captures the magnitude of the lift coefficient variation (ΔC_l) and the main trends related with actuation chordwise position. Ultimately this approach may enable the design of airfoils specifically tailored for flow control through DBD employment, potentially decreasing the power required for active flow control.

III

ACTIVE STALL CONTROL ROTOR DESIGN

The previous part investigated DBD plasma actuators, providing insight into their performance and modeling approaches to include DBD actuation effects.

This part describes the design of the Active Stall Controlled Rotor. Chapter 6 explains a methodology developed to design airfoils suited to employ actuation in a wind energy environment. Both DBD plasma and Boundary Layer Transpiration (BLT) are considered as actuation technologies and results indicate (2 to 4 times) more efficient airfoil sections may be obtained. Finally, chapter 7 describes the planform design of the ASC rotor, in a servo-structural-aerodynamic optimization framework. The potential reduction in cost of energy is investigated by comparing the ASC rotor with state-of-the-art pitch controlled machines .

6

DESIGN OF ACTUATED AIRFOILS FOR WIND ENERGY

*Here am I floating in a tin can, far above the world,
planet Earth is blue, and there is nothing I can do*

Major Tom (David Bowie)

This chapter describes a methodology for designing airfoils suitable to employ actuation in a wind energy environment. The novel airfoil sections are baptized WAP (Wind Energy Actuated Profiles). A genetic algorithm based multiobjective airfoil optimizer is formulated by setting two cost functions. One cost function for wind energy performance and the other representing actuation suitability. The wind energy cost function compares the candidate airfoils' performance with 'reference' wind energy airfoils, considering a probabilistic approach to include the effects of turbulence and wind shear. The actuation suitability cost function is developed considering HAWT active stall control, including two different control strategies designated by 'enhanced' and 'decreased' performance. Two different actuation types are considered, namely boundary layer transpiration and dielectric barrier discharge plasma. Results show that using WAP airfoils provides much higher control efficiency than adding actuation on reference wind energy airfoils, without detrimental effects in non-actuated operation. The WAP sections yield an actuator employment efficiency that is 2 to 4 times larger than obtained with reference wind energy airfoils, at equivalent wind energy performance. Regarding geometry, and compared to typical wind energy airfoils, WAP sections for decreased performance display an upper surface concave aft-region, while for increased performance a convex upper surface aft-region is obtained. The results demonstrate the potential of including actuation effects in the airfoil design process, thus enabling novel HAWT control strategies.

This chapter has been submitted to Wind Energy Journal - WE-15-0180 (2015)

6.1. INTRODUCTION

In recent years the increasing size of horizontal axis wind turbines (HAWT) and the tendency to install wind farms further offshore demand robust design solutions. Modern active stall control (ASC) is a concept in which power regulation above rated wind speeds is achieved employing add-ons (actuators) which actively provoke stall. This means the pitch mechanism of HAWT is used in emergency situations only (*i.e.* not for power regulation). Since the pitch mechanism is responsible for a significant share [23] of HAWT component failure, a more robust design solution can thus be achieved. Previous research however (chapter 2 of this dissertation) showed that to successfully implement ASC it is necessary to incorporate the actuation effects while designing airfoil sections.

Different arguments are considered when designing airfoils for HAWT blades. For in-board stations structural requirements lead to thick (and hence stiff) profiles, while towards the blade tip aerodynamic performance becomes more important, resulting in thinner airfoils. Within desirable aerodynamic characteristics, different requirements are often aimed for. Large lift-to-drag ratio allows for increased power extraction at a given rotor area, and a large design lift contributes to aerodynamic damping [110] and may lead to reduced chord, decreasing blade mass and cost. On the other hand, restricted $C_{l_{max}}$ [131] has often also been a requirement in wind energy (WE) airfoils, as early fixed pitch machines were employed, since a reduced $C_{l_{max}}$ also decreases the maximum aerodynamic power generated over the wind speed envelope. Additionally, roughness insensitivity is fundamental in WE airfoils [13], mostly because leading edge (LE) soiling is often present and leads to early transition. Besides all these requirements, WE airfoils experience oscillations in the angle of attack (AOA), *e.g.* due to wind shear, turbulence, yaw misalignment, etc., which means a point design [84] type of airfoil is not adequate.

In order to use actuation effectively, airfoils should be designed to incorporate the effect of the actuator, achieving larger $\delta \frac{C_l}{C_d}$, *i.e.* larger control authority, than if the actuators are implemented on an already existing airfoil. Also, and particularly for machines designed to harvest energy such as HAWTs, the design of airfoils for actuation may yield the same control authority with a smaller power input, thus increasing the efficiency of the actuator. Several types of actuators have been considered for WE application, including mechanical, fluidic, plasma, etc., with excellent reviews given in [6] and [59].

The present study considers boundary layer transpiration (BLT) and dielectric barrier discharge (DBD) plasma as actuators. The effect of each actuator is introduced in a viscous-inviscid panel code [31], [32], which calculates the airfoil performance with and without actuation. The design challenge is formulated as a multi-objective optimization problem in section 6.2. Section 6.3 describes the cost functions used to grade the airfoil performance, in terms of WE and actuation suitability, in subsections 6.3.1 and 6.3.2 respectively. Section 6.4 explains the methodology used for modelling the actuation employment. Results are presented in 7.6 and finally conclusions are stated in section 6.6.

6.2. OPTIMIZATION SET-UP

The airfoil design process is posed as a multi-objective optimization problem solved with a genetic algorithm, following the methodology outlined in [31]. Airfoil shapes are approximated with CST parametrization [75] employing 19 coefficients for the discretization. The

genetic algorithm considers 150 airfoil candidates per generation, and each simulation case is ran for 50 generations. For more detailed information the reader is referred to [31].

6.3. COST FUNCTION DEFINITION

In the multi-objective optimization framework two cost functions (CF) are defined. CF1 describes airfoil suitability for HAWT application and CF2 expresses actuation suitability. Three lift and drag polars are calculated for each airfoil candidate. The first computation is termed *clean* configuration and does not prescribe the transition location (free transition). In the second polar the transition location is set at $x_{tr} = 0.05$ and $x_{tr} = 0.1$ for the upper and lower surface respectively[139], and is referred to as *rough* configuration. The third computation does not prescribe the transition location but includes the effect of the actuator, and is termed *actuation* configuration. All aerodynamic polars are calculated for Reynolds number $Re = 9 \times 10^6$ (typical of large off-shore HAWT), with angle of attack (AOA) ranging from $\alpha \in [0;20]$ *deg* in steps of 0.2 *deg*.

6.3.1. CF1 - WIND ENERGY SUITABILITY

A 'reference' WE airfoil is defined, which is representative of profiles designed for and used in HAWT blades. This airfoil is compared with the different airfoil candidates during the optimization. Considering an outboard station airfoil, the relative thickness is fixed at 21%. In view of manufacturability and stiffness constraints, the TE region thickness of the airfoil candidates is enforced to exceed a lower limit based on the geometry of typical WE airfoils with 21% thickness to chord ratio. The reference airfoil is characterized with aerodynamic performance (Φ) for different design goals, by calculating the mean obtained from a set of airfoils typically used in HAWT blades. Table 6.1 shows the airfoils used to define the 'reference' WE airfoil while table 6.2 displays the different aerodynamic design goals considered.

Table 6.1: WE airfoils considered

Airfoil Index	Airfoil (i)
1	DU93-W-210
2	RISO-A1-21
3	FFA-W-211
4	AA-207-A1

The airfoil performance is expressed using two different AOA. The optimum incidence α_{opt} maximizes the lift-to-drag ratio, and the stall AOA α_{stall} is the angle at which the slope of the lift polar is zero, expressed with:

$$\alpha_{opt} \rightarrow \max \left(\frac{C_l(\alpha)}{C_d(\alpha)} \right) = \frac{C_l(\alpha_{opt})}{C_d(\alpha_{opt})} \quad \alpha_{stall} \rightarrow \frac{dC_l}{d\alpha}(\alpha_{stall}) = 0 \quad (6.1)$$

The aerodynamic coefficients used to calculate the performance indexes indicated in table 6.2 are not the values obtained directly with the aerodynamic calculation code [138],

Table 6.2: Reference airfoil definition

Reference Airfoil Performance	Design Goals (j)
$\Phi_{j\ ref} = \frac{\sum_{i=1}^4 \Phi_j(i)}{4}$	$\Phi_1 = \bar{C}_l(\alpha_{opt})$
	$\Phi_2 = \frac{\bar{C}_l}{\bar{C}_d}(\alpha_{opt})$
	$\Phi_3 = -\left \bar{C}_l(\alpha_{opt}) - \bar{C}_{l\ rough}(\alpha_{opt}) \right $
	$\Phi_4 = \frac{\alpha_{stall} - \alpha_{opt}}{\bar{C}_l(\alpha_{stall}) - \bar{C}_l(\alpha_{opt})}$

but rather the 'representative' force coefficients \bar{C}_l and \bar{C}_d . These representative values are introduced to account for the AOA perturbations experienced by the airfoils due to turbulence and wind shear. The values of \bar{C}_l and \bar{C}_d are estimated with a probabilistic approach (subsection 6.3.1) and expressed in eq 6.12. The cost function representing the airfoil WE suitability is defined as the sum of different penalties, where each penalty expresses the deviation of a particular aerodynamic characteristic of the candidate airfoil from the 'reference' airfoil. The penalties pn are calculated in percentages from the performances expressed in table 6.2 with:

$$pn_i = \left[\frac{\Phi_{iref} - \Phi_{icnd}}{\Phi_{iref}} \times 100 \right]^k \quad \text{where} \quad \begin{cases} k=1 & \text{if } \Phi_{iref} \leq \Phi_{icnd} \\ k=2 & \text{if } \Phi_{iref} > \Phi_{icnd} \end{cases} \quad (6.2)$$

where the double subscript *cnd* denotes the airfoil candidate analyzed. The exponent in expression 6.2 translates a design choice, by considering airfoil candidates should come close to the reference WE airfoil on all performance indexes Φ rather than outperforming the reference airfoil on a specific design goal. The value of the cost function representing the airfoil's suitability to WE applications is finally obtained with:

$$CF_{WE} = \sum_{i=1}^4 pn_i \quad (6.3)$$

PROBABILISTIC DESIGN APPROACH

Because of wind field spatial and temporal gradients, the AOA experienced by a HAWT airfoil will continuously vary. The present study considers a probabilistic design approach to account for AOA oscillations originating from both atmospheric turbulence and wind shear, though other phenomena (*e.g.* yaw misalignment) contribute to AOA oscillations [81].

The effect of turbulence on AOA oscillations is estimated by defining the turbulent perturbed inflow speed U_{TP} in terms of an instantaneous perturbation intensity δ :

$$U_{TP} = U_\infty(1 - \delta) \quad (6.4)$$

where U_∞ is the 10 minute averaged wind speed at hub height. It is assumed turbulent perturbations act only locally and do not affect the rotor regime. Accordingly the blade pitch mechanism has no time to act, and thus the local pitch angle β remains constant.

Considering the large inertia of the HAWT rotor, the rotational speed Ω does not change during the perturbation. Additionally the axial and tangential induction factors a and a' are assumed to remain constant throughout the perturbation, since they are related with the HAWT wake dynamics which has characteristic time-scales of several seconds [124]. Under these assumptions and using the inflow diagram [91] the inflow angle in a locally perturbed wind field is expressed:

$$\tan\phi = \frac{U_\infty(1+\delta)(1-a)}{\Omega r(1+a')} \quad (6.5)$$

in which r is the local radius. Recalling the blade pitch is assumed constant, the AOA perturbation are explicitly written:

$$\alpha_\delta(\delta) = \arctan\left(\frac{1+\delta}{b}\right) - \arctan\left(\frac{1}{b}\right), \quad b = \frac{\Omega r}{U_\infty} \frac{r}{R} \frac{1+a'}{1-a} \quad (6.6)$$

Since atmospheric boundary layer (ABL) turbulence can be modeled as a stochastic process described by a Gaussian distribution [1], the probability density function (PDF) for a given perturbation is given by:

$$p_\delta = \frac{e^{-\frac{1}{2}\left(\frac{\delta}{I}\right)^2}}{I\sqrt{2\pi}} \quad (6.7)$$

where I represents the turbulence intensity. Since expression 6.6 defines a monotonic C^1 function, the PDF for the turbulence induced AOA perturbation may be written:

$$p_{\alpha_{\delta T I}}(\alpha_\delta|U) = \left| b \left(1 + \tan^2 \left[\alpha_\delta + \operatorname{atan} \left(\frac{1}{b} \right) \right] \right) \right| \cdot \frac{e^{-\frac{1}{2} \left(\frac{b \tan \left[\alpha_\delta + \operatorname{atan} \left(\frac{1}{b} \right) \right] - 1}{I} \right)^2}}{I\sqrt{2\pi}}, \quad U = \frac{\Omega r}{b} \left(\frac{1+a'}{1-a} \right) \quad (6.8)$$

In addition to turbulence, the influence of wind shear on AOA oscillations is also considered. By approximating the ABL velocity profile with the logarithmic law [91] it is possible to express the temporal wind speed variation with:

$$U(t) = U_\infty \frac{\ln\left(\frac{h_0 - r \cos(\Omega t)}{z_0}\right)}{\ln\left(\frac{h_0}{z_0}\right)} \quad (6.9)$$

where h represents height, h_0 is hub height and z_0 expresses the surface roughness. The time t is set to zero when the HAWT blade is pointing downwards. Because wind shear is translated into a wind speed oscillation felt by the blade section, it is sufficient to consider only half a revolution to capture all possible wind speeds experienced by an airfoil. By relating the elapsed time with the revolution period T it is possible to use eq. 6.9 to obtain the probability of occurrence of a given wind speed due to wind shear:

$$p_U(U) = \frac{2}{T} \left| \frac{\ln\left(\frac{h_0}{z_0}\right) z_0 \left(\frac{h_0}{z_0}\right)^{\frac{U}{U_\infty}}}{U_\infty r \Omega \sin \left[\operatorname{acos} \left(\frac{h_0 - z_0 \left(\frac{h_0}{z_0}\right)^{\frac{U}{U_\infty}}}{r} \right) \right]} \right| \quad (6.10)$$

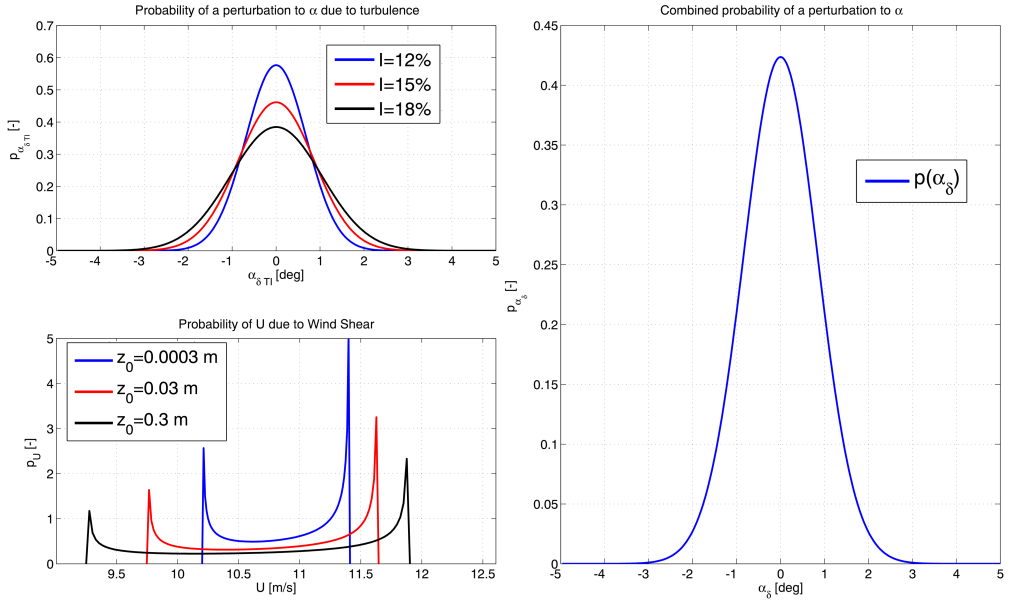


Figure 6.1: Probability Distribution Functions

The probability of occurrence of an AOA perturbation including the effects of both wind shear and turbulence is finally obtained by performing a numerical convolution:

$$p_{\alpha_{\delta}}(\alpha_{\delta}) = \sum_i^{N_U} p_U(U) \times \left(\sum_j^{N_{\alpha}} p_{\alpha_{\delta} T I}(\alpha_{\delta} | U) \right) \quad (6.11)$$

The parameters used in the present study to compute the probability of occurrence of an AOA perturbation are shown in table 6.3. Figure 6.1 illustrates the probability distributions described, while displaying the sensitivity of the method to surface roughness length and turbulence intensity.

Table 6.3: Parameters for probabilistic analysis

Parameter	Value
U_{∞}	11 m/s
B	3
R	60 m
r	45 m
c	3 m
z_0	0.0003 m
h_0	100 m
Ω	1.25 rad/s
I	15 %

Finally, the expected or representative aerodynamic force coefficients are determined:

$$\bar{C}_l(\alpha) = \int_a^b C_l(\alpha) p(\alpha) d\alpha \quad , \quad \bar{C}_d(\alpha) = \int_a^b C_d(\alpha) p(\alpha) d\alpha \quad (6.12)$$

where the limits of integration are such that 99% of all possible occurrences are captured. A more detailed derivation of the probability for both atmospheric turbulence and wind shear AOA perturbation is included in Appendix A.

One should also note expression 6.12 implicitly assumes that no unsteady effects are present. In reality, wind field spatial and temporal gradients together with HAWT blade deflections and vibrations often lead to unresolved time-dependent phenomena [88] [81] affecting C_l and C_d , such as dynamic stall and stall hysteresis. However, Appendix B shows that using the parameter values from table 6.3, from Kaimal's turbulence spectrum [1], unsteady effects arising from atmospheric turbulence should not dominate the experienced aerodynamic coefficients.

The present study does not include unsteady effects in the airfoil design process, also because the airfoil candidates are (implicitly) compared with WE airfoils in terms of the lift curve slope. And if the lift curve slope is similar the dynamic response should also be similar [118], [80]. Moreover, it can also be argued that flow control actuators may be used to mitigate transient/unsteady aerodynamic effects, as shown for DBD plasma actuators control of dynamic stall [109] and stall hysteresis [7].

6.3.2. CF2 - ACTUATION SUITABILITY

The cost function expressing airfoil actuation suitability depends on the desired application and actuator type. Having HAWT ASC in mind, the aerodynamic power produced above rated wind speed should be constant. Power regulation above rated wind speed could be achieved by varying Ω , but this would either lead to very large blade loads [23] (high λ solution) or increase generator loads (low λ solution), both of which most likely lead to a more expensive HAWT [41]. Accordingly, the design choice is made that the airfoil should yield constant aerodynamic torque above rated wind speed, while the rotational speed is also held constant. From BEM [91], the contribution of a blade section to the aerodynamic torque Q is given by:

$$q = dQ = \frac{1}{2} \rho c U_{eff}^2 (C_l \sin(\phi) - C_d \cos(\phi)) r dr \quad (6.13)$$

where U_{eff} is the effective air speed at the blade section. If the HAWT pitch system is not used for power regulation above rated wind speed, increasing wind speed leads to increased AOA experienced by the blade section. From the point of view of airfoil design, two distinct strategies aiming at constant torque above rated wind speeds are considered: One option is to employ actuation to enhance the airfoil performance below rated wind speed, in terms of $C_l(\alpha_{opt})$ and $\frac{C_l}{C_d}$. With this approach the amount of actuation is decreased as wind velocity increases beyond rated speed, such that the aerodynamic torque is kept constant. A second option is to employ actuation to decrease airfoil performance above rated wind speed, such that the maximum torque produced over the range of operational wind speeds is restricted. Both design solutions are illustrated in figure 6.2. The dots and corresponding numbers along the C_l curves in figure 6.2 show relevant points for the different

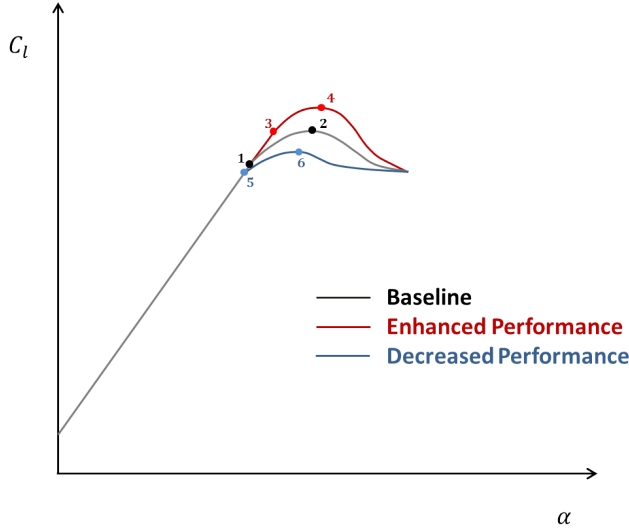


Figure 6.2: Example Baseline and Actuated Lift Polars

polars. Odd numbers represent the AOA of maximum $\frac{C_l}{C_d}$, *i.e.* α_{opt} , while even numbers indicate the AOA at which the sectional aerodynamic torque is maximum.

The cost functions representing actuation suitability are calculated considering both the variation in aerodynamic power obtained with actuation and the power required for actuation. Such a formulation expresses the energetic efficiency of the actuation employed, since an airfoil is more adequate for actuation if a larger change in aerodynamic power is produced from a smaller expended power. In the case of enhanced aerodynamic performance, and referring to figure 6.2, the cost function is written as:

$$CF_{act} = \frac{P_{act}}{\int_{r_1}^{r_2} (q_3 - q_1) \Omega dr} \quad (6.14)$$

where P_{act} represents the actuation power required per blade. For the case of decreased aerodynamic performance, the actuation cost function is expressed by:

$$CF_{act} = \frac{\int_{r_1}^{r_2} (q_6 - q_1) \Omega dr}{P_{act}} \quad (6.15)$$

The limits of integration in expressions 6.14 and 6.15 represent the radial position at which actuation starts (r_1) and finishes (r_2). One should note the actuation suitability cost functions are formulated considering the power needed to perform actuation over a HAWT blade, rather than only sectional contribution. This design choice is justified because when BLT is employed the power consumed at a given section is dependent on the actuation employed over the rest of the blade [89], and accordingly for a fair comparison the airfoil actuation suitability must consider the power expended over the whole blade.

6.4. ACTUATION MODELLING

The actuation effects of wind energy actuated profiles (WAP) are determined using a viscous-inviscid panel-method formulation. Previous work describes the aerodynamic modelling used for BLT and for DBD plasma actuators. For detailed information the reader is referred to [31] and [32].

6.4.1. BOUNDARY LAYER TRANSPARATION

In the present study suction employment corresponds to 'enhanced' performance, while blowing translates the 'decreased' performance case. The power consumption required to perform BLT depends on whether the airfoil performance is enhanced or decreased. It is assumed that friction forces arising from the flow in the blade's inner channel are negligible, so the pump used has efficiency $\eta = 1$. If blowing is employed, the decreased pressure on the blade's suction side should be sufficient to promote transpiration [89], and accordingly the actuation power is estimated by analogy with a centrifugal pump [45] while including Coriolis effects [14]. Based on preliminary investigations (chapter 2 of this dissertation) and since the airfoil sectional properties are of interest, the transpiration coefficient C_q is fixed along the span. The transpired mass at each blade section is given by:

$$\dot{m}_T(r) = \rho U_{eff}(r) c(r) C_q dr \quad , \quad C_q = \frac{V_t L_p}{U_{eff} c} \quad (6.16)$$

where L_p denotes the porous length over which transpiration is enforced and V_t expresses the transpiration velocity. The radial chord distribution follows the planform of the reference 5 MW turbine [60] such that the power required to perform blowing per HAWT blade is estimated with:

$$P_{act} = P_{blow} = \int_0^{r_2} 3\dot{m}_I(r)\Omega^2 r dr \quad , \quad (6.17)$$

where $\dot{m}_I(r)$ represents the inner channel mass flow rate, required to provide the air to be transpired throughout the blade, calculated with:

$$\dot{m}_I(r) = \begin{cases} \int_{r_1}^{r_2} \rho v_t \Omega r c(r) x_p dr & \text{if } r < r_1 \\ \int_{r_1}^{r_2} \rho v_t \Omega r c(r) x_p dr - \int_{r_1}^r \rho v_t \Omega r c(r) x_p dr & \text{if } r > r_1 \end{cases} \quad (6.18)$$

If suction is considered, the pressure difference across the blade surface must promote transpiration through the porous material, and the amount of suction is empirically related with the pressure difference across the porous material [89]. In addition, to employ suction at the outboard section of the blade, bringing the air from the tip to the root, it is necessary to overcome the (static) radial pressure gradient inside the blade. The power needed to employ suction is computed by summing the pressure difference required for transpiration with the static radial pressure, and subtracting the power added to the rotor by the Coriolis force, which in this case contributes to the rotor rotation. The power required to perform suction per HAWT blade is estimated with:

$$P_{act} = P_{suc} = \int_0^{r_2} \left(\frac{R_1 \Omega^2 r^2 v_t^2 + R_2 \Omega r v_t}{\rho} + \Omega^2 r - 2\Omega^2 r \right) \dot{m}(r) dr \quad (6.19)$$

where R_1 and R_2 are constants [89] describing the porous material properties. Table 6.4 shows the parameter values used in the present study. Three different actuation power levels are considered for each airfoil optimization case. The expended power relative to the HAWT rating and correspondent transpiration coefficient are also illustrated in table 6.4. The details of the BLT power consumption estimation are given in Appendix C.

Table 6.4: Parameters used for BLT actuation power computation

Parameter	Value
r_1	35 m
r_2	55 m
ρ	1.23 kg/m ³
R_1	2000 Pa.s ² /m ²
R_2	2000 Pa.s/m
C_q	{0.0017; 0.00085; 0.00043}
Power Level	{0.005; 0.01; 0.02}

6.4.2. DIELECTRIC BARRIER DISCHARGE PLASMA ACTUATOR

For DBD plasma actuators the co-flow (towards the TE) configuration is employed to enhance airfoil performance while the counter-flow (towards the LE) configuration is used to limit the maximum torque produced. Analogously to BLT, three actuation power levels are investigated for DBD actuation. In order to maximize the actuator thrust F_T , the dielectric material permittivity should be as low as possible [132]. According to [73], if the plasma actuator is properly tuned, a given actuation power consumption corresponds to a fixed plasma length, equivalent to plasma body force length L_p . However, the present study allows for different actuation lengths at a given actuation power consumption. This is because from an airfoil design perspective it may be beneficial to employ the same plasma-induced thrust over a body force length which does not minimize power consumption. Essentially one is interested in the plasma configuration that maximizes the impact of the DBD actuator on the aerodynamic loads at an airfoil level, which does not necessarily maximize actuator efficiency in terms of (electrical) energy expended. For the cost function computation the power consumption of the DBD does not depend on the external flow direction [104], and as such is the same for enhanced and decreased performance. Assuming the ratio between DBD thrust and aerodynamic forces is constant over the actuated region, and under the approximation $U_{eff} \approx \Omega r$, the power consumption per HAWT blade is calculated with:

$$P_{act} = P_{DBD} = P_{Plasma}(r_0) \int_{r_1}^{r_2} \left(\frac{r}{r_0} \right)^2 dr \quad (6.20)$$

where $P_{Plasma}(r_0)$ represents the power consumed per unit meter at the center of the actuated region, corresponding to $r_0 = 45m$ (table 6.3). For DBD actuation the power lev-

els are ten times the values imposed for BLT. This choice is motivated by three arguments. Firstly, because of the large effective velocities at the spanwise station considered ($U_{eff} \approx 60 \text{ m/s}$) the DBD actuator will need to impart a large plasma body force such that its influence is 'felt' by the airfoil flow, and a large actuation force entails a large power consumption. Secondly, the variation in the airfoil polars induced by DBD actuation must be large enough such that the multi-objective optimizer 'sees' a difference with respect to the clean case, and hence is able to converge to a Pareto front. Lastly, most applications of DBD actuators for airfoil separation control employed pulsed actuation [100] [108] which requires less power than constant actuation; namely for large HAWT application, successful pulsed actuation [130] has been used with a duty cycle of 10%, effectively expending one tenth of the power used for constant actuation, hence making it equivalent to BLT power consumption considered. The DBD actuation power levels and correspondent plasma body force are given in table 6.5.

Table 6.5: Parameters used for DBD actuation power computation

Power Level[-]	$P_{Plasma}(r_0) [\frac{W}{m}]$	$F_T [\frac{N}{m}]$
0.05	4085	1.09
0.10	8170	2.18
0.20	16340	4.36

6.5. RESULTS

6.5.1. POST-PROCESSING

The airfoils are labeled according to actuation amount, relative thickness, actuation type employed, control objective and level of compromise between actuation and WE suitability. The nomenclature is explained in table 6.6. For each simulation, the Pareto fronts from the multi-objective optimization contain the set of airfoils which are optimum in terms of the defined cost functions. To select a particular airfoil from the Pareto front it is necessary to define the desired level of compromise between the two cost functions CF_{WE} and CF_{Act} . In the present study a graphical criterium is employed based on the Pareto front geometry. The cost function values are normalized such that the transformed Pareto front contains only airfoils with cost function values ranging from 0 to 1 expressed with :

$$CF'_i(Air\ foil) = \frac{CF_i(Air\ foil) - Min(CF_i)}{Max(CF_i) - Min(CF_i)} \quad (6.21)$$

The airfoil sections representing different compromise levels are selected by dividing the normalized design space in three equal-angled slices, as illustrated in figure 6.3. Each slice includes the airfoil sections particularly suited to WE, actuation employment and the compromise between the two. The WAP selected to represent each compromise level is the airfoil closest to the intersection between the Pareto front and the line at the center of each compromise level slice (figure 6.3). The method used to select the WAP for each compromise level is somewhat arbitrary, since the two cost functions are non-linear and piecewise defined and accordingly the cost function values are not necessarily in the same order of magnitude. However by using the normalized space one attempts to define reasonable

compromise levels, at least such that major airfoil geometry and actuation topology trends can be identified. In reality however the exact weight each cost function should have is ultimately the designer's choice.

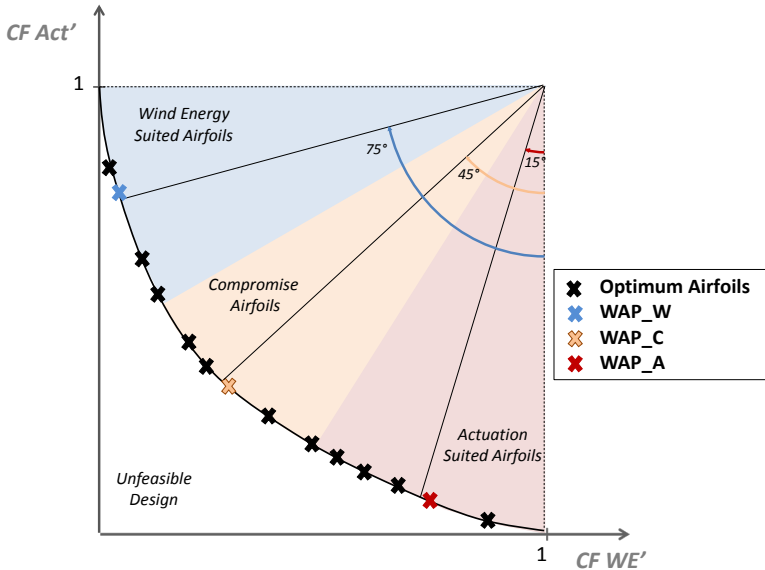


Figure 6.3: Illustration of Compromise Level Selection Procedure

Table 6.6: WAP Nomenclature

Parameter	Value/Designation
Relative Thickness	0.21
Actuation Power relative to HAWT rating	{0.5; 1; 2} (%) for BLT and {5; 10; 20} (%) for DBD
Compromise Level	'W' for Wind Energy 'A' for Actuation and 'C' for Compromise
Actuation Type	'T' for Transpiration and 'P' for Plasma
Control Objective	'D' for Decreased Performance and 'E' for Enhanced Performance

6.5.2. BLT AIRFOIL SECTION GEOMETRIES AND TRENDS

Figures 6.4 and 6.5 show the results obtained for each multiobjective optimization, for different control objectives and actuation power levels, while illustrating the correspondent airfoil shapes. Generally speaking, the optimized airfoil sections retain some characteristics of typical WE profiles. Most WAPs have a relatively small LE radius, particularly for 'decreased' performance. Such a geometric configuration promotes early transition, making the airfoil performance less sensitive to roughness effects. Additionally the S-shaped lower surface is also seen in most WAPs, which is a common feature in WE airfoils because the 'aft-loading' allows for larger C_l values below rated conditions.

Regarding decreased performance, figure 6.4a shows the Pareto fronts obtained with

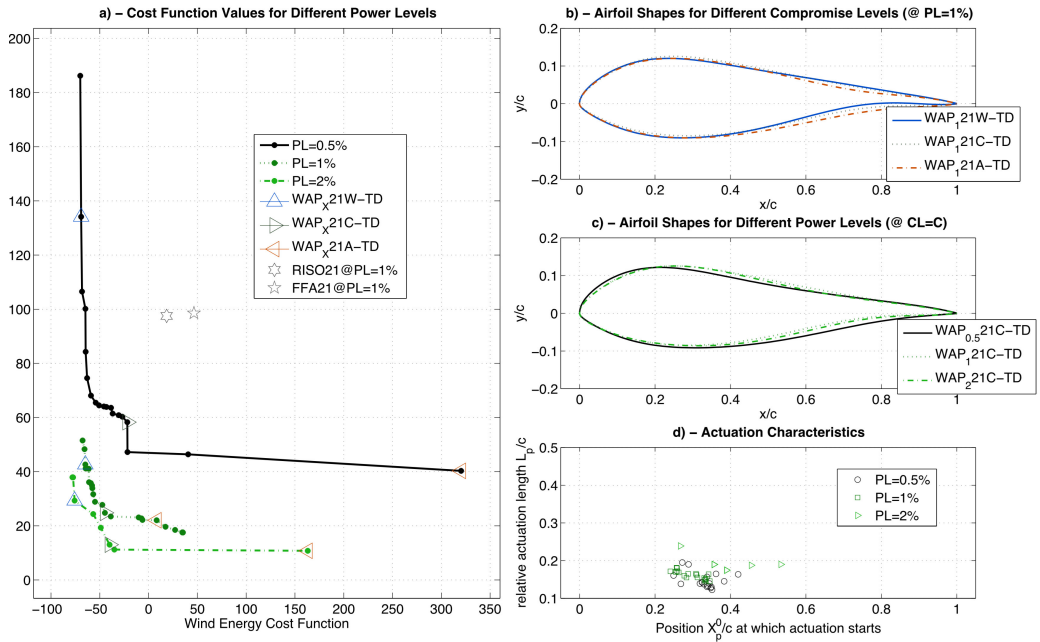


Figure 6.4: WAP - Transpiration Decreased Performance - *a)* Cost Function Values, *b)* Compromise Level Shapes, *c)* Power Level Shapes, *d)* Actuation Characteristics

different power levels, while each WAP is marked with a triangle. Results show that a larger efficiency is obtained for larger actuation power levels, since the ratio of aerodynamic power obtained to actuation power needed (eq 6.15) is smaller for increasing actuation power. The cost functions' value of reference WE airfoils are also included in figure 6.4*a*, for the case of 1% actuation power level; one can see the WAP at the same WE cost function value yields approximately four times the actuation authority obtained with a reference WE profile, in terms of aerodynamic power as defined by the actuation cost function. Figure 6.4*b* shows the optimized airfoil contour for different compromise levels, illustrating the evolution of the WAP shape along the Pareto front obtained with 1% actuation power level. While for the WE compromise level ($WAP_{1,21W-TD}$) the airfoil shape is very similar to reference WE profiles, the actuation suited case ($WAP_{1,21A-TD}$) displays a slightly concave upper surface towards the TE. Such a trend is expected because the concave region increases the maximum adverse pressure gradient, bringing the flow closer to separation, similar to a Stratford type [126] pressure distribution. Such a feature makes the airfoil more suitable for the decreased performance type of actuation since separation is achieved with smaller transpiration amounts. The decreased upper surface thickness in the aft region leads to a local increase in lower surface thickness since a minimum total thickness is enforced (section 6.3.1). The influence of the actuation power level is displayed in figure 6.4*c*. As the actuation power decreases ($WAP_{0.5,21C-TD}$) the WAP contour tends to impose a steeper pressure recovery, thus facilitating flow separation when actuation is employed. Figure 6.4*d* shows the

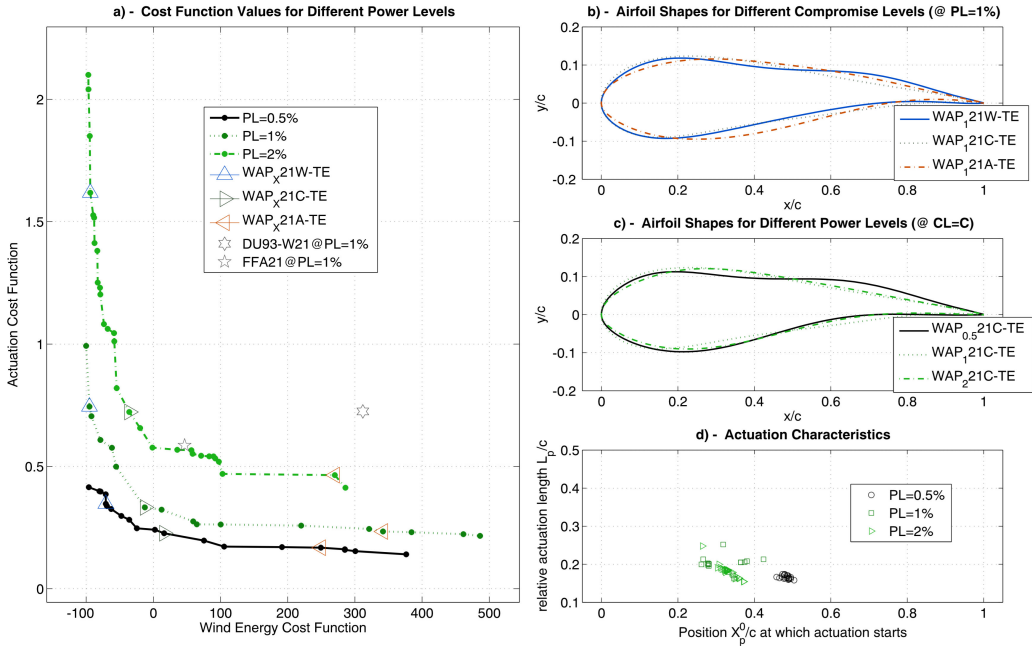


Figure 6.5: WAP - Transpiration Enhanced Performance - *a*) Cost Function Values, *b*) Compromise Level Shapes, *c*) Power Level Shapes, *d*) Actuation Characteristics

actuation characteristics of the WAPs for different power levels. For most optimized airfoils the actuation employment starts at relative chord position $X_p^0/c \approx 0.35$, which is consistent with the maximum adverse pressure gradient location shown in figures 6.4*b* and 6.4*c*.

Figure 6.5 shows the results obtained for enhanced performance. A larger efficiency is obtained for smaller actuation power levels (figure 6.5*a*), unlike for decreased performance. Additionally, for similar WE cost function values the actuation authority obtained with WAPs is approximately two times (equation 6.14) what is obtained with reference WE profiles. Regarding airfoil geometry, figures 6.5*b* and 6.5*c* show airfoil sections with the opposite trend to the decreased performance case, since the upper surface has an increased convexity towards the TE. Additionally the WAP shapes display a somewhat concave upper surface region around the mid-chord position. Such a shape is suited for the enhanced performance objective since it allows for a large operational lift coefficient if suction is employed (figure 6.8). Regarding the influence of the actuation power level, figure 6.5*c* shows that as the actuation power is smaller ($WAP_{0.5}21C-TE$) the upper-surface aft region becomes more convex. This feature enables larger control authority at reduced actuation usage, while the actuation chordwise position moves aft (figure 6.5*d*) compared to large actuation power levels.

At this point it also noted that the transpiration chordwise location obtained for the

WAP sections in both decreased and enhanced performance control objectives is usually after the airfoil maximum thickness. Referring to chapter 2 of this dissertation, this is a favorable result since in principle structural considerations would not prevent the installation of a porous panel in a HAWT blade (to perform BLT) at the chordwise locations shown in figures 6.4d and 6.5d.

6.5.3. PLASMA ACTUATION AIRFOIL SECTION GEOMETRIES AND TRENDS

The plasma actuation optimization cases are now discussed. In general, results are similar to BLT simulations, both in terms of airfoil contour and cost function trends. For decreased performance (figure 6.6), and similarly to BLT results, increased actuation power levels lead to larger actuation efficiency as defined in expression 6.15. For plasma however the expected actuation efficiency is approximately twice of what is obtained with reference WE sections, while the value of the actuation cost function is one order of magnitude smaller (eq 6.15) than for BLT because the plasma actuation power level is ten times larger.

Regarding geometry, figures 6.6b and 6.6c show the trend of increased concavity in the

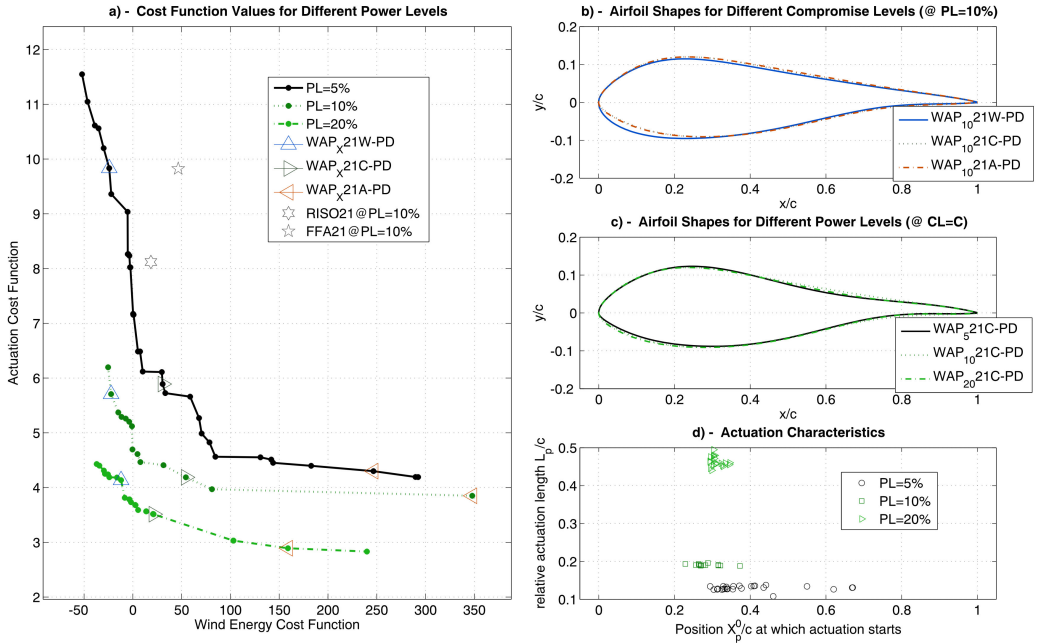


Figure 6.6: WAP - Plasma Decreased Performance - a) Cost Function Values, b) Compromise Level Shapes, c) Power Level Shapes, d) Actuation Characteristics

aft region for the actuation suited ($WAP_{10}21A - PD$) and for decreased actuation power ($WAP_521C - PD$) cases. The actuation characteristics in figure 6.6d show a clear trend of increasing actuation length L_p with increasing power level, while the actuation starting position X_p^0 does not vary significantly.

Regarding enhanced performance, results are also similar to what was obtained with

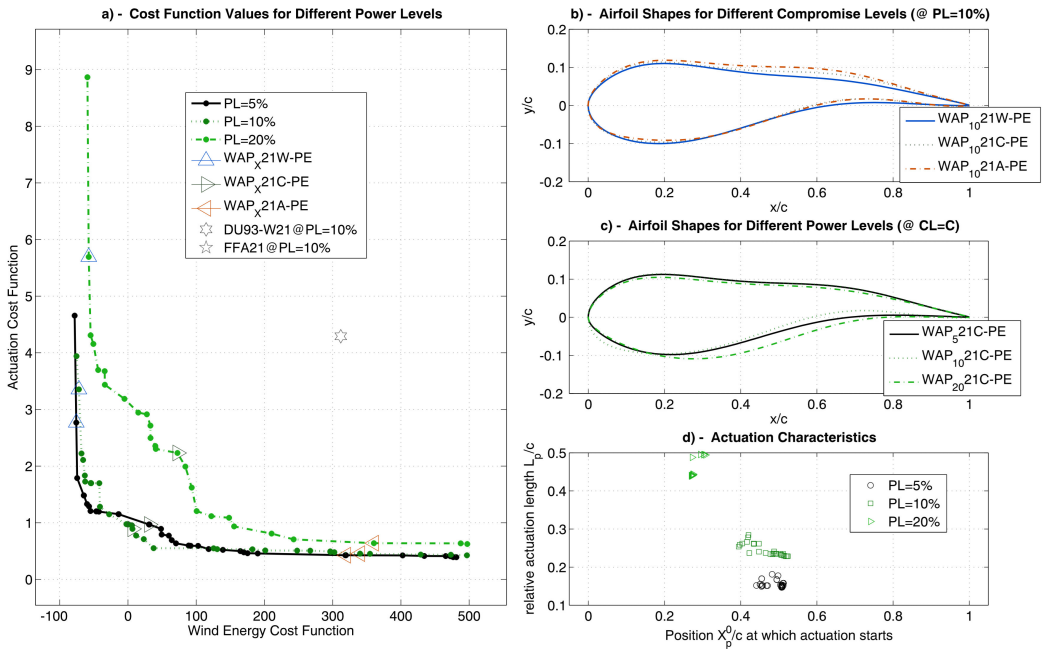


Figure 6.7: WAP - Plasma Enhanced Performance - *a)* Cost Function Values, *b)* Compromise Level Shapes, *c)* Power Level Shapes, *d)* Actuation Characteristics

BLT. Referring to figure 6.7*a*, decreasing actuation power levels lead to larger actuation efficiency, even though for smaller power levels the *WAP* with largest efficiency depends on the compromise level considered. Comparing with reference WE airfoils' performance, figure 6.7*a* shows the actuation authority obtained with (*WAP*₁₀21C – *PE*) is increased by a factor 4. Figures 6.7*b* and 6.7*c* show the airfoil geometry obtained is similar to the BLT actuation case, the upper surface having increased convexity towards the trailing edge and a somewhat concave upper surface region around the mid-chord position. These features become more pronounced in the actuation suited airfoil *WAP*₁₀21A – *PE*, while the WE compromise level section *WAP*₁₀21W – *PE* is more similar to typical WE airfoils. Figure 6.7*c* shows that for smaller power levels the TE convexity and mid-chord concavity features become more pronounced, enabling larger control authority at reduced actuation employment. Figure 6.7*d* displays a clear trend of increasing actuation length L_p with increasing power level, while the actuation starting stance X_p^0 moves towards the LE.

6.5.4. WAP AERODYNAMIC PERFORMANCE

An example of the aerodynamic characteristics obtained with *WAP* airfoils is shown in figure 6.8. The case of decreased performance considering BLT is illustrated in figures 6.8*a* and 6.8*b*, while enhanced performance with plasma actuation is shown in 6.8*c* and 6.8*d*.

The aerodynamic polars of conventional WE airfoils are also shown for comparison. Computation of the actuation cost functions is based on the values of sectional aerodynamic torque contribution q at specific operational points along the aerodynamic polars (equations 6.14 and 6.15). Accordingly q_1 , q_3 and q_6 are also signaled in figure 6.8. For decreased performance, it is clear that $WAP_{121C} - TD$ has similar aerodynamic characteristics to the reference WE airfoil. However the operational points q_1 and q_6 along C_l and C_d curves are much closer than for the $RISO - A1 - 21$ airfoil. This means the maximum torque produced by the HAWT is effectively restricted, since the difference between aerodynamic sectional torque obtained below and above rated speeds is smaller than for a reference WE airfoil.

Regarding enhanced performance the aerodynamic characteristics of $WAP_{121C} - PE$ are somewhat different from typical WE airfoils. Even though the maximum lift to drag ratio is similar, α_{opt} and $C_l(\alpha_{opt})$ are larger than for the $DU93 - W210$ section. The increased operational lift is most likely enabled by the large Reynolds number considered, as discussed in section 6.5.5. Nevertheless, the $WAP_{121C} - PE$ shape increases the effect of actuation considerably when compared to the reference WE airfoil. Figures 6.8c and 6.8d show the operational points q_1 and q_3 are more distant in the $WAP_{121C} - PE$ polars than in the reference case. Ultimately this means the optimized airfoil enables larger actuation induced increase in lift to drag ratio compared to $DU93 - W210$ section, fulfilling the enhanced performance control objective.

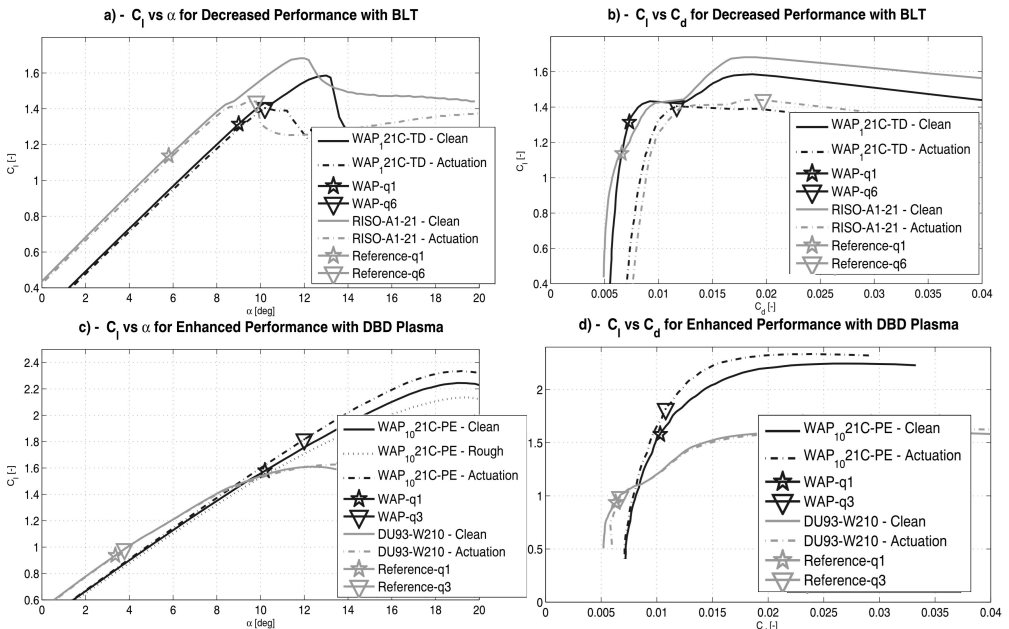


Figure 6.8: Airfoil Aerodynamic Polars - a) and b) Decreased Performance with BLT, c) and d) Enhance Performance with DBD Plasma

6.5.5. CONSIDERATIONS ON THE EFFECT OF THE REYNOLDS NR AND ROUGHNESS

The results shown in figures 6.4 to 6.7 are obtained for $Re = 9 \times 10^6$, characteristic of large offshore HAWT operation at above-rated wind speeds. One should keep in mind however that the viscous-inviscid panel code may not provide the accuracy obtained at smaller Reynolds numbers, for which it was originally tailored [138]. It has been shown [134] that RFOIL may underpredict $C_l(\alpha_{Stall})$ by 6.5% at $Re = 9 \times 10^6$ for airfoils with similar thickness-to-chord ratio. Nevertheless, in the optimization cases carried out the airfoil candidates are compared with the performance of 'reference' WE airfoils obtained also at $Re = 9 \times 10^6$, and as such the trends identified remain valid. Previously it has been suggested to employ correction factors [134] to RFOIL drag prediction, while one could also think of using such a correction factors for the lift coefficient, as to improve the agreement with experimental results. In the present study however no such (empirical) corrections are applied, again on the grounds that the airfoil candidates' performance is compared with the simulated 'reference' WE airfoil polars.

The increased WAP performance in terms of the wind energy cost function (negative values in figures 6.4 to 6.7) compared to the reference airfoil can be explained by considering the aerodynamic sections used to define the reference WE airfoil were originally designed for smaller Reynolds numbers ($Re \approx 3 \times 10^6$). That means that, at $Re = 9 \times 10^6$, the achievable WE airfoil performance defined in terms of the indexes shown in table 6.2 is probably higher than obtained with the reference airfoils considered, particularly regarding $C_l(\alpha_{opt})$. However, to the authors' knowledge no public domain data is available for WE airfoils designed for $Re > 3 \times 10^6$, justifying the approach used in the present study to prescribe the reference WE airfoil performance.

As mentioned in section 6.3.1, the roughness sensitivity of WAP sections is evaluated by comparing the *clean* and *rough* lift polars at α_{opt} . Figure 6.8c shows that for enhanced performance the lift coefficient at optimum incidence practically does not change when transition is forced. Such results are promising because $WAP_{1021C} - PE$ is sensitive to lift enhancement actuation for large AOA while relatively insensitive to roughness effects at optimum incidence.

6.6. CONCLUSIONS

This chapter presented a comprehensive study of airfoil sections suitable to employ actuation in a WE environment, named WAP (Wind Energy Actuated Profiles). The airfoils are designed with a genetic algorithm multiobjective optimizer, formulated by setting two cost functions. The WE cost function compares the candidate airfoils' aerodynamic characteristics with reference WE airfoils', while considering a probabilistic approach to include the effects of turbulence and wind shear. The actuation suitability cost function considers two different control strategies designated by 'enhanced' and 'decreased' performance, and expresses the ratio of expended and obtained power. Two different actuation types are considered, namely BLT and DBD plasma.

Results show that using WAP airfoils provides much higher control efficiency than adding actuation on the reference WE airfoils, without detrimental effects in non-actuated operation. The WAP sections yield an actuator employment efficiency that is 2 to 4 times

larger than obtained with reference WE airfoils, at equivalent WE performance. For the 'decreased' performance control objective results indicate a larger efficiency at larger actuation power levels, while for the 'enhanced' case the opposite trend is found. Regarding geometry, the WAPs obtained employing BLT and plasma actuation are similar to each other. This is encouraging and indicates that the resulting airfoil sections converge towards the optimal shapes. Generally speaking, and compared to typical WE airfoils, WAP sections for decreased performance display an upper surface concave aft-region, while for increased performance a convex upper surface aft-region is obtained.

Future research should include pulsed actuation of DBD actuators, since it is normally the case of real application for HAWTs. Nevertheless, the present study emphasizes there is much to gain in designing airfoils from the beginning to include actuation effects, especially compared to the current method of employing actuation on already existing airfoils. It is clear that designing wind energy and actuation tailored airfoils paves the way for new HAWT control strategies to become seriously considered, namely active stall control.

7

PLANFORM OPTIMISATION ASC ROTOR

*Run, rabbit run. Dig that hole, forget the sun.
And when at last the work is done,
don't sit down, it's time to dig another one.*

Roger Waters

This chapter addresses the design of Horizontal Axis Wind Turbine rotors tailored to Active Stall Control operation. An optimization study employs an aero-structural-servo formulation to investigate planform geometry design but also actuation scheduling, rated rotational speed and spanwise laminate skin thickness. Results show that, compared to variable-pitch turbines, ASC planform displays increased chord at inboard stations with decreased twist angle towards the tip, while the above-rated rotational speed is smaller. Flow control actuation is employed to trim the loads across the operational wind speed envelope and hence reduce load overshoots and associated capital costs. The expected cost-of-energy of the ASC rotor does not indicate a significant decrease compared to state-of-the-art pitch machines, but appears to be at least competitive when the pitch system is effectively mitigated. Additionally, results indicate Active Stall Control becomes interesting if the actuation system allows for further operational cost reduction via fatigue load-alleviation, since the actuation trimming load system is anyhow included in an ASC machine.

7.1. INTRODUCTION

Recently the tendency to install wind farms further offshore along with the increasing size of HAWT drives the search for robust design solutions. While current offshore HAWT are variable-speed pitch-regulated machines, alternative rotor concepts are being considered for future wind energy production. Some examples include Bend-Twist coupled Stall-regulated HAWTs [24], Yaw-controlled [33] rotors, and the more mature Smart-Rotor machine [11] [12] [5]. Modern ASC is another concept, in which HAWT power regulation above rated wind speeds is achieved employing add-ons (flow control actuators) which actively provoke stall. With such a design philosophy the pitch mechanism of HAWT would be used in emergency situations only (*i.e.* not for power regulation), potentially leading to increased availability [23] and hence decreasing the cost of energy. This chapter presents an optimization study in which the HAWT rotor is tailored for ASC operation.

Numerous HAWT rotor geometry optimization studies have been reported [43], [10]. Among others, previous efforts aimed at blade mass minimization [54], energy capture maximization [141] and passive load alleviation [18]. The current optimization study is aimed at tailoring the HAWT rotor to ASC operation, by designing blade twist(θ) and chord (c) spanwise distribution. The optimizer additionally considers blade laminate thickness (t) to ensure structural integrity and actuation scheduling (ξ) for aerodynamic load control across the operational wind speed envelope. The above-rated rotational speed (Ω_R) is also considered as a design variable. As such, the present optimization effort minimizes the cost-of-energy (COE) in an servo-aero-structural framework.

The structure of this study is as follows: section 7.2 describes the aero-structural framework, and section 7.3 explains the Actuation System(AS) modelling. The optimization setup is detailed in section 7.4 and the Energy Cost Function is described in 7.5. Finally the optimized blade planform and modelled cost reduction are shown in section 7.6 and conclusions are presented.

7.2. AERO-STRUCTURAL FRAMEWORK

The present work studies the aero-structural response of the HAWT rotor using a standard blade element momentum (BEM) model coupled to a non-linear Timoshenko beam for structural analysis [39]. The BEM model includes a tip-loss correction [117] and accounts for wind shear when computing the aerodynamic loading at each annulus. The non-linear beam formulation is particularly suited to capture the deformation of flexible blades, and thus adequate to model large stall-controlled HAWT rotors. The aero-structural coupling uses the principle of virtual work, by equating the internal (structural) and external (aerodynamic) forces with generalized displacements, and is evaluated at $N_s=60$ points along the span. The solution is found iteratively with a Newton-Raphson scheme, thus providing the HAWT rotor's static aeroelastic response. For further information on the aero-structural module the interested reader is referred to [39].

The current study considers the *NREL 5 MW* machine as baseline and as such the NREL [60] reference HAWT parameters are used. The turbine operational parameters are illustrated in table 7.3, while table 7.1 shows the chord and twist radial distribution and table 7.2 shows mass and stiffness sectional properties.

Table 7.1: Baseline Blade Planform Parameters

r (m)	Twist(deg)	Chord(m)	Airfoil
8.33	13.3	4.17	<i>Cylinder</i>
11.75	13.3	4.56	<i>DU00 – W2 – 401</i>
15.85	11.48	4.65	<i>DU00 – W – 350</i>
19.95	10.16	4.46	<i>DU00 – W – 350</i>
24.05	9.01	4.25	<i>DU97 – W – 300</i>
28.15	7.80	4.00	<i>DU91 – W2 – 250</i>
32.25	6.54	3.75	<i>DU91 – W2 – 250</i>
36.35	5.36	3.50	<i>DU93 – W – 210</i>
40.45	4.19	3.26	<i>DU93 – W – 210</i>
44.55	3.13	3.01	<i>WAP₁₀ – 18C – PD</i>
48.65	2.31	2.76	<i>WAP₁₀ – 18C – PD</i>
52.75	1.52	2.51	<i>WAP₁₀ – 18C – PD</i>
56.17	0.86	2.31	<i>WAP₁₀ – 18C – PD</i>
58.90	0.37	2.09	<i>WAP₁₀ – 18C – PD</i>
61.63	0.11	1.42	<i>WAP₁₀ – 18C – PD</i>

Consistently with the chord and twist distributions, the airfoil section spanwise distribution is also matched to the NREL reference blade. The blade sectional aerodynamic coefficients include rotational corrections and correspond to a blade with aspect ratio $AR = 17$ [87]. Figure 7.1 illustrates the values of lift C_l and drag C_d for the different airfoil sections along the span. It is noted the most outboard airfoil section is changed with respect to the NREL machine. Instead an actuation tailored airfoil is employed [105], further described in section 7.3.

7.3. ACTUATION SYSTEM MODELLING

7.3.1. CONTROL STRATEGY

As discussed in chapter 2, it is fundamental to have a holistic design approach, including airfoil section, blade planform and control strategy seamless integration. When considering fixed-pitch HAWT machines, different power (and load) control strategies [23] may be conceived. Considering the reference NREL geometry, figure 7.2 shows the aerodynamic rotor Torque (Q) and Power (P) obtained without blade-pitching above rated wind speeds, providing insight on the challenge posed by power (and load) regulation of fixed-pitch HAWT.

Referring to figure 7.2, power production above rated wind speeds could be regulated by increasing the rotational speed Ω . Such a control philosophy is usually termed *high λ* solution, where λ represents the *tip-speed-ratio* defined as the ratio between rotational speed and wind velocity at the rotor tip. This power regulation strategy decreases the operational AOA over the blade section, but has two strong disadvantages. Since very large rotational speeds would be necessary, the aerodynamic thrust T becomes very large compared to a pitch-controlled machine, which means the blades need to be stronger, heavier and more expensive. Additionally, because such a control strategy implies a broad range of rotational speeds, dynamic/excitation analysis puts further constraints on the turbine structure [36]

Table 7.2: Baseline Blade Structural Parameters

r (m)	m (kg/m)	$EI_{FLAP}(N.m^2)$	$EI_{EDGE}(N.m^2)$	$GJ(N.m^2)$	$EA(N)$
8.33	400.6	5528.36E+6	8063.16E+6	1570.36E+6	4493.95E+6
11.75	426.3	4691.66E+6	7167.68E+6	855.90E+6	4169.72E+6
15.85	352.8	2568.96E+6	5048.96E+6	335.92E+6	3147.76E+6
19.95	339.3	2050.05E+6	4501.40E+6	261.00E+6	2613.97E+6
24.05	321.9	1588.71E+6	3995.28E+6	200.75E+6	2146.86E+6
28.15	294.7	1102.38E+6	3447.14E+6	144.47E+6	1632.70E+6
32.25	263.3	681.30E+6	2734.24E+6	81.19E+6	1168.76E+6
36.35	241.6	408.90E+6	2334.03E+6	57.45E+6	922.95E+6
40.45	200.2	238.63E+6	1584.10E+6	35.98E+6	648.03E+6
44.55	165.0	126.01E+6	1183.68E+6	20.90E+6	531.15E+6
48.65	138.9	90.88E+6	797.81E+6	16.28E+6	375.75E+6
52.75	107.2	61.05E+6	518.19E+6	9.07E+6	244.04E+6
56.17	90.2	39.36E+6	395.12E+6	7.08E+6	181.52E+6
58.90	68.7	26.52E+6	281.42E+6	5.33E+6	100.08E+6
61.63	49.1	10.08E+6	101.63E+6	2.64E+6	36.90E+6

Table 7.3: Baseline Turbine Parameters

Parameter	Value
B	3
R	62.5 [m]
N_s	60
N_{cp}	15
h_0	90 [m]
λ_{opt}	7.5
U_{CI}	5 m/s
U_{rated}	11.4 m/s
U_{CO}	25 m/s
Weibull shape k	2.3
Weibull scale λ	10.5

which may also lead to more expensive HAWT design.

Another possible power regulation strategy is referred to as *low λ* solution. In this approach the rotational velocity is decreased as the wind speed increases, as to keep the power production constant above rated wind speed. Figure 7.2 shows however the obtained aerodynamic torque is larger than at rated conditions, leading to a heavier, more expensive [41] HAWT generator and gearbox than for a pitch-controlled machine with same rated power. Additionally, since this strategy relies on increasing the local angle of attack to promote stall, sectional aerodynamic forces may experience unwanted hysteresis effects [81], particularly due to wind shear and turbulence.

Even though different control strategies are technically feasible, the preferred solution should attempt to minimize the expected COE. With this in mind, the present study considers the rotational speed is constant above rated wind speed, which may be expressed as:

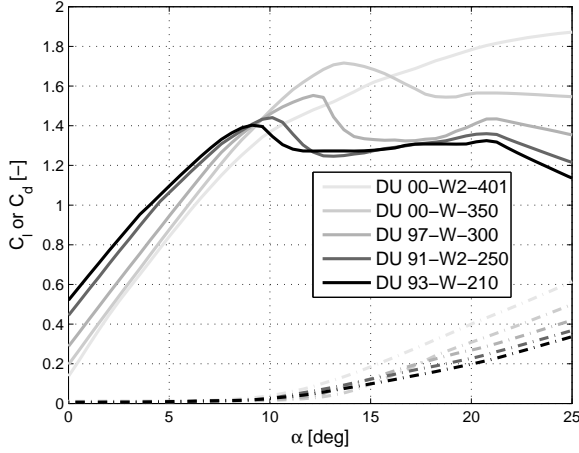


Figure 7.1: Aerodynamic Polars along blade span

$$\begin{cases} \Omega(U) = \frac{U\lambda_{opt}}{R} & \text{if } U \leq U_R \\ \Omega(U) = \Omega_R & \text{if } U > U_R \end{cases} \quad (7.1)$$

where Ω_R denotes the (above) rated rotational speed, also included in the optimization scheme. This power regulation strategy design-choice is made referring to figure 7.2. It is anticipated that keeping the rotor speed constant above rated conditions may become more economically attractive than both *high* λ and *low* λ solutions. Since in an ASC machine the aerodynamic loads might be trimmed across the operational wind speed envelope, it is possible the power and loads are regulated at a constant rotational speed. Additionally, the choice of constant rotational speed above rated wind speed is consistent with the conditions for which the actuation tailored airfoil (described in subsection 7.3.2) is designed for.

It is noted that expression 7.10 is a simplification of real rotational speed variation usually enforced in pitch controlled HAWT, since there is normally a constant speed region before reaching rated power to limit torque, noise emission and tip deflection. Nevertheless, for the present study it is not relevant because the wind speed range is discretized with bins of 2 m/s.

7.3.2. ACTUATED AIRFOIL SECTION

The efficient operation of any flow control actuation device is dependent on the specific application. The current effort considers ASC, and as such 'efficient' actuation employment is associated with actuator authority, in terms of actuation-induced variation of sectional aerodynamic coefficients $\Delta C_l, \Delta C_d$. Previous studies have shown that employing a 'flow-control configured' airfoil [99] may result in large actuation-induced ΔC_l compared to standard airfoil sections.

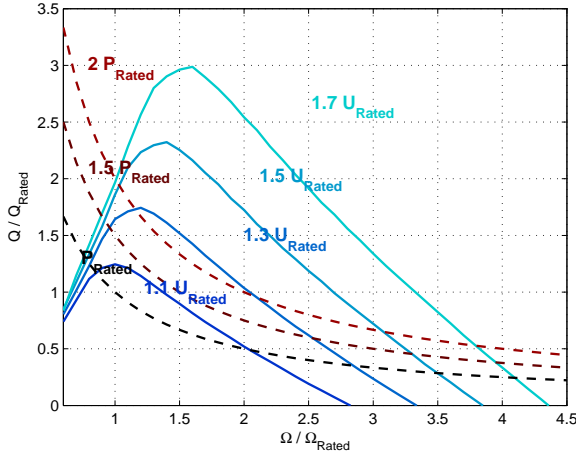


Figure 7.2: NREL rotor loading obtained without blade pitching above rated wind speeds

The present study considers an airfoil section suitable to employ actuation in a wind energy environment, designed specifically with ASC in mind (chapter 6 of this dissertation). The airfoil was designed with a genetic algorithm based multiobjective optimizer, considering both WE performance and actuation suitability as cost functions, thus termed Wind Energy Actuated Profile (WAP). As discussed in chapter 6, the design methodology ensures the airfoil satisfactory WE performance (in terms of $C_{l_{opt}}$, C_l/C_d , stall characteristics and roughness insensitivity) while having an actuation energetic efficiency that is 2 to 4 times that of reference airfoils.

Figure 7.3 shows the lift and drag versus angle of attack obtained with the WAP airfoil, for both *clean* and *actuated* operation. It is noted the present study assumes ASC acts to limit rotor aerodynamic torque above rated wind speeds, and as such actuation effectively decreases the blade section lift, corresponding to the so-called *decreased performance* control strategy described in chapter 6.

In the context of ASC rotor optimization, the value of the aerodynamic coefficients C_l, C_d should be dependent of the actuation level, such that the rotor loads may be regulated across the operational wind speed envelope. In the present study the actuation level is expressed by ξ , which parametrizes the actuated airfoil aerodynamic characteristics with:

$$C_l(\alpha) = (1 - \xi)C_l^{clean}(\alpha) + (\xi)C_l^{act_{MAX}}(\alpha) \text{ with } \xi \in [0; 1] \quad (7.2)$$

$$C_d(\alpha) = (1 - \xi)C_d^{clean}(\alpha) + (\xi)C_d^{act_{MAX}}(\alpha) \text{ with } \xi \in [0; 1] \quad (7.3)$$

Equations 7.2 and 7.3 show that the actuation effect, in terms of the variation in aerodynamic coefficients, is bounded between the *clean* and the *act_{MAX}* configurations. In other words, the aerodynamic polar *act_{MAX}* is obtained with the maximum actuation level

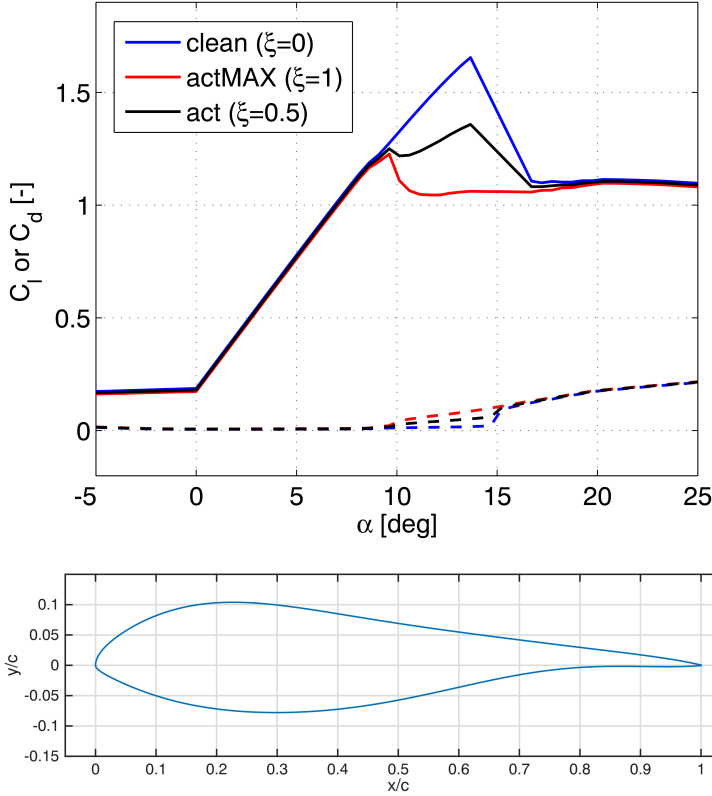


Figure 7.3: WAP₂₀ – 18C – PD Airfoil *top* - Aerodynamic Characteristics for *clean* and *actuated*_{MAX} operation *bottom* - Section Contour

($\xi = 1$), which in the present case typically corresponds to the smallest C_l and largest C_d possible at a given angle of attack.

7.3.3. ACTUATION POWER CONSUMPTION

When determining the ASC rotor design, it is necessary to take the power requirements of the actuation system into account, particularly since power consumption may become considerable for some types of flow control actuators [132],[116]. In the present case, the maximum actuation power consumption was used specifically to design the actuation-tailored airfoil section, corresponding to the *act*_{MAX} polar shown in figure 7.3.

To determine the actuation system electrical power consumption $P_{ELEC_{act}}$ at a given actuation level ξ , the current study uses a linear approximation:

$$P_{ELEC_{act}}(\xi) = \xi P_{actMAX} \quad (7.4)$$

where $P_{actMAX} = 0.2P_{NREL5MW}$, corresponding to the specified airfoil section characteristics shown in figure 7.3. It is noted expression 7.4 is a simplification, since the variation of C_l and required actuation power are not necessarily proportional over the entire actuation level or angle of attack range. However, previous research (chapter 2) indicates that, regarding DBD plasma actuators and particularly Boundary Layer Transpiration (BLT), the actuation induced ΔC_l is roughly proportional to the actuation power, and as such expression 7.4 is considered valid for ASC rotor design. An additional simplification used in the current effort is that the C_l variation imposed by the actuation system is constant across the actuated blade span region. More complex actuation scheduling design solutions could be adopted, which include different actuation levels at different spanwise positions. Nevertheless the optimization formulation (section 7.4) already employs several types of variables in the design space vector, including twist, chord, blade laminate thickness and rotational speed. As such, the present study keeps the actuation level constant along the blade radius ($\xi \perp r$) to increase the robustness of the optimizer algorithm, thus keeping the amount of variables considered within a reasonable limit while allowing diverse ASC rotor design space exploration. It is noted however that the actuation level does vary with operational wind speed $\xi = f(U)$, as explained in section 7.4.

Having an offshore HAWT in mind, it is desirable that the power consumed by the actu-

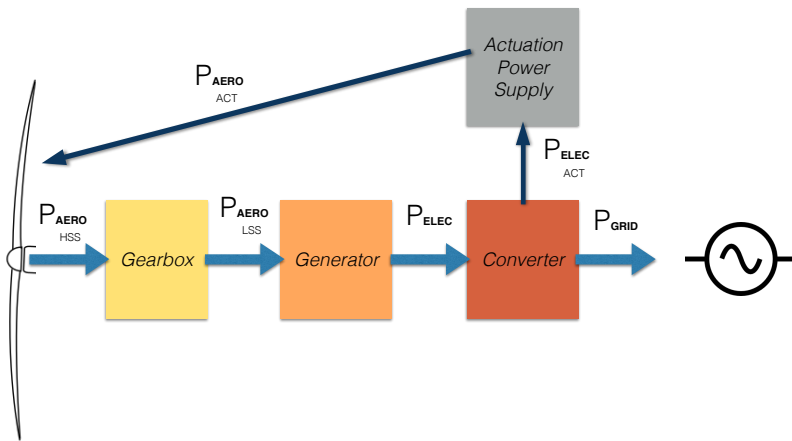


Figure 7.4: Nacelle Schematic Layout Depicting Power Fluxes

ation system is provided by the turbine itself, such that the system is capable of independent operation. Figure 7.4 shows a schematic of the envisioned HAWT nacelle component layout, illustrating the respective power fluxes.

7.4. OPTIMIZATION SET-UP

The present study uses a gradient based algorithm (Matlab *fmincon*) to solve the minimization problem. The partial derivatives of the cost function (section 7.5) with respect to each design variable are also supplied to the gradient algorithm. This allows for a fast evaluation of the response and its sensitivities to each design variable, enabling efficient computations. The geometric design space is described employing $N_{CP}=15$ control points along the span, with twist (θ), chord (c) and laminate thickness (t_{lam}) defined at each control point. Additionally, the optimization considers different actuation schedule values $\xi(U)$, each prescribed at an above rated wind speed, while the rated rotational wind speed (Ω_R) is also an explicit design variable.

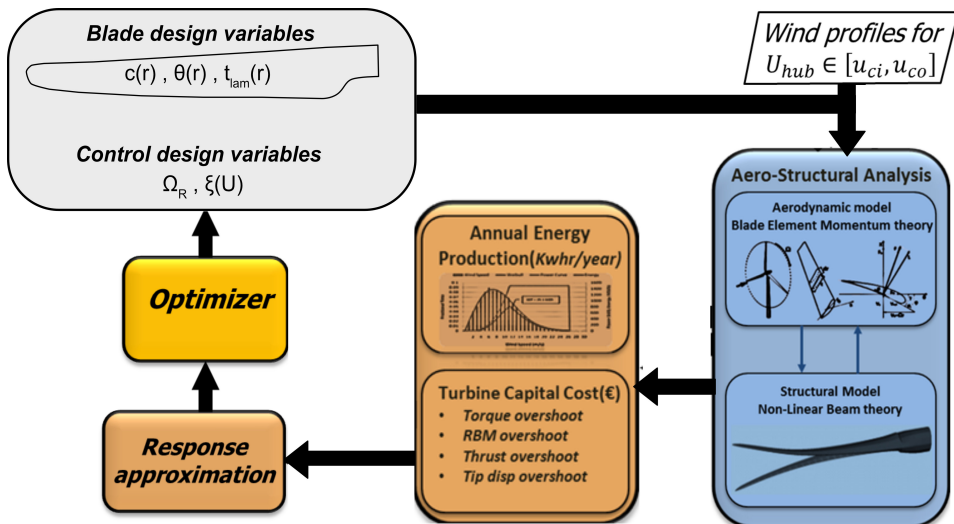


Figure 7.5: Optimization Flowchart (adapted from [39])

Within the optimization framework, the blade section mass and stiffness are (implicit) design variables. This is achieved by modeling the structural blade section as a thin-walled structure [27]. As such the laminate thickness and chord are used in the optimizer framework to scale the blade sectional mass m with:

$$m = m_{ref} \times \frac{t_{lam}}{t_{lamref}} \times \frac{c}{c_{ref}} \quad (7.5)$$

The components of the blade sectional stiffness scale differently with laminate thickness and chord [27]. Flapwise and edgewise bending stiffness and torsional bending stiffness are scaled with:

$$S = S_{ref} \times \frac{t_{lam}}{t_{lamref}} \times \left(\frac{c}{c_{ref}}\right)^3 \quad \text{for} \quad S \equiv EI_{FLAP}, EI_{EDGE}, GJ \quad (7.6)$$

Whereas extensional and shear stiffness are scaled with

$$S = S_{ref} \times \frac{t_{lam}}{t_{lamref}} \times \frac{c}{c_{ref}} \quad \text{for} \quad S \equiv EA, GA \quad (7.7)$$

7.4.1. OPTIMIZATION CONSTRAINTS

As mentioned before, the present study utilizes Matlab's *fmincon*, which explicitly allows to impose linear and non-linear constraints on the design space. Within the current framework, both the twist and chord radial variation were limited using variational constraints following [98]. This is achieved by defining a function g to express the locally enforced radial constraint in parametric space ϕ . For the spanwise twist distribution $\theta(r)$ this is expressed as:

$$\left(\frac{d\theta}{dr}\right)^2 \leq \eta_\theta^2, \quad g_\theta(\phi) = \frac{1}{J^2} \left(\frac{d\theta}{d\phi}\right)^2 - \eta_\theta^2 \leq 0 \quad (7.8)$$

Compliance of the radial derivative across the entire blade span is enforced by employing an integral Lagrangian formulation defined as:

$$\int_0^1 g_\theta \lambda J d\phi \leq 0 \quad (7.9)$$

where the Lagrange multipliers are defined by λ . For the spanwise chord distribution $c(r)$ the formulation is identical to equations 7.8 and 7.9. Having manufacture constraints and aerodynamic spanwise performance in mind, the chord and twist radial gradients were limited to twice the maximum value of the *NREL 5 MW* machine, as expressed below.

$$\begin{cases} \eta_\theta = 2 \max(|\frac{d\theta}{dr}|_{NREL}) \\ \eta_c = 2 \max(|\frac{dc}{dr}|_{NREL}) \end{cases} \quad (7.10)$$

In addition to planform geometry, the optimization framework also imposes structural constraints, namely on the blade root section stress ($\sigma(r=0)$) and maximum out-of-plane tip deflection ($w(r=R)$). The optimizer forces the aforementioned variables to follow the *NREL 5 MW* machine values. It is noted the *NREL 5 MW* machine was designed to be pitch-controlled, and as such experiences a different loading across the operational wind speed envelope than the envisioned active-stall controlled HAWT. Nevertheless, the rated power and overall machine topology are similar, and as such the *NREL 5 MW* HAWT blade root stress level and deformation are used as a reference for the current active stall control machine.

$$w(r=R)_{ASC} \leq w(r=R)_{NREL} \quad (7.11)$$

$$\sigma(r=0)_{ASC} \leq \sigma(r=0)_{NREL} \quad (7.12)$$

7.5. COST FUNCTION DEFINITION

This section describes the cost function used for evaluating each ASC rotor design iteration. The cost function value is formulated in terms of the COE, by computing both the expected annual energy production and the price of HAWT components.

7.5.1. HAWT OPERATIONAL ENVELOPE

The HAWT operational envelope is determined for each ASC rotor design iteration. The aero-structural code described in section 7.2 is used to estimate the power production and wind turbine loads over the operational wind speed range. The expected annual energy production (AEP) is determined with:

$$AEP = availability \times \int_{U_{CI}}^{U_{CO}} P_{GRID}(U) f(U) dU \quad (7.13)$$

where $P_{GRID}(U)$ expresses the power production at a given wind speed. By recalling figure 7.4, the produced power is computed with:

$$P_{GRID}(U) = P_{AERO}(U) - P_{ELEC_{act}}(U) \quad (7.14)$$

and thus accounts for the actuation system power consumption. To estimate the yearly energy production (equation 7.13) the probability of occurrence of a given wind speed $f(U)$ is also considered. The probability of occurrence is calculated with a Weibull distribution [51], in which the shape and scale parameters are chosen to match an off-shore [97] wind climate. The limits of integration U_{CI} and U_{CO} in expression 7.13 correspond to the cut-in and cut-out wind speeds, respectively. The parameter values used for calculating the AEP are shown in table 7.3.

The present study estimates the impact of HAWT loads on the COE by considering the maximum load occurring over the operational wind speed range. In other words, it is assumed the maximum (static) load is the design driver for each HAWT component [41]. For the cost function definition, three different design-driving load types are explicitly considered: rotor thrust, rotor torque and rotor power. Accordingly, and for each load type, the load overshoot is defined as the ratio between the maximum wind-speed range load divided by the maximum load obtained with the reference turbine [60]:

$$L_{OS}^k = \frac{\max(L^k(U))}{\max(L_{REF}^k(U))} \quad (7.15)$$

in which L_{OS}^k denotes the load overshoot for each load type k , and the subscript REF translates the reference turbine loading.

7.5.2. HAWT COST MODEL

The cost of a HAWT corresponding to a given ASC rotor iteration is estimated following the methodology described in [41]. The COE is estimated with :

$$COE = \frac{FCR \cdot ICC}{AEP} + AOE \quad (7.16)$$

where FCR is the fixed charge rate and ICC is the initial capital cost. The annual operating expenses (AOE) are defined with:

$$AOE = \frac{OM + LRC}{AEP} + LLC \quad (7.17)$$

in which OM are the levelized operation and maintenance costs, LRC is the levelized replacement/overhaul cost and LLC is the land lease cost. The present study assumes the LLC is unaffected by the blade design, while the remaining components of the COE are dependent on the ASC rotor iteration.

As mentioned before, and following the methodology from [41], the cost of each HAWT component is related to a specific load type. For example, the cost of the generator scales with maximum rotor torque, while the cost of the HAWT tower depends on the rotor thrust. Table 7.4 shows the specific load type k driving each component. At this point it is noted the blade mass also has a direct impact on the machine ICC . Even though the blade mass is not an explicit design variable in the optimization framework, the combination of laminate thickness t_{lam} and sectional blade chord c required to meet structural constraints (section 7.4) may result in a total blade mass variation. Consistently with [41], it is assumed the ICC of the blades and rotor hub scale linearly with the blades' total mass.

The present cost model assumes some cost parcels have a fixed value, namely transport, port and staging equipment, installation, permits, personnel equipment and scour protection. Additionally the present study prescribes the rotor radius R and as such [41] a constant cost for the nose cone, main bearings, yaw drive and bearings, mainframe, control hardware and marinization. It is noted the electrical interface is calculated assuming a 7 by 7 array spacing, similar to existing off-shore wind farms [102],[19].

Table 7.4: Reference Turbine Component ICC Breakdown

HAWT Component	ICC percentage	Load Type
Blades	8	blade mass
Hub	1	blade mass
Low Speed Shaft	<1	rotor torque
Gearbox	7	rotor torque
Main brakes	<1	rotor torque
Generator	3	rotor torque
Power Electronics	4	rotor power
Electrical Connections	2	rotor power
Hydraulics and Cooling	<1	rotor power
Nacelle	<1	rotor power
Tower	7	rotor thrust
Support Structure	16	rotor thrust
Electrical Interface	13	rotor power

Within the optimization framework, the solver attempts to minimize the relative COE , that is the ratio between a given ASC rotor iteration and the pitch-controlled NREL turbine COE . It is noted that estimating the cost of each component in this relative way is a simpli-

fication. Naturally if there are significant load overshoots one might expect topology variation in the HAWT components, which may imply an altogether different component cost. In practice the current study assumes only moderate (< 1.5) load overshoots are present, rendering the presented cost model valid for ASC rotor optimization.

The sensitivity of HAWT cost to each load overshoot type is different. Figure 7.6 illus-

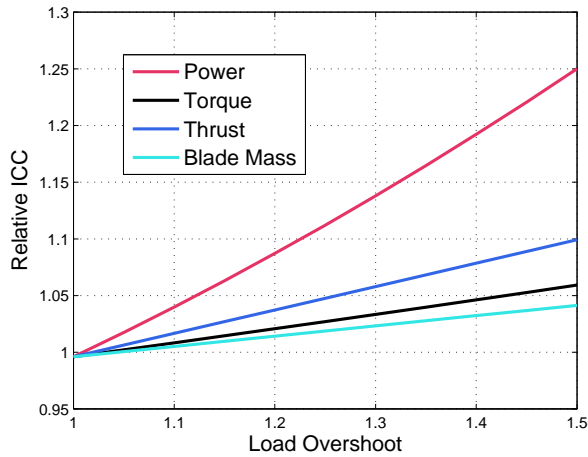


Figure 7.6: ICC Sensitivity to Different Load Overshoots

trates the variation obtained in HAWT *ICC* for different load overshoot types and values. The relatively small increase in HAWT *ICC* compared to the large overshoots is explained because the turbine components represent only a fraction of the total *ICC* of each HAWT installed offshore. Figure 7.6 also shows that the HAWT *ICC* is particularly sensitive to rotor power and thrust overshoot, compared to rotor torque or blade mass increase. This is consistent with the reference HAWT component *ICC* breakdown shown in table 7.4.

7.6. RESULTS

The results obtained for the rotor optimization are now presented, including explicit planform design variables (figure 7.7), obtained operational load envelope (figure 7.8) and optimizer evolution across iteration number. Figure 7.7*a* and 7.7*b* show the variation of the considered planform parameters along the span.

It can be seen the optimized chord distribution displays larger values at inboard stations, compared to the baseline (*NREL*) case. Since the blade's inboard sections have a small contribution to power production and general aerodynamic loading, it is instead argued that the increased chord values allow for a blade mass decrease, also shown in figure 7.7*d*, and hence contribute to cost reduction. This is also consistent with the optimized laminate skin thickness spanwise distribution, illustrated in figure 7.7*c*, which shows a decreased skin thickness at inboard stations compared to the baseline turbine. Recalling expressions 7.5 to 7.6, one can understand how a chord increase (figure 7.7*a*) allows a laminate

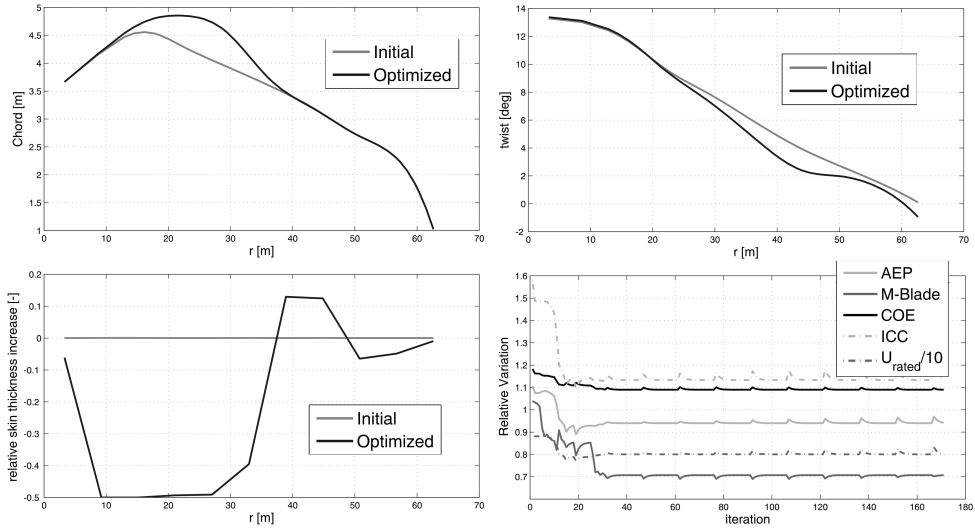


Figure 7.7: Optimization Results - Planform Variables Evolution

thickness and blade mass decrease, while ensuring sectional stiffness. The increased laminate thickness towards the outboard region, at approximately $r/R = 0.75$, is also attributed to stiffness requirements, specifically because the tip deflection is most efficiently reduced if new material is added nearing the outboard region of the blade. Despite the consistency regarding optimized chord and laminate thickness distribution towards reduced COE , it is noted the inboard chord decrease may be a consequence of the optimization scheme and not strictly characteristic of the ASC rotor. Specifically, it may be argued that if a more detailed structural analysis was carried out, particularly including blade buckling, the result shown in figure 7.7a could become unfeasible.

Figure 7.7b illustrates the twist spanwise distribution. Compared to the initial blade, the optimized planform has smaller twist angle at the outboard stations. This means the optimization locally increases the operational angle of attack, effectively inducing aerodynamic stall at the blade sections. Moreover, and referring to figure 7.3, the increase in operational angle of attack can also be explained as the optimization scheme brings the airfoil section to the AOA which provides the largest actuation induced ΔC_l .

Figure 7.8a shows the initial and optimized power curve, across the operational wind speeds. The power curve of the pitch-controlled *NREL* machine is also shown for comparison. It can be seen that throughout the optimization, the employed algorithm significantly decreases the maximum power, which results in a decreased power overshoot and hence decreases the modeled turbine ICC , also shown in figure 7.7d. Compared to the baseline pitch-controlled machine, the optimized active-stall controlled HAWT shows equivalent power capture at wind speeds below $U = 12\text{ m/s}$, as opposed to larger wind speeds at which increased power is captured with the optimized ASC HAWT. All in all, the expected AEP of the active-stall controlled machine is smaller than for a pitch-controlled machine, as illus-

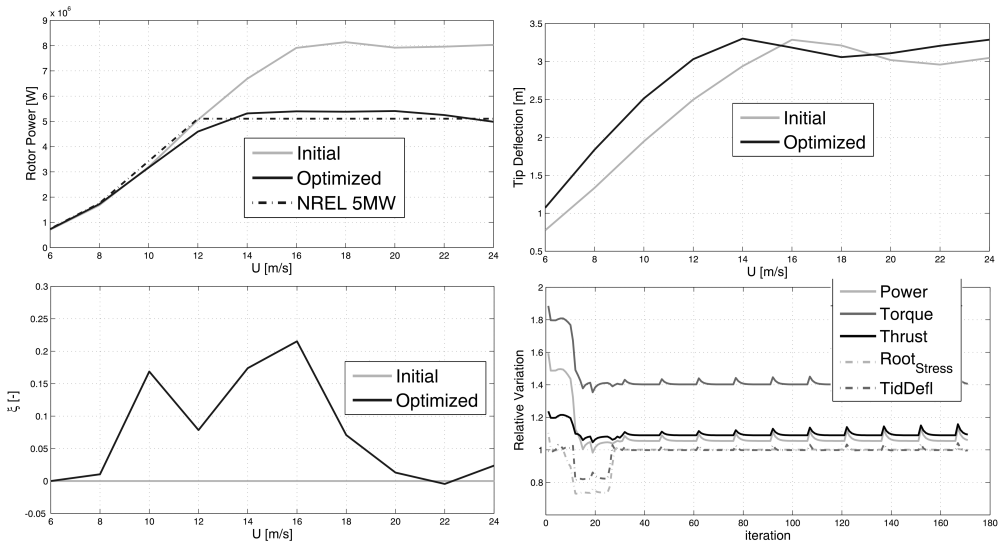


Figure 7.8: Optimization Results - Operational Load Envelope

trated in figure 7.7*d*.

Figure 7.8 shows flow control actuation is used to trim the loads at relatively high wind speeds (14-16 m/s). At larger wind speeds actuation is less used as the stalled blade sections naturally produce smaller lift and hence power and torque overshoots. Overall, and keeping figure 7.6 in mind, it is understandable that the optimizer opts for decreasing rotational speed, and hence limits power overshoot, while allowing large torque overshoots, since power and thrust contribute to ICC much more than torque. Finally, figure 7.8 also shows the optimized ASC rotor meets structural load constraints, as blade tip deflection and blade root stress match the *NREL* reference values after iteration 30.

7.7. DISCUSSION AND COE

The current ASC rotor optimization study includes the AEP and the cost of the turbine components. However, (at least) three factors are not explicitly considered. Namely the variation in pitch system cost, variation in operational costs and the initial capital cost of the actuation system and its components.

With a HAWT machine employing ASC to regulate power above rated wind speed, the pitch system could be used in emergency situations only. Besides being used more seldom, such a control strategy would also avoid small amplitude adjustments, which are in general detrimental [50] to the lifetime of bearing mechanisms. However, to accurately estimate the potential ICC decrease of the pitch system requires a detailed dynamic load envelope analysis [50] which is beyond the scope of the present effort. Instead the current study investigates the impact of the pitch system cost on the COE employing a parametrization of

the pitch system cost decrease, according to:

$$ICC_{PS_{ASC}} = ICC_{PS_{ref}} * f_{PS} \quad (7.18)$$

in which f_{PS} represents the *pitch system factor*, and translates the fraction by which the pitch system cost is reduced, compared to the reference NREL machine.

The effect of employing ASC on the operational costs of a HAWT is also uncertain. On one hand the reduced usage of the pitch system could in principle lead to a decrease in failure rate and hence reduced maintenance and replacement costs associated with the pitch mechanism. On the other hand, in an ASC machine there will be additional operational costs associated with the flow control actuator used for power regulation, since no actuator is maintenance free. However, it is impossible to accurately estimate how large such operational costs will be because the present study considers novel actuation types, for which effective operational failure rates and maintenance costs may only be assessed with long-term effective field testing. As such, and similarly to the pitch system ICC, the operational costs are parametrized with:

$$(OM + LRC)_{ASC} = (OM + LRC)_{ref} * f_{OC} \quad (7.19)$$

where f_{OC} denotes the factor by which operational costs may be reduced with respect to the NREL reference pitch-controlled machine.

Additionally the costs related with the actuation system (AS) itself need to be considered. Though it is possible to estimate such costs for a particular application [130], it is difficult to predict what the ICC_{AS} might become for industrial applications which benefit from actuation system unit cost decrease, due to leaner (and larger) production/manufacture processes. To tackle the issue a parametrization is also used, according to:

$$ICC_{AS} = ICC_{PS_{ref}} * f_{AS} \quad (7.20)$$

where f_{AS} is the fraction relating the initial capital cost of the actuator system (ICC_{AS}) with the reference pitch system cost ($ICC_{PS_{ref}}$).

The effect of the different cost factors on the ASC rotor COE compared to the reference NREL machine is illustrated in figure 7.9. As to investigate the range of COE one might (more) realistically expect from the proposed ASC HAWT, different cost scenarios are considered. Specifically, a very conservative scenario in which the pitch system cost is the double of the NREL machine, and the actuation system cost is the same as the NREL pitch system cost ($f_{PS} = 2$, $f_{AS} = 1$). The other scenario considered is most optimistic, assuming the pitch system and actuation system have no cost ($f_{PS} = 0$, $f_{AS} = 0$). The underlying assumption is that a reasonable estimate of the ASC machine COE lies between the two scenarios. For comparison, the COE of the reference pitch-controlled machine is also shown. Additionally, a vertical dashed line is included at $f_{OC} = 0.85$, which corresponds to the failure rate [23] of the pitch system in state-of-the-art machines, compared to other components' failure rates. As such, the vertical red line may be interpreted as an indication of the maximum OM cost reduction obtained with the ASC machine, compared with pitch controlled HAWT.

Figure 7.9 shows the ASC machine may be competitive with the reference pitch-controlled machine, even though no significant COE decrease is expected. Figure 7.9 also shows COE

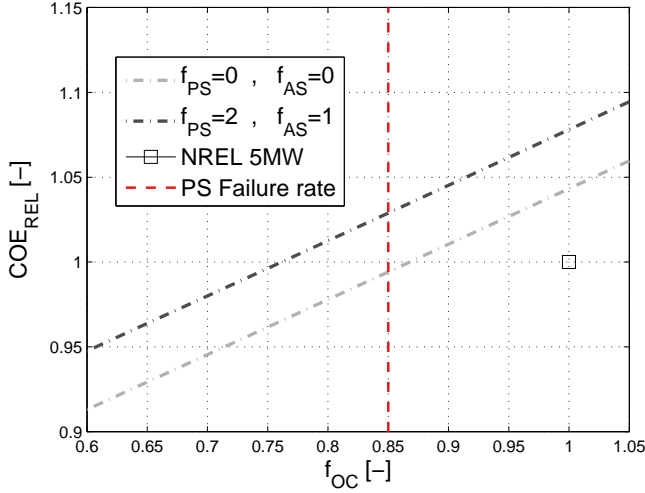


Figure 7.9: Estimated COE versus operation/maintenance f_{OC} cost, under different scenarios of actuation system f_{AS} and pitch system f_{PS} cost. Vertical dashed line indicates failure rate of state-of-the art pitch systems [23]

is very sensitive to OM costs, much more than to pitch (f_{PS}) and actuation system (f_{AS}) costs.

As a final remark, two important notes are made. Though this chapter describes a somewhat intricate optimization framework to design an ASC HAWT, a more extensive analysis is required to arrive at a definite conclusion on the economic potential of the ASC machine. Specifically, it is (at least) necessary to perform fatigue and extreme loads analysis, as well as more detailed structural modeling, namely to investigate structure instabilities such as buckling. As such, time domain (non-static) aeroelastic simulations should be performed in future studies addressing the ASC concept.

As second note, the suggestion is made for future studies to consider the employment of ASC not only for power regulation but also for (unsteady) load alleviation. Figure 7.9 shows significant COE reduction becomes possible if OM costs are decreased, which may be obtained *e.g.* from reduced load fluctuation and fatigue [12]. As such, and since the flow control actuation system in ASC HAWT is anyhow employed for regulating the power production, it may be used as well to tackle transient loads. Particularly for DBD plasma actuators, the nearly unlimited bandwidth of operation ensures the required dynamic range [11] for HAWT load alleviation and fatigue decrease is available.

7.8. CONCLUSION

This chapter describes an optimization framework, in which a HAWT rotor is tailored to ASC operation, in a static aero-structural-servo formulation. The effort includes a complex set of design variables, including planform design but also actuation scheduling, rated ro-

tational speed and spanwise laminate skin thickness.

Results show that, compared to variable-pitch turbines, ASC planform shows increased chord at inboard stations with decreased twist angle towards the tip, resulting in increased AOA. Actuation is employed to trim the loads and hence reduce load overshoots. Comparing with state-of-the-art pitch machines, the ASC rotor has decreased AEP, decreased blade mass and increased ICC.

As for the expected *COE* of the ASC rotor, the results obtained do not indicate a significant decrease compared to pitch-controlled machines, but ASC appears to be at least competitive with state-of-the-art HAWTs. Additionally, and even though not explicitly considered in the present study, ASC may become very interesting if the actuation system allows for further OM cost reduction via fatigue load-alleviation.

8

CONCLUSION

No fim de tudo dormir. No fim de quê? No fim do que tudo parece ser..., Este pequeno universo provinciano entre os astros, Esta aldeola do espaço, E não só do espaço visível, mas até do espaço total.

Álvaro de Campos (Fernando Pessoa)

8.1. CONCLUSIONS

This dissertation studies the concept of modern active stall control ASC for large HAWTs. Starting with a feasibility study, and addressing both ASC airfoil and rotor planform design. Regarding the active flow control system, emphasis was put on characterization and modeling of AC-DBD plasma actuators, since this type of actuation sparked greater interest when compared to other flow control devices.

A preliminary study on ASC for large-scale HAWT (**chapter 2**) showed the concept is feasible only if the blade and the airfoils are designed from the beginning to incorporate AFC devices. Additionally, the preliminary study also highlighted the need to investigate DBD actuator performance and modelling in a HAWT environment. As such, three studies (chapters 3, 4 and 5) were carried out, addressing specific aspects of DBD actuation.

Chapter 3 investigated the effect of external flow velocity on DBD performance, particularly on DBD actuation momentum transfer to air. Experimental results captured smaller actuation forces at low free stream velocities ($U \leq 20 \text{ m/s}$) due to wall friction effects, but at larger velocities, up to $U = 60 \text{ m/s}$, no significant influence was measured. This results implies that for modern HAWT, and particularly for the investigated ASC machine, the effect of external flow on DBD thrust may be neglected. However, by using a semi-analytical model, extrapolation to larger velocities indicates up to 15% variation in DBD actuator thrust for $U = 200 \text{ m/s}$. The second study concerning DBD actuation addresses the frequency response of actuator region flow, corresponding to **chapter 4**. The developed methodology describes the local flow response to actuation in *pulse mode*, which has often been proposed for HAWT applications [130] [109]. Though simple, the proposed LTI approach may in principle be used to design and optimize AFC systems in different flow control scenarios. **Chapter 5** contributes to further enhance design and optimization possibilities of DBD actuation, by incorporating DBD plasma effects in an airfoil design code. An IBL formulation including DBD plasma effects is introduced, valid for turbulent, incompressible flow applications, and as such directly relevant to modern HAWT employment. Experimental results of an airfoil equipped with DBD actuation compare reasonably with the model data. As such, the proposed formulation allows to incorporate DBD actuation effects in the airfoil design process, which ultimately enables more efficient AFC employment in general, and is of particular relevance to investigate the ASC concept.

Building on the DBD actuation insight from chapters 3, 4 and 5, the design of an ASC rotor was addressed in chapters 6 and 7. Specifically, **chapter 6** provides a methodology to design airfoils, which incorporates AFC effects (chapter 5) on aerodynamic performance. The airfoil design methodology relies on a multi-objective genetic algorithm [31], which in this case is formulated to evaluate 2 distinct cost functions. The two cost functions represent WE performance and actuation suitability, and thus the optimized airfoil sections are simultaneously tailored to WE performance and actuation employment. Results show WAP sections have similar geometric features to reference WE airfoils, and show comparable WE performance. Results also show WAP sections enable more efficient AFC employment than reference WE airfoils, with energetic actuation efficiency 2 to 4 times larger. Ultimately, the novel airfoil sections provide larger control authority (ΔC_l) at smaller actuation power con-

sumption, and thus allow for novel HAWT control strategies to be conceived, including ASC. Within the context of this dissertation, it is noted that if pulse actuation (chapter 4) would be included in the airfoil design process, it is anticipated even more efficient (lower power consumption) WAP sections could be obtained. The final step in the investigation of the ASC concept is the design of the ASC rotor, as presented in **chapter 7**. The ASC rotor design includes blade planform geometry, blade laminate thickness, actuation scheduling and rotational speed. As such, the control strategy design and rotor blade design are coupled, while blade structural constraints are met, in an integrated gradient-based optimization loop. The ASC rotor blades include the WAP sections (chapter 6), as to ensure efficient actuation employment. Results show that, compared to the reference pitch-controlled machine, the ASC rotor has decreased twist towards the outboard sections, such that the optimized rotor blades favor aerodynamic stall at larger wind speeds. Additionally results demonstrate the actuation employment is successfully scheduled throughout the operational wind speed envelope, thus trimming aerodynamic loads and ultimately limiting HAWT component cost. Results also show the expected *COE* of the optimized ASC HAWT is comparable to the pitch-controlled machine, particularly if the OM cost decreases from mitigating the pitch system. Overall, it was found the expected *COE* depends heavily on the OM cost, which may be cumbersome to estimate. Nevertheless, results also indicate that if the ASC actuation system is used for load alleviation, in addition to power regulation, the resulting *COE* could be further decreased.

All in all, the present research work addressed the scientific goals as described in chapter 1, both regarding the ASC concept and DBD actuation AFC technology. Specifically, the main conclusions concerning each part (and chapter) may be stated as:

8.1.1. ASC FEASIBILITY STUDY

- A significant portion of the blades (**chapter 2**) must be actuated to regulate the aerodynamic loads across the wind speed envelope, and the actuators must be effective especially at large AOA.
- Different actuation technologies have advantages and drawbacks. BLT may produce LE stall and thus has a large authority, while TEJs yield significant changes in the lift coefficient but only in the linear region of the lift polar.
- AC-DBD plasma actuators become attractive because of simple construction, negligible mass and absence of moving parts, though more detailed research is required to assess control authority at the large Reynolds numbers being considered.
- Active stall control of HAWT appears feasible only if the blade and the airfoils are designed from the beginning to be active stall controlled.

8.1.2. DBD ACTUATOR CHARACTERIZATION AND MODELING

Regarding AC-DBD plasma actuators' performance characterization and modeling, three specific topics were investigated. The research outcome is geared towards the realization

of large scale industrial HAWT machines, as it addresses topics concerning AC-DBD performance under external flow velocities characteristic of modern HAWTs, and also AC-DBD actuator effect incorporation into an viscous-inviscid airfoil performance prediction method.

- An experimental study (**chapter 3**) showed the influence of the external flow velocity on the momentum transfer capability of DBD plasma actuators, for both counter-flow and co-flow configurations.
- Load cell measurements of the DBD plasma actuator force showed for $20\text{m/s} \leq U_\infty \leq 60\text{m/s}$ the measured force is increasing in the case of co-flow forcing, while in counter-flow forcing the measured force is nearly constant.
- The experimental load-cell data shows significant changes in the wall shear force for low free stream velocities or quiescent conditions, which suggests the actuation-induced wall jet may 'camouflage' load-cell measurements aiming at DBD thrust determination, which implies AC-DBD plasma actuators may already be stronger than previous (quiescent) studies claimed.
- The measured actuator power consumption did not change significantly with different external flow speeds, but plasma light emission showed a clear trend of increasing intensity for larger free stream velocities in the case of counter-flow forcing.
- A simple semi-analytical model was proposed to estimate the influence of the external flow velocity on the momentum transfer of DBD actuators, showing satisfactory agreement with experimental data at different external flow speeds for both co-flow and counter-flow DBD configurations.
- Extrapolation of the model to larger flow speeds indicates the DBD force varies by at least 10% as the external flow speed reaches 200 m/s , even though it is unclear whether (dynamic) pressure effects might become dominant for such large external flow velocities.

- A second study on AC-DBD actuators (**chapter 4**) addressed the frequency response of actuator-region flow to actuator induced perturbations. The application case is representative of DBD plasma operation in pulse mode, providing a semi-analytical methodology which captures experimental DBD actuation trends.
- The developed analytical model includes the effect of external flow velocity and viscosity, while employing a linearization of the Navier-Stokes equations to model the local fluid response to actuator perturbations in an LTI formulation, thus providing actuation region flow system response.
- Model results indicate the operational frequency range of the actuator increases as the external flow velocity increases. Viscosity essentially decreases the magnitude of actuator induced perturbations.

- Reasonable agreement is obtained between analytical and experimental data for a typical DBD plasma actuator, both in quiescent and laminar flow.
- Results show an efficient and simple approach towards prediction of the response of a convective flow to pulsed actuation, which might be used to design and optimize DBD actuation in different flow control scenarios.
- Still regarding DBD actuator modeling, a method (**chapter 5**) is proposed to include the influence of DBD plasma actuators in viscous-inviscid codes used for airfoil design, suited to incompressible, turbulent flows.
- The influence of the plasma body-force is modelled by performing an asymptotic expansion to the Navier-Stokes equations, and introducing additional force terms in von von Kármán integral equations.
- An experimental study of PIV measurements on an airfoil equipped with DBD plasma actuators was used for validation, and results show the proposed model captures the magnitude of the variation in IBL parameters induced by the plasma actuation.
- The modelling approach also captures the magnitude of the lift coefficient variation (ΔC_l) and the main trends related with actuation chordwise position.
- Ultimately the approach may enable the design of airfoils specifically tailored for flow control through DBD employment. Among other things, this entails potentially decreasing the power required for active flow control and actuation authority enhancement.

8.1.3. ASC DESIGN AND OPTIMIZATION

Finally addressing the design of the ASC rotor, this dissertation investigated both airfoil sections tailored to ASC and rotor planform and control strategy design. The main conclusions may be stated as:

- Novel airfoil sections (**chapter 6**) suitable to employ actuation in a WE environment (WAP) provide much higher control efficiency than adding actuation on reference WE airfoils, without detrimental effects in non-actuated operation.
- By designing the airfoils with a genetic algorithm multiobjective optimizer, formulated by setting two cost functions, the approach simultaneously considers wind energy performance and actuator employment suitability.
- The WAP geometry obtained for the two different actuation types considered, namely BLT and DBD plasma, is similar.

- Compared to reference WE airfoils, WAP sections for decreased performance have an upper surface concave aft-region, while for enhanced performance a convex upper surface aft-region is obtained.
 - The WAP sections yield an actuator employment efficiency that is 2 to 4 times larger than obtained with reference WE airfoils, at equivalent WE performance.
 - As such designing wind energy and actuation tailored airfoils may pave the way for new HAWT control strategies to become seriously considered, among which active stall control.
-
- Addressing the complete rotor planform design, a HAWT rotor was tailored to ASC operation (**chapter 7**) in an aero-structural-servo optimization study. Both blade chord and twist spanwise distribution were considered in the design, and also actuation scheduling, rated rotational speed and spanwise laminate skin thickness.
 - Since the optimizer uses a gradient-based algorithm for searching the solution, different initial design points were considered for the optimization cases in an effort to broadly explore the design space, though no claims are made on the globality of optimal solution found.
 - Compared to variable-pitch turbines, ASC planform displays increased chord at in-board stations with decreased twist angle towards the tip, resulting in increased AOA. Actuation is employed to trim the loads across the operational wind speed envelope and hence reduce load overshoots and associated costs.
 - Comparing with state-of-the-art pitch machines, the expected COE of the ASC rotor does not indicate a significant decrease, but appears to be at least competitive with pitch-controlled HAWTs if the pitch system is effectively mitigated.
 - It is foreseen ASC might become cost-effective if the actuation system would allow for further OM cost reduction via fatigue load-alleviation, besides power regulation for ASC.

8.2. RECOMMENDATIONS

From challenges faced and ideas appearing throughout this research process, some suggestions for future work are provided below:

As a general recommendation, and though stated before, it is suggested that holistic design approaches are used as much as possible. Otherwise valid design solutions are

often discarded too early. Additionally, it is important to have clear design objectives and critically assess the underlying cause of results obtained with different optimization schemes, making sure the intended design objectives are met.

Though chapter 4 provides a simple approach to predict local flow response to pulsed actuation, care has to be taken for large pulse frequencies. Higher-order modeling of the fluid region under actuation is expected to provide better agreement at higher pulse frequencies and as such future research could attempt it.

Another suggestion for future research could be to expand the application of the LTI approach developed in chapter 4 to turbulent flows. This would greatly expand the range of flow control scenarios that could be directly addressed with an LTI approach, namely including modern HAWT applications.

Experiments with DBD actuators provide (at least) two recommendations. Avoid using *Teflon* as dielectric material and verify constant actuator spanwise configuration. Otherwise, this author believes electric current concentration may lead to much faster localized dielectric breakdown and consequent experimental frustration.

Future research could expand the effort shown in chapter 5 to include pulsed actuation of DBD actuators in an IBL framework. Even though the path to go about it is not trivial, this would potentially allow for the design of more efficient airfoils. Pulse operation of DBD actuation is normally the case of real application for HAWTs, more energetically efficient and probably leads to an increased actuator lifetime compared to constant schedule DBD actuation.

More generically, the call is made for better modeling of airfoil stall. Although many fine aerodynamicists have met frustration in trying to tackle stall analytically, a more direct, empirical path is suggested. The accuracy of predicting the maximum lift coefficient C_{lMAX} would be directly increased if viscous-inviscid methods are calibrated for different Reynolds numbers.

It is also suggested that future efforts may employ WAP methodology to conceive novel HAWT control strategies and correspondent airfoils, *e.g.* tailored for load-alleviation [120] or increased HAWT power capture [130] (somewhat similar to the *enhanced performance* WAP).

Though chapter 7 estimated the COE of the ASC concept compared to the reference pitch machine, more dedicated cost modeling is suggested. Particularly, a more accurate estimation of the OM costs in a HAWT machine with decrease employment of pitch-system, such as ASC, might be obtained by modeling pitch system mechanism and bearings' damage [50].

Beyond the ASC rotor optimization presented in chapter 7, the final ASC rotor blade

should be checked for structural instabilities, particularly for failure under buckling, since the ASC rotor experiences a larger operational envelope than the reference pitch-controlled machine.

A combination of the ASC rotor with the passive stall control concept appears extremely interesting. Specially if blade bend-twist coupling is tailored together with ASC scheduling to control the loads across larger operational envelopes. Future efforts could attempt at merging the two HAWT control strategies to arrive at a potentially cost-efficient machine.

A final suggestion for future research would be to investigate an ASC concept to perform also load trimming aimed at fatigue load alleviation. Such a HAWT concept would be more distant from a sturdy passive-stall control [39] machine and instead share features with the "Smart-Rotor" concept [11]. It is envisioned the cost-effectivity of such a machine relies on the trade-off between added rotor complexity and the fatigue load alleviation capability, and their impact on OM costs.

BIBLIOGRAPHY

- [1] IEC 61400-1 ed3: Wind turbines - part 1: Design requirements. Technical report, International Electrotechnical Commission, 2005.
- [2] T. Abe, Y. Takizawa, S. Sato, and N. Kimura. Experimental study for momentum transfer in a dielectric barrier discharge plasma actuator. *AIAA Journal*, 46(9):2248–2256, 2008.
- [3] D. E. Ashpis, M. C. Laun, and E. L. Griebeler. Progress toward accurate measurements of power consumptions of DBD plasma actuators. In *50th AIAA Aerospace Sciences Meeting Including the New Horizons Forum and Aerospace Exposition*, 2012.
- [4] M. Atkinson, J. Poggie, and J. Camberos. Control of high-angle-of-attack reentry flow with plasma actuators. *Journal of Spacecraft and Rockets*, 50(2):337–346, 2013.
- [5] T. Barlas. *Active aerodynamic load control on wind turbines: Aeroservoelastic modeling and wind tunnel experiments*. PhD Dissertation, TUDelft, 2011.
- [6] T. Barlas and G. van Kuik. Review of state of the art in smart rotor control research for wind turbines. *Progress in Aerospace Sciences*, 46:1–27, 2010.
- [7] E. Battle, R. Pereira, and M. Kotsonis. Airfoil stall hysteresis control with dbd plasma actuation. *55th AIAA Aerospace Sciences Meeting, AIAA Science and Technology Forum and Exposition, Grapevine, TX*, 2017 - Control ID: 2551726.
- [8] J. Baughn, C. , B. Peterson, T. McLaughlin, C. Enloe, G. Font, and C. Baird. Momentum transfer for an aerodynamic plasma actuator with and imposed boundary layer. *44th AIAA Aerospace Sciences Meeting and Exhibit*, 2006-168.
- [9] N. Benard and E. Moreau. Capabilities of the dielectric barrier discharge plasma actuator for multi-frequency excitations. *Journal of Physics D: Applied Physics*, 43(14), 2010.
- [10] E. Benini and A. Toffolo. Optimal design of horizontal-axis wind turbines using blade-element theory and evolutionary computation. *Journal of Solar Energy Engineering*, 124:357–363, 2002.
- [11] L. Bergami. *Smart Rotor Modelling - Aero-Servo-Elastic Modeling of a SmartRotor with Adaptive Trailing Edge Flaps*. Springer, 2014.

- [12] L. Bernhammer. *Smart Wind Turbine : Analysis and Autonomous Flap*. PhD Dissertation, TUDelft, 2015.
- [13] F. Bertagnolio, N. Sorensen, J. Johansen, and P. Fuglsang. Wind turbine airfoil catalogue - R-1280. Technical report, Ris, 2001.
- [14] M. Birsanu. Aerodynamic tip design of a wind turbine equipped with boundary layer suction. Master's thesis, TUDelft, 2011.
- [15] M. Blaylock, R. Chow, A. Cooperman, and C. van Dam. Comparison of pneumatic jets and tabs for active aerodynamic load control. *Wind Energy*, DOI: 10.1002/we.1638, 2013.
- [16] P. Bletzinger, B. N. Ganguly, D. Van Wie, and A. Garscadden. Plasmas in high speed aerodynamics. *Journal of Physics D: Applied Physics*, 38(4):R33–R57, 2005.
- [17] C. Boeijs, H. de Vries, I. Cleine, E. van Emden, and G. Zwart. Fluidic load control for wind turbine blades. *47th AIAA Aerospace Sciences Meeting*, Orlando, Florida, 2009.
- [18] C.L. Bottasso, F. Campagnolo, A. Croce, and C. Tibaldi. Optimization-based study of bend twist coupled rotor blades for passive and integrated passive/active load alleviation. *Wind Energy*, 16:1149–1166, 2012.
- [19] BOW. <http://www.4coffshore.com/windfarms/barrow-united-kingdom-uk01.html>.
- [20] W. W. Bower, J. T. Kegelman, A. Pal, and G. H. Meyer. A numerical study of two-dimensional instability-wave control based on the Orr–Sommerfeld equation. *Physics of Fluids*, 30(4):998–1004, 1987.
- [21] V. Brederode. Fundamentos de aerodinâmica incompressível. *Instituto Superior Técnico, Lisbon*, 1997.
- [22] M. Brunner, M. Blaylock, A. Cooperman, and C. van Dam. Comparison of CFD with wind tunnel tests of microjets for active aerodynamic load control. In *50th AIAA Aerospace Sciences Meeting, Nashville, Tennessee*, 2012.
- [23] B. Bulder, H. Hendricks, P. van Langen, C. Lindenburg, H. Snel, P. Bauer, H. Polinder, R. van Rooij, H. Subroto, and M. Zaayer. The ICORASS feasibility study. Technical report, ECN - E-07-010, 2007.
- [24] M. Capellaro. *Aeroelastic Design and Modeling of Ben Twist Coupled Wind Turbine Blades*. PhD thesis, University Stuttgart, 2013.
- [25] L. N. Cattafesta and M. Sheplak. *Actuators for active flow control*, volume 43 of *Annual Review of Fluid Mechanics*. 2011.
- [26] P. Chassaing, R. Antonia, F. Anselmet, L. Joly, and S. Satrkar. *Variable Density Fluid Turbulence*. Springer, 2002.

- [27] R. D. Cook and W. C. Young. *Advanced Mechanics of Materials*. Macmillan, 1985.
- [28] T. C. Corke, M. L. Post, and D. M. Orlov. SDBD plasma enhanced aerodynamics: concepts, optimization and applications. *Progress in Aerospace Sciences*, 43(7-8):193–217, 2007.
- [29] J. Cousteix and J. Mauss. *Asymptotic Analysis and Boundary Layers*. Springer, 2007.
- [30] A. Cristofolini, C. A. Borghi, and G. Neretti. Charge distribution on the surface of a dielectric barrier discharge actuator for the fluid-dynamic control. *Journal of Applied Physics*, 113(14), 2013.
- [31] G. de Oliveira. Wind turbine airfoils with boundary layer suction: A novel design approach. Master's thesis, TUDelft, 2011.
- [32] G. de Oliveira, R. Pereira, D. Ragni, and M Kotsonis. Modeling DBD plasma actuators in integral boundary layer formulation for application in panel methods. *AIAA - Fluid Dynamics Conference (Submitted)*, 2015.
- [33] E. de Vries. Two blades - condor wind's 5MW offshore turbine. *WINDPOWER*, <http://www.windpowermonthly.com/article/1073749/two-blades—condor-winds-5mw-offshore-turbine>, 2011.
- [34] A. Dialoupis. Active flow control using plasma actuators - application on wind turbines. Master's thesis, TUDelft, 2014.
- [35] M. Drela and M. Giles. Viscous-inviscid analysis of transonic and low reynolds number airfoils. *AIAA*, 25:1347–1355, 1987.
- [36] D. M. Eggleston and F. S. Stoddard. *Wind Turbine Engineering Design*. van Nostrand Reinhold, 1987.
- [37] R. J. Englar. Circulation control pneumatic aerodynamics: Blown force and moment augmentation and modification; past, present and the future. *AIAA Journal*, 2000.
- [38] C. L. Enloe, M. G. McHarg, and T. E. McLaughlin. Time-correlated force production measurements of the dielectric barrier discharge plasma aerodynamic actuator. *Journal of Applied Physics*, 103(7), 2008.
- [39] E. Ferede, M. Abdalla, and G.J.W. van Bussel. Isogeometric framework for aeroelastic wind turbine rotor analysis. *Wind Energy*, (Submitted), 2016.
- [40] J. Ferry and J. Rovey. Thrust measurement of dielectric barrier discharge plasma actuators and power requirements for aerodynamic control. *5th Flow Control Conference*, 43:917–928, 2010.
- [41] L. Fingersh, M. Hand, and A Laxson. Wind turbine design cost and scaling model - tp-500-40566. Technical report, NREL, 2006.

- [42] M. Forte, J. Jolibois, J. Pons, E. Moreau, G. Touchard, and M. Cazalens. Optimization of a dielectric barrier discharge actuator by stationary and non-stationary measurements of the induced flow velocity: Application to airflow control. *Experiments in Fluids*, 43(6):917–928, 2007.
- [43] P. Fuglsang and H. Madsen. Optimization method for wind turbine rotors. *Journal of Wind Engineering and Industrial Aerodynamics*, 80:191206, 1999.
- [44] M. Gad-el Hak. *Flow Control - Passive, Active and Reactive Flow Management*. Cambridge University Press, 2006.
- [45] R. Gasch and J. Twele. *Wind Power Plants: Fundamentals, Design, Construction and Operation*. Teubner-Verlag, 2007.
- [46] B. Gibson. Laminar flow control of a flat plate boundary layer using dielectric barrier discharge plasma. *PhD dissertation, University of Adelaide*, 2012.
- [47] D. Greenblatt, A. Ben-Harav, and H. Mueller-Vahl. Dynamic stall control on a vertical-axis wind turbine using plasma actuators. *AIAA Journal*, 52(2):456–462, 2014.
- [48] S. Grundmann and C. Tropea. Active cancellation of artificially introduced Tollmien-Schlichting waves using plasma actuators. *Experiments in Fluids*, 44(5):795–806, 2008.
- [49] K Hall, E. Jumper, T. Corke, and T. McLaughlin. Potential flow model of a plasma actuator as a lift enhancement device. *43rd AIAA Aerospace Sciences Meeting and Exhibit*, page 0783, 2005.
- [50] T. Harris, J.H. Rumbarger, and C.P. Butterfield. Wind turbine design guideline dg03: Yaw and pitch rolling bearing life - nrel tp-500-42362. Technical report, NREL, 2009.
- [51] J. Hennessey. Some aspects of wind power statistics. *Applied Meteorology*, 16:119–128, 1977.
- [52] G. Hernandez. Laminar-turbulent transition on wind turbines. *PhD Dissertation, DTU*, 2011.
- [53] [http://www.ewea.org/fileadmin/files/library/publications/statistics/EWEA Annual-Statistics-2014.pdf](http://www.ewea.org/fileadmin/files/library/publications/statistics/EWEA%20Annual-Statistics-2014.pdf).
- [54] W. Hu, D. Park, and D. Choi. Structural optimization procedure of a composite wind turbine blade for reducing both material cost and blade weight. *Engineering Optimization*, 45:1469–1487, 2013.
- [55] P. Huerre and P. Monkewitz. Local and global instabilities in spatially developing flows. *Annual Review of Fluid Mechanics*, 22:473–537, 1990.

- [56] P. Jamieson, A. Bowles, A. Derrick, and D. Leithead. Innovative concepts for aerodynamic control of wind turbine rotors. *Journal of Wind Engineering and Industrial Aerodynamics*, 39:395–404, 1992.
- [57] B. Jayaraman and W. Shyy. Modeling of dielectric barrier discharge-induced fluid dynamics and heat transfer. *Progress in Aerospace Sciences*, 44(3):139–191, 2008.
- [58] B. Jayaraman, S. Thakur, and W. Shyy. Modeling of fluid dynamics and heat transfer induced by dielectric barrier plasma actuator. *Journal of Heat Transfer*, 129:517–525, 2007.
- [59] S. Johnson, C. van Dam, and D. Berg. Active load control techniques for wind turbines. Technical report, SANDIA - SAND2008-4809, 2008.
- [60] J. Jonkman, S. Butterfield, W. Musial, and G. Scott. Definition of a 5-mw reference wind turbine for offshore system development. Technical report, NREL-TP500-38060, 2009.
- [61] R. Jousset, A. Leroy, R. Weber, H. Rabat, S. Loyer, and D. Hong. Plasma morphology and induced airflow characterization of a DBD actuator with serrated electrode. *Journal of Physics D: Applied Physics*, 46(12), 2013.
- [62] T. N. Jukes and K. . Choi. Dielectric-barrier-discharge vortex generators: characterisation and optimisation for flow separation control. *Experimental Fluids*, 52:329–345, 2012.
- [63] T. N. Jukes, K. . Choi, G. A. Johnson, and S. J. Scott. Turbulent drag reduction by surface plasma through spanwise flow oscillation. In *3rd AIAA Flow Control Conference*, volume 3, pages 1687–1700, 2006.
- [64] T. N. Jukes, K. . Choi, T. Segawa, and H. Yoshida. Proceedings of the institution of mechanical engineers, part I. *Journal of Systems and Control Engineering*, 222:347, 2008.
- [65] J.C. Kaimal, J.C. Wyngaard, Y. Izumi, and O.R. CotSpectral characteristics of surface-layer turbulence. *Journal Meteorological Society*, 98:563–589, 1972.
- [66] E. Kerschen. Boundary layer receptivity theory. Technical report, Air Force Office Scientific Research, 1993.
- [67] M. Kotsonis. Dielectric barrier discharge actuators for flow control - diagnostics, modeling , application. *PhD Dissertation, TUDelft*, 2012.
- [68] M. Kotsonis and S. Ghaemi. Experimental and numerical characterization of a plasma actuator in continuous and pulsed actuation. *Sensors and Actuators, A: Physical*, 187:84–94, 2012.
- [69] M Kotsonis, S Ghaemi, L Veldhuis, and F Scarano. Measurement of the body force field of plasma actuators. *Journal of Physics D: Applied Physics*, 44:045204, 2011.

- [70] M. Kotsonis, R. Giepmans, S. Hulshoff, and L. Veldhuis. Numerical study of the control of tollmien-schlichting waves using plasma actuators. *AIAA Journal*, 51:DOI: 10.2514/1.J051766, 2013.
- [71] M. Kotsonis and L. Veldhuis. Experimental study on dielectric barrier discharge actuators operating in pulse mode. *Journal of Applied Physics*, 108:113304, 2010.
- [72] J. Kriegseis, A. Duchmann, C. Tropea, and S. Grundmann. On the classification of dielectric barrier discharge plasma actuators: A comprehensive performance evaluation study. *Journal of Applied Physics*, 114(5), 2013.
- [73] J. Kriegseis, S. Grundmann, and C. Tropea. Power consumption, discharge capacitance and light emission as measures for thrust production of dielectric barrier discharge plasma actuators. *Journal of Applied Physics*, 110:013305, 2011.
- [74] J. Kriegseis, S. Grundmann, and C. Tropea. Airflow influence on the discharge performance of dielectric barrier discharge plasma actuators. *Physics of Plasmas*, 19(7), 2012.
- [75] B. Kulfan. Universal parametric geometry representation method - CST. *45th Aerospace Sciences Meeting and Exhibit AIAA, Reno, Nevada* - <http://dx.doi.org/10.2514/6.2007-62>, 2007.
- [76] A. Kuryachi, D. Rus'yanov, and S. Chernyshev. Modeling the system of electro-gasdynamic final-control elements. *Fluid Dynamics*, 46:764–774, 2010.
- [77] J.C. Lagarias, J.A. Reeds, M.H. Wright, and P.E. Wright. Convergence properties of the nelder-mead simplex method in low dimensions. *SIAM Journal of Optimization*, 9:112–147, 1998.
- [78] V. Lago, R. Jousot, and J. . Parisse. Influence of the ionization rate of a plasma discharge applied to the modification of a supersonic low reynolds number flow field around a cylinder. *Journal of Physics D: Applied Physics*, 47(12), 2014.
- [79] G. Larsen, W. Bierbooms, and S. Hansen. Mean gust shapes - r-1133. Technical report, RISO, 2003.
- [80] J. Larsen, S. Nielsen, and S Krenk. Dynamc stall models for wind turbine airfoils. *Journal of Fluids and Structures*, 23, 2007.
- [81] J. Leishman. Challenges in modeling the unsteady aerodynamics of wind turbines. *21st ASME Wind Energy Symposium*, Reno,NV, 2002.
- [82] J. Leishman. *Principles of Helicopter Aerodynamics*. Cambridge Aerospace Series, 2006.
- [83] S. B. Leonov. Review of plasma-based methods for high-speed flow control. In *AIP Conference Proceedings*, volume 1376, pages 498–502, 2011.

- [84] R. Liebeck. On the design of subsonic airfoils for high lift. *AIAA 9th Fluid and Plasma Dynamics Conference*, pages No.76–406, 1976.
- [85] A. V. Likhanskii, M. N. Shneider, S. O. MacHeret, and R. B. Miles. Modeling of dielectric barrier discharge plasma actuator in air. *Journal of Applied Physics*, 103(5), 2008.
- [86] A. V. Likhanskii, M. N. Shneider, D. F. Opaits, R. B. Miles, and S. O. Macheret. Numerical modeling of dbd plasma actuators and the induced air flow. In *38th AIAA Plasmadynamics and Lasers Conference*, volume 2, pages 1060–1072, 2007.
- [87] C. Lindenburg. Aeroelastic modelling of the LMH64-5 blade - DOWEC. Technical report, Energy Research Center of the Netherlands, 2002.
- [88] D. Lobitz. Flutter speed predictions for mw-sized wind turbine blades. *Sandia National Laboratories*, 2004.
- [89] J. Lousberg. Boundary layer control in wind turbine blade design. Master's thesis, TUDelft, 2008.
- [90] P. Lundsager. Interim report on the measurements on the gedser windmill. *Gedser Test Group*, 1978.
- [91] j. Manwell, J. McGowan, and A. Rogers. *Wind Energy Explained-Theory, Design and Application*. John Wiley and Sons, 2002.
- [92] F. Massines, A. Rabehi, P. Decomps, R. Ben Gadri, P. Ségur, and C. Mayoux. Experimental and theoretical study of a glow discharge at atmospheric pressure controlled by dielectric barrier. *Journal of Applied Physics*, 83(6):2950–2957, 1997.
- [93] L. G. McKnight. Drift velocities and interactions of negative ions in oxygen. *Physical Review A*, 2(3):762–770, 1970.
- [94] H. Meier and Bradshaw P. *Perspectives in Turbulence Studies*. 1987.
- [95] L. Mihet-Popa and V. Groza. Modeling and simulation of a 12 mw active-stall constant-speed wind farm. DOI: 10.5772/17397, 2011.
- [96] E. Moreau. Airflow control by non-thermal plasma actuators. *Journal of Physics D: Applied Physics*, 40(3):605–636, 2007.
- [97] E. Morgan, M. Lackner, R. Vogel, and L. Baise. Probability distributions for off-shore wind speeds. *Energy Conversion and Management*, 52:15–26, 2011.
- [98] A. P. Nagy. *Isogeometric Design Optimisation*. PhD thesis, TUDelft, 2011.
- [99] R. N. Nelson, T. Corke, H. Othman, M. Patel, and T Vasudevan, S. Ng. A smart wind turbine blade using distributed plasma distributed plasma actuators for improved performance. In *46th Aerospace Sciences Meeting, Nevada*, 2008.

- [100] D. M. Orlov, T. Apker, C. He, H. Othman, and T. C. Corke. Modeling and experiment of leading edge separation control using sdbd plasma actuators. 15:10651–10668, 2007.
- [101] D. M. Orlov, G. I. Font, and D. Edelstein. Characterization of discharge modes of plasma actuators. *AIAA Journal*, 46(12):3142–3148, 2008.
- [102] OWEZ. Windpark egmond aan zee / noordzeewind official website.
- [103] S. Pavon, DorierJ-L, Ch. Hollenstein, P. Ott, and P. Leyland. Effects of high-speed airfoils on a surface dielectric barrier discharge. *IOP-Journal of Physics D:Applied Physics*, 40(doi:10.1088/0022-3727/40/6/021):1733–1741, 2007.
- [104] R. Pereira, D. Ragni, and M. Kotsonis. Effect of external flow velocity on momentum transfer of dielectric barrier discharge plasma actuators. *Journal Applied Physics*, 2014.
- [105] R. Pereira, W.A. Timmer, G. de Oliveira, and G van Bussel. Design of actuated airfoils for wind energy. *Wind Energy*, 2015(Submitted).
- [106] P. Poisson-Quinton and L. Lepage. Survey of french research on the control of boundary layer and circulation. 1961.
- [107] C. Porter, J. Baughn, T. McLaughlin, C. Enloe, and G. Font. Plasma actuator force measurements. *AIAA Journal*, 45:DOI: 10.2514/1.24497, 2007.
- [108] M. L. Post and T. C. Corke. Separation control on high angle of attack airfoil using plasma actuators. *AIAA Journal*, 42(11):2177–2184, 2004.
- [109] M. L. Post and T. C. Corke. Separation control using plasma actuators: Dynamic stall vortex control on oscillating airfoil. *AIAA Journal*, 44(12):3125–3135, 2006.
- [110] F. Rasmussen, J. Petersen, and H. Madsen. Dynamic stall and aerodynamic damping. *Transactions of the ASME*, 121:150–155, 1999.
- [111] T. R. Richards and H.E. Neustadter. DOE/NASA mod-oa wind turbine performance. *DOE/NASA 1004-78/13 NASA TM-78916*, 1978.
- [112] D. Rizzetta and M. Visbal. Plasma flow control simulations of a low-Reynolds number low-aspect-ratio wing. *Computers and Fluids*, 70:95–114, 2012.
- [113] J. Roth, D. M. Sherman, and S. P. Wilkinson. Electrohydrodynamic flow control with a glow-discharge surface plasma. *AIAA journal*, 38(7):1166–1172, 2000.
- [114] H. Schlichting. Boundary layer theory. *McGraw-Hill, New York*, 1947.
- [115] A. Seifert, A. Darabi, and I. Wygnanski. Delay of airfoil stall by periodic excitation. *AIAA Journal*, 33, 1996.
- [116] A. Seifert, D. Greenblatt, and I. J. Wygnanski. Active separation control: An overview of Reynolds and Mach numbers effects. *Aerospace Science and Technology*, 8(7):569–582, 2004.

- [117] W.Z. Shen, R. Mikkelsen, J.N. Sorensen, and C. Bak. Tip loss corrections for wind turbine computations. *Wind Energy*, 8:457–475, 2005.
- [118] W. Sheng, R. Galbraith, and F. Coton. A modified dynamic stall model for low mach numbers. *Journal of Solar Engineering*, 130:031013–1/031013–10, 2008.
- [119] K. Singh and S. Roy. Force approximation for a plasma actuator operating in atmospheric air. *Journal of Applied Physics*, 103:013305, 2008.
- [120] J. Smit, L.O. Bernhammer, S.T. Navalkar, L. Bergami, and M. Gaunaa. Sizing and control of trailing edge flaps on a smart rotor for maximum power generation in low fatigue wind regimes. *Wind Energy*, doi: 10.1002/we.1853., 2015.
- [121] A.M.O. Smith and N. Gamberoni. Transition, pressure gradient, and stability theory. Technical report, Douglas Aircraft Co., Rep ES 26388, 1956.
- [122] D. J. L. Smith. Turbulent boundary layer theory and its application to blade profile design - cp no 868. *Ministry of Aviation, Aeronautical Research Council*, 1966.
- [123] H. Snel, R. Houwink, G.J.W. van Bussel, and A. Bruining. Sectional prediction of 3D effects for stalled flow on rotating blades and comparison with measurements. In *Proceedings of the European Community Wind Energy Conference*, Lubeck-Travemunde, Germany, 8-12 March 1993, pp. 395-399.
- [124] H. Snel and J.G. Schepers. Engineering models for dynamical inflow phenomena. *Journal of Wind Engineering and Industrial Aerodynamics*, 39:267–281, 1992.
- [125] D Sontag. *Mathematical control theory: Deterministic finite dimensional systems*. ISBN 0-387-984895(Springer), 1998.
- [126] B Stratford. Flow in the laminar boundary layer near separation. *Royal Aircraft Establishment*, R. & M. No. 3002, 1954.
- [127] B. Stratford. The prediction of separation of the turbulent boundary layer. Technical report, National Gas Turbine Establishment, Farnborough, 1958.
- [128] T.W. Swafford. Analytical approximation of two-dimensional separated turbulent boundary-layer velocity profiles. *AIAA Journal*, 21:923926, 1983.
- [129] M. Tanaka, K. Amemori, H. Matsuda, N. Shimura, H. Yasui, and T. Osako. Field test of plasma aerodynamic controlled wind turbine. *EWEA Conference*, 2013.
- [130] M. Tanaka, T. Osako, H. Matsuda, K. Yamazaki, N. Shimura, M. Asayama, Y. Oryu, and S. Yoshida. The world's first trial for application of plasma aerodynamic control on commercial scale turbine. *EWEA conference*, PO.ID - 005, 2014.
- [131] J Tangler and D. Somers. NREL airfoil families for hawts. Technical report, NREL, 1995.

- [132] F. Thomas, T. Corke, M. Iqbal, A. Kozlov, and D. Schatzman. Optimization of dielectric barrier discharge plasma actuators for active aerodynamic flow control. *AIAA Journal*, 47:2169–2178, 2009.
- [133] B. Thwaites. *Incompressible Aerodynamics*. Cambridge University Press, 1961.
- [134] W.A. Timmer. An overview of naca 6-digit airfoil series characteristics with reference to airfoils for large wind turbine blades. *47th AIAA Aerospace Sciences Meeting*, page 268, 2009.
- [135] M. Tucsnak and G. Weiss. Well-posed systems-the LTI case and beyond. *Automatica, International Federation of Automatic Control*, 30:1757–1779, 1987.
- [136] Y.G. Utkin, S. Keshav, J. Kim, J. Kastner, I Adamovich, and M. Samimy. Development and use of localized arc filament plasma actuators for high-speed flow control. *Journal of Physics D: Applied Physics*, 40:685–694, 2007.
- [137] J.L. van Ingen. A suggested semi-empirical method for the calculation of the boundary layer transition region. Technical report, Delft University of Technology - VTH-74, 1956.
- [138] R.P.J.O.M. van Rooij. Modification of the boundary layer calculation in rfoil for improved airfoil stall prediction. *Report IW-96087R, Institute for Wind Energy, TUDelft*, 45(5):223–236, 1996.
- [139] R.P.J.O.M. van Rooij and W.A. Timmer. Roughness sensitivity considerations for thick rotor blade airfoils. *AIAA*, 125:–0350, 2003.
- [140] R. Varney. Drift velocity of ions in oxygen, nitrogen and carbon monoxide. *Physical Review*, 89(4):708–711, 1953.
- [141] P. Veers, D. Lobitz, and G. Bir. Aeroelastic tailoring in wind-turbine blade applications. Technical report, Sandia National Labs, 1999.
- [142] L. Viterna and R.D. Corrigan. Fixed pitch rotor performance of large horizontal axis wind turbines. *DOE/NASA Workshop on Large Horizontal Axis Wind Turbines*, Cleveland, Ohio, USA, 1981.
- [143] J. Williams. Laplace transforms, problem solvers. *George Allen and Unwin, ISBN 0-04-512021-8*, 1973.
- [144] R. K. Zeytounian. *Asymptotic Modelling of Fluid Flow Phenomena*. Kluwer, 2002.

APPENDIXES

APPENDIX A - DERIVATION OF PROBABILITY FUNCTIONS FOR WAP DESIGN

Turbulence

To arrive at the probability distribution function of a perturbation in the α we de-

fine:

$$g : \delta \rightarrow \alpha_\delta \quad \wedge \quad g^{-1} : \alpha_\delta \rightarrow \delta \quad (8.1)$$

since $g \in C^1$ is a monotonic function, the probability distribution for the AOA is written as:

$$p_\alpha(\alpha) = \left| \frac{1}{g'(g^{-1}(\alpha))} \right| \cdot p_\delta(g^{-1}(\alpha)) \quad (8.2)$$

where

$$g(\delta) = \operatorname{atan}\left(\frac{1+\delta}{b}\right) - \operatorname{atan}\left(\frac{1}{b}\right) \quad \text{where } b = \lambda\mu \frac{1+a'}{1-a} \quad (8.3)$$

$$g^{-1}(\alpha) = b \tan \left[\alpha + \operatorname{atan}\left(\frac{1}{b}\right) \right] - 1 \quad (8.4)$$

$$g'(\delta) = \frac{b}{(1+\delta)^2 + b^2} \quad (8.5)$$

Wind Shear

The height a blade section experiences can be obtained with

$$h = h_0 - r \cos(\Omega t) \quad (8.6)$$

The cumulative distribution function of time can thus be expressed with:

$$CDF(t) = \frac{t}{\frac{T}{2}} \quad (8.7)$$

where T represents the period of revolution. By deriving eq. 8.7 and inserting it in 8.2, we obtain the probability of occurrence of a given wind speed due to wind shear (eq:6.10).

APPENDIX B - ON THE ASSUMPTION OF UNSTEADY FLOW IN WAP DESIGN

To assess the probability of occurrence of unsteady effects we use Kaimal's spectrum [65], defined with:

$$\frac{f S(f)}{\sigma^2} = \frac{4f \frac{L}{U_{infly}}}{\left(1 + 6f \frac{L}{U_{infly}}\right)^{\frac{5}{3}}} \quad (8.8)$$

Noticing that zero th and second order spectral moments yield the identities[79]

$$\begin{cases} E[\sigma^2(u)] = \int_0^\infty S(f) df \\ E[\sigma^2(\dot{u})] = \int_0^\infty S(f) f^2 df \end{cases} \quad (8.9)$$

Since they u and \dot{u} are uncorrelated and normally distributed, and given that their mean value is zero, the joint probability function is found with:

$$p(u, \dot{u}) = p(u) \times p(\dot{u}) \quad (8.10)$$

The representative frequency arising from instantaneous turbulence may be described by comparing u and \dot{u} with a sinusoidal oscillation, such that:

$$u(t) = A \sin(\omega t) \rightarrow \frac{f_{rep}}{2\pi} = \omega \approx \frac{\dot{u}}{u} \quad (8.11)$$

Finally by using eq:8.11 and introducing the unsteady criterium of Leishmann [82] according to which unsteady effects are present if $k > 0.05$, it is possible to compute the probability of occurrence of unsteady effects. Figure A1 shows the probability for different effective and wind speeds.

APPENDIX C - POWER CONSUMPTION ESTIMATION FOR BLT IN HAWT

The estimation of power consumption is done by referring to figure A2. Neglecting friction forces, in case blowing is applied the power removed from the rotor is estimated starting from the centrifugal acceleration:

$$a_{CF} = \Omega^2 r \quad (8.12)$$

By multiplying with the air density we can obtain the centrifugal force at a radial element:

$$dF_{CF} = \rho A \Omega^2 r dr \quad (8.13)$$

The corresponding power per unit span removed from the rotor due to centrifugal forces is estimated with:

$$dP_{CF} = \rho A \Omega^2 r V_r dr \quad (8.14)$$

Additionally to the centrifugal force, the Coriolis force also extracts energy from the rotor. The magnitude of the Coriolis acceleration is :

$$a_{CO} = 2\Omega V_r \quad (8.15)$$

By multiplying with the air density we can obtain the Coriolis force at a radial element:

$$dF_{CO} = 2\rho A \Omega V_r dr \quad (8.16)$$

Noticing that the Coriolis force acts in the plane normal to the rotational speed (Ω), it is possible to obtain the contribution to power by multiplying 8.16 with the radius and the rotational speed, obtaining:

$$dP_{CO} = 2\rho A \Omega^2 r V_r dr \quad (8.17)$$

Summing both Centrifugal and Coriolis contributions to the power removed per unit span, and introducing the (inner channel) mass flow rate $\dot{m}(r) = \rho A V_r$, the power consumption per blade is computed with:

$$P_{BLOW} = \int_0^{r_2} 3\dot{m}(r)\Omega^2 r dr \quad (8.18)$$

The inner channel mass flow rate is computed with

$$\begin{cases} \dot{m}(r) = \dot{m}_{TOT} \text{ if } r < r_1 \\ \dot{m}(r) = \dot{m}_{TOT} - \int_{r_1}^r \rho v_t \Omega r c(r) x_p dr \text{ if } r > r_1 \end{cases} \quad (8.19)$$

where v_t is the relative transpiration speed, and x_p is the fraction of airfoil chord over which there is transpiration, expressed by:

$$v_t = \frac{V_t}{V_{eff}} \quad , \quad x_p = \frac{X_p}{c} \quad (8.20)$$

The radial chord distribution is assumed to be:

$$c(r) = 6 - \frac{r}{15} \quad (8.21)$$

following the planform of the reference 5 MW turbine [60] for $30 < r < 60$. The variable \dot{m}_{TOT} denotes the total air mass flux in the blade's inner channel, and is calculated with:

$$\dot{m}_{TOT} = \int_0^{r_2} \rho v_t \Omega r c(r) x_p dr \quad (8.22)$$

In the case suction is considered, the pressure difference across the blade surface must be such that transpiration is promoted through the porous material. The amount of transpiration is empirically related with the pressure difference across the porous material:

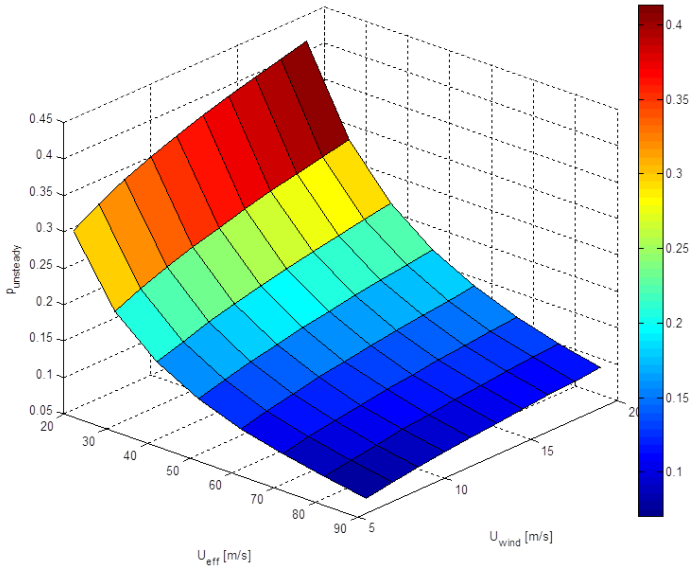
$$\Delta p_{TRANSP} = R_1 V_t^2 + R_2 V_t \quad (8.23)$$

where $R_1 \approx R_2 \approx 2000$ are typical values assumed [14] for the porous material properties. In addition, to employ suction at the outboard section of the blade, bringing the air from the tip to the root, it is necessary to overcome the (static) radial pressure gradient inside the blade::

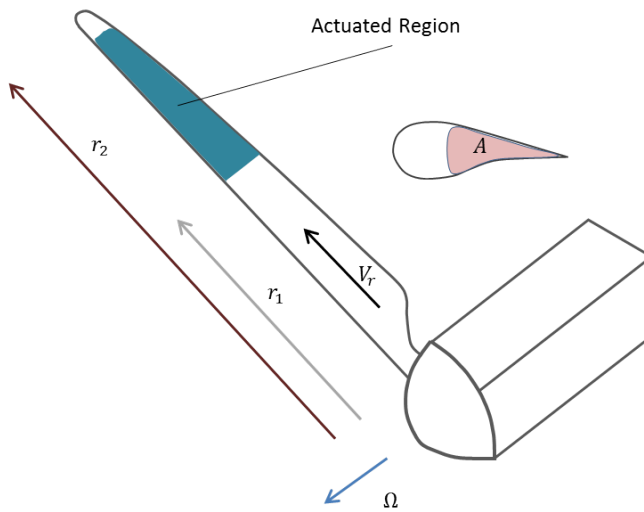
$$\frac{dp_{STATIC}}{dr} \bigg|_{STATIC} = \frac{dF_{CF}}{dr} \frac{1}{A} = \rho \Omega^2 r \quad (8.24)$$

The power per unit span required to perform suction is computed by summing the pressure difference required for transpiration (eq:8.23) and the static radial pressure (eq:8.24) and subtracting the power added (eq:8.17) to the rotor by the Coriolis force, which in this case contributes to the rotor rotation. This is expressed by:

$$P_{SUC} = \int_0^{r_2} \left(\frac{R_1 \Omega^2 r^2 v_t^2 + R_2 \Omega r v_t}{\rho} + \Omega^2 r - 2\Omega^2 r \right) \dot{m}(r) dr \quad (8.25)$$



A1 - Probability of Occurrence of Unsteady Effects



A2 - Sketch defining variables for the Power Consumption

LIST OF SCIENTIFIC CONTRIBUTIONS

Contributions in Conference Proceedings:

Pereira, R., van Bussel, G. J. W., and Timmer, W. A. (2014). *Active stall control for large offshore horizontal axis wind turbines; a conceptual study considering different actuation methods* In Journal of Physics: Conference Series (Vol. 555, No. 1, p. 012082). IOP Publishing.

Pereira, R., Ragni, D. and Kotsonis, M., *The effect of external flow velocity on the momentum transfer of DBD plasma actuators*, AIAA 43rd Fluid Dynamics Conference, California, June 2013,doi: 10.2514/6.2013-2493

Pereira, R., van Bussel, G.J.W. and Timmer, W.A., *HAWT Optimization Including Active Stall Control* , 9th Wind Energy PhD Conference, Visby, Sweden, September 2013

Pereira, R., van Bussel, G. J. W., and Timmer, W. A., *Global optimization of horizontal axis wind turbine rotors including active stall control* , EWEA 2014, Barcelona, March 2014

de Oliveira, G., **Pereira, R.**, Ragni, D. and Kotsonis, M., *Modelling DBD Plasma Actuators in Integral Boundary Layer Formulation for Application in Panel Methods*, AIAA 45th Fluid Dynamics Conference, Dallas,Texas, June 2015

Bal, S., **Pereira, R.**, de Oliveira, G., Ragni, D., *Modeling the Influence of DBD Plasma Actuators on the Skin Friction in IBL Formulation*, 54th AIAA Aerospace Sciences Meeting, AIAA SciTech Forum and Exposition 2016, San Diego, January 2016

Battle, E., **Pereira, R.**, de Oliveira, G., Kotsonis, M., *Airfoil Optimisation for DBD Plasma Actuator in a Wind Energy Environment: Design and Experimental Study*, 55th AIAA Aerospace Sciences Meeting, AIAA SciTech Forum and Exposition 2017, Grapevine 2017

Battle, E., **Pereira, R.**, Kotsonis, M., *Airfoil Stall Hysteresis Control with DBD Plasma actuation*, 55th AIAA Aerospace Sciences Meeting, AIAA SciTech Forum and Exposition 2017, Grapevine 2017

Journal Publications:

Pereira, R., Pavel, M. and Schepers, G., *Validating the Beddoes-Leishman Dynamic Stall Model for HAWT environment using MEXICO data*, Wind Energy Journal, 16, 2; 207-219; 2012

Pereira, R., Ragni, D. and Kotsonis, M., *The effect of external flow velocity on the momentum transfer of DBD plasma actuators*, Journal of Applied Physics 116, 103301 (2014); doi: 10.1063/1.4894518

Pereira, R., Kotsonis, M., de Oliveira, G. and Ragni, D. *Analysis of Local Frequency Response of flow to actuation: Application to the dielectric barrier discharge plasma actuator*, Journal of Applied Physics 118, 153301 (2015); doi: 10.1063/1.4933292

de Oliveira, G., **Pereira, R.**, Ragni, D. and Kotsonis, M., *Modelling DBD Plasma Actuators in Integral Boundary Layer Formulation for Application in Panel Methods*, submitted to AIAA journal, (2016-03-J055173)

Pereira, R., Timmer, W.A., de Oliveira, G. and van Bussel, G.J.W., *Design of Actuated airfoils for Wind Energy*, submitted to Wind Energy Journal (WE-15-0180)

Pereira, R., Ferede, E. , Timmer, W.A. and van Bussel, G.J.W., *Optimization of Active Stall Controlled Rotor for HAWT* to be submitted to Journal of Renewable Energy

ABOUT THE AUTHOR

Ricardo Balbino dos Santos Pereira was born in Almada, Portugal, on the 30th November 1984. From a young age he showed an interest in mechanisms and machines, as demonstrated by his ambitious *Lego* creations.



He got his Masters degree in Aerospace Engineering from both TUDelft and Lisbon's Instituto Superior Técnico in 2010.

He loves comic books and board games, traveling, and spending time with his friends. He is curious, he likes challenges, and he is convinced he can be both a musician and a scientist.